SISSA

**Scuola
Internazionale
Superiore di
Studi Avanzati**

Physics Area - PhD course in
Astrophysics and Cosmology

The Black Hole Mass Function:
From Stellar to Supermassive

Candidate:
Alexander Sicilia

Supervisors:
**Prof. Andrea Lapi
Dr. Lumen Boco**

ITN Advisors:
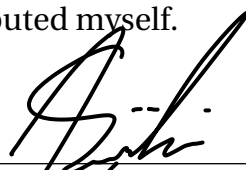**Prof. David Alexander
Prof. Francesco Shankar**
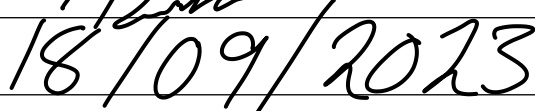
Declaration of Authorship

I, Alexander Sicilia, declare that this thesis titled, "The Black Hole Mass Function: From Stellar to Supermassive" and the work presented in it are my own. I confirm that:

- This work was done wholly or mainly while in candidature for a research degree at this University.

- Where any part of this thesis has previously been submitted for a degree or any other qualification at this University or any other institution, this has been clearly stated.

- Where I have consulted the published work of others, this is always clearly attributed.

- Where I have quoted from the work of others, the source is always given. With the exception of such quotations, this thesis is entirely my own work.

- I have acknowledged all main sources of help.

- Where the thesis is based on work done by myself jointly with others, I have made clear exactly what was done by others and what I have contributed myself.

Signed:

Date: 18/09/2023

"*There is nothing like looking, if you want to find something. You certainly usually find something, if you look, but it is not always quite the something you were after.*"

- J. R. R. Tolkien

SCUOLA INTERNAZIONALE SUPERIORE DI STUDI AVANZATI

Abstract

SISSA
Physics area

Doctor of Philosophy

The Black Hole Mass Function: From Stellar to Supermassive

by Alexander Sicilia

The overall purpose of this thesis is to establish the black hole (BH) mass function, from stellar to supermassive. We divide this work into two: 1) the stellar black hole mass function covering the mass range $m_\bullet \sim 5 - 150\, M_\odot$; 2) the supermassive BH mass function spanning $M_\bullet \sim 10^{6-10}\, M_\odot$; the intermediate BH mass function ($M_\bullet - 10^3 - 10^5\, M_\odot$) will be a byproduct of the continuity equation approach used to track supermassive BH growth and allow for the stitching together of a complete BH mass function. We incorporate a wide range of disciplines including: galaxy evolution, stellar evolution, and black hole evolution. We seek to create a self-contained, self-consistent, model that spans from the present day to $z \sim 10$, which can be used to make estimations of future observational predictions specifically in regards to gravitational wave instruments (Laser Interferometer Space Antenna, Deci-hertz Interferometer, and Einstein Telescope) and electromagnetic detections (James Webb Space Telescope and *Athena*).

Regarding the stellar BH mass function, we mainly consider the standard, and likely dominant, production channel of stellar mass BHs constituted by isolated single/binary star evolution. Specifically, we exploit the state-of-the-art stellar and binary evolutionary code SEVN, and couple its outputs with redshift-dependent galaxy statistics and empirical scaling relations involving galaxy metallicity, star-formation rate and stellar mass. The resulting relic mass function $\mathrm{d}^2 N / \mathrm{d}V\, \mathrm{d}\log m_\bullet$ as a function of the BH mass $m_\bullet$ features a rather flat shape up to $m_\bullet \approx 50\, M_\odot$ and then a log-normal decline for larger masses, while its overall normalisation at a given mass increases with decreasing redshift. We highlight the contribution to the local mass function from isolated stars evolving into BHs and from binary stellar systems ending up in single or binary BHs. We also include the distortion on the mass function induced by binary BH mergers, finding that it has a minor effect predominantly at the high-mass end. We estimate a local stellar BH relic mass density of $\rho_\bullet \approx 5 \times 10^7\, M_\odot\, \mathrm{Mpc}^{-3}$, which exceeds by more

than two orders of magnitude that in supermassive BHs; this translates into an energy density parameter $\Omega_\bullet \approx 4 \times 10^{-4}$, implying that the total mass in stellar BHs amounts to $\lesssim 1\%$ of the local baryonic matter. We show how our mass function for merging BH binaries compares with the recent estimates from gravitational wave observations by LIGO/Virgo, and discuss the possible implications for dynamical formation of BH binaries in dense environments like star clusters. We highlight that our results can provide a firm theoretical basis for a physically-motivated light seed distribution at high redshift, to be implemented in semi-analytic and numerical models of BH formation and evolution.

In terms of the supermassive BH mass function, we consider two main mechanisms to grow the central BH, that are expected to cooperate in the high-redshift star-forming progenitors of local massive galaxies. The first is the gaseous dynamical friction process, that can cause the migration toward the nuclear regions of stellar-mass BHs originated during the intense bursts of star formation in the gas-rich host progenitor galaxy, and the buildup of a central heavy BH seed $M_\bullet \sim 10^{3-5}\,M_\odot$ within short timescales $\lesssim$ some 10^7 yr. The second mechanism is the standard Eddington-type gas disk accretion onto the heavy BH seed, through which the central BH can become (super)massive $M_\bullet \sim 10^{6-10}\,M_\odot$ within the typical star-formation duration $\lesssim 1$ Gyr of the host. We validate our semi-empirical approach by reproducing the observed redshift-dependent bolometric AGN luminosity functions and Eddington ratio distributions, and the relationship between the star-formation and the bolometric luminosity of the accreting central BH. We then derive the relic (super)massive BH mass function at different redshifts via a generalised continuity equation approach, and compare it with present observational estimates.

Finally, we reconstruct the overall BH mass function from the stellar to the (super)massive regime, over more than ten orders of magnitudes in BH mass. Overall we have found that the number of black holes within the observable Universe (a sphere of diameter around 90 billion light years) at present time is about 40 billion billions (i.e. about 40×10^{18}).

This thesis is based on the following publications and submitted papers:

1. The Black Hole Mass Function across Cosmic Times. I. Stellar Black Holes and Light Seed Distribution, by **Sicilia, A.**; Lapi, A.; Boco, L.; Spera, M.; Di Carlo, U. N.; Mapelli, M.; Shankar, F.; Alexander, D. M.; Bressan, A.; Danese, L.; *The Astrophysical Journal, Volume 924*(2), Page 18, January 2022.

2. The Black Hole Mass Function across Cosmic Times. II. Heavy Seeds and (Super)Massive Black Holes, by **Sicilia, A.**; Lapi, A.; Boco, L.; Shankar, F.; Alexander D. M.; Allevato, V.; Carolin, V.; Massardi, M.; Bressan, A.; Danese, L.; *The Astrophysical Journal, Volume 934(2)*, Page 20, July 2022.

3. Evolution of Galaxy Star Formation and Metallicity: Impact on Double Compact Object Mergers, by Boco, L.; Lapi, A.; Chruslinska, M.; Donevski, D.; **Sicilia, A.**; Danese, L.; *The Astrophysical Journal, Volume 907*(2), Page 15, February 2021.

4. Growth of massive black hole seeds by migration of stellar and primordial black holes: gravitational waves and stochastic background, by Boco, L.; Lapi, A.; **Sicilia, A.**; Capurri, G.; Baccigalupi, C.; Danese, L.; *Journal of Cosmology and Astroparticle Physics, Volume 2021*(10), Page 28, October 2021.

5. TOPSEM, TwO Parameters Semi Empirical Model: Galaxy Evolution and Bulge/Disk Dicothomy from Two-Stage Halo Accretion, by Boco, L.; Lapi, A.; Shankar, F.; Fu, H.; Gabrielli, F.; **Sicilia, A.**; *The Astrophysical Journal*, Submitted.

Acknowledgements

It would be foolish of me to begin a series of well deserved thank yous without writing the first to my family, who over the course of these three years have been cheering loud back in Ol' Blighty. For all the days I have been in Trieste, or aboard, not a sun has set without a phone home always happy to chat wind, rain, or shine; though the wind and rain has mostly come from the British side of the call.

To Andrea and Lumen, the two who greeted me on the other side and have taken this journey with me, I thank you. It has been a mission to complete this PhD over the course of roughly a year and half, but we managed and I could not be more grateful for all the help you have given. From proofreaders, to code checkers, to complete courses in Astrophysics, there is nothing you haven't been able to do. Cheers!

For someone who has spent most his life in a town of roughly 30,000 people, the leap to a city in another country sporting 200,000 was daunting. I have been welcomed into an amazing community, to name a few Barry, Giulietta, Rick, Maria, Francesco, Nick, Hugh, Stuart, Florjan. I have left two to thank separately, Louie and Laura, who deserve more than simply a thank you, next round's on me. Two friends who I hope I will have the opportunity to share a pint with again, be it in Trieste or in the far lands of America.

To my friends back in the UK, I might have been over 1,000 miles away but never have I felt closer to you all. Countless nights staying awake chatting absolute nonsense, only to be reminded I live a timezone ahead. Always a laugh, always a smile, and always some ridiculous quote uttered that even with context sheds no light on the reason.

Lastly, to the examiners, thank you for taking the time to read this work I appreciate it massively!

I feel I must sign off the same way I do with all my presentations.

With all that said, pub?

Contents

List of Figures

xviii

List of Tables

List of Abbreviations

Λ**CDM**	**L**ambda **C**old **D**ark **M**atter
ADAF	**A**dvection-**D**ominated **A**ccretion **F**low
AGB	**A**symptotic **G**iant **B**ranch
AGN	**A**ctive **G**alactic **N**ucleus
AIC	**A**ccretion **I**nduced **C**ollapse
BAO	**B**aryonic **A**coustic **O**scillation
BH	**B**lack **H**ole
BHMF	**B**lack **H**ole **M**ass **F**unction
CMB	**C**osmic **M**icrowave **B**ackground
COSMIC	**C**ompact **O**bject **S**ynthesis and **M**onte **C**arlo **I**nvestigation **C**ode
DECIGO	**D**eci-hertz **I**nterferometer **G**ravitational wave **O**bservatory
DF	**D**ynamical **F**riction
DM	**D**ark **M**atter
EdS	**E**instein **d**e **S**itter
EHT	**E**vent **H**orizon **T**elescope
ETG	**E**arly **T**ype **G**alaxy
FLRW	**F**riedmann **L**emaître **R**obertson **W**alker
FMR	**F**undamental **M**etallicity **R**elation
GSMF	**G**alaxy **S**tellar **M**ass **F**unction
GW	**G**ravitational **W**ave
IMF	**I**nitial **M**ass **F**unction
ISM	**I**nter**S**tellar **M**edium
IR	**I**nfra**R**ed
LBS	**L**ittle **B**lue **S**pheroids
LF	**L**uminosity **F**unction
LIGO	**L**aser **I**nterferometer **G**ravitational waves **O**bservatory
LISA	**L**aser **I**nterferometer **S**pace **A**ntenna
LTG	**L**ate **T**ype **G**alaxy
NS	**N**eutron **S**tar
PISN	**P**air **I**nstability **S**uper**N**ova
PPISN	**P**ulsational **P**air **I**nstability **S**uper**N**ova
SED	**S**pectral **E**nergy **D**istribution
SEVN	**S**tellar **EV**olution for **N**-body

SFG	**S**tar Forming **G**alaxy
SFR	**S**tar Formation **R**ate
SMBH	**S**uper**M**assive **B**lack **H**ole
UV	**U**ltra**V**iolet
WIMP	**W**eakly **I**nteracting **M**assive **P**article
ZAMS	**Z**ero **A**ge **M**ain **S**equence

Physical Constants

Boltzmann constant	$k_B = 1.38 \times 10^{-16}\ \mathrm{erg\,K^{-1}}$
Gravitational constant	$G = 6.67 \times 10^{-8}\ \mathrm{g^{-1}\,cm^3\,s^{-2}}$
Parsec	$\mathrm{pc} = 3.09 \times 10^{18}\ \mathrm{cm}$
Proton mass	$m_p = 1.66 \times 10^{-24}\ \mathrm{g}$
Speed of light	$c = 2.99792458 \times 10^{10}\ \mathrm{cm\,s^{-1}}$
Year	$\mathrm{yr} = 3.16 \times 10^7\ \mathrm{s}$
Mass of the Earth	$M_\oplus = 5.97 \times 10^{27}\mathrm{g}$
Solar luminosity	$L_\odot = 3.90 \times 10^{33}\ \mathrm{erg\,s^{-1}}$
Solar mass	$M_\odot = 1.99 \times 10^{33}\ \mathrm{g}$
Solar metallicity	$Z_\odot = 0.0153$
Solar oxygen abundance	$12 + \log(O_\odot/H_\odot) = 8.76$
Dimensionless Hubble parameter	$h = 0.67$
Hubble constant	$H_0 = 100\,h\ \mathrm{km\,s^{-1}\,Mpc^{-1}}$
Critical density	$\rho_c = 2.8 \times 10^{11}\,h^2\,M_\odot\,\mathrm{Mpc^{-3}}$
Density parameter of matter	$\Omega_\mathrm{m} = 0.32$
Density parameter of baryons	$\Omega_\mathrm{b} = 0.05$
Density parameter of dark matter	$\Omega_\mathrm{DM} = 0.27$
Density parameter of radiation	$\Omega_\mathrm{r} = 5 \times 10^{-5}$
Density parameter of the lambda	$\Omega_\Lambda = 0.68$

Chapter 1

From Nothing to Structure

The night sky and human history are one in the same story, be it through wayfinding by the ancient Polynesians to ride the waves on star plotted courses from island to island or the many mythologies which tale the origin of the scattered stars in the Milky Way to more modern events including scientific debates as to our position in our solar system and galaxy. The sun, be it pulled by chariot or orbiting about us, has regulated life on Earth, rising in the morning and setting in the evening thus defining the day. The very concept of time, the continual movement forward, is imprinted on all living things by this periodic motion. Whether you are a pagan worshipper during the Solstice at Stonehenge or seated in prayer in religious halls, the sky has impacted your life dramatically.

The advancement of astrophysics and cosmology as a science lay much by the wayside of history, with observers valiantly trying limited by naked eye. It was not until the 16th century, during the renaissance when we see great changes in the ways we imagine the cosmos. Copernicus brought forward the notion that the Earth was not the centre of existence, that in fact the centre might be the Sun; giving rise to the heliocentric model and the Copernican Principle. A century later brought us Galileo and the telescope, no longer were we restricted by the resolution of our biology.

As history etched forward our understanding of the size of the Universe would extend further, the 20th century commenced with the debate as to the position of distant nebulae in the sky. Some suggested they resided inside our Milky Way, others beyond, but it would be Edwin Hubble, whilst observing the Andromeda nebula in 1920, who determined that many of these nebulae were too distant to be housed in our galaxy and were, in fact, galaxies in their own right. With this discovery and the new revelations on the theory of gravity by Einstein, that of General Relativity, the Universe was becoming increasingly large and the centre less and less defined. The 1950s saw another disagreement, the great big bang debate which waged between George Gamow and Fred Hoyle. Gamow proposed what we now know as the

big bang model of the Universe, whilst Hoyle argued for the steady-state theory which saw no defined beginning or end. It would be the discovery of the Cosmic Microwave Background (CMB), in 1964, at Bell Labs, which would conclude the debate and lead to our modern understanding of the big bang origin of the Universe.

In this Chapter, we shall discuss the basic principles which allow us to describe our Universe focusing on the field of cosmology. First addressing its geometry, through the metric which will be used to determine distances and the most famous of measurements redshift (Sect. 1.1). In Sect. 1.2 we introduce dynamics and evolution. Next, we confront the measurable parameters which define Universe models (Sect. 1.3) before undertaking some examples of their impact on the epochs that are characterised by different species domination (Sect. 1.4). We conclude this Chapter by examining how perturbations in the early Universe evolve to form the grand scale structures, haloes, that become homes to galaxies (Sect. 1.5). Discussions more focused on the field of astrophysics will be deferred to Chapter 2. Novel research can be found beginning Chapter 3 (though an understanding of Chapter 2, Sect. 2.3.2 is highly encouraged prior to beginning Chapter 4), based primarily on the papers Sicilia et al. 2022a, 2022b, for all those interested in the findings of this thesis.

The contents of both Chapters 1 and 2 are possible through the works of Weinberg 1972, 2008 and Cimatti et al. 2020. In addition, lecture material from courses taken at the University of Sussex (given by Antony Lewis, David Seery, Robert Smith, Peter Thomas, and Stephen Wilkins) and SISSA (Carlo Baccigalupi, Enrico Barausse, Alessandro Bressan, and Andrea Lapi) has been used extensively, and, though this material is not publicly available, it would be remissive to omit their mention.

1.1   Geometry

The following will tackle the fundamentals of describing the geometry of the Universe, including the cosmological principle (Sect. 1.1.1), the metric (Sect. 1.1.2) and its use in the definition of distances (Sect. 1.1.3). Redshift will be introduced and established (Sect. 1.1.4) before we conclude with the effect geometry has on the measurements of distances pertinent to observations (Sect. 1.1.5).

1.1.1   The Cosmological Principle

The Copernican Principle, the notion we are not privileged observers, supplanted the idea that all orbited about Earth, but its influence did not end there. The cosmological principle, inspired by Copernicus' heliocentric theory, states that our Universe is homogeneous and isotropic on large enough scales. The consequence of such a statement implies that there is a symmetry in the spatial coordinates, three rotational and three translational. The principle was given little supporting evidence until the discovery of the CMB (see Fig. 1.1), which found a highly isotropic image of the radiation emitted during a period known as recombination that has a maximal photon temperature deviations of $\delta T/T \sim 10^{-5}$. Furthermore, with the advancements in computer processing power, simulations of galaxy distributions consistently produced cosmic webs which gave additional credence to the principle by reinforcing the notion of homogeneity. The caveat being that large enough scales must be considered (> 100 Mpc), meaning the inhomogeneity of Earth is not a damning counter.

Let us take a short aside. It might be believed that homogeneity begets isotropy or isotropy begets homogeneity meaning one only needs the CMB to prove such a principle, this is not the case. Consider electrodynamics briefly, and a constant electric field between infinite planes of opposite charge. At any point between these two planes the field lines can be considered homogeneous, there is spatial symmetry, but they cannot be considered isotropic, as there is a preferred direction towards the negative plate. Now, instead, consider a point charge, if we position ourselves on the point charge we would consider the scenario to be isotropic, we have rotational symmetry, but this situation is not homogeneous due to the radically decreasing electric charge density. Placing ourselves anywhere else other than the point charge will break the isotropy of the scenario as well. It is, therefore, a naïve assumption to say a homogeneous Universe would too be isotropic or vice-versa, and thus proving both independently is required.

1.1.2   The FLRW Metric

With the foundational notion of the cosmological principle we can move forward toward what is known as a space-time metric, and for our purposes we wish to produce the Friedmann-Lemaître-Robertson-Walker (FLRW) metric in spherical coordinates. Due to homogeneity and isotropy we have three spatial and three rotational symmetry derived from six Killing vectors, such a space is defined to be maximally symmetric. A consequence of this maximal symmetry is that all geometries defined as such are unique through their
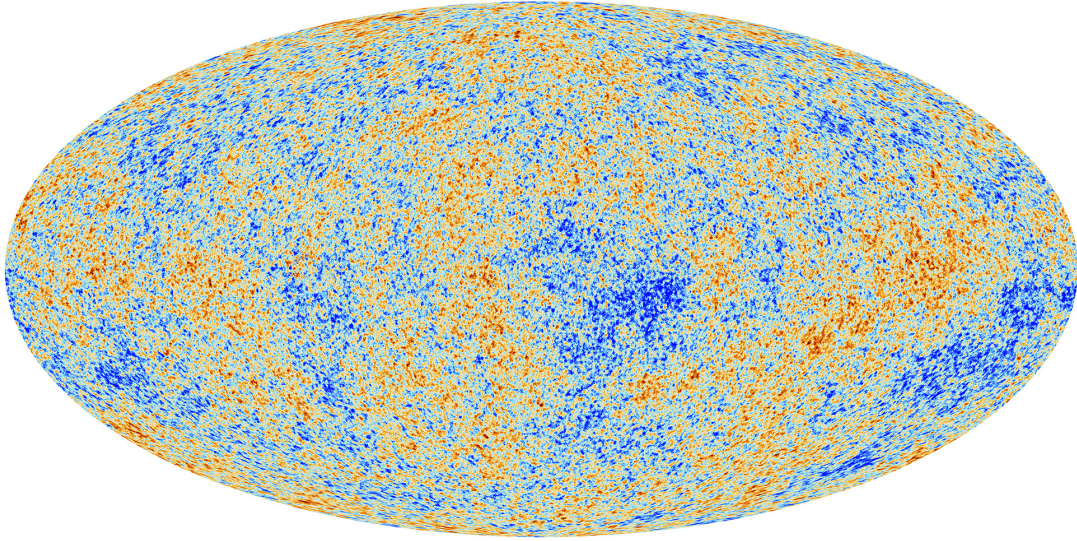
FIGURE 1.1: The Cosmic Microwave Background from the 2013 Planck data release.
Credits: https://www.esa.int/ESA_Multimedia/Images/2013/03/Planck_CMB

curvature and eigenvalues (where the latter is often known as a signature).

For the development of the FLRW metric we must begin with a sphere embedded in a space defined by four spatial dimensions with some radius

$$x^2 + y^2 + z^2 + w^2 = b^2, \tag{1.1}$$

where (x, y, z) are our usual Cartesian coordinates, w is our fourth dimensional coordinate, and b is the radius of the sphere. The line element for such a sphere, in spherical polars, is given by

$$ds^2 = g_{ij}\mathrm{d}x^i\mathrm{d}x^j = a^2\left[\frac{dr^2}{1 - kr^2} + r^2 d\Omega^2\right], \tag{1.2}$$

with the metric g_{ij}, $d\Omega^2 = d\theta^2 + \sin\theta d\phi^2$, $k = |b^2|/b^2$, a is some scaling component, and x^i indicates a coordinate from our system - in this case $(x^1, x^2, x^3) = (r, \theta, \phi)$.

We can extend this frame further without breaking maximal symmetry by introducing a fourth temporal component separate from the spatial components which has some orthogonal universal time[1], where at each given time t we have a maximally symmetric spatial subspace which does not break the restrictions laid down by the cosmological principle. We are left with the

---

[1]A consequence of such implementation is that our spatial coordinates become comoving with time, which will be given definition shortly.

FLRW space-time metric,

$$ds^2 = -c^2 dt^2 + a^2(t)\left[\frac{dr^2}{1-kr^2} + r^2 d\Omega^2\right], \tag{1.3}$$

where we use a signature of $(-, +, +, +)$. It is also true that we can define a gauge such that $c = 1$ without consequence on the form of the metric and thus we shall from hereafter.

The coefficient a has since become dependant on our new temporal variable t and is known as the scale factor, which in essence describes the scale evolution of the Universe which we will return to in Sect. 1.2.2 when we examine in more detail the consequences of Einstein's field equations. It is restricted to only evolve in terms of time, since such a development in the spatial coordinate would violate homogeneity, additionally it must, too, act equally on all spatial components for the exact same reason.

Remaining is our free variable k, the curvature, which due to its definition takes only three distinct values

$$k = \begin{cases} 1 & \text{for a closed Universe;} \\ 0 & \text{for a flat Universe;} \\ -1 & \text{for an open Universe.} \end{cases} \tag{1.4}$$

There is one final alteration which can be made to the metric, and that is a change in variables from $r \to \chi$, such a transformation will resolve one subtle problem with the metric and that is for $k = 1$, $r = 1$ then $\mathrm{d}s^2 \to \infty$. Setting

$$r = S_k(\chi) = \begin{cases} \sin \chi & k = 1; \\ \chi & k = 0; \\ \sinh \chi & k = -1. \end{cases} \tag{1.5}$$

returns the metric

$$ds^2 = -dt^2 + a^2(t)[d\chi^2 + S_k(\chi)d\Omega^2], \tag{1.6}$$

where our coordinate system becomes (t, χ, θ, ϕ) and are all said to be co-moving coordinates, whose positions do not change with the expansion of the Universe.

1.1.3 Cosmological Length, Area, and Volume

The line element $\mathrm{d}s$ allows us to describe any distance, through a coordinate system and a metric g_{ij}, where latin symbology extends over the numerals

$\{1, 2, 3\}$. With this in mind we can express any dimensional quantity simply as

$$\int_B^A ds = \int_B^A |g_{ij}dx^i dx^j|^{\frac{1}{2}}, \tag{1.7}$$

where we sum over the indices i and j. Due to the Cosmological Principle, $g_{ij} = 0$ for $i \neq j$ thus we can express the three base dimensional definitions as

$$dL = ds_i = \sqrt{|g_{ii}|}dx^i \tag{1.8}$$

$$dA = ds_i ds_j = \sqrt{|g_{ii}g_{jj}|}dx^i dx^j \tag{1.9}$$

$$dV = ds_i ds_j ds_k = \sqrt{|g_{ii}g_{jj}g_{kk}|}dx^i dx^j dx^k, \tag{1.10}$$

being length, area, and volume respectively, with $i \neq j \neq k$.

The length between two points in the FLRW metric can be defined by assuming an observer in the centre of our reference frame and following along a radial geodesic until some point χ. Eq. 1.8 can be used, returning the form

$$d_p(t) = \sqrt{|g_{11}|}dx^1 = a(t)\int_0^\chi d\chi' = a(t)\chi. \tag{1.11}$$

which is known as the proper distance. It can be seen that the proper length is a scaling of our comoving coordinate χ caused by the expansion of the Universe experienced by the observer. It is also common to write the comoving distance as $d_c(t)$ and express it in terms of the proper distance

$$d_c(t) = \chi = \frac{d_p(t)}{a(t)}. \tag{1.12}$$

1.1.4   Redshift

Let us consider the dynamics of expansion on the observation of some distance galaxy emitting light. Imagine a pulse of light emitted at time t_{emit}, then another pulse emitted by the same galaxy some moment $t_{\text{emit}} + \delta t_{\text{emit}}$ later. An observer will observe such emissions of light at t_{obs} and $t_{\text{obs}} + \delta t_{\text{obs}}$ respectively. Let us follow these two pulses of light, and arrange our scenario such that the photons[2] follow a radial geodesic using our comoving coordinate system with the observer positioned at the centre. With this setup let us return to Eq. 1.3, the FLRW line element, the radial geodesic means

---

[2]Photon always follow null line elements, therefore $ds = 0$.

dθ = dϕ = 0 and expressing for an inward travelling photon

$$dt = -a(t)d\chi. \tag{1.13}$$

The two paths are described by

$$\int_{t_{\text{emit}}}^{t_{\text{obs}}} a(t)^{-1}dt = -\int_{\chi_{\text{emit}}}^{0} d\chi = \chi_{\text{emit}}; \tag{1.14}$$

$$\int_{t_{\text{emit}}+\delta t_{\text{emit}}}^{t_{\text{obs}}+\delta t_{\text{obs}}} a(t)^{-1}dt = -\int_{\chi_{\text{emit}}}^{0} d\chi = \chi_{\text{emit}}. \tag{1.15}$$

If we consider δt_i to be significantly small than we are left with

$$\frac{\delta t_{\text{obs}}}{\delta t_{\text{emit}}} = \frac{\lambda_{\text{obs}}}{\lambda_{\text{emit}}} = \frac{a(t_{\text{obs}})}{a(t_{\text{emit}})} \equiv 1 + z. \tag{1.16}$$

We can define our system such that $a(t_{\text{obs}}) = 1$ therefore giving the relation $a(t) = 1/(1 + z)$, which is commonly taken.

Here we have cosmological redshift z, which describes the effects of the expansion on the wavelength shift of photons as they travel. Objects in the sky with $z > 0$ appear redder, or in other words their colour has shifted towards red hence the name; it is also true that objects can have $z < 0$ which are said to be blueshifted, with the most famous being the Andromeda Galaxy (M31). The general terms is redshift, and thus z will be referred to as redshift from hereafter.

1.1.5 Distance Measures

So far when determining the distance between two points we have forced our scenarios to operate only on radial geodesics, let us consider a scenario where our object changes on an angular trajectory. Consider an object with some length l and sustained angle dθ, the distance to the object is therefore

$$d\theta = \frac{l}{d_{\text{A}}} \implies d_{\text{A}} = \frac{l}{\text{d}\theta} \tag{1.17}$$

where d_{A} is said to be our angular diameter distance. If we assume dχ = dϕ = 0 then using our proper distance measure with only angular change we obtain

$$d_{\text{A}} = \frac{a(t)S_k(\chi)\text{d}\theta}{\text{d}\theta} = a(t)S_k(\chi) \implies d_{\text{A}} = \frac{d_{\text{c}}}{1+z} \quad \text{for} \quad k = 0. \tag{1.18}$$

Thus we have the following relationship between the angular diameter distance of an object and its comoving distance assuming a flat universe.

There is another type of distance that needs to be analysed, it can be noted that light is affect by the geometry of our Universe through redshifting effects thus it would be required that we examine how light describes the distance between two points. The derivation of such a distance measurement is more involved, requiring the examination of the number of photons received by an observer. The set up is to imagine that a galaxy, emitting a band of light with luminosity L, is being observed by a telescope some distance d_L away then the flux f sustained by the telescope would follow the basic equation

$$f = \frac{L}{4\pi d_{\mathrm{L}}^2}. \tag{1.19}$$

The conclusion of the derivation gives an equation in a comparative form,

$$f_{\mathrm{band}} = \frac{L_{\mathrm{band}}}{4\pi(1+z)^2 S_k(\chi)^2}, \tag{1.20}$$

which can be related to Eq. 1.19 if the luminosity distance takes the form

$$d_{\mathrm{L}} = (1+z)S_k(\chi) = (1+z)^2 d_{\mathrm{A}} \implies d_{\mathrm{L}} = (1+z)d_{\mathrm{c}} \quad \text{for} \quad k = 0. \tag{1.21}$$

To summarise, for a flat ($k = 0$) Universe,

$$d_{\mathrm{c}} = \chi;$$
$$d_{\mathrm{A}} = (1+z)^{-1}d_{\mathrm{c}};$$
$$d_{\mathrm{L}} = (1+z)d_{\mathrm{c}},$$

represent the relationships between measured distances.

1.2   Dynamics

There is much we can learn from the geometry of the Universe, and for observations an accurate understanding is critical, but the Universe needs to be considered as a moving, flowing system. The dynamical nature will allow us to gather more understanding as to the Universe's development over time, allowing us to examine the past, present, and predict the future. To follow will be the introduction of Hubble's Law (Sect. 1.2.1), probably the most well-known law in Astrophysics and Cosmology, and the evolution of

the Universe through the Friedmann Equations (Sect. 1.2.2). We will conclude by introducing the density parameters, observational variables critical to cosmology (Sect. 1.2.3).

1.2.1 Hubble's Law

The timeline of the discovery of Hubble's Law is not simply the work of Edwin Hubble, but the combination of Observers and Theorists over years. A Doppler-like shifting effect was first measured by Vesto Slipher (Slipher 1913). Slipher examined the change in spectral emission observed in his galactic catalogue to those done in a lab and noted their difference, he is credited with publishing the first known documentation of galactic redshift. In 1915, Albert Einstein (Einstein 1915) published his field equations which were then solved seven years later by Alexander Friedmann (Friedmann 1922), whose work we will considered in Sect. 1.2.2. This supported the expansionist theory of the Universe which would then be given observational evidence by Georges Lemaître in 1927. Hubble's work in 1929, which accredited him with the law, conclusively ended a field-wide debate on the size of the Universe and reaffirmed Lemaître's work on an expansion constant.

The form of Hubble's Law is considered to be analogous to a Doppler shift

$$z \approx \frac{H_0}{c} r \implies v = H_0 r. \tag{1.22}$$

Here we have redshift, z, the speed of light, c, the proper distance, r, and, the introduced factor, Hubble's Constant, H_0. The value of Hubble's constant has changed over time as more accurate data has been observed. It begun with Lemaître and Hubble's derivations of 625 $\text{kms}^{-1}\text{Mpc}^{-1}$ and 500 $\text{kms}^{-1}\text{Mpc}^{-1}$ respectively (Lemaître, 1927; Hubble, 1929); to more modern valuations such as 73.2 ± 1.3 $\text{kms}^{-1}\text{Mpc}^{-1}$ and 67.66 ± 0.42 $\text{kms}^{-1}\text{Mpc}^{-1}$ by Hubble Space Telescope/Gaia catalogue (Riess et al. 2020) and Planck Mission (Planck Collaboration 2018) respectively. There is much debate over what might cause the variation in the results produced by each method (be it the method itself, equipment, or something else) but currently distance ladder measurements tend to favour higher values of H_0 whilst those relying on CMB and Baryonic Acoustic Oscillations favour lower.

Though Hubble's Law is famously a law derived from observations, posthumously it has been given a theoretical derivation. It begins with considering the concept of a look-back time, t_{LB}, this is defined as a time system that compares time elapsed in reference to the the Big Bang; if the present day occurs at time t_0, the estimated age of the Universe, and a galaxy emitted

a photon at time t then

$$t_{\text{LB}} = t_0 - t. \tag{1.23}$$

From this point we would consider the scale factor at time t which can be converted using Eq. 1.23 and then complete a Taylor expansion about t_0, with $t_{\text{LB}} \ll t_0$. The derivation is involved but in the process we can define from the expansions two important variables. The first is the Hubble parameter (the time dependent equivalent of the Hubble Constant),

$$H(t) = \frac{\dot{a}(t)}{a(t)}, \tag{1.24}$$

where the dot indicates a temporal derivative, and the second is the deceleration parameter,

$$q(t) = -\frac{\ddot{a}(t)a(t)}{\dot{a}(t)^2}, \tag{1.25}$$

with the double dot indicating a double temporal derivative. We can equate the Hubble parameter to the Hubble constant via

$$H(t_0) = \frac{\dot{a}(t_0)}{a(t_0)} = H_0. \tag{1.26}$$

1.2.2 Friedmann Equations

Until now we have relied on a few elements to be correct, those being the cosmological principle and gravity being a metric theory which are both needed to form the FLRW metric. We now move to further describe the evolution of the Universe, and to do so we must introduce Einstein's Theory of General Relativity, so we can arrive at his Field Equations which have Alexander Friedmann's solutions. It is reassuring that none of this background work would be incorrect if General Relativity where to be disproved tomorrow, if gravity turned out not to be a metric force, however, then it would be back to the chalkboard.

Let us begin, here presented is the compact form of the field equations

$$R_{\mu\nu} - \frac{1}{2}Rg_{\mu\nu} + \Lambda g_{\mu\nu} = \frac{8\pi G}{c^4}T_{\mu\nu}, \tag{1.27}$$

where $R_{\mu\nu}$ is the Ricci tensor, R is the Ricci scalar, Λ is the Cosmological Constant, and $T_{\mu\nu}$ is the stress-energy tensor. The derivation to define the Friedmann Equations is long, and involves a strong understanding of the use of summation notation in order to make it more readable, the results,

however, appear simple. Of important note from the derivation is the requirement to take the stress-energy tensor to be that of a perfect fluid ($T_{\mu\nu} = \text{diag}(\rho, P, P, P)$). The solutions take the following form, we will drop the time dependency on the scale factor for visual clarity,

$$\ddot{a} = -\frac{4\pi G}{3}\left(\rho + \frac{3P}{c^2}\right)a + \frac{1}{3}\Lambda c^2 a, \tag{1.28}$$

$$\dot{a}^2 = \frac{8\pi G}{3}\rho a^2 + \frac{1}{3}\Lambda c^2 a^2 - kc^2 \tag{1.29}$$

where a is our scale factor, ρ is density, P is pressure, and k is the curvature.

There is a third equation, which can be found one of two ways: either through the combination of the first and second solution or by using the First Law of Thermodynamics. Regardless of method the final solution takes the form

$$\dot{\rho} + 3H\left(\rho + \frac{P}{c^2}\right) = 0, \tag{1.30}$$

This final expression is key as it will allow us to examine the evolution of the density of the Universe.

With Eq. 1.30 we can begin to learn how the density of the Universe changes in terms of the scale factor, which in turn gives us an understanding of the relationship between density and redshift. Since we have assumed a perfect fluid then we have the following relationship between density and pressure

$$P_w = w\rho_w c^2, \tag{1.31}$$

where w is the constant which governs the equation of state of the fluid. This constant will take several forms, depending on the fluid we are considering, but we shall leave that for the end. By substituting this into Eq. 1.30 and separating variables we can conclude a generic relationship between the density and scale factor in terms of the constant w,

$$\rho_w = \rho_{w,0}a^{-3(1+w)}, \tag{1.32}$$

where $\rho_{w,0}$ is the density at present day.

With the general form we can now probe different possible Universes. One common example is the Dusty Universe, this is a Universe filled with cold pressureless particles or dust and best describes a Universe which is dominated by the presence of matter. The equation of state constant is $w = 0$, since the scenario is pressureless and thus $P_m \ll \rho_m c^2$, this leads to

$$\rho_m = \rho_{m,0}a^{-3}, \tag{1.33}$$

where 'm' denotes this matter dominated situation. This result is intuitive, if you assume density to only be comprised of matter then you have a decreasing density in the three spatial directions like a box growing larger whilst the gas content remains the same.

The next scenario is a Universe filled with radiation, as opposed to matter, this is a relativistic Universe and has the following equation of state constant $w = 1/3$. This ultimately returns

$$\rho_{\rm r} = \rho_{\rm r,0} a^{-4}, \tag{1.34}$$

where 'r' indicates radiation. Once more, we have expansion in the three spatial directions but we also have an extra scaling factor caused by the redshifting of light.

There is one more final case that will be of interesting note, and is in relation to the Λ term in Eq. 1.27. For a universe dominated by vacuum energy the field equations become $\Lambda g_{\mu\nu} \propto T_{\mu\nu}$, this corresponds to a equation of state relation $P = -\rho$, and thus $w = -1$ implying

$$\rho_\Lambda = \rho_{\Lambda,0}, \tag{1.35}$$

meaning a constant energy density.

The timeline of the Universe follows epochs of component domination. In the early era radiation is expected to dominate and due to its domination the evolution of the energy density best follows that described by $w = 1/3$. Since radiation defuses by a scale factor faster than matter eventually the Universe will move to a matter dominated period, and its energy density is best described by $w = 0$. Lastly the cosmological constant, or vacuum energy, will become dominant compared to both matter and radiation and the evolution of the energy density is then best described by $w = -1$.

1.2.3 Density Parameters

When considering the geometry of our Universe we introduced a curvature factor k and appeared to have quickly forgotten its existence, let us now return to k. Let us introduce a new density known as the Critical Density, representing the average density value to ensure a flat universe. To find the form of this new density, consider Eq. 1.29 when $k = 0$

$$\dot{a}^2 = \frac{8\pi G}{3} \rho(t) a^2 - kc^2 = \frac{8\pi G}{3} \rho(t) a^2, \tag{1.36}$$

note that the Λ term has been absorbed by allowing $\rho(t) = \rho_{\rm m}(t) + \rho_{\rm r}(t) + \rho_\Lambda$ with $\rho_\Lambda = -\Lambda c^2/4\pi G$. Rearrange for ρ the critical density is,

$$\rho_{\rm crit}(t) = \frac{3H^2(t)}{8\pi G}. \tag{1.37}$$

With this new density our former representation of densities becomes slightly redundant as they do not translate any information regarding the Universe's fixed geometry that we have imposed. We therefore shall rescale all our densities in to the density parameters

$$\Omega_{\rm m}(t) \equiv \frac{\rho_{\rm m}(t)}{\rho_{\rm crit}(t)}; \tag{1.38}$$

$$\Omega_{\rm r}(t) \equiv \frac{\rho_{\rm r}(t)}{\rho_{\rm crit}(t)}; \tag{1.39}$$

$$\Omega_\Lambda(t) \equiv \frac{\rho_\Lambda}{\rho_{\rm crit}(t)}. \tag{1.40}$$

Let us not stop here, there is one more density parameter we can define, and that includes returning to Friedmann once again. Consider now Eq. 1.29 without the assumption that the Universe is flat

$$\dot{a}^2 = \frac{8\pi G}{3}(\rho_{\rm m}(t) + \rho_{\rm r}(t) + \rho_\Lambda)a^2 - kc^2. \tag{1.41}$$

Dividing through by $\dot{a}$ we form the density parameters and an additional k based term

$$1 = \Omega_{\rm m}(t) + \Omega_{\rm k}(t) + \Omega_\Lambda(t) - \frac{kc^2}{H^2(t)a^2}. \tag{1.42}$$

We can equate the final term to be equivalent to a density parameter, which shall be called the curvature parameter and takes the form

$$\Omega_{\rm k}(t) = -\frac{kc^2}{H^2(t)a^2} \tag{1.43}$$

and all together we have the following relation which is always true

$$1 = \Omega_{\rm m}(t) + \Omega_{\rm r}(t) + \Omega_\Lambda(t) + \Omega_{\rm k}(t). \tag{1.44}$$

Observations seeking to determine the values of these parameter resolve them at $t = t_0$, much like how observations of the Hubble Constant are determinations of the value of the Hubble parameter at present day. Thus it is more common to find the density parameters in their present day form,

$\Omega_{X,0} = \Omega_X(t = t_0)$.

The first two Friedmann equations can be expressed in terms of these parameters. The first

$$q(t) = \frac{1}{2}\Omega_m(t) + \Omega_r(t) - \Omega_\Lambda(t). \tag{1.45}$$

becomes a new expression for the deceleration parameter. By understanding the evolution of these parameters we can answer a fundamental question of our Universe, whether or not it is accelerating; the criteria are

$$\text{Accelerating Universe}: \quad \frac{1}{2}\Omega_m(t) + \Omega_r(t) < \Omega_\Lambda(t);$$

$$\text{Decelerating Universe}: \quad \frac{1}{2}\Omega_m(t) + \Omega_r(t) > \Omega_\Lambda(t).$$

Current present day estimates of the density parameter fall in line with the notion that the Universe is accelerating.

The second equation becomes an alternative representation for the Hubble parameter, and uses the present day values of the density parameters

$$H^2 = H_0^2(\Omega_{m,0}a^{-3} + \Omega_{r,0}a^{-4} + \Omega_{\Lambda,0} + \Omega_{k,0}a^{-2}). \tag{1.46}$$

1.3   Parameterising a Universe

We have so far defined our geometry using the FLRW metric, and the evolution of the Universe is described by the Friedmann equations. In doing so we have shown a series of variables which characterise this evolution, and together they create cosmological models. Here we will briefly overview how observers determine the values of these new variables.

The most common, and the one used for this work, is the Lambda Cold Dark Matter (ΛCDM) model, where a cosmological constant is assumed and the corresponding dark matter is considered a weakly interacting massive particle (WIMP) with mass $m_{DM}c^2 > 1$ GeV. Dark matter itself is a form of baryonic matter which is not detectable by the emission or absorption of radiation, whilst WIMPs are those which cease significant interaction early in the Universe's history, and are non relativistic which allows them speeds low enough to form structures.

Other forms of dark matter are hot ($m_{DM}c^2 > 0.2$ eV) and warm ($m_{DM}c^2 > 1$ keV), though these are ruled out as possibilities due to the scale at which structures can be form by particles corresponding to these masses. CDM

is no perfect solution, and due to it assumed hierarchical formation process (where smaller structures form and merge to create larger structures) observations do not meet simulation prediction of structure abundance, with simulations predicting the number of small scale dark matter structures much higher than observations return. This is dubbed the missing satellite problem, and is a hurdle which must be considered in all cosmological models.

The ΛCDM model has characteristic values corresponding to

$$\theta_0 = \{H_0 \approx 100h \,\mathrm{kms^{-1}Mpc^{-1}}, \Omega_{\mathrm{m},0} \approx 0.3,$$
$$\Omega_{\mathrm{r},0} \approx 5 \times 10^{-5}, \Omega_{\Lambda,0} \approx 0.7, \ \Omega_{k,0} \approx 0\}, \quad (1.47)$$

where $h \approx 0.7$ is the dimensionless Hubble parameter, $k = 0$, and $\Omega_{\mathrm{m},0} = \Omega_{\mathrm{b},0} + \Omega_{\mathrm{DM},0}$ is the density parameters of baryonic and dark matter respectively; these two new variables take the values $\Omega_{\mathrm{b},0} \approx 0.05$ and $\Omega_{\mathrm{DM},0} \approx 0.25$.

Let us consider, in brief, methods which can be used to measure these parameters. This will be very much akin to a whistle stop tour of approaches, since the in depth details of which are not of major importance for the development of this work but are merely mentioned to allow for further appreciation as to the partnership between theoretical and observational cosmology.

- Type Ia Supernova: The spectacular conclusion of stars with mass $\lesssim$ $8\mathrm{M}_\odot$, when the white dwarf remnant exceeds its maximum possible mass and collapses further into a neutron star. Such an event is able to outshine its host galaxy with peak brightness of absolute magnitude $M = -19$. Along with other known standard candles, objects of known or fixed luminosity such as Cepheid variable stars allowing for more accurate distance calibration, Type Ia supernovae are able to use luminosity distance estimations to probe parameters such as Hubble's Constant.

- Gravitational Waves: New to the scene of parameter probing, gravitational waves are ripples in space-time that occur when large enough objects can cause the shrinking of the distance between two points detectable by laser interferometers. Using large mass binary pairs, neutron star-neutron star or greater, one can return their luminosity distance and, pairing this with methods used to obtained the redshift of the gravitational wave source, an estimate for Hubble's Constant.

- Lensing: Gravitational lensing by intermediate object causes the light from the emitter to warp around the obstruction. This can come in two forms: weak lensing when light shears and creates a mildly distorted

image; strong lensing, when the light is completely bent about the object creating what is called an Einstein ring. Distant measurements can be highly uncertain, and many lensing images are required to gather an accurate understanding of the effect within a region of space. Regardless, the link between lensing, geometry, and matter allow for this approach to be used for determining cosmological parameters.

- Cosmic Microwave Background: The CMB, the fingerprint of recombination, shows the isotropic and homogeneous nature of our Universe with temperature differentials no more than $\delta T/T \sim 10^{-5}$. From this we can extract a temperature power (and polarization) spectrum (see Fig. 1.2), with three notable peaks which can tell us much about the Universe. The first informs us about the curvature, due to its relation with acoustic oscillations on the size of the horizon at matter-radiation decoupling and thus its angular distance. The first peak corresponds to scales which have compressed once, the second are scales which have rarefracted after compression, and its amplitude drop is connected to the gravity of baryons thus it provides information on the baryon density parameter, Ω_b. The third peak represents oscillations which have compressed again (odd peaks will always signify a compression, even a rarefraction) and its amplitude is connected to the total matter density Ω_m.

- Big Bang Nuecleosynthesis: From the initial Big Bang was a Universe filled with radiation, as temperature cooled leptons began to form, then came baryons, and finally nucleons once $T < 10^9$ K. This formation of hydrogen, deuterium, helium, and lithium is known as big bang nucleosynthesis and their relative abundance constrains the cosmic baryon fraction $f_b = \Omega_b/\Omega_m$ and thus provides insight into these cosmological parameters.

- Baryonic Acoustic Oscillations: Once matter has decoupled from radiation their independent baryonic acoustic oscillations (BAOs) continue and can be captured in the matter power spectrum. These BAOs are sensitive to the development of $H(z)$ and d_A, which in ΛCDM is determined by the interplay between Ω_m and Ω_Λ. To use BAOs to probe cosmological parameters one must break the degeneracy between the two variables, before one is able to begin recreating the matter power spectrum.
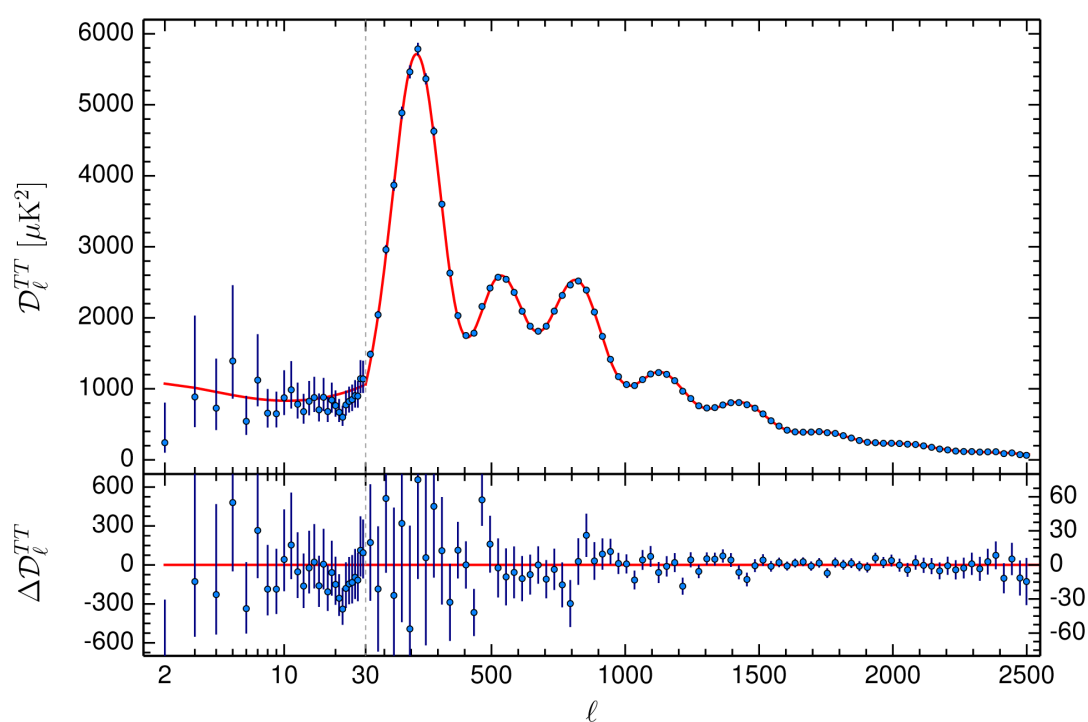
FIGURE 1.2: Power spectrum of the CMB temperature fluctuations with best fit and residuals. Credits: https://www.cosmos.esa.int/web/planck/picture-gallery

1.4   A Universe in Motion

Earlier it was stated that the Universe, in a simplified history, has gone through three eras of species domination. During its infant millions of years the Universe was dominated by radiation, before radiation became sub-dominant to matter, and eventually the cosmological constant would reign supreme in our Universe. The question arising is when did the Universe transition from epoch to epoch.

Matter-radiation equality

First on the envelope is the transition from radiation to matter, for this we will assume that all other components of the Universe are negligible, i.e. $\rho_\Lambda \ll \rho_{\mathrm{m}}$. The point of equality would be when the energy densities of both are equal and thus we simply have

$$\rho_{\mathrm{r}}(a_{\mathrm{EQ}}) = \rho_{\mathrm{m}}(a_{\mathrm{EQ}}). \tag{1.48}$$

Converting to the present and redefining for observable we can produce the following equation

$$\Omega_{\mathrm{r},0} a_{\mathrm{EQ}}^{-4} = \Omega_{\mathrm{m},0} a_{\mathrm{EQ}}^{-3}. \tag{1.49}$$

Implying the point of matter-radiation equality can be given by the expression

$$z_{\mathrm{EQ}} = \frac{\Omega_{\mathrm{m},0}}{\Omega_{\mathrm{r},0}} - 1, \tag{1.50}$$

within ΛCDM, this equates to a redshift value of matter-radiation equality to be $z_{\mathrm{EQ}} \approx 6000$.

Matter-Λ equality

If we follow the previous analysis but replace all references to ρ_{r} with ρ_Λ, remembering $\rho_\Lambda = \rho_{\Lambda,0}$, we acquire

$$z_\Lambda = \left(\frac{\Omega_{\Lambda,0}}{\Omega_{\mathrm{m},0}} \right)^{\frac{1}{3}} - 1. \tag{1.51}$$

For our model this gives a matter-Λ equality value of $z_\Lambda \approx 0.33$.

Moment of Acceleration

It should not be immediately assumed that the z_Λ coincides with the moment when the Universe begins to accelerate, and this can be checked using our deceleration parameter, q. Beginning with Eq. 1.45 let us set $q = 0$

$$\Omega_m + 2\Omega_r = 2\Omega_\Lambda \tag{1.52}$$

We shall put this in terms of the present day density parameter, which for the matter parameter has a relation as such

$$\Omega_m = \frac{\rho_m}{\rho_{crit}} = \frac{8\pi G}{3H^2}\rho_{m,0}a^{-3} = \frac{8\pi G}{3H_0^2}\left(\frac{H_0^2}{H^2}\right)\rho_{m,0}a^{-3} = \Omega_{m,0}a^{-3}\left(\frac{H_0^2}{H^2}\right). \tag{1.53}$$

You can repeat the same process for radiation and the cosmological constant and receive

$$\Omega_r = \Omega_{r,0}a^{-4}\left(\frac{H_0^2}{H^2}\right);$$
$$\Omega_\Lambda = \Omega_{\Lambda,0}\left(\frac{H_0^2}{H^2}\right).$$

Since we are using the present day density parameters we can assume $\Omega_{r,0} \approx 0$ compared to the others and therefore

$$z_{accel} = \left(\frac{2\Omega_{\Lambda,0}}{\Omega_{m,0}}\right)^{\frac{1}{3}} - 1, \tag{1.54}$$

giving us $z_{accel} \approx 0.67$. This means that even before Λ comes to dominate the Universe the accelerating affects of the component has already begun.

1.5 Structure Formation

So far we have spoken much about the Universe as density epochs, defined by the relevance of the corresponding density parameter, and how the interactions and influence of these species can be used to examine the overall evolution. We have not, however, filled our Universe with the very apparent structures we see in the sky, often used to evaluate these parameters. We, therefore, move onto the evolution of, specifically, matter overdensities (Sect. 1.5.2) and their role in the formation of dark matter haloes (Sect. 1.5.3). Firstly, however, the Horizon Problem (Sect. 1.5.1).

1.5.1   The Horizon Problem

To tackle structure formation we must first understand the concept of the particle horizon. A particle horizon is defined by the physical distance light could have travelled since the Big Bang. If a particle is at a point, it does not know of the existence of any particle beyond its horizon. To define a horizon it is best to introduce the concept of conformal time η, which in our reference frame is equal to the comoving distance, and defines the maximum distance a photon could have travelled

$$\eta = \int_0^\eta d\eta = \int_0^t \frac{1}{a(t')} dt'. \tag{1.55}$$

Spaces within a conformal time/distance are considered to be in casual contact. Solving the conformal time for a radiation dominated universe, the scenario considered in the early Universe, finds a conformal time/distance 300 Mpc, or $\sim 1°$ of the sky. This is not in agree with the CMB, which shows correlations spanning the complete sky, indicating that the early Universe must have been in complete casual contact. This is the Horizon Problem, explaining how the Universe was once entirely in casual contact during the time of big bang expansion.

A period of rapid inflation is currently the best supported theory, and states that before radiation domination there was a period where $H \sim$ constant and the scale factor $a \sim \exp(Ht)$, indicating exponential growth. Under such conditions our conformal time takes the form[3]

$$\Delta\eta = (aH)^{-1}. \tag{1.56}$$

Using a Hubble time H^{-1}, which roughly equates to the age of the Universe, we have a restriction on how far light can travel, therefore the limit of casual contact. Since physical scale λ_{phys} expand with the Universe, according to the scale factor, and during inflation $H \sim$ constant, then these scales will drop out of contact when $\lambda_{\text{phys}} \gtrsim H^{-1}$. Even the comoving scale λ can lose casual contact with itself, and defines whether something is inside ($\lambda \lesssim (aH)^{-1}$) or outside ($\lambda \gtrsim (aH)^{-1}$) the horizon.

---

[3]Inflation models split the Big Bang into two phases, the inflationary phase and the Hot Big Bang phase when radiation domination begin. The Hot Big Bang occurs at $t = 0$, therefore the integral in Eq. 1.55 is taken from $t \to 0$.

1.5.2 Evolution of Matter Perturbations

Structures themselves - galaxies, stars, planets - are much more dense than the surrounding Universe. For them to form we must consider the evolution of overdense points as the Universe expands, since it is a reasonable assumption to make that these overdensities will eventually result in the development of the structures in our sky.

To best understand we must consider the conservation of stress-energy, this is the conservation of the component in General Relativity which results in the Friedmann Equations. Beginning with Eq. 1.30 we can convert this to be in reference of our new conformal time

$$\rho' = -3\mathcal{H}(\rho + P), \tag{1.57}$$

where $'$ indicates a derivative in conformal time, $\mathcal{H} = aH = a'/a$. Perturbing this equation with respect to the background creates a complicated expression which introduces additional factors referencing the peculiar velocity and relativistic effects all due to the change in motion with respect to the local flow, similar to those of fluid mechanics. Following conservation laws a general expression, known as the relativistic Euler equation, is derived

$$v' + \mathcal{H}v + \frac{P'}{\rho + P}v + \frac{\nabla \delta P}{\rho + P} + \nabla\Phi = 0, \tag{1.58}$$

where v is the fluid velocity and $\nabla\Phi$ is the effects of the gravitational potential. The equation above applies collectively for total matter, as well as for any non-interacting component, meaning that each component's individual stress-energy tensor is conserved.

It should be of important note that we can define the sound speed as $c_\mathrm{s} = \delta P / \delta \rho$.

Perturbations in Radiation Domination

The first epoch to consider is the radiation dominated era, when the Universe expanded according to a^{-4}, which had $P = \rho/3$ and $c_\mathrm{s} = 1/3$. The conservation laws state

$$\Delta' + \frac{4}{3}\nabla \cdot v = 0, \tag{1.59}$$

$$v' + \frac{1}{4}\nabla\Delta = -\nabla\Phi \tag{1.60}$$

for scales in the sub-horizon regime; the combination of both gives

$$\Delta'' - \frac{1}{3}\nabla^2\Delta = 2\mathcal{H}\bar{\Delta}, \tag{1.61}$$

where we define $\Delta = \delta\rho/\rho$ and the bar indicates an average. In harmonic space we can use the wave number, k, in replace of ∇, giving a much more workable expression. Let us consider sub-horizon scales such that $k \gg \mathcal{H}$, noting that $k \propto \lambda^{-1}$, then

$$\Delta'' + \frac{k^2}{3}\Delta = 0. \tag{1.62}$$

This is a harmonic differential equation and therefore has an oscillating solution which can take the form

$$\Delta = A\sin\left(\frac{k\eta}{\sqrt{3}} + \alpha\right), \tag{1.63}$$

where A is the amplitude and α is the angular offset. These acoustic oscillations, as they are known, correspond to perturbations which are undergoing collapse that are halted by the pressure caused by radiation allowing them to expand once again.

Baryonic matter is coupled to radiation up until the point of recombination (when the interactions between photons and baryons are no longer significant and neutral atoms can form), therefore baryonic perturbations follow the perturbation growth of radiation, more specifically at three-quarters the amplitude, before this event. Photon diffusion between hot and cold regions causes the damping of radiation oscillations and therefore baryonic oscillations, since both are coupled, which slowly smooths perturbations - this is Silk damping (Silk 1968). Baryonic matter, however, decouples from radiation meaning perturbations on scale large enough persist beyond recombination allowing for their growth to continue.

Dark matter, however, is influenced only by the effects of the gravitational potential of the perturbation, which tends towards zero as perturbations expand in physical size during radiation domination. Examining the perturbation growth of dark matter results in a logarithm growth function, known as the Mészáros effect (Mészáros 1974), caused by the lack of resisting gravitational potential thus dark matter perturbation do not grow during radiation domination.

Perturbations in Matter Domination

Recall now that matter is formed from two components, dark and baryonic with the former being the more dominant of the pair. When considering a perturbation in matter we take it to be pressureless, and if we consider events to be after the Epoch of Recombination then radiation no longer has influence over matter, they are said to be decoupled. The laws of conservation state that

$$\Delta'_m + \nabla \cdot v_m = 0 \tag{1.64}$$

for matter, and

$$v'_m + \mathcal{H}v_m + \nabla(c_s^2 \Delta_m) = -\nabla\Phi \tag{1.65}$$

as stated in Eq. 1.58. The scene for matter perturbations can become a jumble of different component equations, but boils down to one for the total matter and another for baryonic matter. Let us consider the results of baryonic matter in perturbations at sub horizon scales

$$\Delta''_b + \mathcal{H}\Delta'_b + k^2 c_{s,b}^2 \Delta_b - \frac{3}{2}\mathcal{H}^2 \Delta_m = 0 \tag{1.66}$$

where we are once more in harmonic space. When $k^2 c_{s,b}^2 \Delta_b > (3/2)\mathcal{H}^2 \Delta_m$ the pressure of the baryonic perturbation can oppose the influence of gravitational collapse. We can, therefore, define the point at which the pressure can no longer support the perturbation, and in terms of a scale we call this the Jeans' length with form

$$\lambda_J = a\lambda = c_{s,b}\sqrt{\frac{\pi}{G\rho}} \tag{1.67}$$

with $k = 2\pi/\lambda$ and $\Delta_b \approx \Delta_m$. This scale defines the divide between growing and oscillating perturbations, where those above this scale will continue to grow. The evolution of the Jeans' length is critical as it sets a limit on the size of matter perturbations during each epoch, with Jeans' length decreasing in value beyond matter-radiation equality.

For matter as a whole we must look to

$$\Delta''_m + \mathcal{H}\Delta'_m - \frac{3}{2}\mathcal{H}^2 \Delta_m = 0 \tag{1.68}$$

where we can use $a \propto \eta^2$ in the matter dominated era to resolve this expression. The solutions to such a differential equation are two-fold, a decaying solution $\Delta \propto \eta^{-3} \propto a^{-3/2}$ and a growing solution $\Delta \propto \eta^2 \propto a$. This means perturbations which are shorter than the Jeans' length will grow with the scale

factor until the Jeans' length becomes large enough and all matter perturbations collapse.

All together we produce a complete history of the growth of perturbations in the Universe:

1. All perturbations go through some initial phase of growth governed by the increasing size of the horizon.

2. As the horizon continues to grow more perturbations of differing size enter, radiation and matter will begin to oscillate due to the conflict between pressure and gravity whilst dark matter perturbations stagnate in size.

3. Once matter-radiation equality occurs dark matter perturbation will begin to grow, whilst matter and radiation are still locked in oscillation.

4. In the lead up to recombination Silk damping will begin to soften radiation perturbations, ultimately impacting coupled matter.

5. At recombination, matter decouples from radiation and falls into the potential wells of the still growing dark matter perturbations, leading to a period of extreme matter perturbation growth.

6. Growth of dark and baryonic matter will continue until it leaves the linear regime, where the analysis so far ceases to be applicable.

The six stages above are only valid for linear growth, which is defined by a density contrast of $\delta < 1$, meaning that these overdensities are not too different from the background value. The CMB shows that this era had densities within the linear regime, the average perturbation being $\delta < 10^{-5}$, and thus this analysis is compatible with the early Universe. These perturbations, however, are growing their density contrast and eventually will break this linear limit. This means we must consider how a highly contrasting perturbation acts, and this will lead to the development of stable dark matter haloes.

1.5.3   Dark Matter Haloes

We now know how density perturbations grow through the first two domination epochs of the Universe, but we have only allowed for low density contrasts and not examined what might occur if these perturbations become too unlike the background. When dark matter, the dominant component in the matter make up of the Universe, grows it could undergo a number of possible dynamical changes. The question becomes will these dark matter

regions collapse and if they do will they continue to a singularity or reach some stable point.

Formation

To consider the formation of non-relativistic dark matter we restrict our Universe to be one that is known as Einstein-de Sitter (EdS), which is matter only ($\Omega_{\mathrm{m}} = 1$). We must consider some perturbation with density $\rho(\mathbf{r}, t) = \bar{\rho}(t)(1 + \delta(\mathbf{r}, t))$, with density contrast

$$\delta(\mathbf{r}, t) \equiv \frac{\rho(\mathbf{r}, t) - \bar{\rho}(t)}{\bar{\rho}(t)}. \tag{1.69}$$

At some early time t_i we consider $\delta \ll 1$, since the Universe is essentially homogeneous, it will also expand with the Universe, though slower due to self gravitation. This is linear growth, as has been previously stated. Beyond the linear regime the overdensity will reach a turn-around time t_{ta}, when the overdensity begins to collapse, which occurs at density $\rho(t_{\mathrm{ta}}) = 5.55\bar{\rho}(t_{\mathrm{ta}})$. For a homogeneous sphere, collapse will occur at time $t_{\mathrm{coll}} = 2t_{\mathrm{ta}}$. It is common to extrapolate the linear regime to uncover at which density contrast the perturbation will collapse, if linear expansion were to continue. For EdS this amounts to $\delta_{\mathrm{coll}} \approx 1.686$, though assuming ΛCDM returns a value with less than 1% derivation, and thus considered equivalent, due to the limited impact the cosmological parameters have on δ_{coll}. This means that higher contrasting overdensities collapse first in the early Universe, implying that the older the system the higher density contrast it first originated from.

This criteria can be made a function of redshift, and when doing so it becomes the critical overdensity of collapse $\delta_{\mathrm{c}}(z)$ with $\delta_{\mathrm{c}}(0) = \delta_{\mathrm{coll}} \approx 1.686$. Any overdensity with $\delta(t = t_0) = \delta_0 > \delta_{\mathrm{c}}(z)$, will have collapsed, where t_0 is the time at present day.

Though useful spherical collapse is a simplified model of how dark matter haloes might form, for starters overdensities are not perfectly spherical nor uniform in distribution. The benefit of such means that their collapse will eventually halt through relaxation processes that cause virialisation. Dark matter haloes can undergo two forms of relaxation that lead to a pseudo-equilibrium state, either by slower phase mixing or more rapid violent relaxation (Lynden-Bell 1967, Binney & Tremaine 2008). Phasing mixing of dark matter particles will lead to the phase-space distribution becoming uniform and thus time-independent, suggesting a stable system. Violent relaxation, the faster of the processes, is the rapid broadening of the energy distribution, normally noted through rapid oscillations in the halo's size,

caused by a time-dependant gravitational potential which becomes independent of time causing the process to stop.

For spherical collapse, the time it takes to complete these processes are estimated to be $t_{\text{vir}} \approx 2t_{\text{ta}}$, on the same scale as the collapse time, and will reach a virial radius $r_{\text{vir}} \approx r_{\text{ta}}/2$, determined by the virial theorem. This amounts to a characteristic virial overdensity of $\rho(t_{\text{vir}})/\bar{\rho}(t_{\text{vir}}) \approx 18\pi^2 \approx 178$. Expanding this simplified model to the ΛCDM Universe, we instead return

$$\Delta_{\text{c}}(z) = 18\pi^2 + 82y - 39y^2, \tag{1.70}$$

where $y = \Omega_{\text{m}}(z) - 1$, as the critical overdensity of virialisation. $\Delta_{\text{c}}(z)$ increases rapidly between $z = 0 - 2$, going from ~ 101 to ~ 171, and plateauing at ~ 178 for high-z. From this we can define the virial mass (and radius) of a halo in terms of the $\Delta_{\text{c}}(z)$

$$M_\Delta = \frac{4\pi}{3}\Delta_{\text{c}}(z)\rho_{\text{crit}}r_\Delta^3 \tag{1.71}$$

It is often the case that simulations will consider a fixed value for Δ_{c}, when defining haloes, the most common value is $\Delta_{\text{c}} = 200$ and the derived values such as mass and radius are indicated with M_{200} and r_{200}.

Evolution

The early Universe leaves us with haloes of extremely low mass, of the order of the Earth ($< M_\oplus$, Diemand et al. 2005), but simulations and observations suggest haloes can grow as large as $10^{16}\,M_\odot$. The process is three-fold: accretion, mergers, and the fact the initial collapsing mass of dark matter haloes increases with decreasing redshift.

Halo accretion is tricky in numerical simulations, since many forming haloes may seem to be increasing in mass through accretion when the change in their reference density changing with redshift is causing the increase mass (Prada et al. 2006, Cuesta et al. 2008, Kravtsov & Borgani 2012, Diemer et al. 2013). It is instead better to analysis the accretion of diffuse matter into some central region defined at initial collapse of the halo. Here we define the concentration of the halo, which is the $c_\Delta \equiv r_\Delta/r_{\text{s}}$ where r_{s} is the scale radius of the halo, and say $c_{\text{coll}} = c_{\delta(z_{\text{coll}})}$. Doing so shows this pseudo-evolution effect, where the central region of a halo evolves much slower than its outer region giving a false speed to dark matter halo accretion.

There are two types of mergers haloes can undergo, either major mergers between haloes of like mass or minor mergers where one halo has a significantly different mass. In its lifetime a halo will merge with many other

haloes, and tracking this history backwards creates a family tree for a much larger halo in the present day. This analysis cannot be done with telescope and, like much of dark matter halo analysis, is done through N-body simulations (Sheth & Tormen 1999b, Warren et al. 2006, Tinker et al. 2008, Watson et al. 2013). Dark matter halo simulations will consider a timeline, split into snapshots, and track trajectories of particles to follow the movement of haloes, which are given form by some definition, in a cosmological box. The build up of halo mass through the merging of predominantly smaller haloes is call hierarchical merging, where some halo early on becomes the dominant candidate for a region and merges with the majority of smaller halos - which cannot grow because of dwindling supplies.

Mass Function in Theory

A mass function, which in Chapters 3 and 4 will be the focus of this work, is a fundamental statistical formulation when analysing any structural phenomena in the Universe. Its purpose is to track the number density of an object per comoving volume, in this instance dark matter haloes, for a given mass at a given redshift (Castro et al. 2016, Li et al. 2019, Cueli et al. 2021). Its complete integral at a given redshift is designed such that it will return the complete number of, in this instance, haloes for that moment in history.

For a halo mass function, it is common to begin estimations using the Press-Schechter formalism but simulation analysis has adapted this approach by using extended Press-Schechter formalism to account for substructures within large halos themselves. The approach begins from a random Gaussian field defining the density fluctuation field δ_K which is itself related to some overdensity of collapse δ_c, which we have seen previous. The resulting formalism for determining the number density of haloes between some mass M and $M + \mathrm{d}M$ can be derived to be

$$\frac{\mathrm{d}N}{\mathrm{d}M} = \frac{\bar{\rho}}{M^2} \left| \frac{\mathrm{d}\log\sigma_K}{\mathrm{d}\log M} \right| \left[\sqrt{\frac{2}{\pi}} \frac{\delta_c}{\sigma_K} \exp\left(-\frac{\delta_c^2}{2\sigma_K^2} \right) \right], \qquad (1.72)$$

where σ_K is the variance of the Gaussian field. In the large square brackets are the elements most likely to change between different formalism, though this is the basic function originally derived. An example of the halo mass function can be seen in Figure 1.3, where its analysis can be found in Barausse et al. 2021 and references therein.
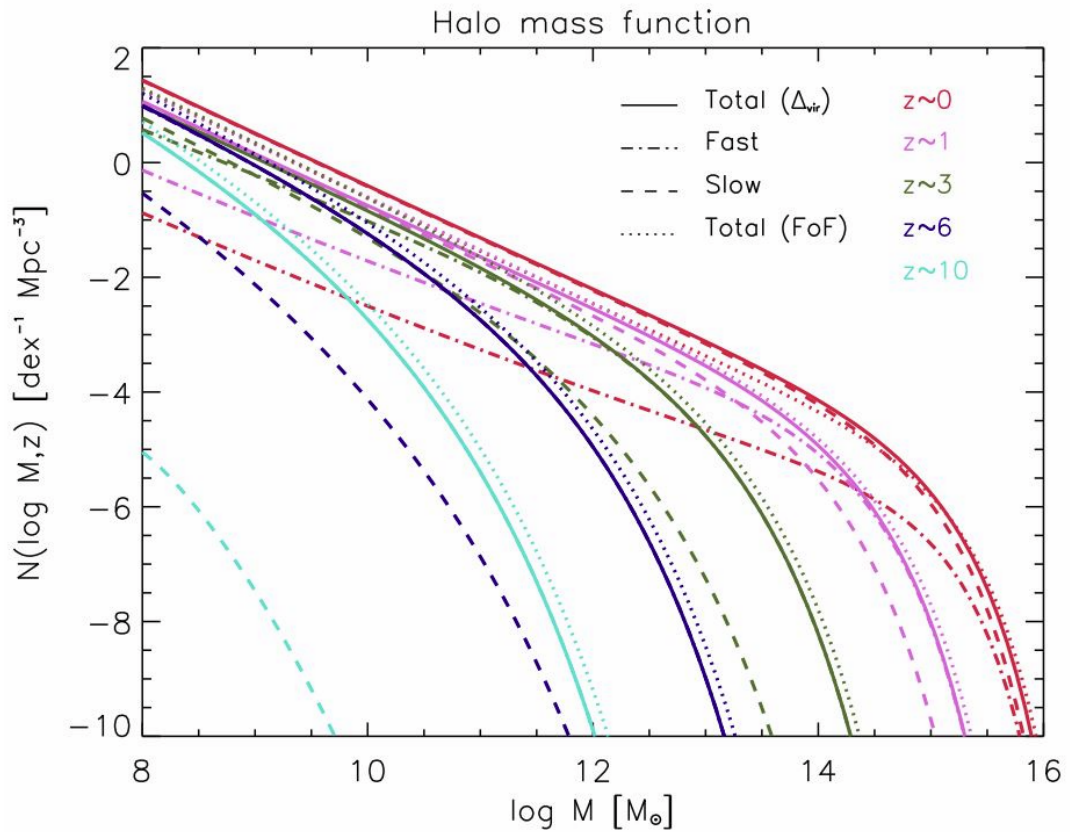
FIGURE 1.3: The Halo Mass Function presented in Barausse et al. 2021. The solid line corresponds to a halo finder using a spherical overdensity approach, with the dash-dotted and dashed lines corresponding to fast collapse growth and slow accretion growth respectively. The dotted line show a comparison with a friends of friends halo finder.

Mass Function in Simulations

Haloes follow long lifetimes, and their ultimate outcome cannot be watched, and it has been made clear that simulations are used to examine haloes as they merge and grow. These simulations are critical as they can be used to test not just haloes, but universe models as the final snapshot must be a recreation of our observed Universe. Simulations are not a unified force though and many differ significantly from each approach, which is riddled with their own benefits and drawbacks (Srisawat et al. 2013, Lee et al. 2014).

Dark matter halo analysis through simulations are able to produce the mass function and merger trees, as well as merger rates and test prescriptions of models. A good example of differences in simulations is the halo finding method, and there are two common approaches. One is the friends of friends method, where particles within a certain so called linking length are gravitationally bound and if particle A and B are bound and particle B and C are, then particle A and C are too bound. There is also the spherical overdensity approach, which acts similar to how we define haloes in theoretical analysis, where we consider some centrally dense point and expand a sphere about it such that its size and mass are in accordance with the virial conditions (where $\Delta_c = 200$ is often taken). Merger trees (Lacey & Cole 1993) themselves are the most common approach to tracking the merger history of a halo, whilst merger graphs are an alternative that attempt to take into account the possibility of halo separation (Thomas et al. 2015, Roper et al. 2020).

The good news, however, is that different approaches manage well to converge on similar results and provide significantly good tests for the halo mass function, merger rate, and merger history following the period of perturbation growth in the Universe when these halos were significantly less massive. The unquestionable truth is that regardless of how these haloes became to be we live in a Universe of galaxies and stars.

So far we have defined a Universe with some geometry, given it a theory of gravity and filled it with species that govern how that geometry grows. We have then taken some initial conditions and expanded quantum fluctuations to form the minute perturbations which would grow into behemoth dark matter haloes. In Chapter 2 we continue this Universe, once nothing and now abundant in structure, and populate it with the spectacular phenomena that excites the night sky.

Chapter 2

From Structure to the Night Sky

Up until now we have considered much about the inner workings of the Universe, its properties and geometry, the very fundamentals of Cosmology. Left to us were haloes of dark matter, filling with baryonic material, it is now time we consider how that baryonic matter might evolve into what we observe in the night sky. It is without question that stars litter what we can observe with the naked eye, but beyond them is a Universe filled with galaxies of countless numbers of stars undergoing a life cycle disconnected from us by all but its light signature. Let us populate these haloes with galaxies (Sect. 2.1), and these galaxies with stars (Sect. 2.2) and consider their cycles which will bring insight towards our final goal, the formation and evolution of black holes (Sect. 2.3).

2.1 Galactic Objects

In this discussion we will encounter the different morphological forms of galaxies (Sect. 2.1.1); discuss the two major galaxy types relevant (Sects. 2.1.2 and 2.1.3); the important scaling relations useful for tracking galactic properties (Sect. 2.1.4); then we conclude with their mass and luminosity functions (Sect. 2.1.5).

This commentary on galaxies is by no means involved, and is intended to be an overview of galaxies with focus on the relevant elements to the future of this work. The field itself is highly complex, and the references provided work as further reading for those interested in the evolving work of galaxy statistics and evolution.

2.1.1 Morphology

Galaxies come in an eclectic mix of many forms, and finding a classification for them is no easy feat. Such attempts can be plagued with numerous difficulties caused by observational bias, by the equipment itself or the available
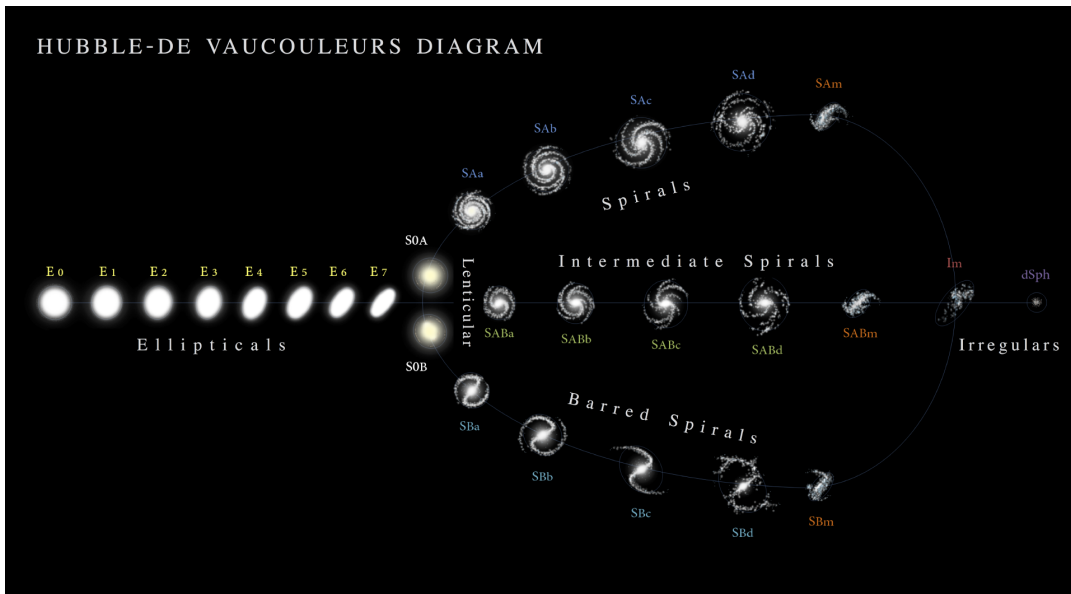
FIGURE 2.1: The Hubble-De Vaucouleurs classification of galaxies. Credit: Antonio Ciccolella & M. De Leo

wavelength of observations - these matters are only exacerbated when extending to high-z galaxies. Further complicating the issues are how two like galaxies in one classification have the potential to exhibit very different behaviours.

Regardless the instinctive natural want to categorise was first completed by Hubble, and extended by Gérard de Vaucouleurs, using a survey of $z \sim 0$ galaxies. This system is rather simple in form, and is widely known and used in astrophysical literature. In Fig. 2.1, we can see a trident representation of galaxies categorised by their morphology. Beginning from the left we have the ellipticals, signified by E, extending from class $0 - 7$[1], which represents the galaxy's eccentricity with lower numerals meaning more circular. At the forking point we see S0 galaxies, called lenticulars, where the faint presence of a central structure can be indicated. The de Vaucouleur revision introduced the splitting of S0 galaxies in those of A and B class, where A represents the galaxy having a central bulge whilst B a central bar. There is also the combination AB, seen in the intermediate spirals path reserved for galaxies which show signs of having both features. The lower case a-d denote a decreasing prominence of the central feature, and the m indicates an irregular form of the classification. Im describes irregular galaxies with no defining

---

[1]The number value is the rounding of 10ϵ where $\epsilon = (a - b)/a$ and a and b are the semi-major and -minor axes respectively.

central feature, and beyond are dwarf galaxies which are classified as galaxies with mass and luminosity an order of magnitude lower than the Milky Way.

A further simplification to this classification is often adopted, and that is the use of Early-Type and Late-Type Galaxies (ETGs and LTGs respectively) for those in the local Universe ($z \sim 0$). ETGs correspond to the left hand side of Fig. 2.1, ellipticals and lenticulars, whilst LTGs represent spirals and irregulars. Since the latter are predominantly found to be star forming they are often associated with star forming galaxies (SFGs), whilst ETGs are commonly seen to be non star forming, said to be passive or quiescent. It should be stressed that common attributes given to galaxies groups do not indicate that all galaxies of said classification share such property, therefore an elliptical, or ETG, can be star forming, for example.

2.1.2 Early-Type Galaxies

We begin with ETGs - the ellipticals, lenticulars, and dwarf variants of the same type. Noted for their limited availability of cold gas, these galaxies are commonly found with little to no star formation and harbour stellar masses in the range of 10^{9-12} M$_\odot$. Their dwarf versions, however, have lower masses $\leq 10^9$M$_\odot$. Due to ETGs having limited star formation, and thus no new stars, the bluer and lower life expectancy population has died out and therefore ETGs appear redder than LTGs, where the redder they appear correlating positively with their stellar mass. This ETG redness constitutes the bulk of the red sequence in the galaxy colour-magnitude relation.

Spectral energy distribution (SED) analysis is the method by which you examine the energy emission of a galaxy as a function of the wavelength, and thus the emissions of the stellar population for a given object. You can either fit a theoretical spectral continuum, full spectral fitting, or examine individual absorption lines - with the Lick indices being useful in breaking the degeneracy between age and metallicity. Either approach will return population ages of greater than a few Gyr, and provide a set of scaling relations: age-velocity dispersion, metallicity-velocity dispersion, and α-element abundance-velocity dispersion; all of which are positively correlated.

Since the velocity dispersion and mass are connected in there own scaling relation, it is common to consider these relations in reference to the mass of the ETG. The sum total of all three states that a more massive an ETG the older its population will be (age-mass relation), the higher its metal enrichment (metallicity-mass relation) and the higher abundance of alpha elements relative to iron (α-element abundance-mass relation). The most
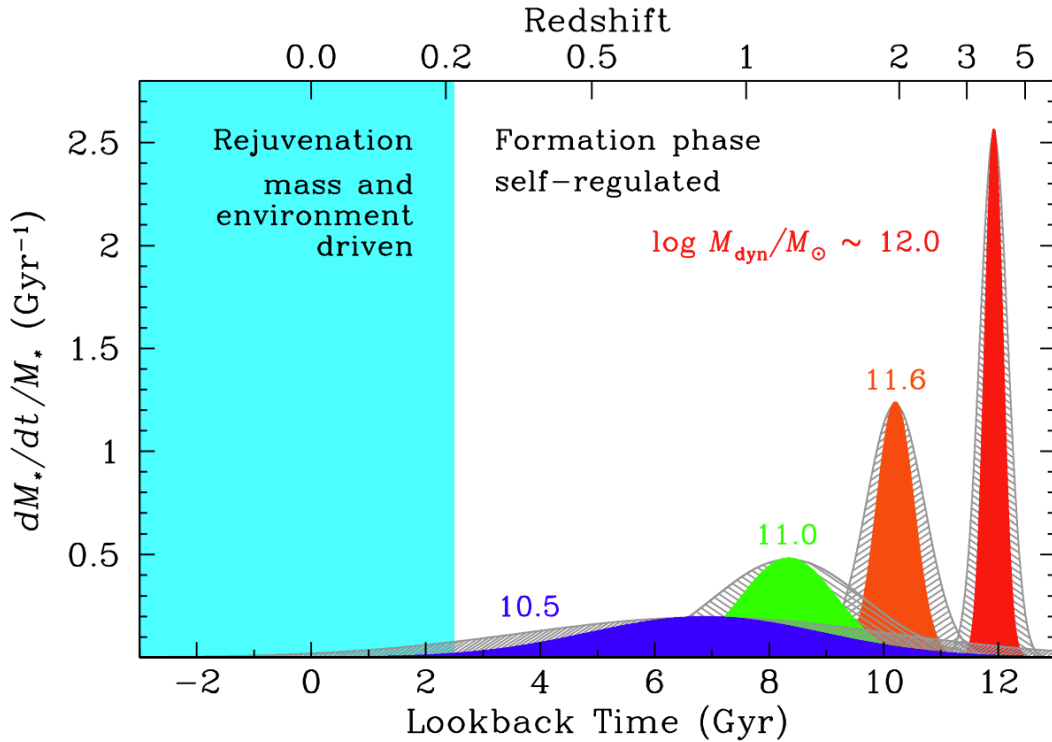
FIGURE 2.2: Model of ETG star formation duration categorised by mass, as seen in Thomas et al. 2010.

massive ETGs have population ages up to roughly the age of the Universe, metal enrichment $\sim 2.5Z_\odot$ and $[\alpha/\text{Fe}] \sim 0.3$. The last of the relations is useful to further understand the evolution of ETGs, since α elements are produced during short timescale events, such as type II supernovae, much heavier elements, critically iron, come from type Ia supernovae. If star formation is short than it can be assumed that the impact of type Ia supernovae is limited by the available time scale and thus the alpha abundance much higher, meaning more massive ETGs much have formed much earlier than those less massive and with a much shorter episode of star formation. The suggestion, brought about by all three of these relations, is that ETGs, specifically ellipiticals, undergo a form of down sizing, where more massive ETGs form earlier than less massive. This is visualised in the sketch in Fig. 2.2. Such a representation is not exact, and galaxies are thought to have many episodes of star formation, but the average of the population can be considered to have one major burst of star formation following the sketch.

The short lived star formation phase of massive ETG progenitors is characterised by a constant star formation rate (SFR) ψ, where a gas depletion

time can be given by

$$t_{\text{depl}} = \frac{M_{\text{gas}}}{\psi}, \tag{2.1}$$

with M_{gas} being the gas mass of the galaxy, after which star formation will rapidly decrease. The initial episode of star formation for ETG progenitors typically lasts 1 Gyr, which presents a critical restriction in galactic evolution modelling and will be address more in Chapter 4. Ultimately, this is a simplistic model since gas reserves are subject to interactions such as stellar feedback. Stars create Strömgen spheres (Strömgen 1939) about themselves, regions of ionised hydrogen or removed gas, through stellar winds and photoionisation, locally restricting the star formation potential. For more massive stars, O and B class, their Strömgen spheres can have radii as large as the stellar disk, releasing it from the galaxy. If the removed gas does not have the escape velocity of the galaxy then it can return to the stellar disk at a later time and alternate location. In addition inflows from galactic accretion, and gas recycling from the conclusion of short lived stars can increase the gas reservoirs. These all are feedback mechanisms which can either be positive (increase ψ) or negative (decrease ψ), impacting the star forming duration of these galaxies.

The extent of an elliptical, its surface brightness profile, for all forms from E0 to S0 is best described by a Sérsic profile with the form

$$I(R) = I_e \exp\left\{ -b_n \left[\left(\frac{R}{R_e} \right)^{1/n} \right] \right\}, \tag{2.2}$$

where I is the intensity, the luminosity per unit area, n is the Sérsic index, and $b_n \approx 2n - 1/3 + 4/(405n)$. The Sérsic index takes values $2 \leq n \leq 10$, where n increases for increasing mass. In several instances the brightness of an elliptical deviates from the estimated Sérsic profile within the central region at some break radius $R_{\text{b}} \sim 0.01 R_{\text{e}}$. Ellipticals which show a drop in the profile in the central region are called cored, whilst those that continue to follow the estimated profile are coreless[2]. The presence of a core, or lack of, correlates with other properties of ellipticals such as, but not limited to, stellar age (younger stars tend to be found in coreless ellipticals), shape (cored are typical triaxial, whilst coreless are oblate spheroids), and α enhancement (with cored ellipticals showing signs of enhancement).

For lenticular galaxies, the surface brightness is more similar to a spiral

---

[2]There is also the case that ellipticals can show an excess of brightness in the central region, meaning the Sérsic profile under predicts. In these instance the ellipticals are still said to be coreless.

galaxy's central bulge with an exponentially declining disk. As such a lenticular surface brightness profile is given by a Sérsic profile with $n = 2$ in the central region (though some lenticulars can lack this central bulge element), and $n = 1$ in the outer disk. The distinct difference between lenticulars and spiral galaxies is their lack of spiral star forming arms in the outer region.

The limitation in star formation for ETGs can be seen in their gas content, specifically the temperature found through X-ray emissions. The temperature of a gas can be estimated through the bremsstrahlung cut off, which for clouds within ETGs returns temperatures in the region of $T \sim 10^{6-7}$ K which is inconducive for star formation. Cold gaseous regions are not entirely absent, leading to the $\psi \neq 0$ in ETGs, and is found in neutral or molecular hydrogen clouds, though their abundance is sparse.

2.1.3 Late-Type Galaxies

Moving to the right hand side of the Fig. 2.1, we have the spiral galaxies, along with irregulars, these are our LTGs or, due to their star forming nature, SFGs. In contrast to ETGs, these galaxies are less massive ($M_{\mathrm{gal}} \approx 10^{9-11} M_\odot$) and have active star formation ($\psi \approx 0.1 - 30 \ M_\odot \mathrm{yr}^{-1}$), with irregulars occupying the lower bounds of these ranges. Since LTGs are actively star forming young, high mass, stars are present within them - primarily in the outer regions, such as the spiral arms of spiral galaxies - and thus they are much bluer in hue compared to ETGs. This means LTGs make up the bulk of the blue cloud in the colour-magnitude diagram of galaxies.

The physical structure of spiral galaxies consists of spiral arms orbiting about a central region, which could be in the form of either a stellar bar ($\sim 60\%$ of all case), stellar bulge, or pseudo-bulge[3]. The surface brightness is two fold, similar to lenticulars, with one Sérsic profile describing the central region and another the outer disk. Typically the outer disk is well described by $n \approx 1$, but the central region is dependent on the nature of the central structure. Spheroidal bulges have a representation closer to ellipticals, with an index $2 \leq n \leq 4$, pseudo-bulges on the other hand experience flattening due to rotational effects and more closely resemble the disk, or central region of a lenticular galaxy, taking values $n \leq 2$. The observation of a spiral galaxy is dependent on their orientation due to their planar shape, meaning a Sérsic profile best describes a spiral galaxy face-on, face-on being when the vector of angular momentum is directed towards the observer. The intensity is therefore a function of the angle of inclination i, $I = I_{\mathrm{obs}} \cos i$. For edge-on spirals ($i = 90°$), where the thickness of the galactic disk can be observed,

---

[3]In some rare instances both a bar and a bulge (typically a pseudobulge) can be present, which is the case for M91.

the stellar luminosity density can be probed using

$$j_{\text{star}} = j_{\star,0} \exp\left(-\left[\frac{R}{R_{\text{d}}} + \frac{|z|}{h_{\star}}\right]\right), \tag{2.3}$$

where $h_{\star}$ is the scaleheight of the disk, $j_{\star,0}$ is the central stellar emissivity, and R_{d} has the relation $h_{\star} \approx 0.1 R_{\text{d}}$ for a thin disk scenario.

The impressive arms of spirals are not a uniform feature across this family of galaxies, and they come in many different forms. There are grand design spirals, those that have few but very distinct sweeping arms; intermediate spirals where the arms are less coherent but still present; flocculent spirals, where the arms are near non-existant, leading more to a disc of stars with vague structure.

All these stellar structures are said to be within the stellar halo of a galaxy. This halo, itself, extends beyond the disc and includes stars not associated with the main body, such as isolated star clusters, diffuse stars, and stellar streams. These structures are still gravitationally bound to their host and are likely the results from merger events or galactic fly-bys, especially in the case of stellar streams. The extent of stellar haloes is hard to judge due to their limited brightness, being formed of diffuse or isolated features, but they do contain some of the galaxies most metal poor regions and thus metal poor population.

To accommodate the high SFR the gaseous make up of LTGs is much cooler than that of ETGs. The interstellar medium (ISM) comes in three flavours, cold ($T \leq 10^2$ K), warm ($10^3 \leq T \leq 10^5$ K), and hot ($T \geq 10^6$ K). The most abundant element is neutral hydrogen HI, which is observable using the 21 cm line caused by the forbidden electron flip transition. If a HI region has a column, line-of-sight, density $N_{\text{HI}} < 10^{21}$ then self-absorption is not significant enough to prevent estimates of the HI mass of a galaxy.

These neutral regions are, in fact, not fully neutral and can contain heavy ionised metals, notable are carbon and oxygen which can be observed through fine structure transition observations caused by collisional interactions. Regions which show signs of these transitions are also known as photodissociation regions, and are notably low in density where ultraviolet (UV) light can penetrate and heat up carbon monoxide (CO) molecules causing these transitions to occur. Probing these regions reveals they are cold ISM.

If the incident light is energetic enough it can excite hydrogen atoms turning them into ionised hydrogen, HI $\rightarrow$ HII, in a process known as photoionisation and happens around O and B class stars. To observe photoionisation the Balmer series for hydrogen is useful, where electrons captured by hydrogen atoms tumble down the fixed available energy levels emitting characteristic photons as they do; in any instance when an electron drops

from some higher energy state straight to the ground energy state of hydrogen it is known as a Lyman emission, which is a crucial grouping of emissions for a myriad of high-z studies. Another such emission is the oxygen doublet, present because oxygen has a similar ionisation potential as hydrogen and its emission comes in the forms of two possible characteristic energies corresponding to wavelengths of 3726 Å and 3729 Å. The doublet is the second strongest feature of SFGs, behind Hα from the Balmer series (transition $3 \rightarrow 2$). Line emissions lead to temperature estimates which show HII regions to be the warm ISM.

Photoionisation from stars is one process in which the galaxy self-regulates star formation through feedback. Another method is through supernovae which send shock waves through the ISM, heating the gas and leading to ionisation. This form of feedback is responsible for the creation of the hot ISM.

Another key gaseous region for LTGs is that of molecular clouds, formed of molecular hydrogen. These regions are extremely dense ($N_H > 10^{21}$ cm^{-2}) and cold ($T < 40$ K), due to the effective cooling mechanisms possible by the molecules, and are ideal locations for cloud collapse to form stars. H$_2$, however, can be photodissociated easily, meaning stars within the vicinity can cause negative feedback, though due to the dense nature of H$_2$ clouds, in some instances, they are able to undergo the process of self-shielding. The outermost layer of molecular hydrogen creates a protective barrier, enduring the brunt of photodissociating photons whilst the internal content is able to stay cool.

There is a close connection between gas availability and star formation, and this is shown in the Schmidt-Kennicutt (Schmidt 1959; Kennicutt, 1989) law which relates the surface density of gas Σ_{gas} to the SFR surface density Σ_{SFR}. The law is simple in form

$$\Sigma_{\text{SFR}} \propto \Sigma_{\text{gas}}^{\gamma}, \tag{2.4}$$

where γ is a value to be determined and is dependant on the galactic population being considered. This scaling relation takes a general value of $\gamma \approx 1.4$, which covers a wide range of SFG types and is the best fit for a total population. The law, however, is not best suited for metal poor or low surface brightness galaxies, which show a raising or lowering of the slope respectively.

A brief mention of the SFR of LTGs, from astroarchaeology we know that the star formation history of SFGs shows an almost constant initial SFR before collapsing exponentially, taking the form $\psi(t) = \exp(-t/t_\psi)$ with $t_\psi > 6$ Gyr.

2.1.4 Scaling Relations

From LTGs and ETGs comes a series of scaling relations, for the work below we need only a few and they will be listed. These include the fundamental metallicity relation, the Magorrian relation (discussion of which will be deferred to Sect. 2.3.1), and the galactic star forming main sequence.

The fundamental metallicity relation (FMR) returns metallicity $Z(...)$, where the dependent variables can differ but in general include at minimum $M_\star$ (Tremonti et al. 2004; Mannucci et al. 2010, 2011; Zahid et al 2010). For this work we use Mannucci et al. 2011[4], the relation takes the form

$$12 + \log\left(\frac{O}{H}\right) = \begin{cases} 8.90 + 0.37 - 0.14s - 0.19m^2 + 0.12ms - 0.054s^2 & \text{for } \mu_{0.32} \geq 9.5; \\ 8.93 + 0.51(\mu_{0.32} - 10) & \text{for } \mu_{0.32} < 9.5, \end{cases}$$

$$(2.5)$$

where $m = \log M_\star - 10$, $s = \log \psi$, and $\mu_{0.32} = \log M_\star - 0.32 \log \psi$. The proxy $12 + \log(O/H)$ is used observationally in place of $Z(\psi, M_\star)$, and the relation between the two is $\log Z \approx 12 + \log(O/H) - 10.575$. The subtracting factor is the combination of the solar oxygen abundance $\log(O_\odot/H_\odot)$ and solar metallicity $Z_\odot$. Fig. 2.3 shows Eq. 2.5.

The galactic star forming main sequence is named such that it is analogue to the main sequence of stars themselves, though the two have little relation. A fundamental relationship for the semi analytics of galactic evolution, the relation seeks to find $\psi(...)$, where the dependencies may change from study-to-study (Speagle et al. 2014; Popesso et al. 2022). Speagle et al. 2014 provides, in its introduction, a myriad of other studies which have been involved in probing the free parameters in the generally expression $\log \psi = \alpha \log M_\star + \beta$, where α and β are those free parameters and are unique for a given redshift. The relationship, itself, is reliable up till $z \sim 6$. For Speagle et al. 2014, $\psi(M_\star, t)$ and takes the form

$$\log \psi = (0.84 - 0.026t) \log M_\star - (6.51 - 0.11t), \qquad (2.6)$$

where t represents the elapsed age of the Universe. Fig. 2.4 shows the form of this relationship for several redshifts.

---

[4]Based off of the established work from Mannucci et al. 2010, which used the SDSS-DR7 including ~ 140000 galaxies.
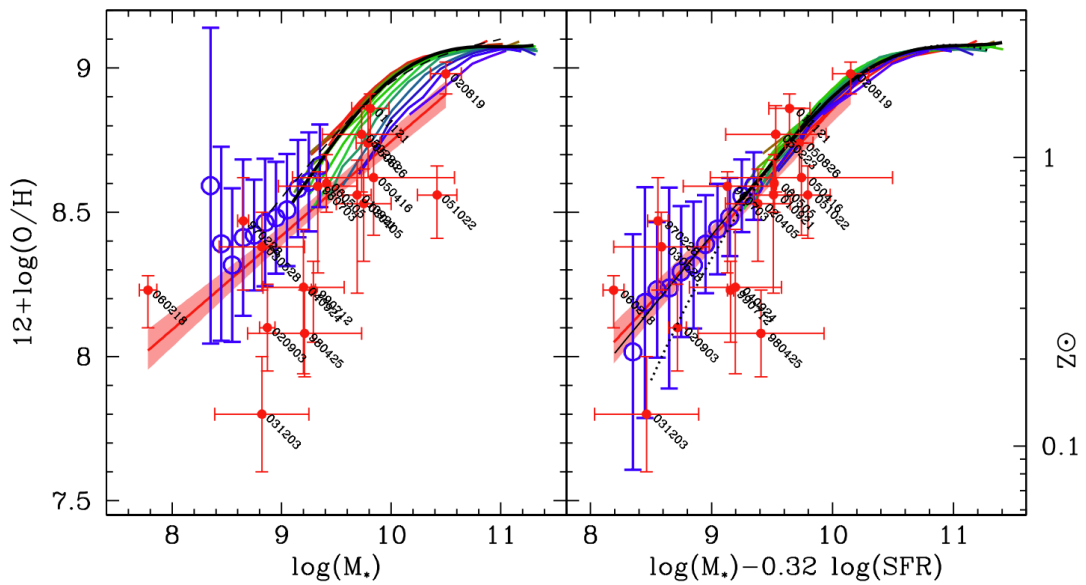
FIGURE 2.3: From Mannucci et al. 2011. In both panels: The coloured lines represent the SDSS galaxies used in Mannucci et al. 2010, with colour scaling red to blue for increasing SFR. The black line is the polynomial fit relation from Mannucci et al. 2010. Red dots represent host galaxies with gamma ray burst detections, blue circles the low mass SDSS galaxies. Left panel also includes: black dashed line representing the relation from Zahid et al. 2010, red line with 1σ band showing the linear fit for gamma ray burst galaxies. Right panel includes: a black dotted line representing the FMR 2nd degree fit extrapolation for SDSS galaxies in Mannucci et al. 2010, and the red line with 1σ band is Eq. 2.5.
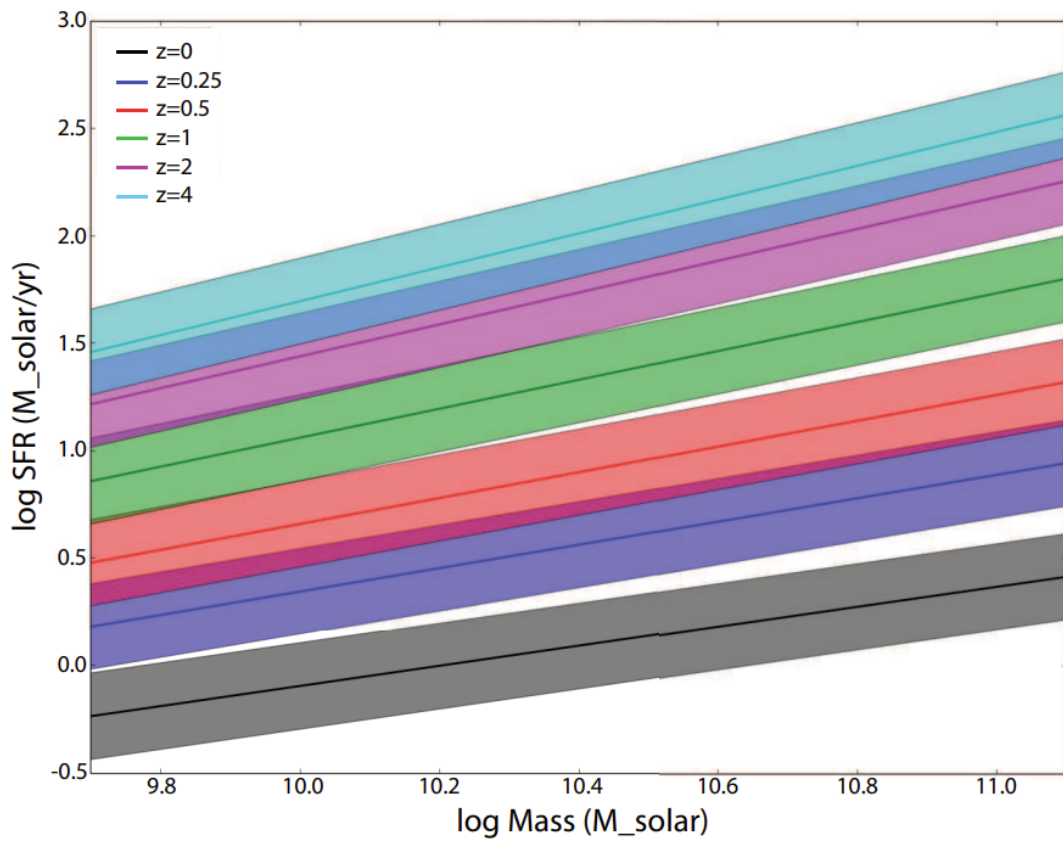
FIGURE 2.4: The galactic star forming main sequence from Speagle et al. 2014.

2.1.5   Mass and Luminosity Function

Mass Function

The mass function is a critical formula in the study of astrophysical populations, this work will consider the black hole mass function, and later we will consider the stellar initial mass function, but galaxies are no exception when it comes to the analysis of a mass function.

For galaxies there are many types of mass functions, including the halo and gas mass function, here we will restrict our discussion only in terms of the stellar mass, also known as the galaxy stellar mass function (GSMF), derived from near-infrared observations. A double Schechter function is found to best represent the data discovered taking the form

$$\frac{\mathrm{d}^2 N}{\mathrm{d}M_\star \mathrm{d}V} = \Phi_1(M_\star) + \Phi_2(M_\star), \tag{2.7}$$

with

$$\Phi_i(M_\star) = \frac{\Phi_i^*}{M_i^*}\left(\frac{M_\star}{M_i^*}\right)^\alpha \exp\left(-\frac{M_\star}{M_i^*}\right) \tag{2.8}$$

where Φ_i^* is a normalisation constant, α is the exponent defining the power-law behaviour when $M_\star \ll M_i^*$, and M_i^* is known as the knee mass corresponding approximately to the value when the exponential decline becomes prominent.

When considering the different galaxy types, that of ETGs and LTGs, we have often mentioned the difference in their stellar masses, with ETGs being the larger. This would thus imply that ETGs would form much the bulk of the higher mass end of the GSMF, whilst LTGs the lower; causing the need for a double Schechter function. Fig. 2.5 shows this relation, where we see how spheroid dominated galaxies, akin to ETGs, dominate the mass function for $M_\star > 10^{10.3} M_\odot$, whilst disk dominated, similar to LTGs, are most prominent in the lower masses.

From a mass function you can derive the density function of the object via the complete mass integral of the function multiplied by the mass in question, for the GSMF this corresponds to

$$\rho_\star = \int \mathrm{d}M_\star M_\star \frac{\mathrm{d}^2 N}{\mathrm{d}M_\star \mathrm{d}V}. \tag{2.9}$$

The density can be broken down, and the relative contribution of each type found; spheroid dominated galaxies constitute $\sim$ 70% of the stellar mass density, whilst disks make up the remaining $\sim$ 30%.
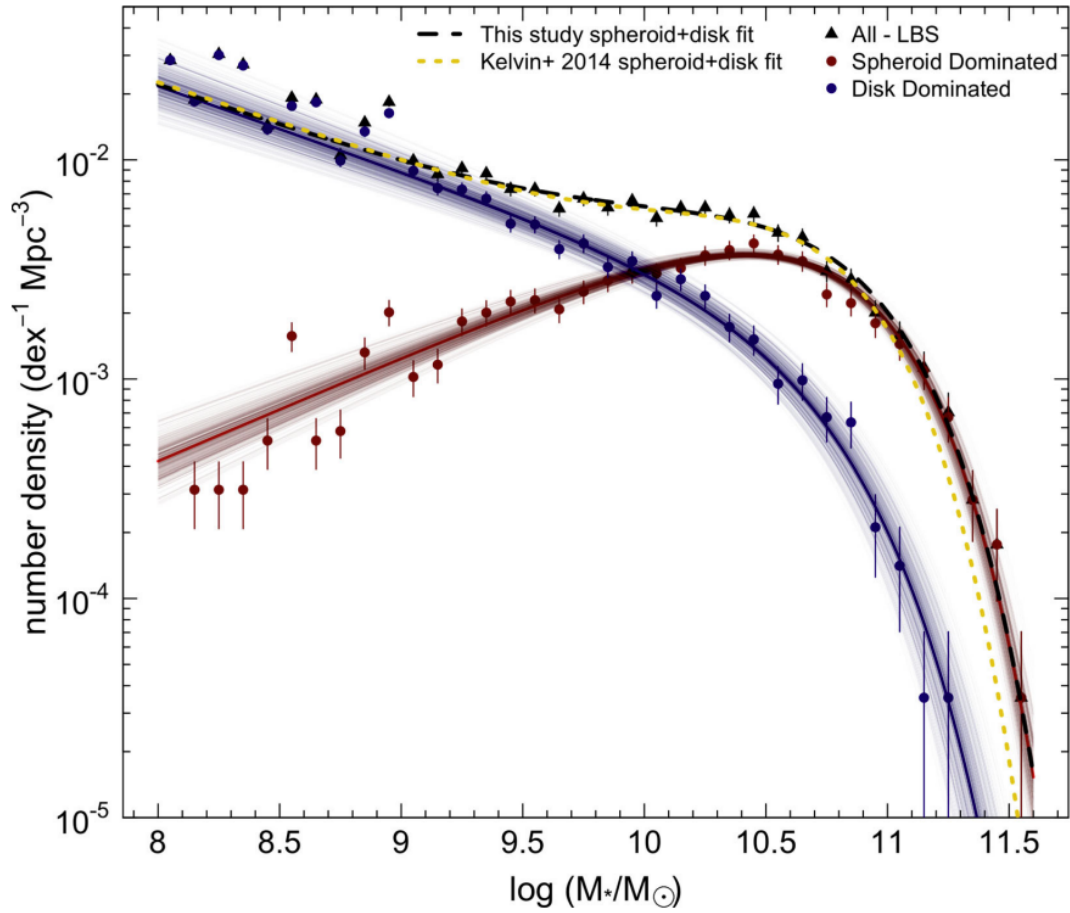
FIGURE 2.5: From Moffett et al. 2016, the GSMF split by dominate morphological component. The red dots and lines represent spheroid dominated (E/S0-Sa) galaxies, blue disk dominated (Sab-Scd/Sd-Irr). The yellow dashed line represents the combined function from Kelvin et al. 2014b.
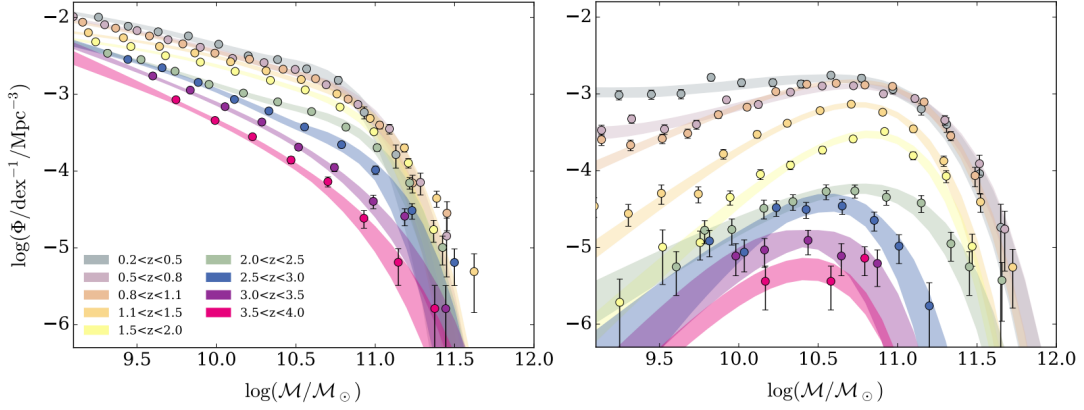
FIGURE 2.6: From Davidzon et al. 2017 for $0.2 < z < 4.0$, with the left panel corresponding to active galaxies and the right panel passive galaxies.

Lastly, we can consider the GSMF as a function of redshift, which sees the continuation of the pattern of a double Schechter function best describing the relationship. Once more you can delve deep and see similar splits in galaxies which are star-forming (more akin to LTGs) and those not (similar to ETGs). Fig. 2.6 shows this evolving relationship through redshift, but further probes into higher redshifts are hindered by the capacity to accurately measure meaningful numbers of galaxies for a statistically significant fit; especially for ETGs, which have naturally low luminosity.

Luminosity Function

Let us now pivot slight to the luminosity function (LF) of galaxies. The representation of such a function is much the same as the GSMF, with a double Schechter function being used to account for the two forms of the population, with the base function for each taking the same form as Eq. 2.7 with $M_\star \to L$

$$\frac{\mathrm{d}^2 N}{\mathrm{d}L\mathrm{d}V} = \Phi_1(L) + \Phi_2(L), \tag{2.10}$$

where the definition of said variables are much the same. We can examine Fig. 2.7, where we can see the different contribution from each morphology type and how the fit differs significantly in the low luminosity edge of the spectrum when observational limitations become a dominating factor.

Different from the GSMF, the LF has a dependency on observed wavelength and thus there is an individual function for each corresponding wavelength. The most common LFs are the star forming variants which are observed in the UV and infrared (IR) bands. The relative accuracy of surveys using these wavelength bands are dependent on sensitivity, with the IR LF
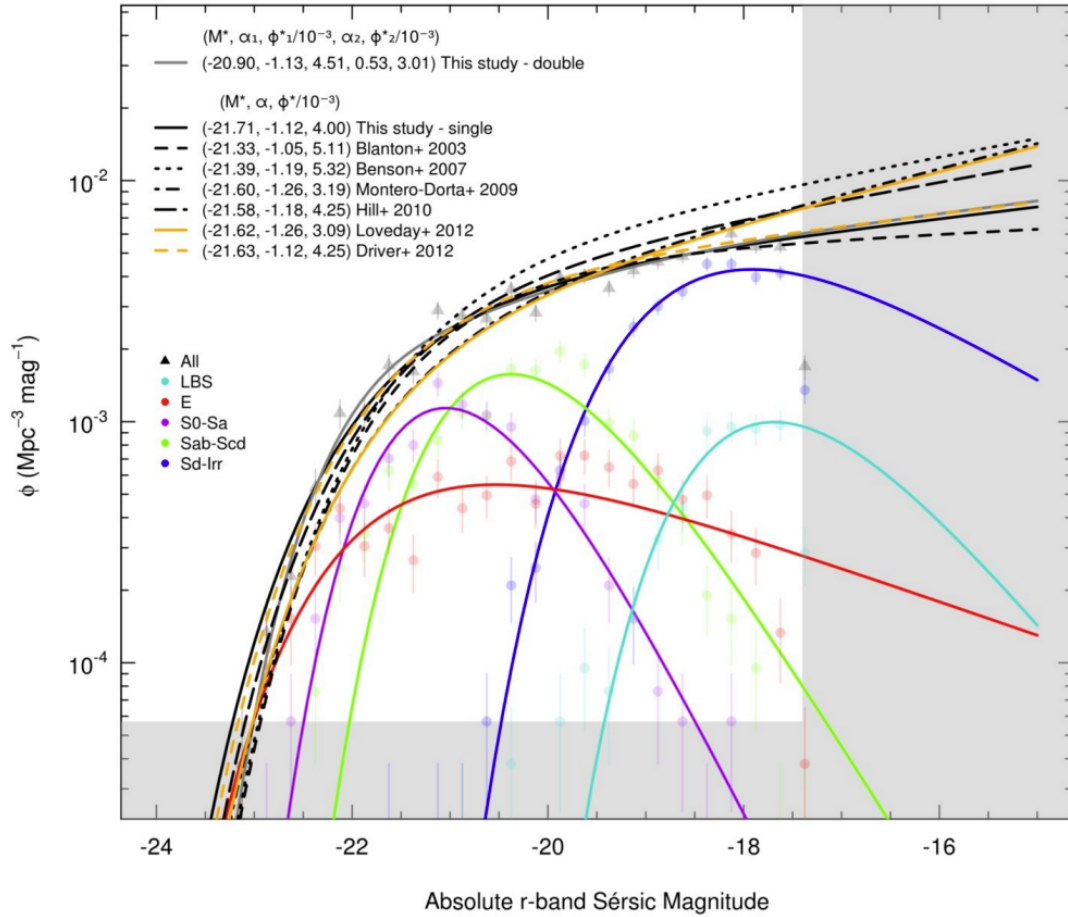
FIGURE 2.7: From Kelvin et al. 2014b, the galactic luminosity function with numerous comparative models. Where coloured lines and associated data points correspond to: total function, black; little blue spheroids (LBS), cyan; ellipticals, red; S0-Sa (lenticulars) type galaxies, purple; Sab-Scd, green; Sd-Irr, blue. The Schechter values for each model are given in the legend, note $M^* \propto L^*$. The grey shaded areas indicate where the Schechter functions of the black and grey lines have not been constrained by data.

being well constrained up to $z \sim 3$, though some approaches do extend as far as $z \sim 6$, whilst the UV LF has good form up until $z \sim 8$. Recent analysis of observations by the James Webb Space Telescope have extended the UV luminosity up to $z \sim 11$ (McLeod et al. 2023) and even $z \sim 16$ (Harikane et al. 2023).

We can also form a luminosity density much the same way as Eq. 2.9

$$\rho_L = \int \mathrm{d}L L \frac{\mathrm{d}^2 N}{\mathrm{d}L \mathrm{d}V}. \tag{2.11}$$

2.2 Stellar Objects

We now move onto stellar objects, stars that populate the galaxies we have discussed in Sect. 2.1. We will take a brief moment to discuss the formation and evolution (Sect. 2.2.2) of stars, but the intricate details will be left to the more intrepid reader. In practice we will reserve ourselves mostly to the observation and classification of stars (Sect. 2.2.1), and more critically the end of their life cycle and their outcomes (Sect. 2.2.3). We shall conclude with the stellar initial mass function (Sect. 2.2.4).

2.2.1 Stellar Observation and Classification

At the heart of stellar astrophysics is an observational science possible by even the most novice of stargazer. If astrophysics were to be supported by pillars, one strong and central would be stellar observations, encapsulating all the way from stars themselves to galactic evolution, and even encroaching on cosmology with their importance in distance measuring and age determination.

The magnitude of a star can be used in place of the luminosity (for absolute magnitude) and flux (for apparent magnitude) and defines a quantity solely dependent on the original variable and the distance. For the apparent magnitude, replacing flux, we define

$$m = -2.5 \log_{10} \left(\frac{f_\star}{f_{\mathrm{ref}}} \right), \tag{2.12}$$

where m is the apparent magnitude, $f_\star$ is the flux of the star, and f_{ref} is the flux of a well defined reference star in the chosen observational spectral band. The absolute magnitude can be defined the same, replace $f_\star \to L$ and the reference luminosity is usually taken to be Vega's luminosity. It is, however,

more useful to define the absolute magnitude in terms of the apparent magnitude, which is commonly observed,

$$m - M = 5\log_{10}\left(\frac{d}{10\,\text{pc}}\right),\tag{2.13}$$

where M is the absolute magnitude and d is the distance to the star in parsecs. The magnitude scale is often described for the apparent as being the observational brightness of a star from Earth, whilst the absolute would be the brightness of the star if it was positioned 10 pc from us. The system originates from the ancient Greeks, categorising stars visible by the human eye into six magnitude categories (and hence the peculiar scale of the system); it was eventually standardised and expanded beyond the original six classifications. The faintest objects typically observable by the naked eye are $m = 6.5$ whilst the Sun sits on the scale at $m = -27$, where higher values indicate fainter objects.

Stellar colours and temperatures form a classification criteria for stars, which can be continuously refined to create ever more categories to describe like groupings. The least defined approach is the letter classification, OBAFGKM, where O-stars are the most massive and hottest all the way to the lightest and coolest at M-stars. The system was further refined with the addition of ten subcategories, defined by the Arabic numerals, where 0 stars are the most luminous of their letter classifications, and 9 the least. Lastly, to expand the system beyond the main sequence the introduction of Roman numerals denotes the star's stage of life. The Sun is classed as a G2V star, meaning it is in a temperature bracket of $\sim 5300 - 5900\,\text{K}$, is rather luminous for its class, and is a main sequence star.

2.2.2 Stellar Formation and Evolution

Stars are birthed from the collapse of dense gaseous regions which have cold temperatures $T \leq 30\,\text{K}$ sustained by effective cooling mechanisms (Wiersma et al. 2009), which can counteract the heat created during the collapsing process. Cooler temperatures allow for the production of molecules, due to reduced photoionisation, including carbon monoxide CO and molecular hydrogen H_2[5] which themselves are effective coolers (Sternberg et al. 2014; Bialy & Sternberg 2019). Since the process of collapse itself causes a rise in

---

[5]It should be noted that these are two examples, and that there are many other possible elements and molecules that can effectively cool a gas cloud. Cooling mechanisms do have a dependency on metallicity (see Sutherland & Dopita 1993 for more on the cooling function of an astrophysical plasma).

temperature molecular cycles are important to maintain internal cooling, allowing for the dissociation and then recreation of molecules, as well as effective shielding mechanisms to prevent incident UV dissociation from the local area (van Dischoeck & Black 1988).

The collapse of some gaseous region to form a star is in depth and follows analysis of the Lame-Emden equation for an isothermal sphere

$$\frac{1}{\xi^2}\frac{d}{d\xi}\left(\xi^2\frac{d\Psi}{d\xi}\right) = e^{-\Psi}, \tag{2.14}$$

where ξ is the dimensionless radius and Ψ is a dimensionless potential. Such an equation has no analytical solutions but by using boundary conditions of $\Psi(\xi = 0) = 0$ and $\Psi'(\xi = 0) = 0$, to avoid divergence at the centre, you find a proportionality with the density following $\rho \propto \xi^{-2}$ and is said to have the profile of a Bonnor-Ebert sphere (Ebert 1955; Bonnor 1956); this is treated as a simplified analogue to the collapse undergone by stars.

Once the collapse has been completed the early life of a star is broken down into three distinct stages

1. A protostar forms from the collapse of a shell of gas within some dense region. This collapse, along with interactions involving generated magnetic fields, triggers stellar jets to burst from the poles of the protostar, causing a feedback that clears the dusty region about the forming core known as the envelope. These jets will continue as long as gas continues to accrete and collapse onto the core.

2. The T Tauri phase, where gas is still accreting but most of the envelope has been evacuated by the core and a perpendicular planetary disc has formed.

3. Jets cease as the protostar enters its Hayashi track[6] (Hayashi 1961), the pre-main sequence phase when hydrogen fusion has not yet begun and the star may still require additional accretion to allow for stable fusion in its core. Protostars can be optical visible since their environment is clear of obstruction, besides the now cooling planetary disc. This is the slowest growth phrase of the three, and can span the order of tens of millions of years.

Ultimately the potential of a protostar is determined by the mass it is able to acquire to allow for internal temperatures to be higher enough to sustain fusion. This threshold is roughly $0.08\,\mathrm{M_\odot}$, and any star below becomes a brown

---

[6]The luminosity-temperature evolutionary tracks protostars follow before joining the main-sequence laid out in the Hertzsprung-Russell diagram (see Fig. 2.8).

dwarf. Once hydrogen fusion has begun the star has entered the zero age main sequence (ZAMS), the large central diagonal strip in the Hertzsprung-Russell diagram seen in Fig. 2.8. Within the Figure a funnel of stars can be seen stretching from the upper left corner of the main sequence towards the top right corner, this is the red giant evolution track. In the bottom left is the concentration accounting for white dwarfs, which have a connection to the red giants through a looping track about the top of the main sequence not seen in the diagram.

The evolution of a star is dependent on its mass[7], which gives an indication of many properties, but more specifically the potential of fusion within its core. The higher mass[8] a star the greater the potential of the core temperature leading to the fusion of heavier elements, even up to iron with the potential of even heavier elements during the collapsing stages of high mass stars. Before collapse can occur, the star will undergo hydrogen fusion as its primary source of energy used to oppose gravitational collapse, until hydrogen is no longer abundant enough to support the star. Hydrogen fusion does not cease completely, and now occurs predominately in material shells surrounding the core in a process called hydrogen shell burning. The central core's mean molecular mass μ_{core} increases as hydrogen converts to helium, and the Schönberg-Chandresekhar limit defines the mass required for a core to begin helium fusion

$$\left(\frac{M_{\mathrm{core}}}{M}\right) \approx 0.37\left(\frac{\mu_{\mathrm{env}}}{\mu_{\mathrm{core}}}\right)^2, \tag{2.15}$$

where M_{core} and μ_{core} are the mass and mean molecular mass of the core respectively, and μ_{env} is the mean molecular mass of the surrounding envelope. Stars with cores above this limit will begin helium fusion, and this indicates a leaving of the main sequence. For low mass stars $M_{\mathrm{ZAMS}} < 1.8\,\mathrm{M}_\odot$ the ignition of helium can be violent and cause a burst in their luminosity called a helium flash. Which size classification of the giant branch the star enters during helium fusion is determined by its mass with higher mass stars $M_{\mathrm{ZAMS}} \approx 10\,\mathrm{M}_\odot$ continuing to the red giant branch whilst those below remain as subgiants.

After helium fusion, for star with $M_{\mathrm{ZAMS}} > 8\,\mathrm{M}_\odot$, carbon-oxygen fusion is possible for the red giant mass range and beyond, and the star has entered the asymptotic giant branch (AGB). This is initiated by the fusion of carbon

---

[7]In fact, the tentative Vogt-Russel theorem states that the structure and evolution of a star can be determined solely from its mass and chemical composition.

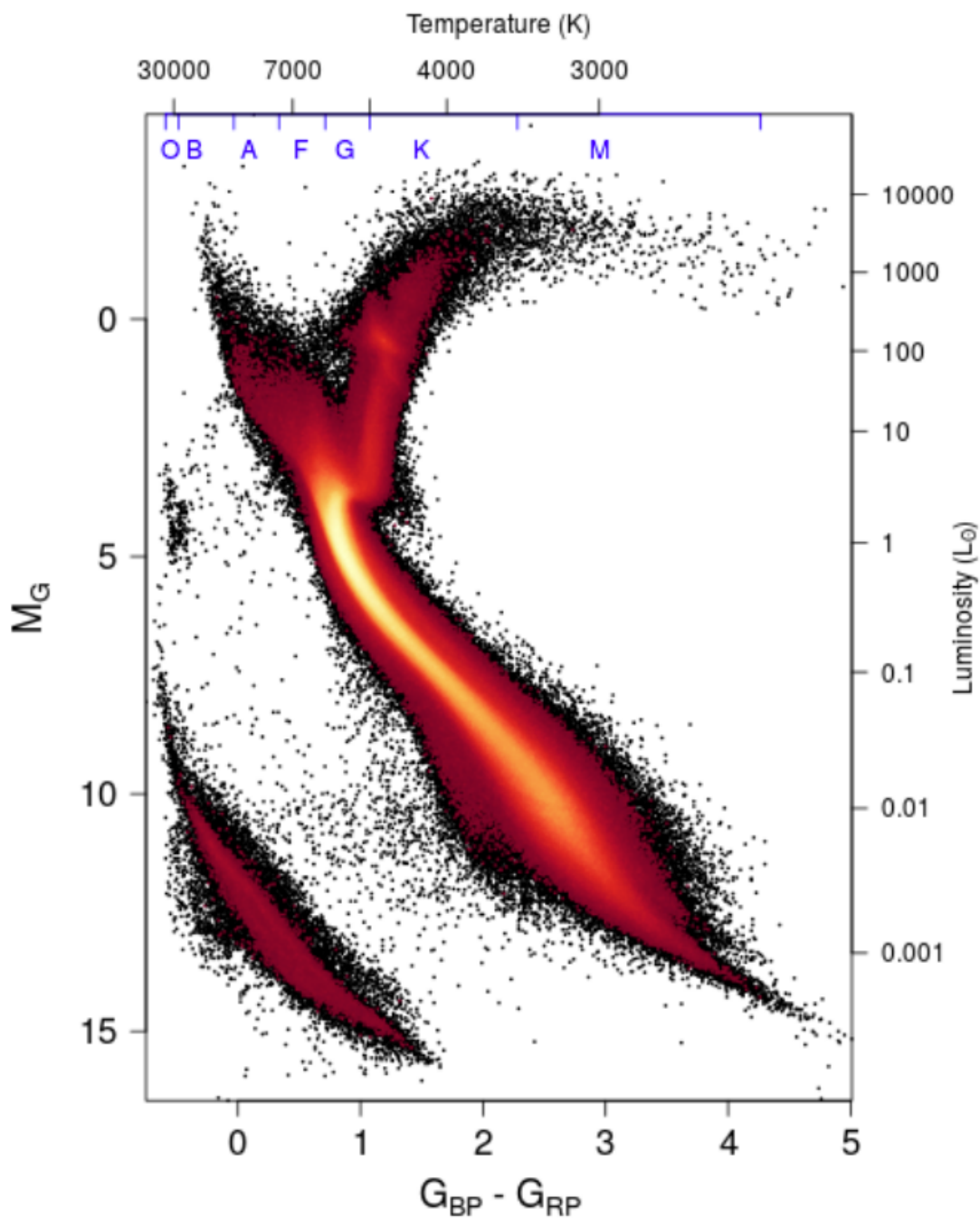[8]More specifically the mass of concern is the ZAMS mass, the mass with which the star enters the main sequence.

FIGURE 2.8: Hertzsprung-Russell Diagram from the Gaia Collaboration DR2 2018. Shows the position of ∼ 4 million stars with respect to their temperature and stellar classification (top axis), luminosity (right axis), Gaia absolute magnitude (left axis), and colour (bottom axis).
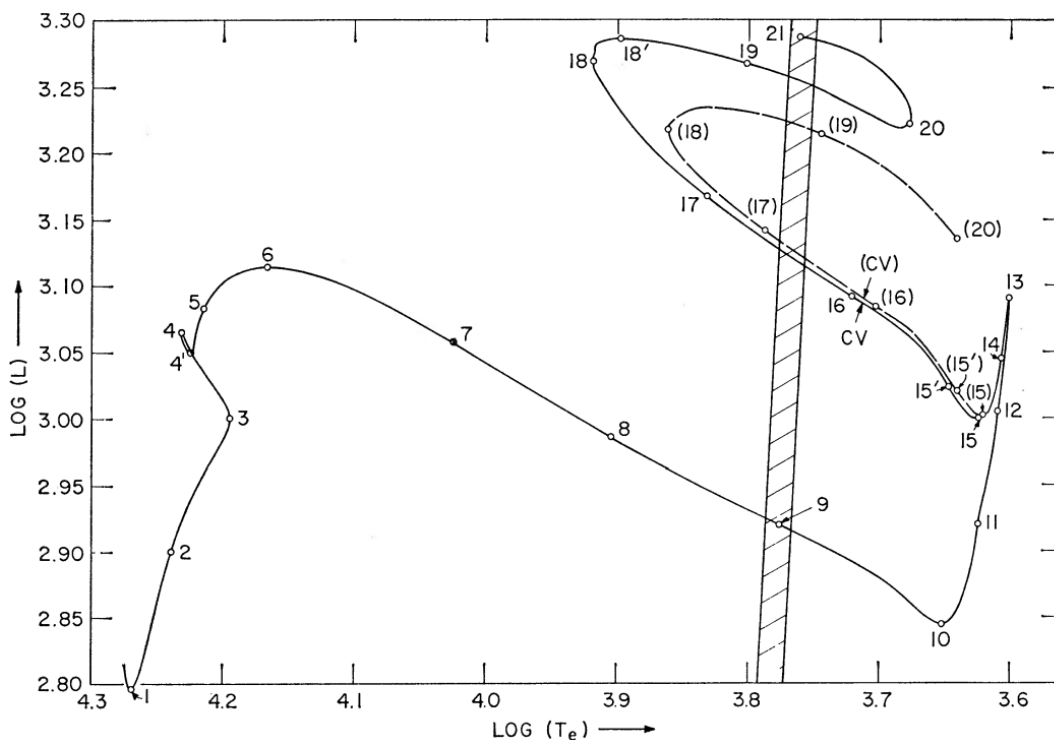
FIGURE 2.9: Estimated evolution track of a $5M_\odot$ star after exiting the Hertzsprung Russel Main Sequence from Iben 1966. Numbers markers indicate evolutionary lifetime markers, with values found in Table 1 of the original paper.

and oxygen in the core, and helium is now left to shell burning. During this phase rapid helium fusion can be triggered in the helium shells, the energy released can force rapid hydrogen fusion in their shells which can replenish lost helium. This flash and replenish process can becomes cyclical, causing the pulsing of the outer envelope of the star and creates a defining divide between the AGB phase and the thermal-pulse AGB phase. Observationally this is seen as a pulsation in the luminosity and surface temperature of the star. Fig. 2.9 shows the luminosity and effective temperature evolution of a 5 $M_\odot$ star from Iben 1966.

At each of these fusion transition is an event known as dredge up, where fused material is pulled from the core into the outer envelope. The dilution of fused material in the outer regions causes a spectra change in the observed star.

Once all possible fusion routes have been exhausted, determined in part by M_{ZAMS}, the battle between gravity and pressure ends in gravity's victory. What is left of stellar evolution is the remnants of catastrophic events during their death, which can span from vast nebulae of dust, white dwarfs, neutron

stars, or even black holes.

2.2.3   The Death of Stars

White Dwarfs

For stars with $M < 8\,\mathrm{M_\odot}$ their conclusion is a white dwarf. These dwarfs are sustained by electron degeneracy pressure, originating from the Pauli exclusion principle which forbids electrons from occupying the same quantum state. To prevent this occupation electrons exert a form of pressure on each other when placed too close together, and the crushing pressure of a dense carbon-oxygen white dwarf is attempting to do exactly that. We can assume the electrons act relativistically and follow the Pauli Uncertainty Principle which leads to the pressure of electron degeneracy being

$$P_\mathrm{e} = \frac{(3\pi^2)^{1/3}}{4}\hbar c \left(\frac{\rho}{\mu_\mathrm{e} m_\mathrm{H}}\right)^{4/3} \tag{2.16}$$

where $\hbar = h/2\pi$ is the reduced Planck's constant, and $\mu_\mathrm{e} \approx 2$ for a white dwarf. If the contracting force of gravity becomes too great than not even electron pressure can resist the force, and such a mass limit is known as the Chandrasekhar mass

$$M_\mathrm{CH} = \frac{2.02(3\pi)^{1/3}}{2}\left(\frac{\hbar c}{G}\right)^{3/2}\left(\frac{1}{\mu_\mathrm{e} m_\mathrm{H}}\right)^2 \approx 1.44\,\mathrm{M_\odot}. \tag{2.17}$$

In binary systems, where one star is a white dwarf and develops a common envelope with its partner star, mass can be transferred from the still formed star to the remnant and lead to the surpassing of the Chandrasekhar limit. In this instance the white dwarf will explode at a characteristic luminosity and is known as the type Ia supernova which we have seen used as a standard candle estimator in Cosmology. The resulting explosion is likely to destroy the white dwarf, but in the instances that no explosion occurs and a remnant remains then accretion induced collapse (AIC) has occurred and the result is a neutron star (The potential of AIC neutron stars is still an active field of debate; for review see Wang & Liu 2020; also see Tauris et al. 2013; Piro & Thompson 2014; Schwab et al. 2016; Ruiter et al 2019) .

Neutron Stars

Neutron stars are the result of more massive stars collapsing, typically those above $8\,\mathrm{M_\odot}$ and below $20\,\mathrm{M_\odot}$. They are formed either from mass accretion

by white dwarfs, potentially, or core collapse supernovae, through type Ib, Ic, and II. Stars in this mass range persist in their nuclear fusion beyond carbon-oxygen all the way to iron, where the core is still able to keep the structure of the star and can support its greater mass through nuclear fusion pressure; however, once the fusion ceases the star will collapse and form a neutron star.

A more favourable state for the core, once fusion ceases, is for electrons and protons to fuse into neutrons leading to the elimination of support by electron degeneracy seen in white dwarfs. The reaction

$$p^+ + e^- \rightarrow n^0 + \nu_e \tag{2.18}$$

leads to the release of a large sums of neutrinos that cause a pressure wave to ripple through the burning shells of remaining elements surrounding the core. This extreme burst of pressure causes the explosion of the remnant layers away from the neutron rich core and can release energy of the order 10^{43} erg s^{-1}.

The remnant neutron star is now only supported by neutron degeneracy pressure

$$P_n = \frac{\pi^3 \hbar^2}{15 m_n} \left(\frac{3N}{\pi V} \right)^{5/3}, \tag{2.19}$$

where N is the number of states available, and V is the volume of the remnant. Like white dwarfs, neutron stars have an upper limit to their allowed mass, which requires solutions to a perfect fluid in general relativity, and is known as the Tolman-Oppenheimer-Volkoff limit (Oppenheimer & Volkoff 1939). Its rough estimate places a limit on neutrons star of about $M \sim 3 \, M_\odot$, but unlike white dwarfs when neutron stars exceed this limit there is no explosion; instead they form a black hole.

Stellar Black Holes

Black holes (BHs) are formed when gravity becomes the ultimate winner in the battle against pressure, once neutron degeneracy pressure has lost there is nothing more which can prevent the collapse to a singularity. The conceptual formation of BHs is trivial, but the processes undertaken during the collapse can differ depending predominantly on mass M_{ZAMS} and metallicity Z.

The outcomes of main sequence stars as a function of their initial mass is best described by Fig. 2.10, which show the interweaving relationship involving metallicity. Pathways of creation for BHs include: supernova events,

direct collapse, Pair-Instability Supernova (PISN; Fowler & Hoyle 1964; Fraley 1968), and Pulsational Pair-Instability Supernova (PPISN; Belczynski et al. 2016b; Woosley 2017).

For stars with $M > 40$ M$_\odot$ a supernova explosion does not occur (Smartt 2015). The hashed white indicates direct collapse, where the star proceeds straight to a BH (Fryer 1999; Fryer & Kalogera 2001; Mapelli et al. 2009; O'Connor & Ott 2011; Fryer et al. 2012; Ertl et al. 2016). This form of direct collapse is not to be confused with the direct collapse of gas clouds into primordial BHs and the production of intermediate BHs with masses higher than those produced by stars[9].

PISN occurs when energetic gamma rays interact with elements causing the production of an electron and a positrons, known as pair production. This lose of gamma ray energies causes a drop in pressure which leads to a runaway effect starting with rapid nuclear fusion and ends in a supernova explosion. The unique aspect of this form of process is the core is completely destroyed, and thus no remnant remains instead leaving behind a heavy element rich planetary nebula.

PPISN works the same as PISN, when regarding pair production, but the process does not cause an unstable collapse. Instead PPISN will strip the star of its mass, this can result in high mass PPISN leading to an uninterrupted PISN whilst low mass stars will end in an explosion that can leave a low mass star instead of a stellar remnant.

Last in the legend corresponds to neutrino-driven supernova, where the star losses roughly $\sim 0.1 M_{\mathrm{bar}}$ with M_{bar} being the baryonic mass of the proto-compact object (See Timmes, Woosley & Weaver 1996, Fryer et al. 2012) through the emission of neutrinos. The level of mass loss can determine the compact remnant's outcome, either a BH or neutron star. With the expulsion of the outer envelope caused by the supernova explosion, material can be returned to the compact remnant through fallback. From high mass neutron stars this can cause a breach of the Tolman-Oppenheimer-Volkoff limit (Chan et al. 2018, 2020; Woolsey et al. 2020).

The combination of all these forms of remnant production creates an ZAMS mass to remnant mass relation, which can be seen in Fig. 2.11, that is critical to stellar evolution simulations and fundamental for this work to produce a stellar black hole mass function.

---

[9]Direct collapse in this instance is used to help explain extreme mass BHs ($M_\bullet \approx 10^{9-10}$ M$_\odot$) at $z \sim 7$ (Mortlock et al 2011; Wu et al. 2015). Observations like these lay as a motivator for this work, and will be addressed more directly in Chapter 4.

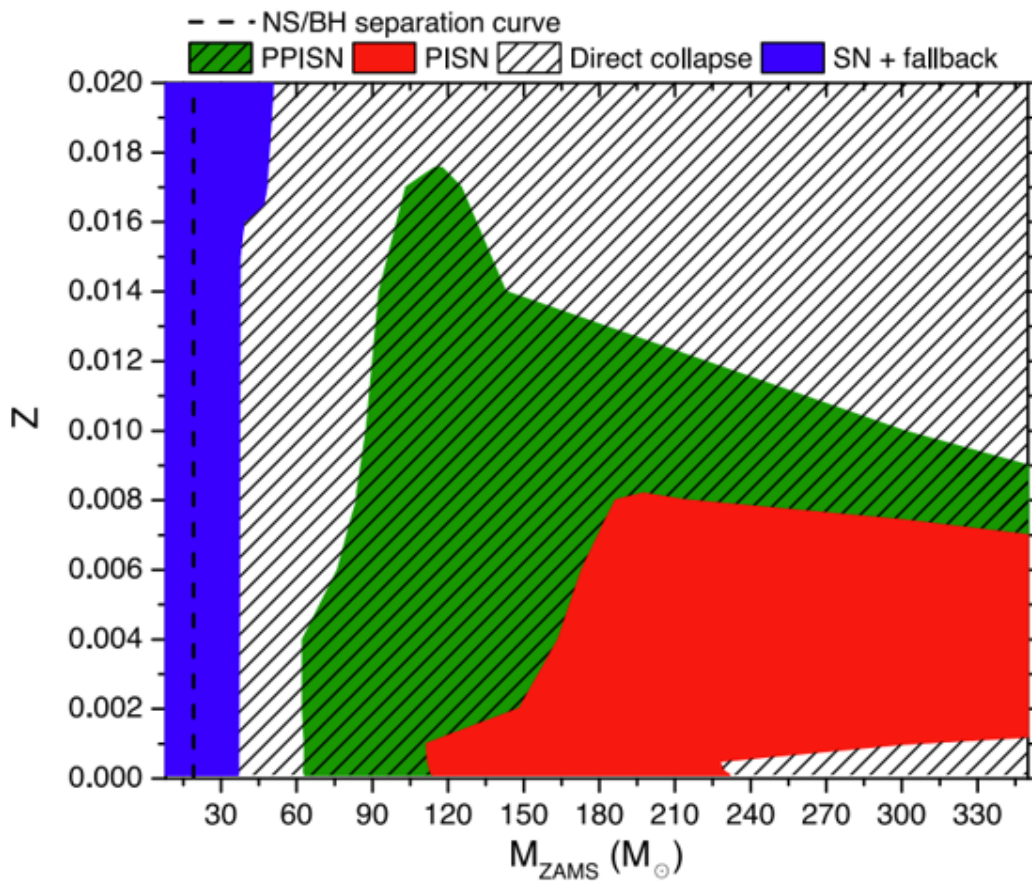FIGURE 2.10: The outcome scenarios for zero-age main sequence (ZAMS) stars as defined by their metallicity, as found in Spera & Mapelli 2017. The blue region corresponds to neutrino-driven core collapse supernova; green, PPISN; red, PISN; white, direct collapse to a BH. The vertical black dashed line ($M_{\text{ZAMS}} \approx 19 M_\odot$) notes the split between neutron star (NS) outcomes and BH outcomes.
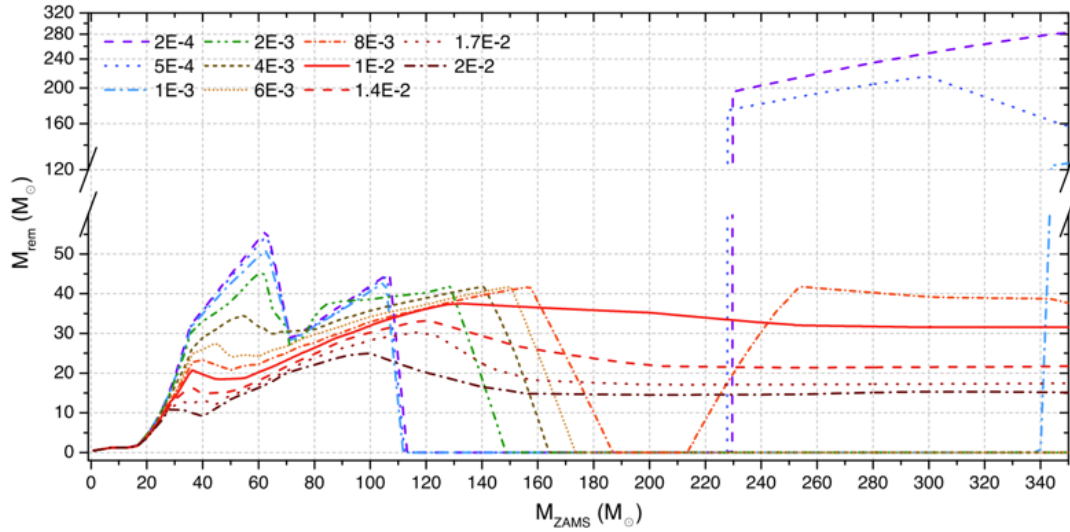
FIGURE 2.11: ZAMS mass to remnant mass relation described in Spera & Mapelli 2017 and used in Chapter 3. Metallicities are as shown and indicated via colour coordination, and the region $65 M_\odot$ to $120 M_\odot$ is omitted due to zero remnants occurring between said masses.

2.2.4   The Initial Mass Function of Stars

The distribution of stars according to their stellar mass is critical in the understanding of stellar populations, statistical analysis of galaxy evolution, and establishing the foundation of stellar simulations. Stars, however, are not all equal as we have seen and the more massive a star is the shorter its life expectancy, this means that stars in a galaxy are not representative of the stellar history. This requires the need for an initial mass function (IMF), which describes the number density of stars of a given mass for some galaxy undergoing a period of star formation.

The exact form of the IMF is a hotly debated topic amongst stellar astrophysicists, but the make up is simple. The most notable are the Salpeter IMF (Salpeter 1955), characterised by a constant decline in abundance from low to high masses, and the Kroupa 2001 and Chabrier 2003 IMFs which see a reduction in the steepness of the declining abundance as you go toward lower masses both occurring at $M_\star \approx 1\,M_\odot$. Kroupa01 will be used for the main body of this work.

The make up of the IMF is set such that

$$\int \phi(m_\star) m_\star \mathrm{d}m_\star = 1\,M_\odot, \tag{2.20}$$

where the total mass formed in stars is equal to 1 $M_\odot$. For the Kroupa01 IMF the mass function $\phi(m_\star)$ is taken to be

$$\phi(m_\star) = \begin{cases} m_\star^{-1.8} & 0.08 \leq m_\star/M_\odot < 0.50; \\ m_\star^{-2.3} & 0.50 \leq m_\star/M_\odot < 1.00; \\ m_\star^{-2.3} & 1.00 \leq m_\star/M_\odot. \end{cases} \quad (2.21)$$

The IMF is determined empirically from observations of the Milky Way[10], this does imply IMFs are representative of the present day IMF but it is assumed that they can be extended beyond the present with minimal compromise.

2.3 (Super)Massive Black Holes

Lastly we come to BHs, more specifically we will discuss the supermassive variant and the active galactic nuclei (AGNs) associated with them. We will begin with a brief overview of AGNs, including prominent relations they share with their host galaxy and the complications the presence of some high-z quasars pose to AGN evolution models (Sect. 2.3.1). This will be followed with an introduction to gaseous dynamical friction, the methods used in this work to overcome the high-z quasar problem (Sect. 2.3.2). Finally, we conclude by showing an overview of the mass and luminosity function of AGNs, discussing the observational undertaking to constrain their form (Sect. 2.3.3).

2.3.1 Active Galactic Nuclei

Galaxies have the potential to emit bolometric luminosities of $L \sim 10^{48}$ erg s^{-1}, consisting of UV radiation and X-ray luminosity exceeding $L_X > 10^{42}$ erg s^{-1} not possible to associate to stellar activity. In addition, there can be the presence of relativistic jets and high radio activity. All these features can indicate the presence of an AGN, which in brief are supermassive black holes (SMBHs; $M_\bullet \sim 10^{6-10}$ M$_\odot$) accreting from a surrounding disk of gas and stars (Lynden-Bell 1969), and come in several types: blazars, quasars, radio galaxy AGNs, Seyfert AGNs[11]. The rate of accretion and an AGN's luminosity

---

[10]For the low mass end of the IMF, determinations can use the Small and Large Magellanic Cloud as a potential population field (Kalirai et al. 2013).

[11]Under the unified model of AGNs, the classification of an AGN is predominantly associated with its observed orientation whilst other features, such as rate of accretion, are secondary factors.

are related

$$L \approx \eta \dot{M}_{\text{acc}} \tag{2.22}$$

where η is the radiative efficiency of the accreting AGN, taken to be between $\eta \approx 0.1 - 0.3$ depending on the accretion scenario considered (thin disk: Shakura & Sunyaev 1973; slim disk: Abramowicz et al. 1988; rotating Kerr BH: Thorne 1974), and $\dot{M}_{\text{acc}}$ is the accretion rate of the SMBH.

It has been determined that the evolution of both the host galaxy and its SMBH are intertwined, this amounts to a series of scaling relations. The most pertinent to this thesis is the Magorrian relation (named for John Magorrian, Magorrian et al. 1998) and sees a pattern between the stellar mass of a galaxy and the mass of its central BH. Commonplace now is to call a relation seeking this connection Magorrian-like (Reines & Volonteri 2015; Shankar et al. 2016, 2020a). For this work the Shankar debiased relation will be predominately used

$$\begin{aligned}
\log \frac{M_{\bullet}}{M_{\odot}} \approx\ & 7.574 + 1.946 \log \frac{M_{\star}}{10^{11}\,\mathrm{M}_{\odot}} \\
& - 0.306 \log^2 \frac{M_{\star}}{10^{11}\,\mathrm{M}_{\odot}} - 0.01 \log^3 \frac{M_{\star}}{10^{11}\,\mathrm{M}_{\odot}}
\end{aligned} \tag{2.23}$$

which hold for the mass range $M_{\star} \sim 10^{10-12}\,\mathrm{M}_{\odot}$ (Fig. 2.12).

If we consider galaxies themselves, we also saw in the same section the main sequence of star forming galaxies (see Fig. 2.4), a $M_{\star} - \psi$ scaling relation. It is no uncertain leap to suggest that through such relations, reliant on the availability of gas, that there would be the BH accretion rate $\dot{M}_{\text{acc}} - \psi$ relation. This relation does exist (Mullaney et al. 2012; Delvecchio et al. 2014; Volonteri et al. 2015; Carraro et al. 2020; Stone et al. 2022) and estimations for it extend to surveys examining X-ray emissions from AGNs up to $z \sim 3.5$. The cause for this connection is not unreasonable, with AGNs expelling large sums of energy into the local environment, along with removal of gas through accretion, the heating of star forming gas can lead to the quenching of star formation.

The correlations between the central AGN, or SMBH, does not cease at mass relations, connections have been found between AGNs and nuclear star clusters (Seth et al. 2008), galaxy velocity dispersion (Gebhardt et al. 2000), bulge luminosity (Gültekin et al. 2009), and even the dark matter halo (Ferrarese 2002); all these relations form pieces in a galaxy-SMBH co-evolution story.

The observation of AGNs has also created complications in our current models of SMBH, with the numerous discoveries of high-z ($z > 7$) high mass ($M_{\bullet} > 10^9\,\mathrm{M}_{\odot}$) quasars (Fan et al. 2006; Mortlock et al. 2011; Venemans et al.
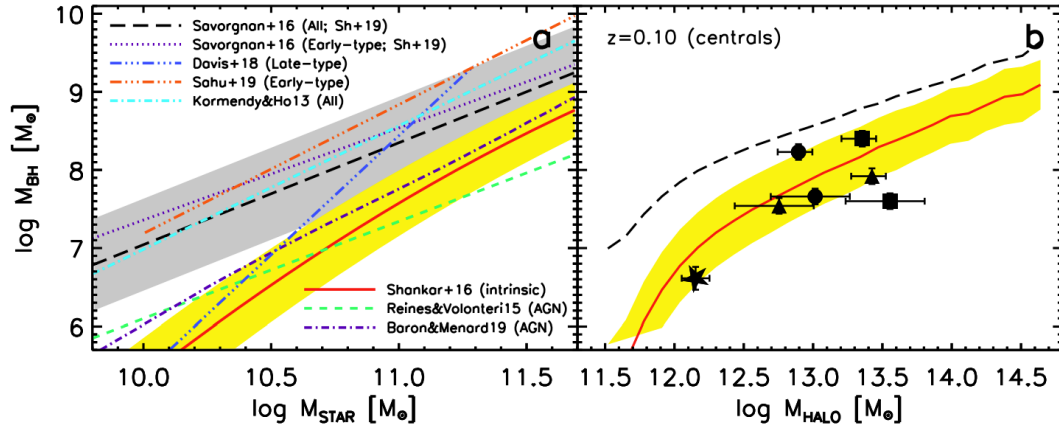
FIGURE 2.12: From Shankar et al. 2020. Left panel: central BH mass-host galaxy stellar mass relation, with coloured lines associated with different labelled Magorrian relations (see legend references). Yellow region represents the unbiased $M_\bullet - M_\star$ relation, and the grey area is the scatter associated with the black dashed line from Savorgnan et al. 2016. Right panel: the relation between the $M_\bullet - M_{\rm halo}$, formed from abundance matching using the observed and unbiased $M_\bullet - M_\star$ relation. The data points are from Powell et al. 2018 (squares); Krumpe et al. 2015, 2018 (triangles and circles); and Sagittarius A* (star; Ghez et al. 2008, Posti & Helmi 2019).

2017a, 2017b, Banadoes et al. 2018, 2021). These AGNs would have < 1 Gyr to grow, and would not be possible through standard Eddington accretion. To overcome this hurdle several solution have been proposed.

The solutions are two-fold: accretion solutions; seed solutions. The former considers accelerating the rate of accretion beyond the standard limits to the super-Eddington regime (Madau et al. 2014; Aversa et al. 2015; Lupi et al. 2016). Eddington accretion is derived through a spherically symmetric model, since accretion rate and luminosity are connected one can derive a maximum possible luminosity for a BH of given mass called the Eddington luminosity $L_{\rm Edd}$. The Eddington ratio takes the place of an accretion rate, $\lambda = L/L_{\rm Edd}$ and is typically $\lambda \leq 1$. The super-Eddingdon regime $\lambda > 1$ is not invalid, since BHs are not required to accrete symmetrically, and therefore allow stellar mass BHs to become supermassive in adequate time.

The latter seed solutions consider the production of heavy seed BHs which are then grown through gas accretion, these heavy seeds start at much higher mass than standard stellar BHs produced through stellar evolution. There are four possible pathways to create a heavy seed BH: massive pop-III ($Z_\star \sim 0$ stars), direct collapse of gas clouds, runaway merger of stars and BHs in globular clusters (Mayar & Bonoli 2019; Volonteri et al. 2021), and gaseous

dynamical friction in central galactic regions (Boco et al. 2020). These solutions allow accretion to begin at $M_\bullet \approx 10^{1.5-4}$ M$_\odot$, and more critically skips the slower accretion rate at lower masses. The existence of one method does not prevent the presence of another, and it is more likely that all these methods function in the development of SMBHs than only one being responsible.

2.3.2   Central black hole growth via Dynamical Friction

For the main body of this thesis, specifically in Chapter 4, we will focus on the growth of SMBHs through a seed based solution derived in Boco et al. 2020 (B20). Gaseous dynamical friction considers the accretion of mass onto a central BH through the merger of numerous stellar mass BHs which have lost orbiting angular momentum through frictional effects caused by dense regions of gas (see Fig. 2.13; Ruderman & Spiegel 1971; Ostriker 1999; Bernal & Sanchez-Salcedo 2013; B20).

    According to gaseous dynamical friction, under a spherical symmetric assumption akin to the central bulge of LTGs or compact ETG progenitors, the low mass accretion hurdle is able to be overcome through the rapid accretion of stellar mass BHs. The scale of this mechanism is dependent on the environment about the central BH, but is seen to extend up to 300 pc where the contribution of stellar mass compact remnants remains constant before dropping off exponentially beyond this radius. This even contribution is able to be maintained due to the increased abundance of compact remnant at further distances counteracting the increased time it takes for such remnants to spiral inward.

    Under the assumption of B20, numerous examples of candidate remnants are found to successful inspiral and contribute their mass (see Table 2.1). This has been shown to create heavy seed intermediate mass BHs ($M_\bullet \sim 10^{4-6}$ M$_\odot$) within 10^7 yr, after which the BH has a mass able to rapidly accrete from its gas surroundings allowing for SMBHs to comfortably appear within ~ 1 Gyr. Thus gaseous dynamical friction is able to overcome the high-z quasar problem present in current observations.

    The timescale of dynamical friction is dependent on the local environment and the dynamics of the compact remnant candidate to be merged, and takes the form

$$\tau_{\mathrm{DF}} = \mathcal{N} \left(\frac{m_\bullet}{100 \, \mathrm{M}_\odot} \right)^a \left(\frac{M_{\mathrm{gas}}}{10^{11} \, \mathrm{M}_\odot} \right)^b \left(\frac{R_{\mathrm{e}}}{1 \, \mathrm{kpc}} \right)^c \left[\frac{j}{j_{\mathrm{c}}(\epsilon)} \right]^\beta \left[\frac{r_{\mathrm{c}}(\epsilon)}{10 \, \mathrm{pc}} \right]^\gamma, \qquad (2.24)$$

where $\mathcal{N}$ is a normalisation constant, $m_\bullet$, j, ϵ are the mass, angular momentum, and energy of the compact remnant respectively; M_{gas} and R_{e} are the
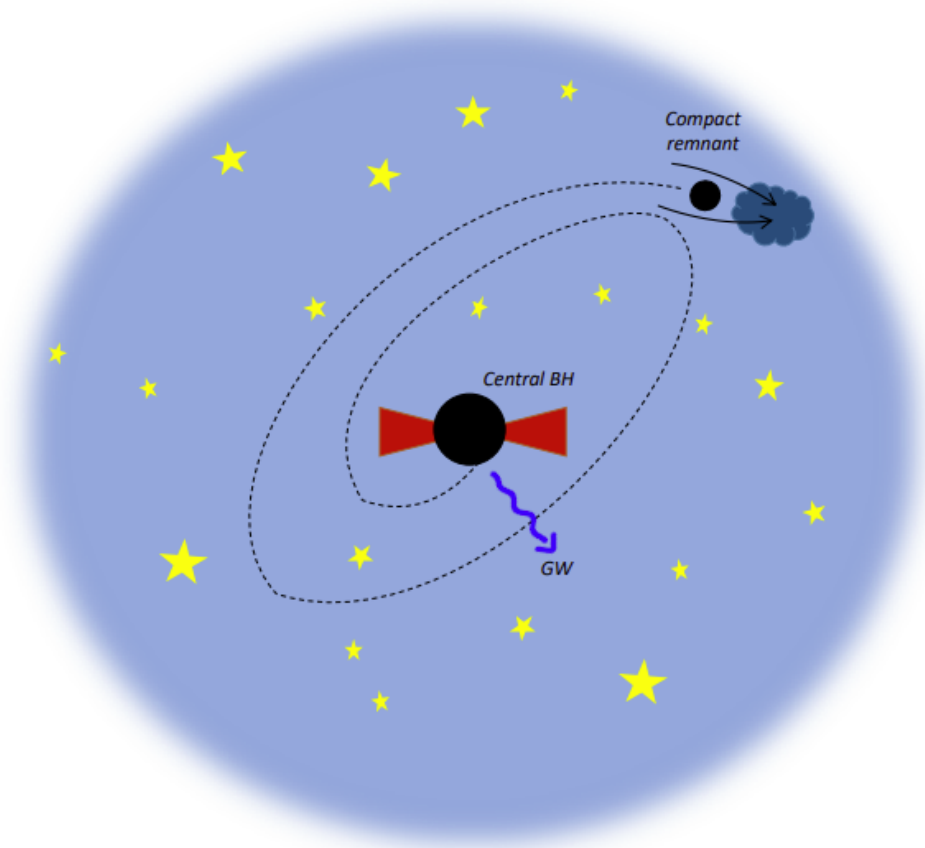
FIGURE 2.13: Schematic from B20, depicting dynamical friction of stellar mass BHs towards a central BHs, where gravitational waves are emitted (GW).

r/pc	$v_r/\sigma(r),\ v_\theta/\sigma(r)$	r_c/pc	j/j_c	$\tau_\mathrm{DF}/\mathrm{Gyr}$			
				$m_\bullet = 1.5\,\mathrm{M_\odot}$	$m_\bullet = 10\,\mathrm{M_\odot}$	$m_\bullet = 40\,\mathrm{M_\odot}$	$m_\bullet = 100\,\mathrm{M_\odot}$
5	1, 1	30	0.18	-	4.1	1.1	0.46
5	1, 0.1	18	0.041	0.75	0.12	0.033	0.014
5	0.1, 1	18	0.41	-	4.0	1.0	0.44
5	0.1, 0.1	4	0.55	0.75	0.12	0.033	0.014
15	1, 1	50	0.31	-	-	9.4	3.9
15	1, 0.1	33	0.064	6.4	1.0	0.28	0.12
15	1, 0.025	33	0.016	0.80	0.13	0.035	0.015
30	1, 1	76	0.41	-	-	-	-
30	1, 0.1	50	0.080	-	4.1	1.1	0.46
30	1, 0.01	50	0.0081	0.79	0.13	0.035	0.015
50	1, 1	100	0.49	-	-	-	-
50	1, 0.1	70	0.089	-	-	3.0	1.2
50	1, 0.01	70	0.0090	2.1	0.35	0.093	0.039
50	1, 0.005	70	0.0045	0.75	0.12	0.033	0.014
150	1, 1	200	0.65	-	-	-	-
150	1, 0.1	150	0.10	-	-	-	10
150	1, 0.01	150	0.010	-	2.8	0.75	0.31
150	1, 0.001	150	0.0010	0.55	0.091	0.024	0.010
300	1, 0.1	26	0.10	-	-	-	-
300	1, 0.01	26	0.010	-	-	3.0	1.2
300	1, 0.001	26	0.0010	2.0	0.33	0.088	0.037
300	1, 0.0005	26	0.00050	0.72	0.12	0.032	0.013

TABLE 2.1: Examples of gaseous dynamical friction timescale from B20, where (-) indicates a timescale longer than 10 Gyr.

gas mass and half-mass radius of the host galaxy; j_c and r_c are the angular momentum and radial distance of the compact remnant if it were to maintain a stable circular orbit about the central region, and is a function of the energy of the remnant. In this work we will adopt the fiducial setup of B20, namely, a 3D Sersic gas density profile $\rho(r) \propto r^{-\alpha} e^{-k(r/R_e)^{1/n}}$ with $n = 1.5$, $\alpha = 1 - 1.188/2n + 0.22/4n^2 \sim 0.6$ and half-mass radius $R_e \sim 1$ kpc. Then the values for the parameters in Eq. (2.24) read $a \approx -0.95$, $b \approx 0.45$, $c \approx -1.2$, $\beta \approx 1.5$, $\gamma \approx 2.5$ and $\mathcal{N} \approx 3.4 \times 10^8$ yr. The effect of different setups on the dynamical friction timescale is discussed in B20.

Gaseous dynamical friction requires the creation of compact remnants, specifically BHs, and thus knowledge of their abundance is pertinent to the effectiveness of the mechanism. Eq. 20 in B20 gives an expression for the birthrate of compact remnants

$$R_{\text{birth}}(m_\bullet, \tau | \psi, z) = \psi \int_{m_{\star,min}} \mathrm{d}m_\star \phi(m_\star) \frac{\mathrm{d}p}{\mathrm{d}m_\bullet}[m_\bullet | m_\star, Z(\tau | \psi, z)] \quad (2.25)$$

where ψ is the SFR, ϕ is the initial stellar mass function, $\mathrm{d}p/\mathrm{d}m_\bullet$ is the probability distribution of compact remnant reflective of the relation seen in Spera et al. 2017 (see Fig. 2.11). This equation will be represented in Chapter 4, Sect. 4.2, Eq. 4.6 in another form where the variables inside the integral can be described as a stellar BH mass function, to be derived in Chapter 3.

Ultimately the returned accretion rate for gaseous dynamical friction can be presented as

$$\dot{M}_{\bullet,\text{DF}} = \int \mathrm{d}m_\bullet m_\bullet \frac{\mathrm{d}\dot{N}_{\text{DF}}}{\mathrm{d}m_\bullet}, \quad (2.26)$$

where $\mathrm{d}\dot{N}_{\text{DF}}/\mathrm{d}m_\bullet$ is the merger rate of compact remnants due to this mechanism. For this work, this accretion rate will work in unison with standard Eddington accretion onto the central BH of the galaxy (see Chapter 4, Sect. 4.3, Fig. 4.2 for examples).

2.3.3 Mass and Luminosity Function of AGNs

We shall conclude with a brief mention of the mass and luminosity functions of AGNs. When considering the mass function of BHs the different mass regimes must be considered separately when determining observational restraints. Stellar mass BH mass function ($M_\bullet \lesssim 10^2 M_\odot$) determinations are reliant on simulations (Spera et al. 2017) and the gravitational wave emissions from stellar mass BH binaries (Abbott et al. 2021a, 2021b; Baxter et al. 2021) using the LIGO/Virgo project. The mass function within the supermassive regime ($M_\bullet \gtrsim 10^6 M_\odot$) is closely linked to the observation of AGNs,

and can be derived from the luminosity function of AGNs which is determined from the observation of AGNs using X-ray and radio telescopes, with $L_X > 10^{42}$ erg s^{-1} setting an X-ray luminosity minimum for AGNs. The intermediate regime ($10^3 M_\odot \lesssim M_\bullet \lesssim 10^6 M_\odot$) is the most uncertain, with observational restrictions few and far between, instead the accretion of light seed BHs can generate a semi-analytic approach to allow a channel for the derivation of an intermediate mass function; as well as considering solutions to overcome the high-z quasar problem.

Fig. 2.14, from Aversa et al. 2015, shows the determination of the SMBH mass function for a semi-analytical approach using both the continuity equation and abundance matching, invoking super-Eddington accretion. In comparison are the functions from Shankar et al. 2009 using scaling relations of the $M_\bullet - M_\star$ (Haring & Rix 2004) and $M_\bullet - \sigma$ (Tremaine et al. 2002) for elliptical galaxies and galactic bulges; Shankar et al. 2012 is similar, using relations from pseudobulges; Vika et al. 2009 uses object-by-object analysis and the $M_\bullet - L$ (McLure & Dunlop 2003) relation.

The AGN bolometric luminosity function is the culmination of observational surveys across multiple wavelength bands, corrected for their individual selection effects. In the introduction of Shen et al. 2020, there is a collective list of the numerous references for each observation band (optical, UV, soft X-ray, hard X-ray, IR) used in the derivation of their quasar luminosity function, which works as a surrogate for the general AGN luminosity function at high-z observations, when less luminous objects are difficult to observe and thus sustain a higher uncertainty.

Fig. 2.15 shows the quasar luminosity function for early ($z > 2.4$) or late ($z < 2.4$) phase observations. The double Schechter form of the function can be seen for both quasar types, and is apparent across all redshifts. Due to the connection between luminosity and accretion rate for AGNs, any model examining the mass evolution of BHs, in particular the derivation of a SMBH mass function, can use the AGN luminosity function to evaluate and scrutinise the resulting Eddington ratio and luminosity values obtained. This means the AGN luminosity function constitutes an important check on mass function models which do not assume an initial luminosity function, and will be discussed in Chapter 4 of this work.
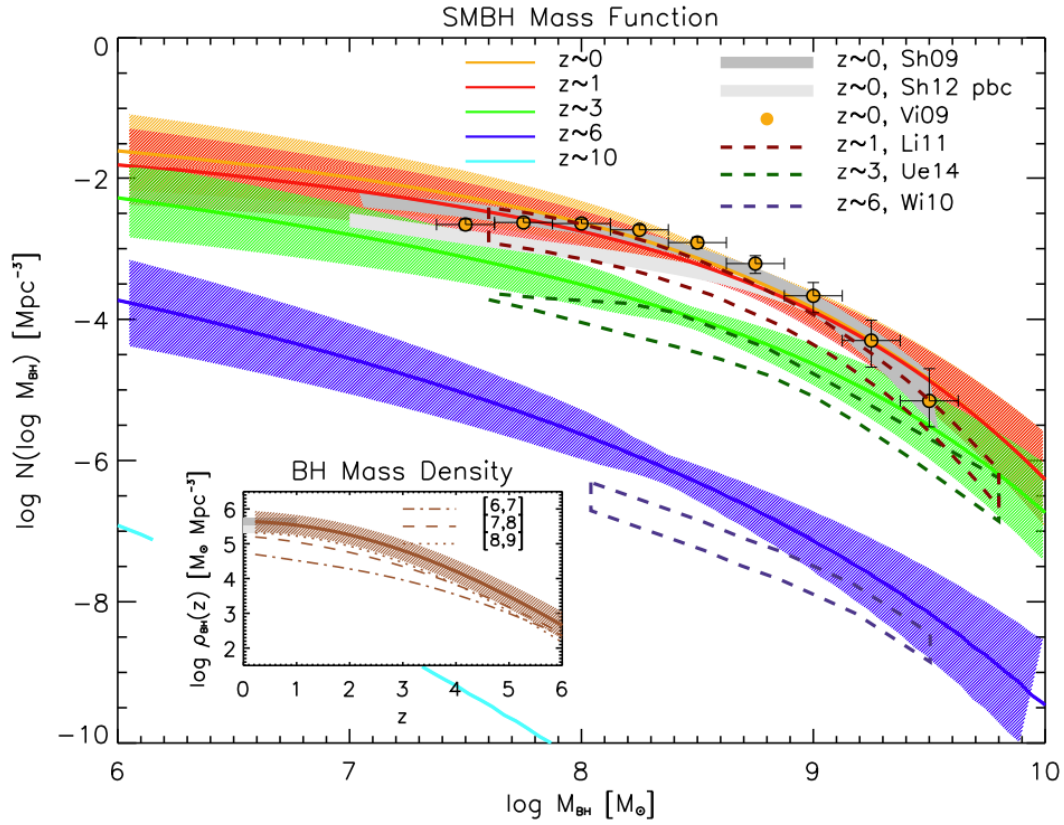
FIGURE 2.14: The SMBH mass function from Aversa et al. 2015. Presented is the mass function for $z \sim 0$ (orange), 1 (red), 3 (green), 6 (blue), 10 (cyan); where the $z \sim 10$ line corresponds to an extrapolation to high-z. The light and dark grey shaded areas correspond to Shanker et al. 2012 and 2009 respectively; the yellow points Vika et al. 2009. The dashed red, green, and blue area are the determinations of the SMBH mass function by Li et al. 2011 at $z \sim 1$, Ueda et al. 2014 at $z \sim 3$, and Willott et al. 2010b at $z \sim 6$ respectively. The inset plot shows the BH mass density function, for the overall mass range (solid line with hatched area) and logarithmic mass ranges [6,7] (dot-dashed), [7,8] (dashed), [8,9] (dotted), with the grey area giving the observational constraints for $z > 0$ mass function by Shankar et al. 2009, 2012 as in the main plot.

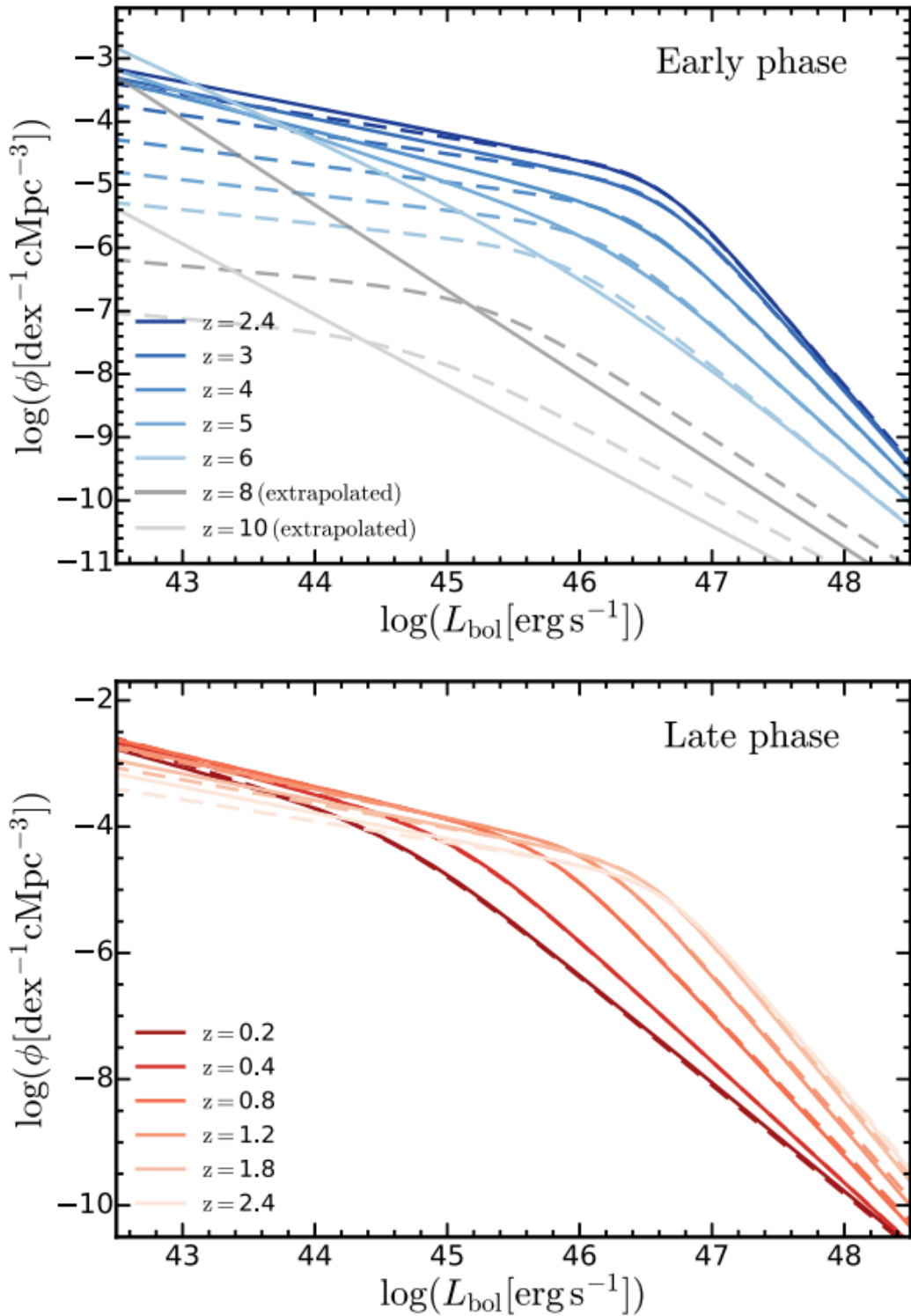FIGURE 2.15: The quasar LF as a function of *z*, split into 'late phase' or quenching (*z* < 2.4) and 'early phase' or build-up (*z* > 2.4) evolution periods. The solid and dashed lines refer to different fitting models, where all can be found and explained in Shen et al. 2020.

Chapter 3

The Stellar Black Hole Mass Function and Light Seed Distribution

With Chapters 1 and 2 concluded, we arrive at the heart of this thesis and begin the task of building a BH mass function beginning with the stellar mass regime ($m_\bullet \sim 5 - 150$ M$_\odot$). This mass function can stand along, but will be implemented in Chapter 4 when considering SMBHs. The following is based on the work undertaken in Sicilia et al. 2022a.

3.1 Introduction

The formation and evolution of BHs in the Universe is one of the major issues to be addressed by modern research in astrophysics and cosmology. In the mass range $m_\bullet \sim 5 - 150 \, M_\odot$, BHs are originated from the final, often dramatic stages in the evolution of massive stars (possibly hosted in binary systems). These compact remnants can produce luminous X-ray binaries (e.g., Mapelli et al. 2010; Farr et al. 2011; Inoue et al. 2016), can constitute powerful sources of gravitational waves for ground-based detectors like the current LIGO/Virgo facility (e.g., Belczynski et al. 2010; Dominik et al. 2015; Spera et al. 2017, 2019; Boco et al. 2019; Abbott et al. 2021a,b), can possibly energise short gamma-ray bursts and associated kilonovas (e.g., Abbott et al. 2020, 2021c; Ackley et al. 2020; Gompertz et al. 2020), can inject strong energy inputs in the primeval Universe (e.g., Mirabel et al. 2011; Justham & Schawinski 2012; Artale et al. 2015; Madau & Fragos 2017; Lehmer et al. 2021), and can provide light seeds for the subsequent growth of more massive BHs (e.g., Madau et al. 2014; Volonteri et al. 2015; Lupi et al. 2016; Pacucci et al. 2017; Boco et al. 2020; Das et al. 2021). At the other end, in the range $M_\bullet \sim 10^6 - 10^{10} \, M_\odot$, supermassive BHs grow mainly by gaseous accretion, that energise the spectacular broadband emission of AGNs. Such

an activity can have a profound impact on galaxy evolution (e.g., Alexander & Hickox 2012; Lapi et al. 2014, 2018; Chapter 2, Sect. 2.3.1), as testified by the strict relationships between the relic BH masses and the physical properties of the hosts (e.g., Kormendy & Ho 2013; Shankar et al. 2016, 2020; Zhu et al. 2021). The intermediate mass range $m_\bullet \sim 10^3 - 10^6\,M_\odot$ is the most uncertain. So far, only tentative evidence of these systems has been identified (see Paynter et al. 2021). However, the chase is open in view of their astrophysical relevance. Most noticeably, they can provide heavy seeds for quick (super)massive BH growth (e.g., Mayer & Bonoli 2019; Boco et al. 2020), as it seems required by the puzzling observations of an increasing numbers of giant monsters $M_\bullet \gtrsim 10^9\,M_\odot$ when the age of the Universe was shorter than $\lesssim 0.8$ Gyr (e.g., Mortlock et al. 2011; Venemans et al. 2017; Banados et al. 2018). Moreover, such intermediate-mass BHs will constitute important targets for space-based gravitational wave detectors like LISA and DECIGO (see eLISA Consortium 2013; Kawamura et al. 2021; also Boco et al. 2021a; Barausse & Lapi 2021).

One of the most fundamental quantity for demographic studies of the BH population is constituted by the relic mass function, namely the number density of BHs per comoving volume and unit BH mass, as a function of redshift. In the supermassive regime, where most of the BH mass is accumulated through gas accretion, this is usually determined from the AGN luminosity function via Soltan (1982)-type or continuity equation arguments (e.g., Small & Blandford 1992; Salucci 1999; Yu & Lu 2004; Merloni & Heinz 2008; Kelly & Merloni 2012; Aversa et al. 2015; Shankar et al. 2004, 2009, 2013, 2020; Chapter 2, Sect. 2.3.3), or from galaxy statistics and scaling relations among galactic and BH properties (e.g., Vika et al. 2009; Li et al. 2011; Mutlu-Pakdil et al. 2016). At the other end, the stellar BH mass function is largely unknown, and the most promising messenger to constrain it is constituted by the gravitational wave emission from coalescing binary BH systems (e.g., Kovetz et al. 2017; Perna et al. 2019; Tang et al. 2020; Ding et al. 2020); a first determination of the primary mass distribution for merging binary BHs has been established by the LIGO/Virgo collaboration (see Abbott et al. 2021a), although it depends somewhat on some assumptions (see Baxter et al. 2021). Therefore a theoretical grasp on the stellar BH mass function at different redshifts is of crucial importance.

In this Chapter, we provide an ab-initio computation of the stellar BH relic mass function across cosmic times, by coupling the state-of-the-art stellar and binary evolutionary code SEVN to redshift-dependent

galaxy statistics and empirical scaling relations involving metallicity, star-formation rate and stellar mass. Note that here we mainly consider the standard, and likely dominant production channel of stellar-mass BHs constituted by isolated single/binary star evolution, and defer to future work the treatment of other formation mechanisms like dynamical effects in dense star clusters (e.g., Miller & Hamilton 2002; Alexander & Natarajan 2014; Antonini et al. 2019), AGN disks (e.g., McKernan et al. 2012; Yang et al. 2019), hierarchical triples (e.g., Kimpson et al. 2016; Fragione et al. 2019) that are thought to produce corrections in the high-mass tail of the mass function, toward the intermediate-mass BH regime.

The plan of the Chapter is straightforward. In Sect. 3.2 we introduce the theoretical background underlying our computation of the stellar BH relic mass function; specifically, we highlight the role of quantities related to galaxy formation (Sect. 3.2.1) and to stellar evolution (Sect. 3.2.2), and show how to include the effects of binary BH mergers (Sect. 3.2.3). In Sect. 3.3 we present our results concerning the stellar BH cosmic birthrate, the redshift-dependent stellar BH relic mass function and relic mass density; we also compare the primary mass distribution for merging BH binaries with the recent estimates from gravitational wave observations by LIGO/Virgo. In Sect. 3.4 we critically discuss how our results depend on the adopted binary stellar evolution code. Moreover, we estimate the effects of binary BH formation in dense environments like (young) star clusters. We also highlight the relevance of our computations in providing a light seed distributions for BH growth at high redshift. Finally, in Sect. 3.5 we summarise our findings and outlook future developments.

Throughout this Chapter, we adopt the standard flat ΛCDM cosmology (Planck Collaboration 2020) with rounded parameter values: matter density $\Omega_M = 0.3$, dark energy density $\Omega_\Lambda = 0.7$, baryon density $\Omega_b = 0.05$, Hubble constant $H_0 = 100\,h\,\mathrm{km\,s^{-1}\,Mpc^{-1}}$ with $h = 0.7$. A Kroupa 2001 IMF in the star mass range $m_\star \sim 0.1 - 150\,M_\odot$ and a value $Z_\odot \approx 0.015$ for the solar metallicity are adopted (see Caffau et al. 2011).

3.2 Theoretical background

We aim at deriving the stellar BH relic mass function, i.e., the number density of stellar BHs per unit comoving volume V and remnant mass $m_\bullet$ accumulated down to redshift z

$$\frac{\mathrm{d}^2 N_\bullet}{\mathrm{d}V\,\mathrm{d}\log m_\bullet}(m_\bullet| > z) = \int_z^\infty \mathrm{d}z'\,\frac{\mathrm{d}t_{z'}}{\mathrm{d}z'}\,\frac{\mathrm{d}^2 \dot{N}_\bullet}{\mathrm{d}V\,\mathrm{d}\log m_\bullet}(m_\bullet|z')\,, \qquad (3.1)$$

and the related stellar BH relic mass density

$$\rho_\bullet(z) = \int \mathrm{d}\log m_\bullet \, m_\bullet \, \frac{\mathrm{d}^2 N_\bullet}{\mathrm{d}V \mathrm{d}\log m_\bullet}(m_\bullet|z) \; . \tag{3.2}$$

In the above Eq. (3.1) the quantity t_z is the cosmic time corresponding to redshift z and $\mathrm{d}^2\dot{N}_\bullet/\mathrm{d}V \mathrm{d}\log m_\bullet$ is the stellar BH cosmic birthrate, i.e. the production rate of BH of given mass per unit comoving volume. In turn, the latter can be expressed as

$$\frac{\mathrm{d}^2 \dot{N}_\bullet}{\mathrm{d}V \mathrm{d}\log m_\bullet}(m_\bullet|z) = \int \mathrm{d}\log Z \, \frac{\mathrm{d}^2 N_\bullet}{\mathrm{d}M_{\mathrm{SFR}} \mathrm{d}\log m_\bullet}(m_\bullet|Z) \, \frac{\mathrm{d}^2 \dot{M}_{\mathrm{SFR}}}{\mathrm{d}V \mathrm{d}\log Z}(Z|z) \tag{3.3}$$

where Z is the metallicity and M_{SFR} is the star formed mass. The first and second factors in the integrand are usually referred to as the stellar and the galactic term, respectively (see Chruslinska & Nelemens 2019; Boco et al. 2021b); we will now describe each of them in some detail, starting with the latter. The main steps toward the computation of the stellar BH relic mass function are sketched in Fig. 3.1.

3.2.1   The galactic term

The galactic term in Eq. (3.3) represents the cosmic SFR density per unit cosmic volume and metallicity; in other words, it constitutes the classic 'Madau' plot (see Madau & Dickinson 2014 and reference therein) sliced in metallicity bins, and as such is mainly related to galaxy formation and evolution. It may be estimated in various ways, starting from different galaxy statistics and empirical scaling laws. We compute it as

$$\begin{aligned}
\frac{\mathrm{d}^2 \dot{M}_{\mathrm{SFR}}}{\mathrm{d}V \, \mathrm{d}\log Z}(Z|z) = & \int \mathrm{d}\log\psi \, \psi \, \frac{\mathrm{d}^2 N}{\mathrm{d}V \, \mathrm{d}\log\psi}(\psi, z) \\
& \times \int \mathrm{d}\log M_\star \, \frac{\mathrm{d}p}{\mathrm{d}\log M_\star}(M_\star|\psi, z) \, \frac{\mathrm{d}p}{\mathrm{d}\log Z}(Z|M_\star, \psi)
\end{aligned} \tag{3.4}$$

where ψ is the SFR and $M_\star$ the stellar mass of a galaxy. Three ingredients enter into the above expression. The first is constituted by the redshift-dependent SFR functions $\mathrm{d}^2 N/\mathrm{d}V \mathrm{d}\log\psi$, expressing the number of galaxies per unit cosmological volume and SFR bin. For these we adopt the determination by Boco et al. (2021, see Fig. 3.2; for an analytic Schechter fit see Eq. 2 and Table 1 in Mancuso et al. 2016a) derived from an educated combination of the dust-corrected UV (e.g., Oesch et al. 2018; Bouwens et
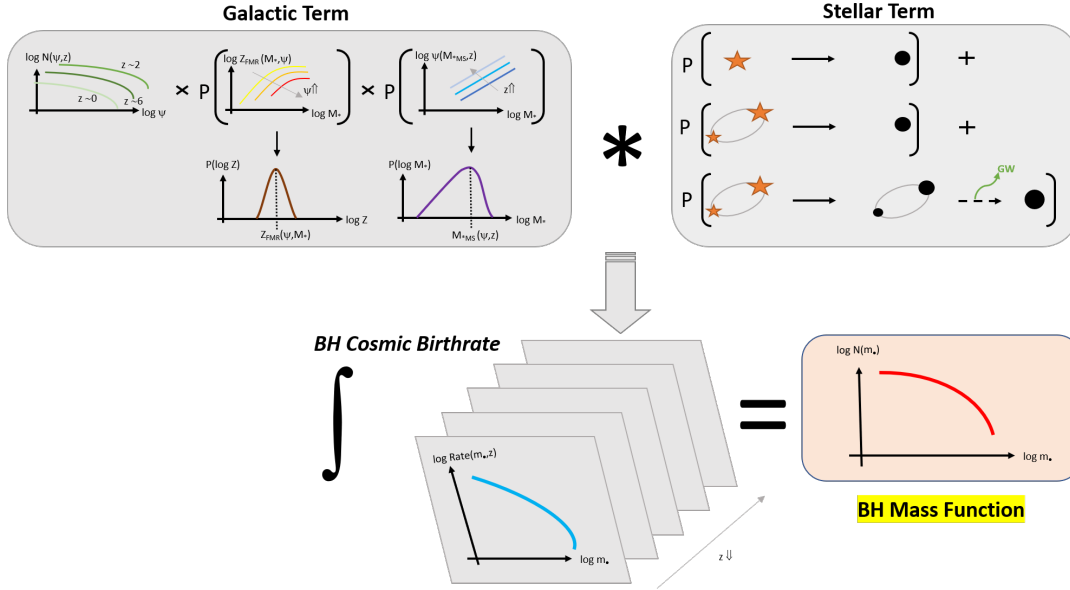
FIGURE 3.1: Schematics showing the main steps to compute the stellar BH relic mass function (Eq. 3.1). This is obtained by integration over redshift of the BH cosmic birthrate (Eq. 3.3), which is in turn determined via the convolution of the galactic and the stellar terms. The galactic term (Eq. 3.4) is computed by convolving the galaxy statistics (based on the SFR function) with the metallicity distribution of a galaxy at given SFR and stellar mass (assumed as a log-normal shape around the fundamental metallicity relation; see Eq. 3.6) and with the stellar mass distribution of a galaxy at given SFR and redshift (built from the redshift-dependent main sequence of star-forming galaxies; see Eq. 3.5). The stellar term (Eq. 4.5) is computed from the stellar and binary evolutionary code SEVN by summing up, for a given IMF, the probabilities per unit star-formed mass that: (i) a single star evolves into a BH remnant (single stellar evolution); (ii) a binary stellar system evolves into a single BH remnant or two BHs no longer bounded (failed binaries); (iii) a binary stellar system evolves into a binary BH (binaries), that may eventually coealesce into a single BH via emission of gravitational waves.

al. 2020), IR (e.g., Gruppioni et al. 2020; Zavala et al. 2021), and radio (e.g.
Novak 2017; Ocran 2020) luminosity functions, appropriately converted in
SFR (see Kennicutt & Evans 2012).

The second ingredient is the probability distribution of stellar mass at
given SFR and redshift:

$$\frac{\mathrm{d}p}{\mathrm{d}\log M_\star}(M_\star|\psi,z) \propto \begin{cases} M_\star & M_\star < M_{\star,\mathrm{MS}}(\psi,z) \\ M_{\star,\mathrm{MS}} \, \exp\left\{-\frac{[\log M_\star - \log M_{\star,\mathrm{MS}}(\psi,z)]^2}{2\,\sigma_{\log M_\star}^2}\right\} & M_\star \geq M_{\star,\mathrm{MS}}(\psi,z) \end{cases}$$

(3.5)

where $M_{\star,\mathrm{MS}}(\psi,z)$ is the observed redshift-dependent galaxy main se-
quence with log-normal scatter $\sigma_{\log M_\star} \approx 0.2$ dex (we adopt the determi-
nation by Speagle et al. 2014; for an analytic fit, see Eq. 2.6). The main
sequence is a relationship between SFR and stellar mass followed by the
majority of star-forming galaxies, apart from some outliers located above
the average SFR at given stellar mass (see Daddi et al. 2007; Sargent et al.
2012; Rodighiero et al. 2011, 2015; Speagle et al. 2014; Whitaker et al. 2014;
Schreiber et al. 2015; Caputi et al. 2017; Bisigello et al. 2018; Boogaard et al.
2018). The expression in Eq. (3.5) holds for an approximately constant SFR
history, which is indicated both by in-situ galaxy formation scenarios (see
Mancuso et al. 2016b; Pantoni et al. 2019; Lapi et al. 2020) and by observa-
tions of ETG progenitors (that have on average slowly rising star formation
history with typical duration of $\lesssim$ 1 Gyr; see Papovich et al. 2011; Smit et
al. 2012; Moustakas et al. 2013; Steinhardt et al. 2014; Cassará et al. 2016;
Citro et al. 2016) and late-type galaxies (that have on average slowly declin-
ing star formation history over long timescale of several Gyrs; e.g., see Chi-
appini et al. 1997; Courteau et al. 2014; Pezzulli & Fraternali 2016; Grisoni
et al. 2017). In this vein, off-main sequence objects can be simply viewed
as galaxies caught in an early evolutionary stage, that are still accumulating
their stellar mass (which grows almost linearly with time for a constant SFR),
and are thus found to be preferentially located above the main sequence or,
better, to the left of it. As time goes by and the stellar mass increases, the
galaxy moves toward the average main sequence relationship, around which
it will spend most of its lifetime before being quenched due to gas exhaus-
tion or feedback processes.

The third ingredient is the probability distribution of metallicity at given
stellar mass and SFR

$$\frac{\mathrm{d}p}{\mathrm{d}\log Z}(Z|M_\star,\psi) \propto \exp\left\{-\frac{[\log Z - \log Z_{\mathrm{FMR}}(M_\star,\psi)]^2}{2\,\sigma_{\log Z}^2}\right\}$$
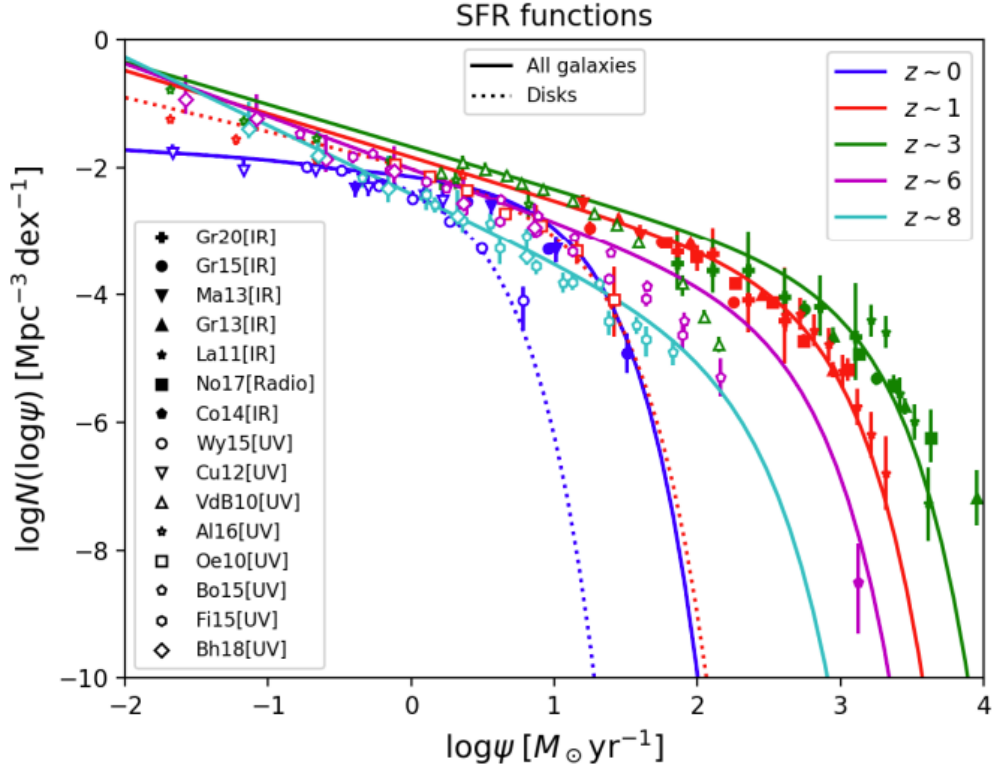
(3.6)

FIGURE 3.2: Redshift dependent SFR function, as seen in the left panel of Boco et al. 2021 Fig 1. Corresponding redshifts: $z \sim 0$ (blue), 1 (red), 3 (green), 6 (magenta), 8 (cyan). Solid lines represent UV plus FIR/(sub)millimetre/radio data (akin to total population), dotted lines represent dust-corrected UV data (akin to disk galaxies). UV data (open symbols): van der Burg et al 2010 (triangles); Bouwens et al. 2016, 2017 (pentagons); Finkelson et al 2015 (hexagons); Cucciati et al 2012 (inverted triangles); Wyder et al 2005 (circles); Oesch et al 2010 (squares); Alavi et al 2016 (stars); Bhatawdeski et al 2018 (diamond). Far-IR/(sub)millimetre data (filled symbols): Gruppioni et al 2020 (plus); Gruppioni et al. 2015 (circle); Gruppioni et al. 2013 (triangles); Magnelli et al. 2013 (inverted triangle); Lapi et al. 2011 (stars); Cooray et al. 2014 (pentagons). Radio data from Novak et al. 2017 (filled squares).

that is assumed to be log-normal with mean $\log Z_{\mathrm{FMR}}(M_\star, \psi)$ and scatter $\sigma_{\log Z} \approx 0.15$ dex provided by the observed fundamental metallicity relation (we adopt the determination by Mannucci et al. 2011; for an analytic fit, see Eq 2.5). This is a relationship among metallicity, stellar mass and SFR of a galaxy which is found to be closely independent of redshift at least out to $z \lesssim 4$ (see Mannucci et al. 2010, 2011; Hunt et al. 2016; Curti et al. 2020; Sanders et al. 2021). In the aforementioned in-situ galaxy formation scenarios (see Pantoni et al. 2019; Lapi et al. 2020; Boco et al. 2021b), the fundamental metallicity relation naturally stems from: an early, rapid increase of the metallicity with galactic age, which for a roughly constant star formation history just amounts to the ratio $M_\star/\psi$; a late-time saturation of the metallicity to a mass-dependent value which is determined by the balance among metal dilution, astration, removal by feedback, and partial restitution by stellar evolution processes and galactic fountains (if present).

In Fig. 3.3 we illustrate the galactic term given by Eq. (3.4). Specifically, we have colour-coded the cosmic SFR density $\mathrm{d}^2\dot{M}_{\mathrm{SFR}}/\mathrm{d}V\,\mathrm{d}\log Z$ per unit comoving volume as a function of redshift z and metallicity $\log Z$. Most of the cosmic star formation occurs around redshift $z \sim 2 - 3$ at rather high metallicity, close to solar values. The metallicity at which most star formation takes place decreases with redshift, but very mildly out to $z \sim 4 - 5$. However, we note that at any redshift there is a long, pronounced tail of star formation occurring at low metallicities, down to $0.01\,Z_\odot$. We discuss possible variations of the prescriptions entering the galactic term in Sect. 3.4.1.

3.2.2 The stellar term

The stellar term in Eq. (3.3) represents the number of BHs formed per unit of star formed mass and remnant mass; as such, it is related to the evolution of isolated or binary stars, and must be evaluated via detailed simulations of stellar astrophysics. The stellar term can be split in various contributions

$$\frac{\mathrm{d}^2 N_\bullet}{\mathrm{d}M_{\mathrm{SFR}}\mathrm{d}\log m_\bullet}(m_\bullet|Z) = \frac{\mathrm{d}^2 N_{\star\to\bullet}}{\mathrm{d}M_{\mathrm{SFR}}\mathrm{d}\log m_\bullet}(m_\bullet|Z)+$$
$$\frac{\mathrm{d}^2 N_{\star\star\to\bullet}}{\mathrm{d}M_{\mathrm{SFR}}\mathrm{d}\log m_\bullet}(m_\bullet|Z) + \sum_{i=1,2} \frac{\mathrm{d}^2 N_{\star\star\to\bullet\bullet}}{\mathrm{d}M_{\mathrm{SFR}}\mathrm{d}\log m_{\bullet,i}}(m_\bullet|Z)$$

$$(3.7)$$

the first comes from the evolution of isolated, massive stars that evolve into BHs at the end of their life (hereafter referred to as 'single stellar evolution'); the second comes from stars that are originally in binary systems but end
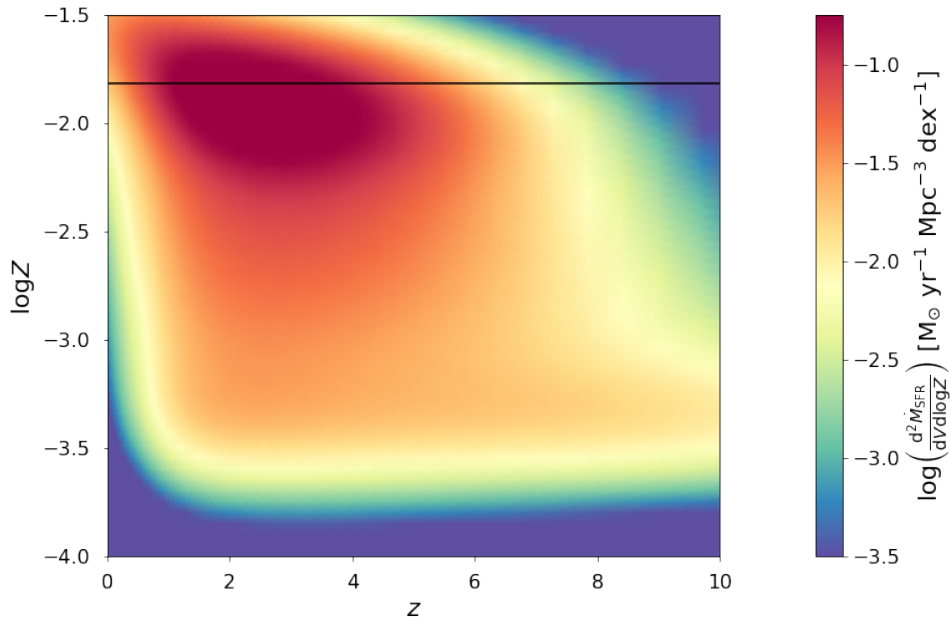
FIGURE 3.3: The galactic term $\mathrm{d}^2\dot{M}_\star/\mathrm{d}V\,\mathrm{d}\log Z$ of Eq. (3.4) expressing the amount of SFR (colour-coded) per unit comoving volume as a function of redshift z (on x-axis) and of metallicity Z (on y-axis). The black horizontal line highlights the solar value $Z_\odot$.

up as an isolated BH because one of the companion has been ejected or destroyed or cannibalized (hereafter 'failed BH binaries'); the third comes from stars in binary systems that evolve into a BH binary with primary mass $m_{\bullet,1}$ and secondary mass $m_{\bullet,2}$ (hereafter 'binaries'). All these terms are strongly dependent on metallicity Z, since this quantity affects the efficiency of the various processes involved in stellar and binary evolution, like mass loss rates, mass transfers, core-collapse physics, etc. Note that other crucial ingredients implicitly entering the above terms are the IMF $\phi(m_\star)$, i.e. the distribution of star masses $m_\star$ per unit mass formed in stars, and the binary fraction $f_{\star\star}$, i.e. the mass fraction of stars originally born in binary systems; both are rather uncertain quantities. As a reference we adopt a universal (i.e., equal for every galaxies at any cosmic time) Kroupa 2001 IMF and a binary mass fraction $f_{\star\star} \approx 0.5$ constant with the star mass $m_\star$. We discuss the impact of these choices on our results in Sect. 3.4.1.

To compute the stellar term, we exploit the outcomes of the SEVN stellar and binary evolution code, that provides directly each of the above contributions (see Spera et al. 2019 for details). However, to add some more grasp on the physics involved, we can provide a handy approximation for the first term referring to isolated stars; this writes as

$$\frac{\mathrm{d}^2 N_{\star\to\bullet}}{\mathrm{d}M_{\mathrm{SFR}}\mathrm{d}\log m_\bullet}(m_\bullet|Z) = (1 - f_{\star\star}) \int \mathrm{d}m_\star\, \phi(m_\star)\, \frac{\mathrm{d}p_{\star\to\bullet}}{\mathrm{d}\log m_\bullet}(m_\bullet|m_\star, Z) \quad (3.8)$$

where $f_{\star\star}$ is the binary fraction, $\phi(m_\star)$ is the IMF, and

$$\frac{\mathrm{d}p_{\star\to\bullet}}{\mathrm{d}\log m_\bullet}(m_\bullet|m_\star, Z) \propto \exp\left\{ -\frac{[\log m_\bullet - \log m_{\star\to\bullet}(m_\star, Z)]^2}{2\,\sigma_{\log m_\bullet}^2} \right\} \quad (3.9)$$

is an approximately log-normal distribution centred around the metallicity-dependent relationship $m_{\star\to\bullet}(m_\star, Z)$ between the remnant mass and the initial ZAMS star mass, with dispersion $\sigma_{\log m_\bullet} \approx 0.15$ dex (see Spera et al. 2017; Boco et al. 2019). Unfortunately, for the other contributions of the stellar term related to binary evolution, an analogous analytic approximation is not viable, so one must trust the outputs of the SEVN code. We discuss the impact of adopting different prescriptions and codes for the computation of the stellar term in Sect. 3.4.1.

In Fig. 3.4 we illustrate the stellar term of Eq. (4.5), split in its various contributions. Specifically, we have colour-coded the distributions $\mathrm{d}^2 N_\bullet/\mathrm{d}M_{\mathrm{SFR}}\,\mathrm{d}\log m_\bullet$ per unit star mass formed M_{SFR} and BH remnant mass $m_\bullet$. The top left panel refers to isolated stars evolving into BHs. It is seen that a roughly constant number of remnants with masses $m_\bullet \sim 5 - 30\,M_\odot$
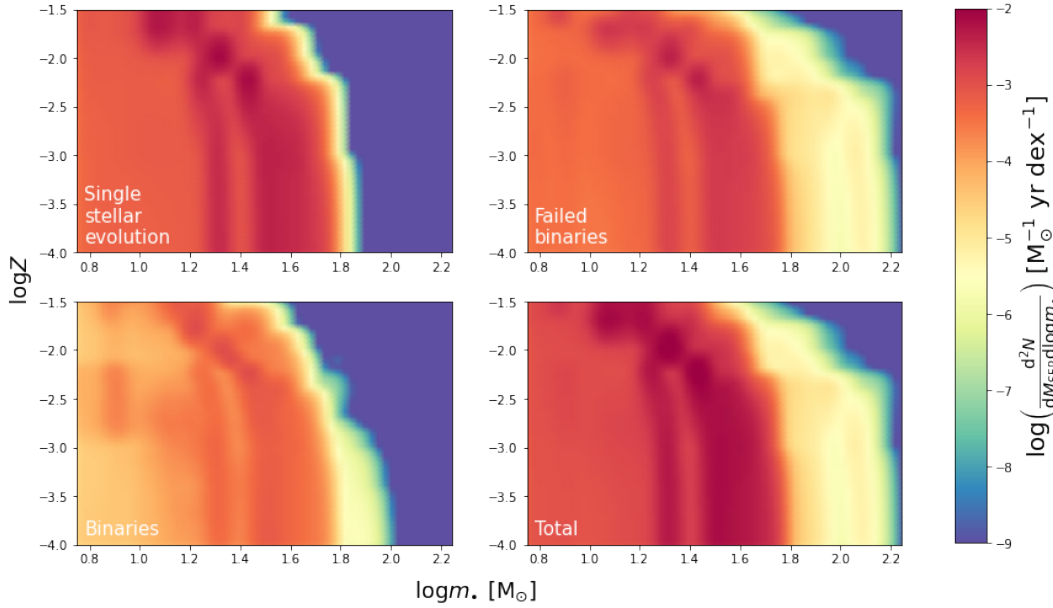
FIGURE 3.4: The stellar term $\mathrm{d}^2 N_\bullet / \mathrm{d}M_{\mathrm{SFR}}\,\mathrm{d}\log m_\bullet$ of Eq. (4.5) expressing the number of BHs per unit star-formed mass (colour-coded) as a function of BH mass $m_\bullet$ (on x-axis) and of metallicity Z (on y-axis). Different panels refer to: isolated stars evolving into single BH (top left); binary stars failing to form a compact binary and instead originating a single BH (top right); binary stars evolving in binary BHs (bottom left); summation of these contributions (bottom right).

is produced per logarithmic BH mass bin at any metallicity. Then there is a peak around $m_\bullet \sim 30 - 60\,M_\odot$, with the larger values applying to metal-poorer conditions, where stellar winds are not powerful enough to substantially erode the stellar envelope before the final collapse. Finally, the distribution rapidly falls off for larger $m_\bullet \gtrsim 50 - 60\,M_\odot$ even at low metallicity[1], due to the presence of pair-instability and pulsational pair-instability supernovae (see Woosley et al. 2002; Belczynski et al. 2016; Woosley 2017; Spera et al. 2017).

The top right panel refers to binary stellar systems failing to form a compact binary, and evolving instead into isolated BHs; this may happen because one of the progenitor stars has been ejected far away or destroyed or cannibalized during binary stellar evolution. The distribution of failed BH binaries differs substantially from single stellar evolution, being skewed toward more massive BHs, and with an appreciable number of remnants of

---

[1]Note that adopting an IMF with an upper star mass limit $m_\star \sim 150\,M_\odot$ avoids dealing with the formation of high-mass remnants $m_\bullet \gtrsim 100\,M_\odot$ by direct collapse.

mass $m_\bullet \sim 50 - 160\, M_\odot$ produced especially at low metallicities. Such massive BH remnants are mainly formed when two (non-degenerate) companion stars merge during a common envelope phase, possibly leaving then a big BH remnant. Finally, note that at high metallicity a non-negligible fraction of BHs in this channel has formed after the low-mass companion star had been ejected far away or destroyed by stellar winds and/or supernova explosions (see Spera et al. 2019 for details). The bottom left panel refers to binary stellar systems evolving into binary BHs; note that the distribution of primary and secondary BHs in the final configuration have been summed over. Although the overall number of binary BHs is substantially lower than the single BHs originated from the other two channels, most of them has a very similar mass spectrum; these remnants have formed from binary stars that underwent minor mass transfer episodes. However, at low metallicity stellar winds are reduced and hence the mass exchanged or lost during binary evolution may be significantly larger, implying a more extended tail toward masses $m_\bullet \lesssim 100\, M_\odot$ with respect to single stellar evolution. Finally, the bottom right panel illustrates the sum of all the previous formation channels.

3.2.3   Binary BH mergers

Tight BH binaries may be able to progressively lose their energy via gravitational wave emission and to merge in a single, more massive BH. The cosmic merging rate of binary BHs can be computed as

$$
\frac{d^2 \dot{N}_{\bullet\bullet\to\bullet}}{dV\, d\log m_{\bullet,i}}(m_\bullet|z) = \int dt_d \int d\log Z
$$
$$
\times \frac{d^2 N_{\star\star\to\bullet\bullet\to\bullet}}{dM_{SFR}\, d\log m_{\bullet,i}}(m_\bullet|Z)\, \frac{dp}{dt_d}(t_d|Z)\, \frac{d^2 \dot{M}_{SFR}}{dV\, d\log Z}(Z|z_{t-t_d})
$$

$$(3.10)$$

where z_t is the redshift corresponding to a cosmic time t, t_d is the time delay between the formation of the progenitor binary and the merger of the compact binary, and $i = 1, 2$. The integrand in the expression above is the product of three terms. The rightmost one is the galactic term that must be computed at a time $t - t_d$. The middle one represents the probability distribution of delay times, possibly dependent on metallicity. The leftmost one is the stellar term that represents the number of binary stellar systems first evolving in a compact binary and then being able to merge within the Hubble time, per unit of formed star mass and compact remnant mass (primary $m_{\bullet,1}$ and secondary $m_{\bullet,2}$); this is a fraction of the third term on the right hand

side of Eq. (4.5). The merger rate is then given by convolution of such a specific stellar term with the galactic term, weighted by the time delay distribution.

As a consequence of binary BH mergers, the stellar BH relic mass function may be somewhat distorted, since a number of low mass BHs are shifted to larger masses. This amounts to applying a merging correction to the original cosmic birthrate $\mathrm{d}^2\dot{N}/\mathrm{d}V\,\mathrm{d}m_\bullet$, that can be computed as follows[2]

$$
\frac{\mathrm{d}^2\dot{N}_{\bullet,\mathrm{mergcorr}}}{\mathrm{d}V\mathrm{d}m_\bullet}(m_\bullet|z) = \frac{\mathrm{d}^2\dot{N}_\bullet}{\mathrm{d}V\mathrm{d}m_\bullet}(m_\bullet|z)
$$

$$
+ \frac{1}{2}\int_{m_\bullet/2}^{m_\bullet}\mathrm{d}m_{\bullet,1}\frac{\mathrm{d}^2\dot{N}_{\bullet\bullet\to\bullet}}{\mathrm{d}V\,\mathrm{d}m_{\bullet,1}}(m_{\bullet,1}|z)\,\frac{\frac{\mathrm{d}^2\dot{N}_{\bullet\bullet\to\bullet}}{\mathrm{d}V\,\mathrm{d}m_{\bullet,2}}(m_\bullet - m_{\bullet,1}|z)}{\int_0^{m_{\bullet,1}}\mathrm{d}m_{\bullet,2}\frac{\mathrm{d}^2\dot{N}_{\bullet\bullet\to\bullet}}{\mathrm{d}V\,\mathrm{d}m_{\bullet,2}}(m_{\bullet,2}|z)}
$$

$$
+ \frac{1}{2}\int_0^{m_\bullet/2}\mathrm{d}m_{\bullet,2}\frac{\mathrm{d}^2\dot{N}_{\bullet\bullet\to\bullet}}{\mathrm{d}V\,\mathrm{d}m_{\bullet,2}}(m_{\bullet,2}|z)\,\frac{\frac{\mathrm{d}^2\dot{N}_{\bullet\bullet\to\bullet}}{\mathrm{d}V\,\mathrm{d}m_{\bullet,1}}(m_\bullet - m_{\bullet,2}|z)}{\int_{m_{\bullet,2}}^{\infty}\mathrm{d}m_{\bullet,1}\frac{\mathrm{d}^2\dot{N}_{\bullet\bullet\to\bullet}}{\mathrm{d}V\,\mathrm{d}m_{\bullet,1}}(m_{\bullet,1}|z)}
$$

$$
- \sum_{i=1,2}\frac{\mathrm{d}^2\dot{N}_{\bullet\bullet\to\bullet}}{\mathrm{d}V\,\mathrm{d}m_{\bullet,i}}(m_\bullet|z)\;;
$$

$$
\tag{3.11}
$$

in the positive terms on the right hand side, the normalisations of the rates have been chosen so as to ensure mass conservation and self-consistency of the integrated merger rates.

We caveat that additional distortions of the relic BH mass function may be induced by dynamical effects and/or hierarchical mergers in dense environments (see Sect. 3.4.2 for a preliminary discussion), by mass growth due to accretion in X-ray binaries or in AGN disks, etc.; these processes are expected to be relevant especially at the high mass end, toward the intermediate-mass BH regime.

---

[2]For the sake of simplicity in Eq. (3.11) we are neglecting the small amount of mass lost as gravitational waves during the coalescence, since we checked that for the purpose of this computation it is practically irrelevant.
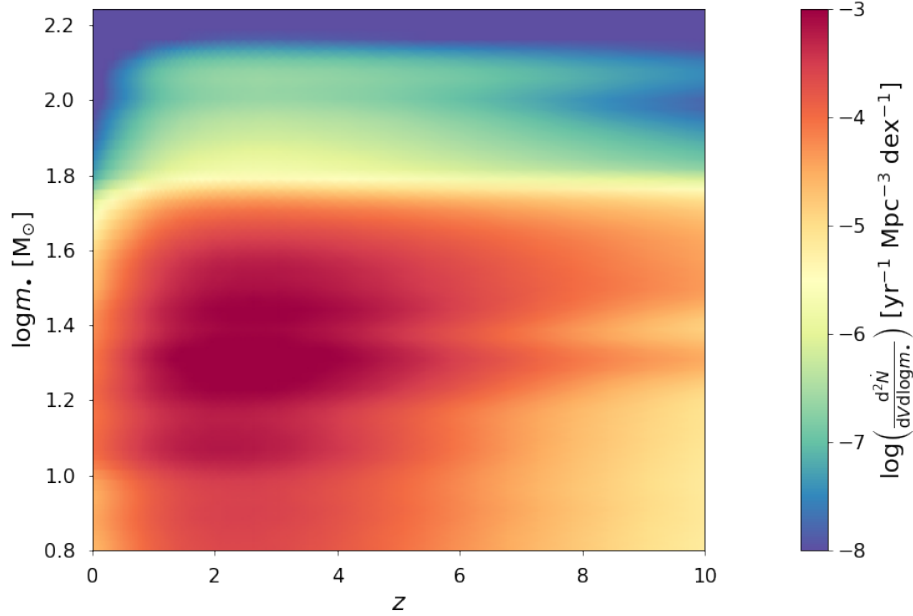
FIGURE 3.5: The stellar BH cosmic birthrate $\mathrm{d}^2\dot{N}/\mathrm{d}V\,\mathrm{d}\log m_\bullet$ (colour-coded) as a function of redshift z (on x-axis) and BH mass $m_\bullet$ (on y-axis).

3.3 Results

In Fig. 3.5 we illustrate the stellar BH cosmic birthrate of Eq. (3.3) as a function of redshift z and remnant mass $m_\bullet$. Specifically, we have colour-coded the birthrate $\mathrm{d}^2\dot{N}_\bullet/\mathrm{d}V\,\mathrm{d}\log m_\bullet$ per unit comoving volume V and BH mass $m_\bullet$. At $z \sim 1-4$ most of the BHs are formed with a rather flat distribution in $\log m_\bullet$ for $m_\bullet \sim 5-50\,M_\odot$, though there is a non-negligible tail up to $m_\bullet \lesssim 160\,M_\odot$ due to stellar mergers (see previous section for details). Moving toward high redshift $z \gtrsim 4$ the mass distribution becomes skewed toward masses $m_\bullet \sim 30-50\,M_\odot$ since these are preferentially produced in the low metallicity environments, while the tail for $m_\bullet \gtrsim 50\,M_\odot$ tends to be reduced because of the decrease in the number density of star-forming galaxies with appreciable SFR.

   In Fig. 3.6 we illustrate the stellar BH relic mass function $\mathrm{d}^2 N_\bullet/\mathrm{d}V\,\mathrm{d}\log m_\bullet$ of Eq. (3.1) as a function of the remnant mass $m_\bullet$ for different redshifts $z \sim 0-10$. At given redshift, the mass function features a roughly constant behaviour for $m_\bullet \sim 5-50\,M_\odot$, followed by a quite steep decline for $m_\bullet \gtrsim 50\,M_\odot$. Noticeably, there are bumps at around $m_\bullet \sim 20\,M_\odot$, $m_\bullet \sim 30-50\,M_\odot$ and $m_\bullet \sim 120\,M_\odot$, that are more pronounced at high
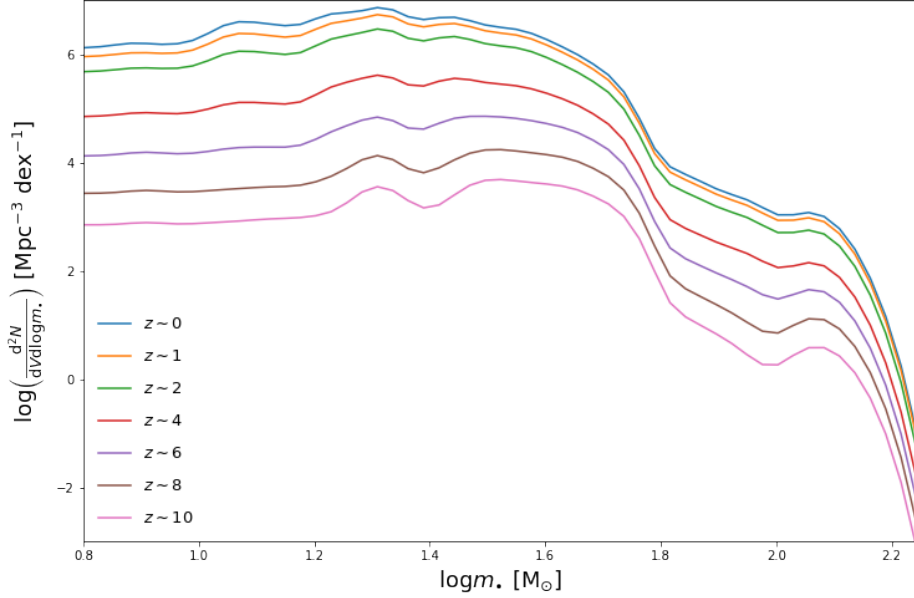
FIGURE 3.6: The stellar BH relic mass function $\mathrm{d}^2N/\mathrm{d}V\,\mathrm{d}\log m_\bullet$ as a function of the BH mass $m_\bullet$ at different redshifts $z \sim 0$ (cyan), $z \sim 1$ (orange), $z \sim 2$ (green), $z \sim 4$ (red), $z \sim 6$ (violet), $z \sim 8$ (brown) and $z \sim 10$ (pink).

redshift (where metallicity is smaller) and progressively washed out toward the local Universe. Such features reflect regions of higher BH numbers that are evident in the stellar term of Fig. 3.4 (in the form of almost vertical darker strips). Specifically, the first two originate from the detailed shape of the metallicity-dependent BH mass spectrum from single stellar evolution, while the third one mainly depends on binary evolution effects.

The mass function increases for decreasing redshift, quite rapidly down to $z \sim 2 - 3$ and then more mildly toward $z \sim 0$. Smoothing out minor features, the mass function can be analytically rendered in the range $m_\bullet \sim 5 - 160\,M_\odot$ via a Schechter+Gaussian shape (Saunders et al. 1990)

$$
\begin{aligned}
\frac{\mathrm{d}^2N}{\mathrm{d}V\,\mathrm{d}\log m_\bullet} \simeq & \mathcal{N}\left(\frac{m_\bullet}{\mathcal{M}_\bullet}\right)^{1-\alpha} e^{-m_\bullet/\mathcal{M}_\bullet} \\
& + \mathcal{N}_G\,\frac{1}{\sqrt{2\pi\sigma_G^2}}\,e^{-(\log m_\bullet - \log \mathcal{M}_{\bullet,G})^2/2\,\sigma_G^2}\;;
\end{aligned}
\tag{3.12}
$$

the Schechter function has normalization $\mathcal{N}$, low-mass power-law index α

	Field, $f_{\text{field}} = 1$						Field + Cluster, $f_{\text{field}} = 0.6$					
z	$\log\mathcal{N}$ [Mpc^{-3}]	$\log\mathcal{M}_\bullet$ [M$_\odot$]	α	$\log\mathcal{N}_G$ [Mpc^{-3}]	$\log\mathcal{M}_{\bullet,G}$ [M$_\odot$]	σ_G	$\log\mathcal{N}$ [Mpc^{-3}]	$\log\mathcal{M}_\bullet$ [M$_\odot$]	α	$\log\mathcal{N}_G$ [Mpc^{-3}]	$\log\mathcal{M}_{\bullet,G}$ [M$_\odot$]	σ_G
0	5.623	0.607	-3.781	2.413	2.021	0.052	6.078	0.704	-2.717	3.496	1.808	0.1846
1	5.429	0.609	-3.859	2.309	2.023	0.051	5.887	0.709	-2.785	3.304	1.843	0.173
2	5.107	0.612	-3.914	2.064	2.024	0.051	5.592	0.713	-2.823	3.008	1.866	0.165
4	4.344	0.634	-3.902	1.419	2.037	0.049	4.796	0.747	-2.782	2.101	1.952	0.132
6	3.614	0.659	-3.866	0.806	2.054	0.045	4.112	0.785	-2.718	1.359	2.012	0.107
8	2.894	0.676	-3.868	0.197	2.066	0.043	3.457	0.816	-2.660	0.685	2.046	0.091
10	2.305	0.680	-3.884	-0.344	2.072	0.042	2.897	0.831	-2.623	0.113	2.059	0.0841

Note - Fits valid in the range $m_\bullet \sim 5 - 160\,M_\odot$. Typical relative uncertainties on the parameters are $\lesssim 10\%$, and typical values of the reduced $\chi_r^2 \lesssim 1$ are found. The results for $f_{\text{field}} = 0.6$ are based on the simulations by Di Carlo et al. (2019, 2020) for young open star clusters.

TABLE 3.1: Fits to stellar BH relic mass function via Eq. (3.12).

and characteristic mass $\mathcal{M}_\bullet$, while the Gaussian (log-normal) has normalization $\mathcal{N}_G$, mean $\mathcal{M}_{\bullet,G}$ and dispersion σ_G. The optimal values of these parameters have been determined via a Levenberg-Marquardt least-squares fit to the numerical mass function for $m_\bullet \sim 5 - 160\,M_\odot$; the results for representative redshifts in the range $z \sim 0 - 10$ are reported in Table 3.1.

In Fig. 3.7 we highlight the contribution of the different stellar evolution channels to the stellar BH relic mass function at $z \sim 0$ and at $z \sim 10$. In the range $m_\bullet \sim 5 - 50\,M_\odot$ the single stellar evolution and the failed BH binaries channels are very similar and dominates over BH binaries. For $m_\bullet \gtrsim 50\,M_\odot$ the single stellar evolution contribution sharply dies (due to the mass gap from pair-instability supernovae, see Sect. 3.2.2) and the binary BH channel abruptly decreases (due to mass loss in common envelope phase, see Sect. 3.2.2), while the contribution from failed BH binaries dominates largely. Such a behaviour in the relative contributions is basically independent of redshift.

In Fig. 3.8 we illustrate the stellar BH relic mass density $\rho_\bullet(z)$ of Eq. (3.2) as a function of redshift z. The mass density increases quite steeply toward smaller redshifts, changing from values $\lesssim 10^5\,M_\odot$ Mpc^{-3} at $z \sim 10$ to $10^7\,M_\odot$ Mpc^{-3} around $z \sim 2 - 3$ and then saturating for lower redshifts up to $5 \times 10^7\,M_\odot$ Mpc^{-3} at $z \sim 0$. The evolution with redshift plainly follows that of the mass density $\rho_\star = (1 - R) \int_0^z \mathrm{d}z' \int \mathrm{d}\log\psi\, \psi\, (\mathrm{d}^2N/\mathrm{d}V\,\mathrm{d}\log\psi)$ in stars within galaxies, that has been computed by integrating the SFR functions and taking into account the recycling fraction $R \approx 0.45$; this corresponds to a local energy density $\Omega_\star \approx 5 \times 10^{-3}$, consistent with classic estimates (e.g., Fukugita & Peebles 2004). On the gross average, we find a ratio of the mass densities $\rho_\bullet/\rho_\star \approx 10\%$; we have checked that this mainly reflects the fraction of stars in the Kroupa IMF with mass $m_\star \gtrsim 20\,M_\odot$ originating BH remnants, appropriately lowered by mass loss in stellar winds and by binary evolution
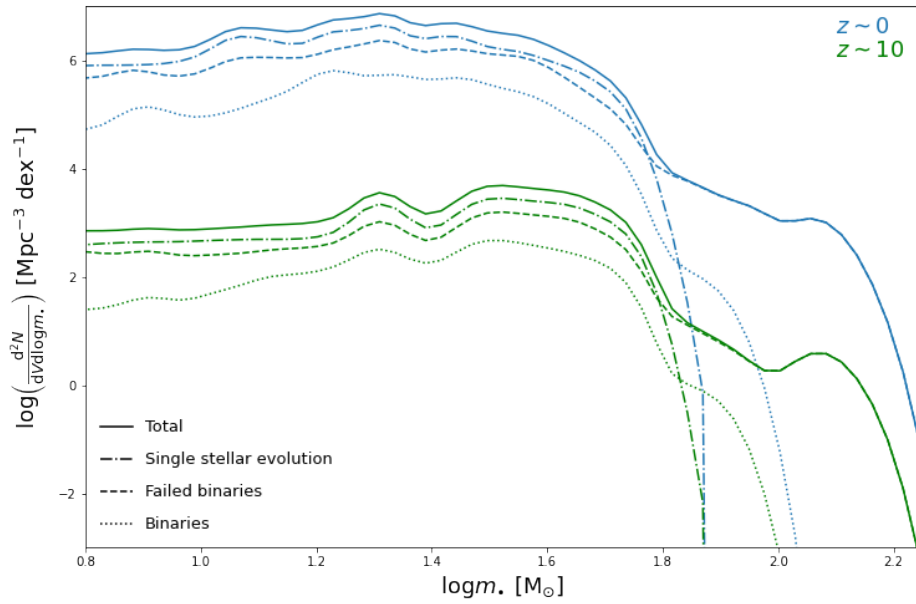
FIGURE 3.7: The stellar BH relic mass function $\mathrm{d}^2 N/\mathrm{d}V \, \mathrm{d}\log m_\bullet$ as a function of the BH mass $m_\bullet$ at redshift $z \sim 0$ (blue) and $z \sim 10$ (green), with highlighted the contribution to the total (solid lines) by single BHs formed from isolated stars (dot-dashed lines), failed BH binaries (dashed lines), and BH binaries (dotted lines).
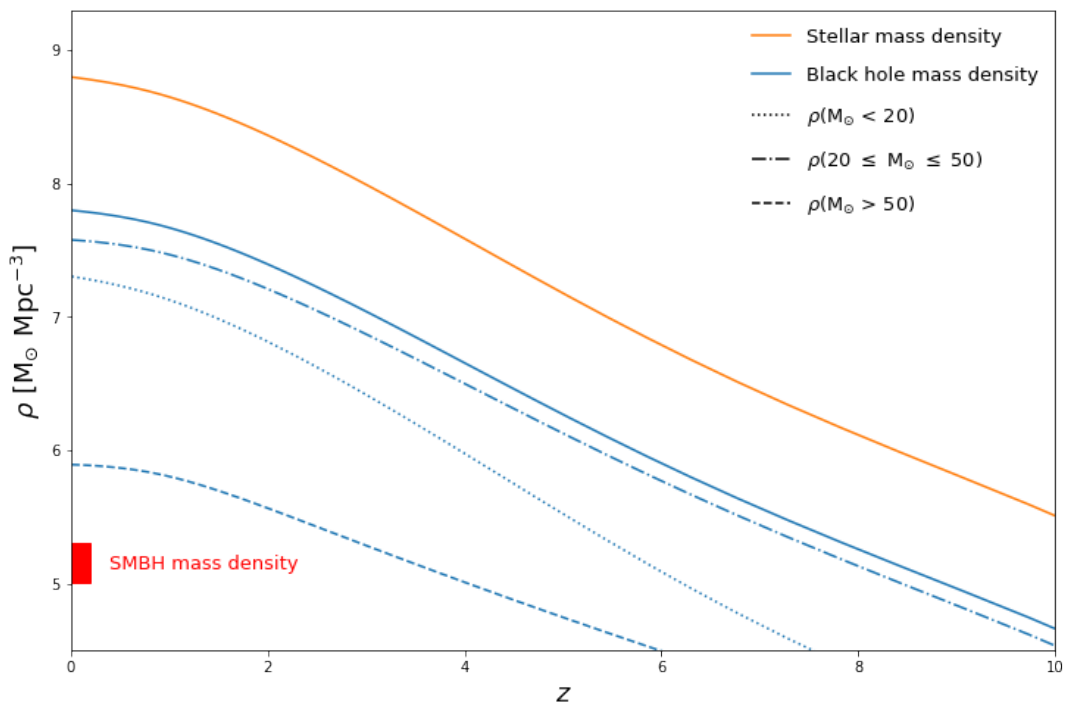
FIGURE 3.8: The relic density $\rho_\bullet$ in stellar mass BHs as a function of redshift z (solid blue line); contribution from different BH mass ranges are also displayed: $m_\bullet/M_\odot \lesssim 20$ (dotted), $20 \lesssim m_\bullet/M_\odot \lesssim 50$ (dashed) and $m_\bullet/M_\odot \gtrsim 50$ (dot-dashed). For reference, the stellar mass density in galaxies is also illustrated (orange line). Moreover, the observational estimate of the mass density in supermassive BHs with $M_\bullet \sim 10^6 - 10^{10} \, M_\odot$ at $z \sim 0$ is shown (Shankar et al. 2020; red shaded area in the bottom left corner).

effects. The local density in stellar mass BHs is substantially larger than that in supermassive BHs with masses $M_\bullet \sim 10^6 - 10^{10} \, M_\odot$, which amounts to $\sim 1 - 2 \times 10^5 \, M_\odot \, \mathrm{Mpc}^{-3}$ (see Shankar et al 2020; see also Kormendy & Ho 2013; Aversa et al. 2015), implying that most of the BH mass in the local Universe is of stellar origin. The ratio of the local mass densities in supermassive to stellar mass BHs is around $\sim 2 \times 10^{-3}$. Finally, we estimate a local BH energy density $\Omega_\bullet \approx 4 \times 10^{-4}$, corresponding to a BH-to-baryon ratio $\Omega_\bullet/\Omega_b \lesssim 10^{-2}$, i.e. the total mass in stellar BHs amounts to $\lesssim 1\%$ of the local baryonic matter.

For the sake of completeness, in Fig. 3.8 we illustrate the contributions to the BH mass density from different mass ranges: $m_\bullet \lesssim 20 \, M_\odot$, $m_\bullet \sim 20 - 50 \, M_\odot$ and $m_\bullet \gtrsim 50 \, M_\odot$. As expected from the shape of the mass function, most of the mass density is contributed by BHs with mass in the interval $m_\bullet \sim 20 - 50 \, M_\odot$. We also note that the mass density of BHs with masses

$m_\bullet \lesssim 20\,M_\odot$ tends to decline more steeply than the total one toward high-redshift, because the production of such small mass BHs is disfavoured in the lower-metallicity environment of high-z galaxies; the opposite holds for the mass density of BHs with larger masses $m_\bullet \gtrsim 50\,M_\odot$.

In Fig. 3.9 we evaluate the impact of binary BH mergers on the relic mass function. In the top left panel we have colour-coded the stellar term $\sum_{i=1,2} \mathrm{d}^2 N_{\star\star\to\bullet\bullet\to\bullet}/\mathrm{d}M_{\mathrm{SFR}}\,\mathrm{d}\log m_{\bullet,i}$ representing the number of binary stellar systems that first evolve in a BH binary and then are able to merge within the Hubble time, as function of metallicity Z and BH mass $m_\bullet$. The remnants contributing to this term are actually a sub-sample of those in the binary stellar term of Fig. 3.4 (bottom left panel). It is evident that the number of merging binary BHs is a small fraction of the total, while its distribution lacks the high-mass tail. This is because to form a tight compact binary, the progenitor stars must have undergone a substantial phase of common envelope, and an ensuing mass loss/envelope ejection (if not, the two progenitors merge prematurely and a single BH remnant is left). The end-product is a binary which can be sufficiently tight to merge within an Hubble time, but typically made of BHs that cannot be more massive than $m_\bullet \lesssim 40 - 50\,M_\odot$ (see Giacobbo & Mapelli 2018; Spera et al. 2019).

In the top right panel we have colour-coded the cosmic merging rate $\sum_{i=1,2} \mathrm{d}^2 \dot{N}_{\bullet\bullet\to\bullet}/\mathrm{d}V\,\mathrm{d}\log m_{\bullet,i}$ constituting the destruction term in Eq. (3.10), as a function of BH mass $m_\bullet$ and redshift z. It is seen that most binary BH mergers occur for redshift $z \sim 1 - 5$ in the mass ranges $m_\bullet \sim 15 - 40\,M_\odot$ and $m_\bullet \sim 5 - 8\,M_\odot$. In the bottom panel, we show the stellar BH relic mass function at $z \sim 0$ with and without the correction for binary BH mergers; the solid lines is the total mass function, while the dashed lines are the contribution from BH binaries. As expected the main changes are at the high-mass end, where an appreciable number of BHs in binaries is shifted toward larger masses by the merging process; however, the net effect on the total mass function is minor.

The contribution to the stellar BH mass function from merging binary BHs can be probed via gravitational wave observations. Recently, the LIGO/Virgo collaborations (Abbott et al. 2021a; see also Baxter et al. 2021) has estimated the primary mass distribution for BH binaries that coalesce around $z \approx 0$; given the quite small cosmological volume probed by the current gravitational wave detectors, this approximately corresponds to the merger rate integrated in a narrow redshift interval $\Delta z \lesssim 0.5$. The expectation from this work is illustrated as a red solid line in Fig. 3.10, and compared with the estimates by Abbott et al. 2021a (blue shaded area) for a powerlaw+peak model and by Baxter et al. 2021 (orange shaded area) for their astrophysically-motivated model (for both determinations the 68%
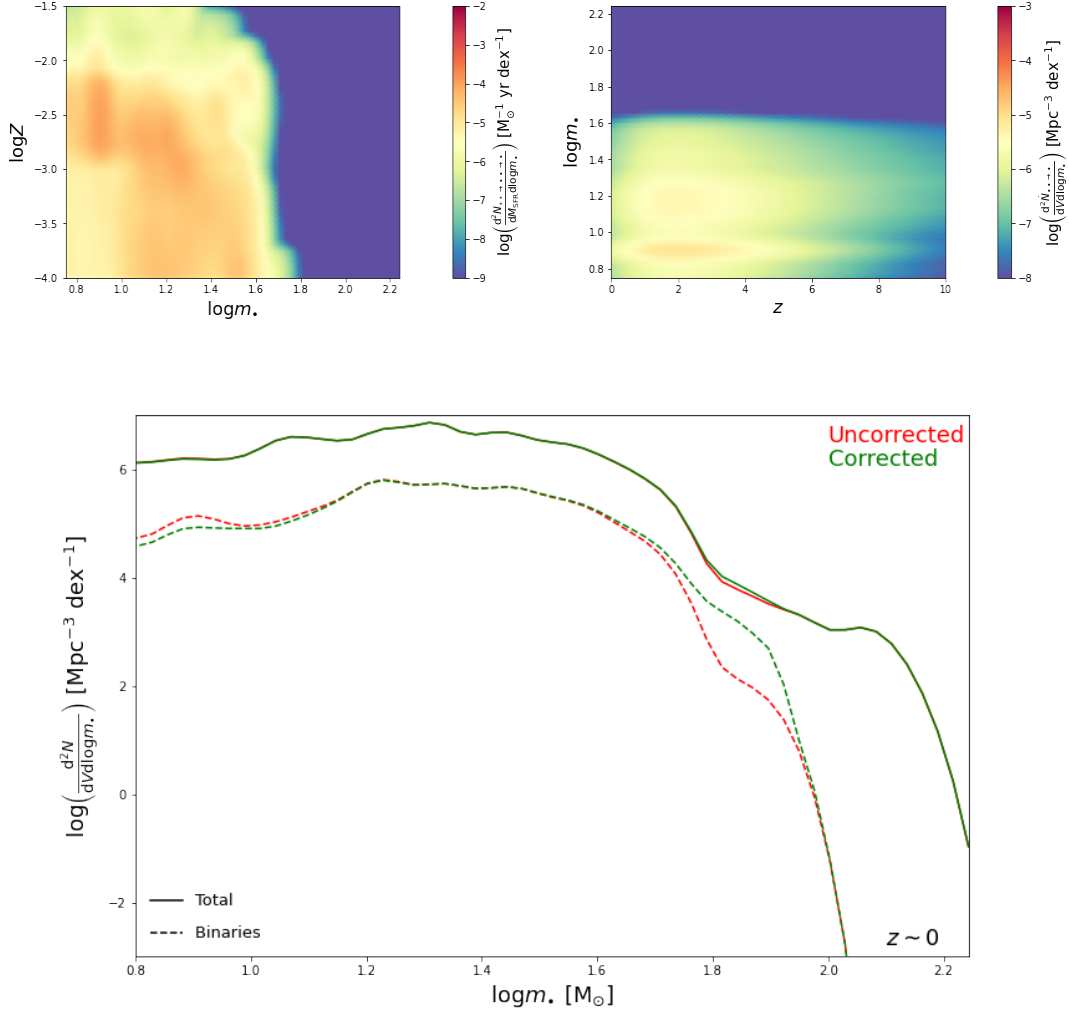
FIGURE 3.9: Impact of binary BH mergers on the stellar BH relic mass function. Top left panel: stellar term $\sum_{i=1,2} \mathrm{d}^2 N_{\star\star\to\bullet\bullet\to\bullet}/\mathrm{d}M_{\mathrm{SFR}} \,\mathrm{d}\log m_{\bullet,i}$ representing the number of binary stellar systems that first evolve in a BH binary and then are able to merge within the Hubble time (colour-coded), as function of metallicity Z and BH mass $m_{\bullet}$. Top right panel: cosmic merging rate $\sum_{i=1,2} \mathrm{d}^2 \dot{N}_{\bullet\bullet\to\bullet}/\mathrm{d}V \,\mathrm{d}\log m_{\bullet,i}$ (colour-coded; see Eq. 3.10) as a function of BH mass $m_{\bullet}$ and redshift z. Bottom panel: stellar BH relic mass function $\mathrm{d}^2 N_{\bullet}/\mathrm{d}V \,\mathrm{d}\log m_{\bullet}$ as a function of BH mass $m_{\bullet}$ at redshift $z \sim 0$, without (red lines) and with (green line) correction for binary BH merging effects; solid lines refer to the total mass function and dashed line to the contribution from binary BHs.
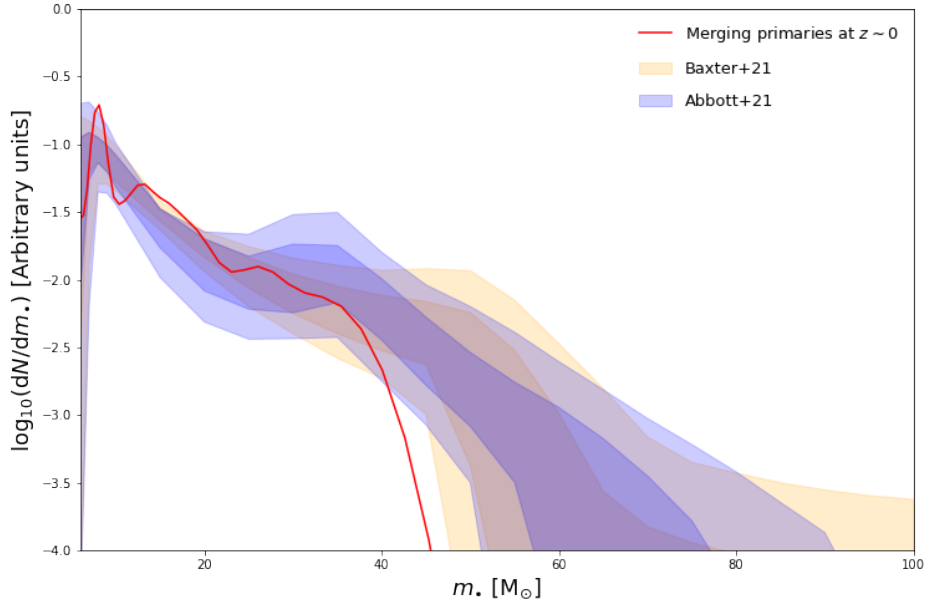
FIGURE 3.10: The BH mass function of merging BH binaries as a function of primary BH mass at $z \approx 0$. The outcome of this work is illustrated by the red solid line. Estimates from the analysis of gravitational wave observations by Abbott et al. (2021a) and Baxter et al. (2021) are reported as blue and orange shaded areas, respectively (for both determinations the 68% and 95% credible intervals are represented with dark and light shades).

and 95% credible intervals are represented with dark and light shades). Our result is in remarkable agreement with these estimates up to $40\,M_\odot$. However, the observed primary mass distribution declines gently for $m_\bullet \gtrsim 40\,M_\odot$ out to $m_\bullet \sim 80 - 100\,M_\odot$ while our model dies off, since stellar evolution effects hinder the presence of very massive BHs in coalescing binaries. This occurs mainly for two reasons (see also Sect. 3.3): the mass gap $m_\bullet \sim 50 - 120\,M_\odot$ for the production of BH due to pair-instability and pulsational pair-instability supernovae; (ii) the substantial mass loss during the common-envelope phase needed to produce a hardened compact binary that can merge within reasonable timescales. We also stress that such a sharp decline is not dependent on the specific galactic prescriptions nor scatter in the adopted relations, but it is instead common to any approach including the production and possible merging of only isolated BH binaries. A viable solution is explored in the next Section.

3.4   Discussion

In this Section we discuss three interesting issues that could potentially affect our results: the impact of the adopted modelling prescriptions; the dynamical formation channel of BH binaries in dense environment such as star clusters; the implication of our work in the formation of light (super)massive BH seeds at high redshift, where such distribution will be used in Chapter 4.

3.4.1   Impact of modeling prescriptions

We warn the reader that the stellar BH relic mass function derived in this Chapter is somewhat dependent on the prescriptions entering the galactic and the stellar terms discussed in Sect. 3.2.1 and 3.2.2. It is beyond the scope of this thesis to address the issue in detail by exploring the variety of modelling recipes, numerical approaches, and associated parameter space present in the literature. However, to provide the reader with a grasp of the related impact on our main results, we discuss the main source of uncertainties and show their impact on the local BH mass function.

As to the galactic term, the main source of uncertainty is constituted by the adopted main sequence and fundamental metallicity relationships. To estimate the related degree of uncertainty, we recomputed the galactic term by using in turn the main sequence relation by Boogaard et al. 2018 in place of our reference by Speagle et al. 2014, and the fundamental metallicity relation by Hunt et al. 2016 in place of our reference by Mannucci et al. 2011. The results are illustrated in Fig. 3.11, and it is seen that the related changes on the stellar BH relic mass function are minor.

As to the stellar term, the main source of uncertainty is constituted by the numerical treatment in the SEVN code of stellar winds, of pair-instability and pulsational pair-instability supernovae, of supernova explosions and natal kicks, of mass transfers and common-envelope phase in binary systems; all these physical processes can have profound impact on the formation and evolution of isolated or binary stellar BHs (see reviews by Postnov & Yungelson 2006; Ivanova et al. 2013; Mapelli 2020 and references therein). To estimate the related degree of uncertainty, we recomputed the stellar term for binaries/failed binaries and the associated relic BH mass function by running a different binary stellar evolution code. We rely on COSMIC (Breivik et al. 2020) since it constitutes a state-of-the-art, community-developed software with extensive online documentation on the Github repository (see https://cosmic-popsynth.github.io/), that upgrades the classic and widespread code BSE (Hurley et al. 2002). As for the parameters regulating mass transfer,
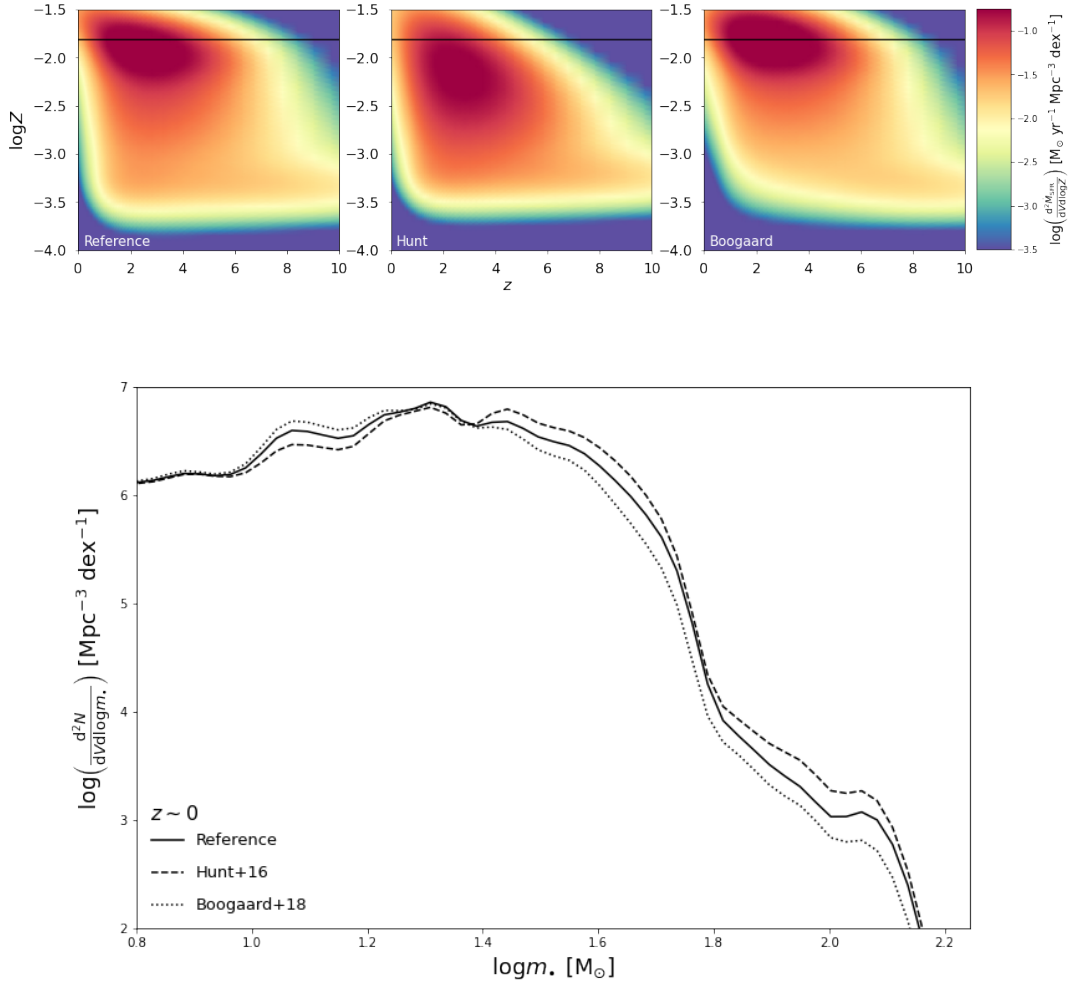
FIGURE 3.11: Impact on the BH mass function of different prescriptions for the galactic term (see Sect. 3.4.1). Top panels: the galactic term of Eq. (3.4) when assuming our reference Speagle 2014 main-sequence and Mannucci et al. 2011 fundamental metallicity relation (left), when changing the fundamental metallicity relation to that by Hunt et al. 2016 (middle), and when changing the main sequence relation to that by Boogaard et al. 2018 (right). Bottom panel: the relic stellar BH mass function at redshift $z \sim 0$ for the three cases just described above.

common envelope, tidal evolution, SN explosion and compact-object birth kicks, we keep the same choices adopted for SEVN, which are described in Spera et al. 2019. The results are presented in Fig. 3.12. The top left and middle panels compare the (total) stellar term from the two codes. It is apparent that the main difference involves the distribution of remnants with mass $m_\bullet \gtrsim 50 - 60\,M_\odot$ that are associated to compact binaries and especially to failed BH binaries (i.e., binary stars have coalesced before evolving into two distinct binary BHs; see also Sect. 3.2.2). Specifically, COSMIC tends to produce less failed BH binaries than SEVN; this is related to the treatment of the common envelope stage, which is indeed one of the most uncertain processes in the evolution of binary stars. The bottom panel illustrates the effects on the relic stellar BH mass function at $z \sim 0$. All in all, the differences are minor out to $m_\bullet \sim 60\,M_\odot$. At larger masses, the mass function built from the COSMIC stellar term decreases rapidly, to imply paucity of remnants with masses $m_\bullet \gtrsim 100\,M_\odot$; contrariwise, the mass function built from the SEVN stellar term is decreasing mildly and actually features a bump around $m_\bullet \sim 150\,M_\odot$, before a cutoff. Anyway, we stress that the major differences occur in a range where the mass function $\mathrm{d}N/\mathrm{d}m_\bullet$ is already decreasing much faster than $m_\bullet^{-1}$.

Among the many parameters entering binary evolution codes, a major role is played by the common envelope parameter α_{CE}, that quantifies the energy available to unbind the envelope (see Ivanova et al. 2013). As in Spera et al. (2019), we have set $\alpha_{\mathrm{CE}} = 5$ throughout this thesis and in the above comparison between SEVN and COSMIC. To have a grasp on the impact of such a choice, we have also run COSMIC with $\alpha_{\mathrm{CE}} = 1$, and show in Fig. 3.12 the resulting stellar term (top right panel) and BH mass function at $z = 0$ (bottom panel, dashed lines). The impact of α_{CE} is rather limited, and mainly affects the high-mass tail of the distribution which is dominated by binary stellar evolution.

Another crucial parameter entering the stellar term is the binary mass fraction $f_{\star\star}$, for which we have assumed a constant value 0.5. However, this is a rather uncertain quantity, that may well depend on the star mass $m_\star$, on the properties of the host galaxy and/or of the local environment, and even on redshift. In fact, observational constraints (e.g., Raghavan et al. 2010; Sana et al. 2012; Li et al. 2013; Sota et al. 2014; Dunstall et al. 2015; Luo et al. 2021) suggest values in the range $f_{\star\star} \approx 0.3 - 0.7$, with a possible increase toward more massive stars. To bracket the effects of different binary fractions on the stellar term and on the relic BH mass function, in Fig. 3.13 we compare the results for our reference $f_{\star\star} = 0.5$ to the extreme cases $f_{\star\star} = 0$ and $f_{\star\star} = 1$. Plainly adopting $f_{\star\star} = 0$ (i.e., no stars born in binaries) cuts the tail of the stellar term and of the BH mass function for $m_\bullet \gtrsim 50 - 60\,M_\odot$,
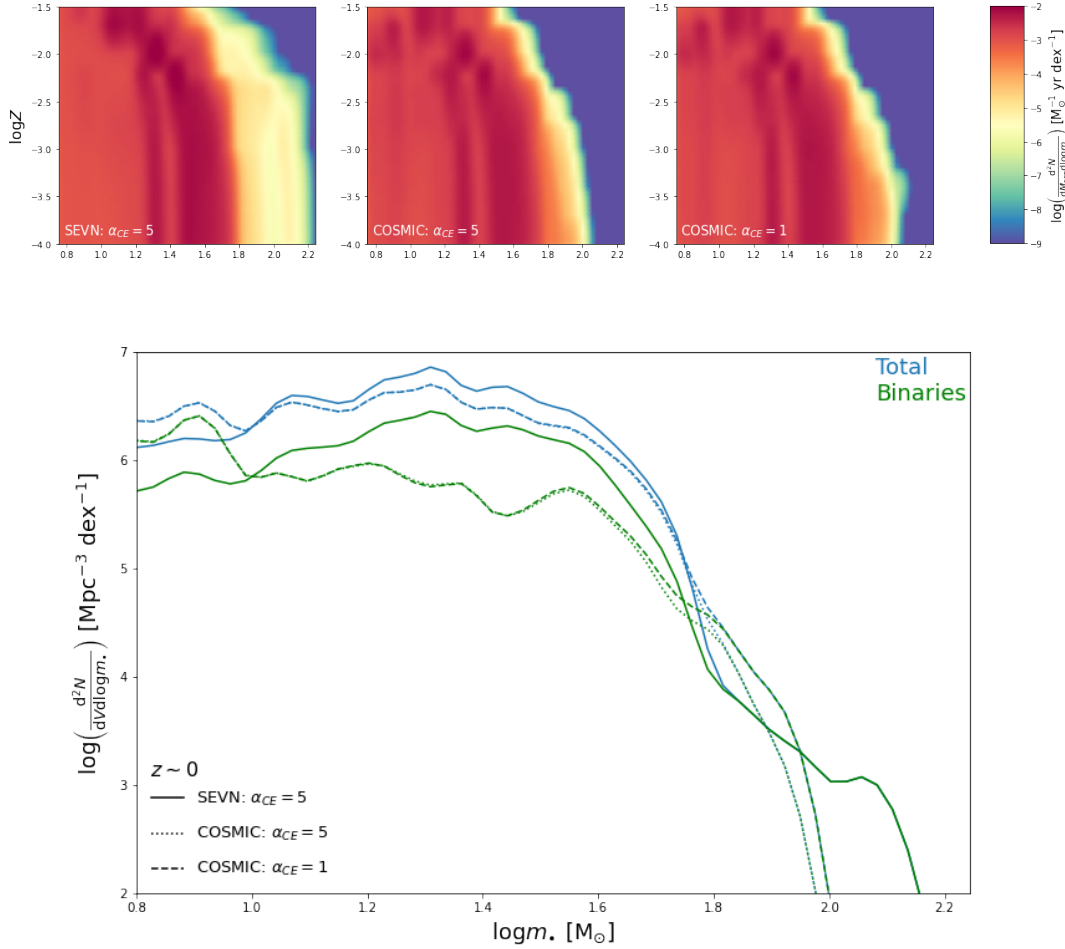
FIGURE 3.12: Impact on the BH mass function of different codes and prescriptions for the computation of the stellar term (see Sect. 3.4.1). Top panels: the (total) stellar term of Eq. (4.5) from the SEVN (left) and the COSMIC (middle) binary stellar evolution codes assuming a common envelope parameter $\alpha_{CE} = 5$ (see Sect. 3.4.1); results with COSMIC (right) for $\alpha_{CE} = 1$ are also shown. Bottom panel: the relic stellar BH mass function at redshift $z \sim 0$ from the SEVN (solid blue line) and the COSMIC (dotted blue line) with $\alpha_{CE} = 5$, and from COSMIC (dashed blue line) with $\alpha_{CE} = 1$; the contribution from binaries is also highlighted (green lines).

that are mostly produced by binary stellar evolution effects; meanwhile, for smaller masses the mass function is increased by the relatively more numerous single stars. Contrariwise, the other extreme case $f_{\star\star} = 1$ (all stars born in binaries), tend to enhance the high-mass tail of the mass function and reduce somewhat the number density of BHs with masses $m_\bullet \lesssim 50 - 60 \, M_\odot$. All in all, it is seen that the differences on the mass function are minor, and especially so for $f_{\star\star} \gtrsim 0.5$.

A final caveat about the IMF is in order. Throughout the Chapter we have self-consistently adopted as a reference the Kroupa 2001 IMF, mainly because it constitutes a standard both in the galaxy formation and the stellar evolution communities (together with the Chabrier 2003 IMF, which anyway would yield almost indistinguishable results) and because we had prompt availability of stellar evolution simulations based on that. Other classic choices like the Salpeter 1955, the Kennicutt 1983 and the Scalo 1986 IMF differ somewhat for the relative amount of star formation occurring below and above 1 $M_\odot$; such a difference is exacerbated in bottom-heavy IMFs like the one proposed to apply in massive ellipticals (e.g., van Dokkum & Conroy 2010) or top-heavy IMFs like the one proposed to apply in the early Universe (e.g., Larson 1998) or in starburst galaxies (e.g., Lacey et al. 2010). It is important to stress that the IMF enters non-trivially both in the galactic and in the stellar term. In the galactic term, an IMF is needed to convert the observed galaxy luminosity functions into a statistics based on an intrinsic physical quantity such as the SFR or the stellar mass; moreover, the determination itself of SFR, stellar masses (hence of the main sequence of star-forming galaxies), star formation history and metallicity via broadband SED fitting rely on the assumption of a specific IMF. Typically, at given SFR more top-heavy IMFs are proportionally richer in massive short-lived stars, and tend to yield a larger restframe UV luminosity/ionising power, a faster chemical enrichment, and a smaller stellar mass locked in long-lived stars. In the stellar term, the IMF is plainly an essential ingredient in determining the relative proportion of compact remnants of different masses (cf. Eq. 3.8). More top-heavy IMFs tend to produce more massive stars per unit SFR, thus in principle more massive BH remnants (and a smaller relative amount of neutron stars), though this is not so straightforward due to mass loss and mass transfers during binary evolution. From the above considerations one could be led to speculate that precision determinations of the BH mass function in an extended mass range would constitute a probe for the IMF; however, this plan, at least presently, struggles against the many and large uncertainties associated with the treatment of binary evolution effects, and against the unexplored degeneracies with the bunch of poorly constrained parameters of galaxy and stellar evolution.

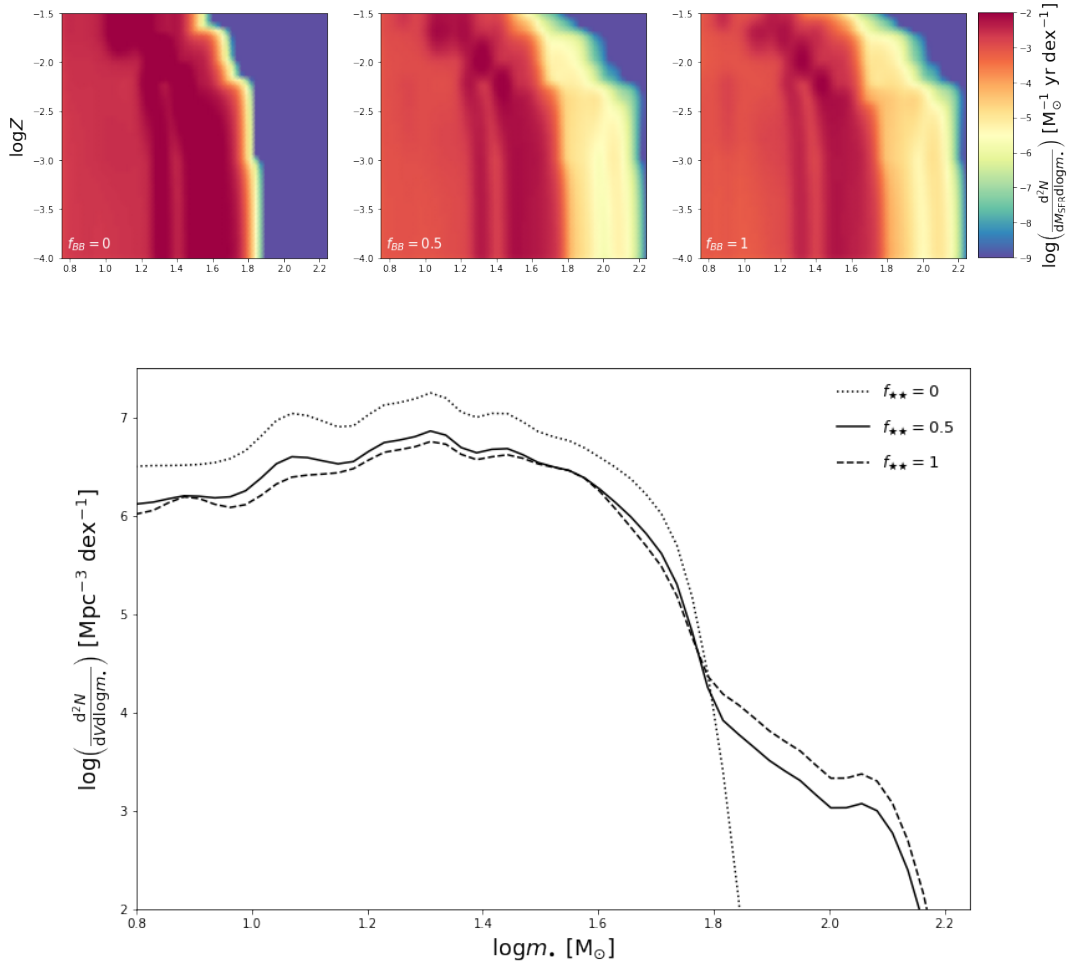FIGURE 3.13: Impact of the binary fraction $f_{\star\star}$ on our results (see Sect. 3.4.1). Top panels: the (total) stellar term of Eq. (4.5) for $f_{\star\star} = 0$ (left; no stars born in binaries), 0.5 (middle; our fiducial case) and 1 (right; all stars born in binaries). Bottom panel: the relic stellar BH mass function at redshift $z \sim 0$ for $f_{\star\star} = 0$ (dotted line), 0.5 (solid) and 1 (dashed).

3.4.2   Dynamical channel

In Fig. 3.10 we highlighted a possible mismatch at $m_\bullet \gtrsim 40\,M_\odot$ between the primary mass distribution for merging BH binaries from isolated binary evolution and the estimates from gravitational wave observations. A viable solution could be that such large primary masses are produced in binary systems formed within the dense environment of young stellar clusters, open clusters, globular clusters, or nuclear star clusters (e.g., Di Carlo et al. 2019, 2020; Rodriguez et al. 2015, 2021; Antonini & Rasio 2016; Kumamoto et al. 2019; Arca-Sedda et al. 2020; Banerjee 2021; Mapelli et al. 2021; Natarajan 2021). The central density of a star cluster can be so high that the orbits of binary stars are continuously perturbed by dynamical encounters with other members. Massive BHs $m_\bullet \gtrsim 40\,M_\odot$ in the pair instability mass gap can then be originated by hardening of BH binaries via dynamical exchanges in three-body encounters, and via the merging of massive progenitor stars; in addition, runaway collisions (i.e., a fast sequence of mergers; e.g., Portegies Zwart et al. 2004; Giersz et al. 2015; Mapelli 2016) in the densest cores of clusters with low metallicity can even produce intermediate mass BHs with $m_\bullet \gtrsim$ some $10^2\,M_\odot$.

To have a grasp on these effects, we proceed as follows. First, we construct the stellar term of Eq. (4.5) from the simulations by Di Carlo et al. 2020, that include dynamical effects in young star clusters. With respect to isolated conditions, an appreciable number of merging binaries with a primary mass $m_\bullet \gtrsim 40\,M_\odot$ is originated via dynamical exchanges, especially at low metallicities. More in detail, BHs with mass $m_\bullet \sim 40 - 65\,M_\odot$ can be formed (even in the field) from the evolution of single stars or stars in loose binaries that retain a fraction of their envelope up to their final collapse. BHs with mass $m_\bullet \gtrsim 65\,M_\odot$ can be originated via collisions of massive stars (eased in star clusters because dynamical encounters can induce fast merging before mass transfer episodes peel-off the primary star). If produced in the field, BHs from both these channels will remain isolated or locked in loose binaries unable to merge; contrariwise, in a star cluster they can acquire a new companion via dynamical exchanges and merge by dynamical hardening and gravitational wave emission. Note that, in contrast, repeated mergers of BHs are suppressed in young star clusters, because of their low escape velocity.

Second, we assume that a fraction f_{field} of the star formation occurs in the field and the complementary fraction $1 - f_{\mathrm{field}}$ occurs in young star clusters (actually most of the stars are formed in young star clusters, but only a fraction of these may be subject to dynamical effects before exiting from the cluster or before the star cluster itself dissolves). Observations (see Goddard et al. 2010; Johnson et al. 2016; Chandar et al. 2017; Adamo et al. 2020)

and cluster formation models (Kruijssen 2012; Pfeffer et al. 2018; Elmegreen 2018; El-Badry et al. 2019; Grudic et al. 2021) indicate that such a fraction is highly uncertain and possibly dependent on properties like the SFR spatial density and redshift; in this exploratory computation, we let the fraction f_{field} vary from 0.2 to 1 (which corresponds to isolated binaries only), and we split the galactic term of Eq. (3.4) accordingly. Finally, we combine the stellar and galactic term so derived to compute the merger rate of Eq. (3.10) and the expected primary mass distribution.

The outcome is illustrated in the top panel of Fig. 3.14 for different values of f_{field} in the range 0.2 to 1. As expected, increasing the fraction of SFR in star clusters (i.e., decreasing f_{field}) produces a progressively more extended tail toward high primary masses, to the point that values $f_{field} \lesssim 0.8$ actually can reconcile the theoretical prediction with the observational estimates. For completeness, in the bottom panel of Fig. 3.14 we show how the dynamical evolution channel affects the relic BH mass function at $z \sim 0$. The marked difference with respect to the model with only isolated binaries is the absence of the drop at around $m_\bullet \sim 60 \, M_\odot$ and of the abrupt cutoff for $m_\bullet \sim 150 \, M_\odot$. Instead, the mass function declines smoothly for $m_\bullet \gtrsim 60 \, M_\odot$. The analytical fits in terms of Eq. (3.12) for the field+cluster mass function with $f_{field} = 0.6$ at representative redshifts are reported in Table 3.1.

Two caveats are in order here. First, in the simulations by Di Carlo et al. 2019, 2020, the treatment of stellar mergers is based on simplified assumptions: no mass-loss and chemical mixing during the merger; instantaneous recovery of hydrostatic equilibrium after the merger; rejuvenation of the merger product according to the simple Hurley et al. 2002 prescriptions. Plainly, these details of the process are quite uncertain, and dedicated hydrodynamical simulations are required to have a better understanding of the final outcome. Second, in estimating the impact of the dynamical formation channel we have considered only young star clusters for the sake of simplicity (and because the prompt availability of in-house dynamical simulations, that are extremely time-demanding to run from scratch). Globular clusters and nuclear star clusters could also be effective environments to build up massive binary BHs, since hierarchical mergers are more efficient in very rich and compact stellar systems (e.g., Miller & Hamilton 2002; Antonini et al. 2019; Mapelli et al. 2021). Hence, including models for globular and nuclear star clusters could allow to reproduce the observed primary BH mass function with an even larger value of f_{field}.
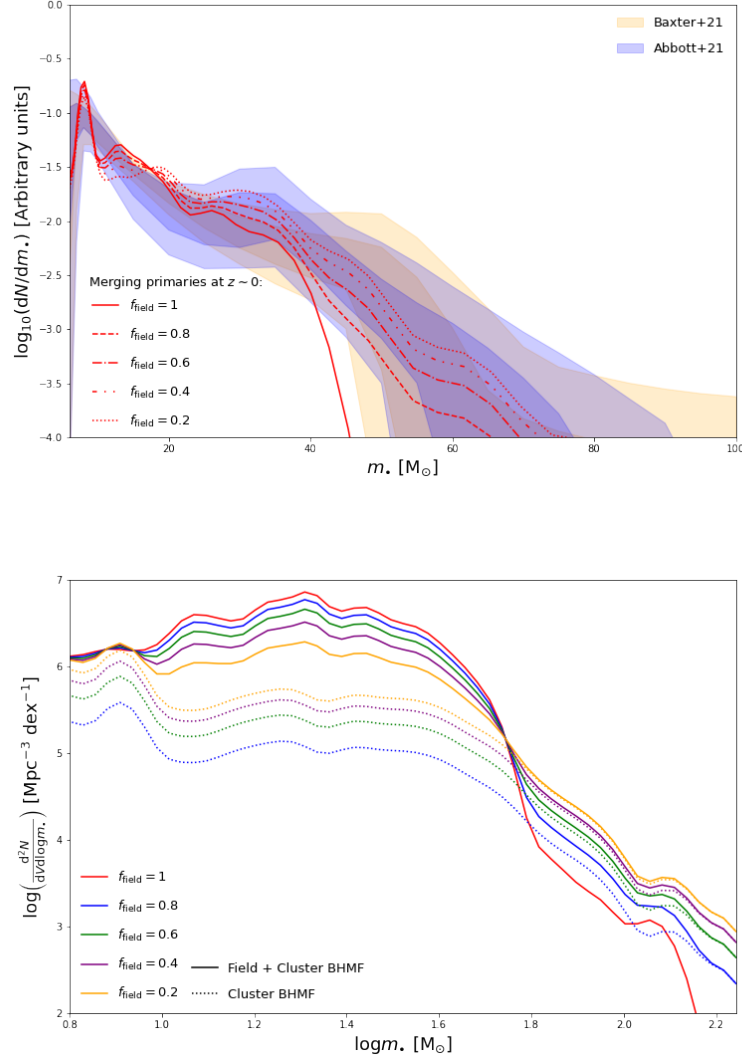
FIGURE 3.14: Top panel: impact of the dynamical formation channel on the BH primary mass distribution of merging BH binaries $z \approx 0$, computed from the simulations for young open star clusters by Di Carlo et al. 2020 (see Section 3.4.2 for details). Lines refers to different fraction of star formation occurring in the field $f_{\mathrm{field}} \approx 1$ (solid; only isolated binaries), 0.8 (dashed), 0.6 (dot-dashed), 0.4 (dot-dot-dashed) and 0.2 (dotted). Estimates from the analysis of gravitational wave observations by Abbott et al. 2021a and Baxter et al. 2021 are reported as blue and orange shaded areas, respectively (for both determination the 68% and 95% credible intervals are represented with dark and light shades). Bottom panel: impact of the dynamical formation channel on the relic BH mass function at $z \sim 0$. Dotted lines refer to the contribution from star clusters and solid lines to the total (field+star clusters) BHMF. Colour-code refers to different fraction of star formation occurring in the field $f_{\mathrm{field}} \approx 1$ (red), 0.8 (blue), 0.6 (green), 0.4 (purple) and 0.2 (yellow).

3.4.3   BH seeds at high redshift

We stress that the stellar BH mass function at high redshift $z \gtrsim 6$ derived in this thesis actually provides a light BH seed distribution in primordial galaxies, as originated by stellar and binary evolution processes. This is complementary to the seed distributions expected from other classic formation channels. The most relevant are basically three (see review by Volonteri 2010 and references therein): BHs formed by Pop III stars in metal-free environments like high-redshift minihalos at $z \gtrsim 20$ (e.g., Madau & Rees 2001); runaway stellar collisions in metal-poor nuclear star clusters (e.g., Devecchi et al. 2012); direct collapse scenarios (e.g., Lodato & Natarajan 2006).

The light seed distributions from these models (extracted from Fig. 3.15 found in Volonteri 2010) are compared in Fig. 3.16 with the mass function at $z \sim 6 - 10$ from stellar BHs presented in this work. Given the appreciable contribution of the latter for masses $m_\bullet \lesssim 150 \, M_\odot$ at redshift $z \lesssim 10$, it will be extremely relevant to include it in numerical simulations, semi-analytic and semi-empirical models of BH formation and evolution at high redshift.

3.5   Summary

In this Chapter we have provided an ab-initio computation of the relic stellar BH mass function across cosmic times. To this purpose, we have exploited the state-of-the-art stellar and binary evolutionary code SEVN, and have coupled its outputs with redshift-dependent galaxy statistics and empirical scaling relations involving galaxy metallicity, star-formation rate and stellar mass. Our main findings are summarized below.

- The relic mass function $\mathrm{d}^2 N / \mathrm{d}V \, \mathrm{d} \log m_\bullet$ as a function of the BH mass $m_\bullet$ features a rather flat shape up to $m_\bullet \approx 50 \, M_\odot$ and then a log-normal decline for larger masses, while its normalization increases with decreasing redshift, quite rapidly down to $z \sim 2 - 3$ and then more mildly toward $z \sim 0$, see Fig. 3.6 and Table 3.1. The local stellar BH mass function could be eventually probed via microlensing observations (see Paczynski 1986; for a review, Mao 2012).

- The local relic BH mass function for $m_\bullet \lesssim 50 \, M_\odot$ is comparably contributed from isolated stars evolving into BH and from binary stellar systems ending up in single BH (failed BH binaries), while binary BHs are subdominant; for higher masses $m_\bullet \gtrsim 50 \, M_\odot$ the single stellar evolution and binary BH channels abruptly decrease, while the failed BH binaries largely dominate. See Fig. 3.7.
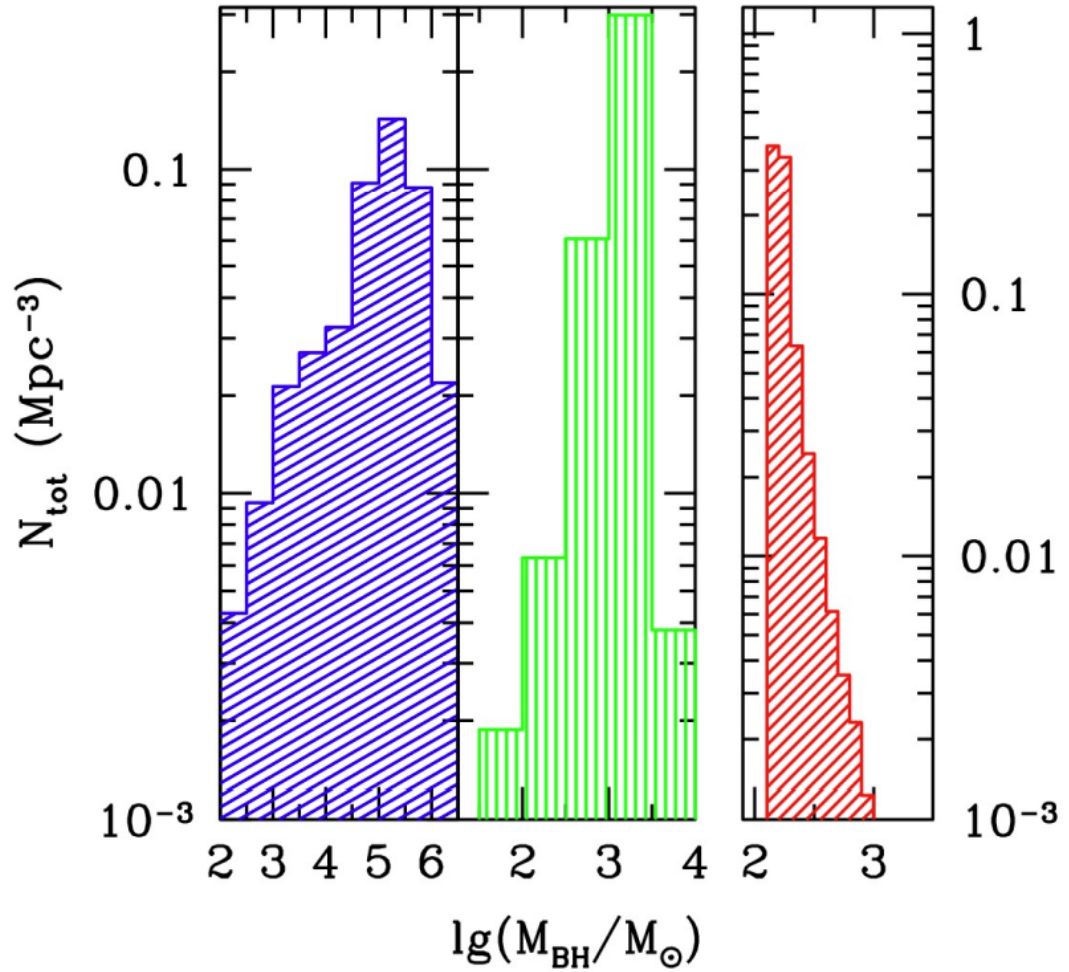
FIGURE 3.15: Light seed distribution from Volonteri 2010 for massive BHs produced through direct collapse (Volonteri et al. 2008b, blue-left), runaway stellar collisions in nuclear star clusters (Devecchi and Volontari 2009, green-middle), Pop-III remnants (Madau & Rees 2001, red-right).

FIGURE 3.16: The light seed distribution at redshift $z \sim 10$ (solid), 8 (dot-dashed), 6 (dashed) and 0 (dotted) from the stellar BH mass function of this work is compared with that expected from pop-III remnants (orange line), runaway stellar collisions in nuclear star clusters (green line), and direct collapse scenarios (blue line); see discussion in Sect. 3.4.3.

- The local stellar BH relic mass density amounts to $\rho_\bullet \approx 5 \times 10^7 \, M_\odot$ Mpc^{-3}, exceeding by more than two orders of magnitude that in superm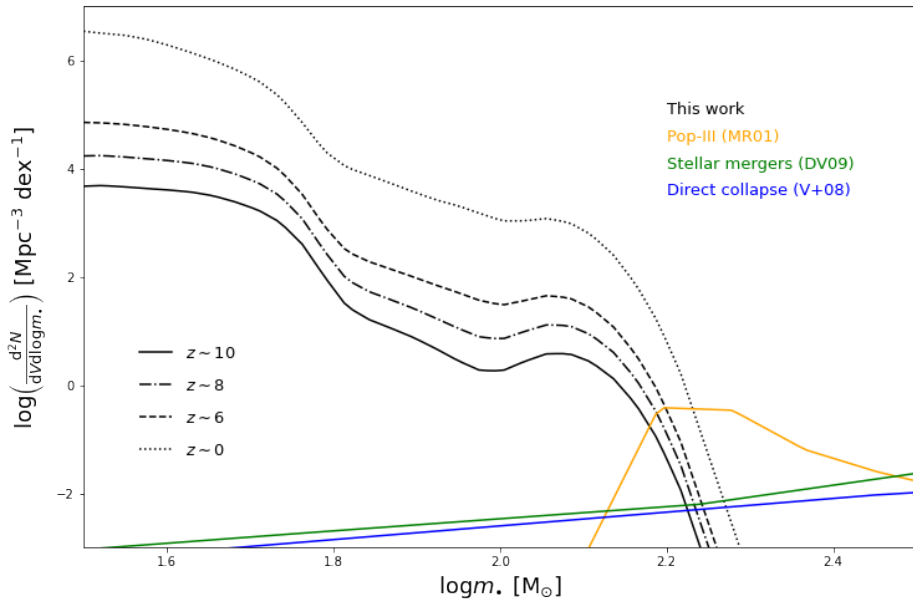assive BHs; this translates into an energy density parameter $\Omega_\bullet \approx 5 \times 10^{-4}$, implying that the total mass in stellar BHs amounts to $\lesssim 1\%$ of the local baryonic matter. See Fig. 3.8.

- The stellar BH relic mass function can be distorted by binary BH mergers, that can redistribute remnants from the low to the high mass range. However, such a reshaping is found to have a minor effect on the mass function at the high-mass end. See Fig. 3.9.

- The distribution of primary masses for merging BH binaries is found to be in remarkable agreement with the recent estimates from gravitational wave observations by LIGO/Virgo out to $m_\bullet \lesssim 40 \, M_\odot$. For larger masses, the observed distribution declines gently while the theoretical one dies off due to a twofold reason: the mass gap from pair-instability and pulsational pair-instability supernovae; and the substantial mass loss during the common envelope phase needed to produce a tight BH binary that can merge within the Hubble time. We have proposed as a viable solution to consider the dynamical formation of merging BH binaries in dense environment like (young) star clusters. See Figs. 3.10-3.14 and Table 3.1.

- We have discussed the impact on the mass function of adopting different physical prescriptions entering the galactic and the stellar term. As for the galactic term, minor differences arise when changing the adopted main sequence of star-forming galaxies and the fundamental metallicity relationship. As for the stellar term, the main differences concern the high mass end of the mass function, and are due to the numerical treatment of binary stellar evolution effects, which are still considerably uncertain even from a theoretical point of view. See Figs. 3.12 and 3.11.

- The BH mass function derived here can provide a firm theoretical basis for a physically-motivated light seed distribution at high redshift; as expected, for masses $m_\bullet \lesssim 150 \, M_\odot$ and redshifts $z \lesssim 10$ it overcomes complementary light seed formation channels, like Pop-III stars, stellar mergers in nuclear star clusters and direct collapse scenarios that are aimed to produce larger mass seeds. It will be worth implementing the light seed distribution from the present work in semi-analytic and numerical models of (super)massive BH formation and evolution, as it can be quite relevant for predictions concerning future gravitational wave observations via Einstein Telescope and LISA. See Fig. 3.16.

Chapter 4

The (Super)massive Black Hole Mass Function and Heavy Seed Distribution

We can now proceed onto the formation of a (super)massive black hole mass function (BHMF), which will include the intermediate mass range. The stellar BHMF will work as the seed distribution for the dynamical friction mechanism seen in Boco et al. 2020 (see Sect. 2.3.2), and work alongside standard Eddington accretion to overcome the time restriction seen in recent quasar observations. Have it be noted that the stellar BHMF is derived as a stand alone function and has been shown to hold rigorously under alteration, with limited impact under exchanges of relations and base stellar evolutionary code (see Section 3.4.1), and can be modified to introduce additional pathways and further refinements in the future. It is, also, noteworthy to declare before we begin that our supermassive BHMF is consistent when removing the dynamical friction channel for mass accretion, which is dependent on our stellar BHMF. The following is based on the work undertaken in Sicilia et al. 2022b.

4.1 Introduction

The formation of (super)massive BHs with masses $M_\bullet \sim 10^{6-10} \, M_\odot$ and their role in galaxy evolution constitute crucial yet longstanding problems in modern astrophysics and cosmology. These monsters are thought to have grown mainly by gaseous accretion onto a disk surrounding the BH (e.g., Lynden-Bell 1969; Shakura & Sunyaev 1973) that energizes the spectacular broadband emission of AGNs, and leaves a BH relic ubiquitously found at the centre of massive galaxies in the local Universe (e.g., Kormendy & Ho 2013; also textbooks by Mo et al. 2010, Cimatti et al. 2020). This paradigm has recently received an astonishing confirmation by the EHT collaboration

(2019, 2022) via the imaging of the BH shadow caused by gravitational light bending and photon capture at the event horizon of M87 and Sgr A*.

Accreting supermassive BHs can have a profound impact on the evolution of the host galaxies (see review by Alexander & Hickox 2012), as testified by the observed tight relationships between the relic BH masses and the physical properties of the hosts, most noticeably the stellar mass or velocity dispersion of the bulge component (e.g., Magorrian 1998; Ferrarese & Merritt 2000; Gebhardt et al. 2000; Tremaine et al. 2002; Kormendy & Ho 2013; McConnell & Ma 2013; Reines & Volonteri 2015; Sahu et al. 2019; Shankar et al. 2016, 2020a; Zhu et al. 2021; Chapter 2, Sect. 2.3.1). These suggest that (apart from short-time stochastic fluctuations) the BH and the bulge stellar mass must have co-evolved over comparable timescales, possibly determined by the energy feedback from the BH itself on the gas/dust content of the host (see Tinsley 1980; Silk & Rees 1998; Fabian 1999; King 2005; Lapi et al. 2006, 2014, 2018; for a review, see King & Pounds 2015). In fact, targeted X-ray observations in the high-redshift star-forming progenitors of local massive galaxies have started to reveal the early growth of a dust-enshrouded (super)massive BH in their nuclear regions (e.g., Mullaney et al. 2012; Page et al. 2012; Delvecchio et al. 2015; Rodighiero et al. 2015, 2019; Fiore et al. 2017; Stanley et al. 2015, 2017; Massardi et al. 2018; Combes et al. 2019; D'Amato et al. 2020), before it attains a high enough mass and power to manifest as a bright AGN and to eventually reduce/quench star formation and partly evacuate gas and dust from the host (e.g., Granato et al. 2001, 2004; Lapi et al. 2014, 2018). Another, albeit more indirect, indication of coevolution for the bulk of the BH and the host stellar mass comes from the similarity between the activity timescales of central BH to the transition timescale of (green valley) galaxies from the blue cloud to the red sequence (see Wang et al. 2017; Lin et al. 2021, 2022; this is true apart from rejuvenations at late cosmic times, see Martin-Navarro et al. 2021).

However, two recent pieces of evidence may suggest that standard disk accretion is not the only process at work in growing a BH to the (super)massive regime. The first is the discovery of an increasing number of active BHs with masses $M_\bullet \gtrsim 10^9\,M_\odot$ at very high redshifts $z \gtrsim 7$ (e.g., Mortlock et al. 2011; Wu et al. 2015; Venemans et al. 2017; 2018; Reed et al. 2019; Banados et al. 2018, 2021; Wang et al. 2019, 2021), when the age of the Universe was shorter than 0.8 Gyr. The second is the robust measurements of extreme BH masses $M_\bullet \gtrsim 10^{9-10}\,M_\odot$ at the center of early-type galaxies with stellar mass $M_\star \gtrsim 10^{11}\,M_\odot$ (e.g., McConnell et al. 2011; Ferre-Mateu et al. 2015; Thomas et al. 2016; Mehrgan et al. 2019; Dullo et al. 2021), that have formed most of their old stellar component during a star-formation episode

lasting some 10^8 yr at $z \gtrsim 1$, as demonstrated by astro-archeological measurements of their stellar ages and α-enhanced metal content (e.g., Thomas et al. 2005, 2010; Gallazzi et al. 2006, 2014; Johansson et al. 2012; Maiolino & Mannucci 2019; Morishita et al. 2019; Saracco et al. 2020; Chapter 2, Sect. 2.1.2). These observations concur to raise the issue of how billion solar mass BHs may have grown in less than a Gyr. In fact, this is somewhat challenging if standard disk accretion starts from a light seed $\sim 10^2\,M_\odot$ of stellar origin and proceeds with the typical Eddington ratios $\lambda \lesssim 1$ as estimated out to $z \sim 6$ in active BHs (see Vestergaard & Osmer 2009; Nobuta et al. 2012; Kelly & Shen 2013; Dai et al. 2014; Kim & Im 2019; Duras et al. 2020; Ananna et al. 2022), that would require an overall time $\gtrsim 0.8/\lambda$ Gyr to attain $\sim 10^9\,M_\odot$. Solutions may invoke mechanisms able to rapidly produce heavy BH seeds $10^{3-5}\,M_\odot$, so reducing the time required to attain the final masses by standard disk accretion (see Natarajan 2014, Mayer & Bonoli 2019, Inayoshi et al. 2020, and Volonteri et al. 2021 for exhaustive reviews). Viable possibilities comprise: direct collapse of gas clouds within a (proto)galaxy, possibly induced by galaxy mergers or enhanced matter inflow along cosmic filaments (e.g., Lodato & Natarajan 2007; Mayer et al. 2010, 2015; Di Matteo et al. 2012, 2017); merging of stars inside globular or nuclear star clusters (e.g., Portegies Zwart et al. 2004; Devecchi et al. 2012; Latif & Ferrara 2016; Kroupa et al. 2020); migration of stellar BHs towards the nuclear galaxy regions via dynamical friction against the dense gas-rich environment in strongly star-forming progenitors of local massive galaxies (e.g., Boco et al. 2020, 2021)[1].

Such a complex picture for the overall (super)massive BH growth may in principle be probed via one of the most fundamental quantities for demographic studies of the BH population, namely the BH mass function, that expresses the number density of BHs per comoving volume and unit BH mass as a function of redshift. For (super)massive BHs, where most of the mass is accumulated through gas disk accretion, this is usually estimated (but still subject to systematics) from the AGN luminosity functions via Soltan (1982)-type or continuity equation arguments (e.g., Small & Blandford 1992; Haehnelt et al. 1998; Salucci et al. 1999; Yu & Tremaine 2002; Yu & Lu 2004, 2008; Merloni & Heinz 2008; Cao 2010; Kelly & Merloni 2012; Aversa et al. 2015; Shankar et al. 2004, 2009, 2013), or from local galaxy mass/luminosity/velocity dispersion functions and scaling relation among

---

[1]When referring to the dynamical friction mechanism, the term 'seeds' is used in a broader sense with respect to the classic meaning in the literature. A seed is usually referred to as the first compact object on which subsequent disk accretion occurs, eventually leading to the formation of a supermassive BH. The heavy seeds formed with the dynamical friction mechanism are by-products of multiple mergers of already-existing stellar-mass BHs (that in turn could be referred as light seeds) forming across a wide redshift range.

these properties and the BH mass (e.g., Vika et al. 2009; Li et al. 2011; Mutlu-Pakdil et al. 2016; Shankar et al. 2016, 2020a).

In a future perspective, a precise assessment of the relic BH mass function is also important to work out detailed predictions for the gravitational wave emission expected from mergers of (super)massive BHs (see the recent potential detection by NANOGrav, Gabriella et al. 2023), that will constitute the primary targets of the upcoming Laser Interferometer Space Antenna mission (e.g., Sesana et al. 2016; Ricarte & Natarajan 2018; for a review, Barausse & Lapi 2021 and references therein) and of ongoing and future Pulsar-Timing Array experiments (e.g., Antoniadis et al. 2022). Thus a theoretical grasp on the (super)massive BH mass function across cosmic times is of crucial importance.

This Chapter is aimed at modeling the BH mass function, from the stellar to the intermediate and (super)massive regime. In Chapter 3 we have focused on the stellar mass BH relic mass function, while in this Chapter we provide an ab-initio computation of the redshift-dependent mass function for (super)massive BHs. We consider two mechanisms to grow the central BH, that likely cooperate in the high-redshift star-forming progenitors of local massive galaxies. The first one is the gaseous dynamical friction introduced by Boco et al. 2020, which can cause the migration of stellar-mass BHs originated during the intense bursts of star formation in the gas-rich central regions of the host progenitor galaxy, and the buildup of heavy BH seeds $\lesssim 10^5 \, M_\odot$ within short timescales $\lesssim$ some 10^7 yr. The second mechanism is the standard Eddington-type gas disk accretion onto the heavy seed, through which the central BH can become (super)massive within the typical star-formation timescales $\lesssim 1$ Gyr of the host galaxy.

Our approach is semi-empirical, requires minimal modelling and a few educated assumptions, and is original in at least three respects: (i) we start from the galaxy SFR functions and derive BH-related statistics by jointly modelling the evolution of the central BH mass and the stellar mass of the host; (ii) we explicitly compute (and do not assume a priori) the heavy seed mass function by exploiting the distribution of stellar mass BHs originated from star-formation (Chapter 3, Sicilia et al. 2022a) and their migration rates due to dynamical friction (Boco et al. 2020); (iii) we determine the detailed shape of the BH growth curve during disk accretion (in particular, we set the Eddington ratio) by requiring that the final BH and host stellar mass satisfy a Magorrian-like relationship, and that the star-formation timescale of the galaxy host is set by the main-sequence relation. We validate our approach by reproducing the observed redshift-dependent bolometric AGN

luminosity functions and Eddington ratio distributions, and the relationship between the star-formation of the host galaxy and the bolometric luminosity of the accreting central BH. We then derive the relic (super)massive BH mass function at different redshifts via a generalised continuity equation approach, and compare it with present observational estimates. At the same time, we provide a robust theoretical basis for a physically-motivated heavy seed distribution at high redshifts. Finally, we put together the results derived in Chapter 3 and this Chapter to reconstruct the overall BH mass function from the stellar to the intermediate to the (super)massive regime, over more than ten orders of magnitudes in BH mass.

The plan of this Chapter is straightforward: in Section 4.2 we describe our semi-empirical framework, in Section 4.3 we present and discuss our results, and in Section 4.4 we summarize our main findings and outline future perspectives. Throughout this Chapter, we continue to adopt the standard flat ΛCDM cosmology (Planck Collaboration 2020) with rounded parameter values: matter density $\Omega_{\mathrm{M}} = 0.3$, dark energy density $\Omega_{\Lambda} = 0.7$, baryon density $\Omega_{\mathrm{b}} = 0.05$, Hubble constant $H_0 = 100\,h$ km s^{-1} Mpc^{-1} with $h = 0.7$, and mass variance $\sigma_8 = 0.8$ on a scale of $8\,h^{-1}$ Mpc. A Kroupa (2001) initial mass function (IMF) in the star mass range $m_{\star} \sim 0.1 - 150\,M_{\odot}$ is adopted.

4.2 Theoretical background

We aim to derive the redshift-dependent (super)massive relic BH mass function $\mathrm{d}^2 N / \mathrm{d} \log M_{\bullet}\, \mathrm{d}V$, i.e., the number density of massive BHs per unit comoving volume V and BH mass $M_{\bullet}$. We rely on two main mechanisms to grow the central BH mass, which are likely to cooperate in the gas-rich star-forming progenitors of local massive galaxies (hosting massive relic BHs): gas disk accretion and stellar BH migration via gaseous dynamical friction. Both processes will require the joint modelling of the stellar and BH mass growth history in a galaxy of given SFR and redshift.

4.2.1 Stellar mass growth

As to the stellar mass growth, we assume a simple two-stage star formation history

$$\dot{M}_{\star}(\tau) = (1 - \mathcal{R})\,\psi\,\Theta_{\mathrm{H}}[\tau \leq \tau_b] \tag{4.1}$$

where ψ is the SFR, $\mathcal{R} \approx 0.45$ is the IMF-dependent gas fraction restituted to the ISM during stellar evolution (with the quoted value applying for a Kroupa IMF), and $\Theta_{\mathrm{H}}[\cdot]$ is the Heaviside step function. Basically, this reflects a constant SFR, that is then abruptly quenched by the radiative/kinetic

power associated to supernova explosions/stellar winds and/or the central BH activity at around the age τ_b. This temporal evolution renders to a good approximation the behaviour expected from state-of-the-art in-situ galaxy evolution models (e.g., Pantoni et al. 2019; Lapi et al. 2020), and is also indicated by SED-modelling studies of high-redshift dusty star-forming galaxies (e.g., Papovich et al. 2011; Smit et al. 2012; Moustakas et al. 2013; Steinhardt et al. 2014; Cassará et al. 2016; Citro et al. 2016; Gonzalez Delgado et al. 2017; Carnall et al. 2019; Williams et al. 2021; Pantoni et al. 2021), and by the observed fraction of IR-detected host galaxies in X-ray (e.g., Mullaney et al. 2012; Page et al. 2012; Rosario et al. 2012; Azadi et al. 2015; Stanley et al. 2015; Carraro et al. 2020) and in IR or optically selected AGNs (e.g., Mor et al. 2012; Wang et al. 2013; Willott et al. 2015; Stanley et al. 2017; Dai et al. 2018; Bianchini et al. 2019; Nguyen et al. 2020; Wang et al. 2021).

Correspondingly, the stellar mass increases as

$$M_\star(\tau) = \begin{cases} (1 - \mathcal{R})\,\psi\,\tau & , \ \tau \leq \tau_b \\[2ex] M_\star(\tau_b) & , \ \tau > \tau_b \end{cases} \tag{4.2}$$

and hereafter we will indicate for convenience $M_{\star,\mathrm{relic}} \equiv M_\star(\tau_b) = (1 - \mathcal{R})\,\psi\,\tau_b$. Note, however, that this is the stellar mass just before the quenching at τ_b, not the relic stellar mass at $z \approx 0$; in fact, at late cosmic times this may be further increased by dry mergers, especially in very massive galaxies (e.g., Rodriguez-Gomez et al. 2016; Buitrago et al. 2017; Lapi et al. 2018).

We can estimate the value of the star-formation duration τ_b by requiring that, just before the quenching, the SFR ψ and the stellar mass $M_\star(\tau_b) = M_{\star,\mathrm{relic}}$ satisfy the redshift-dependent main sequence relationship $\psi_{\mathrm{MS}}(M_\star, z)$ (see Daddi et al. 2007; Rodighiero et al. 2011, 2015; Sargent et al. 2012; Speagle et al. 2014; Whitaker et al. 2014; Schreiber et al. 2015; Caputi et al. 2017; Bisigello et al. 2018; Boogaard et al. 2018; Leja et al. 2022; Rinaldi et al. 2022; Popesso et al. 2022); in other words, the condition

$$\psi_{\mathrm{MS}}(M_{\star,\mathrm{relic}}, z) = \psi \tag{4.3}$$

sets the timescale $\tau_b(\psi, z)$ for any galaxy with SFR ψ and redshift z. We adopt as our reference the main-sequence determination by Speagle et al. (2014)

$$\log \frac{\psi_{\mathrm{MS}}(M_\star, z)}{M_\odot\,\mathrm{yr}^{-1}} \approx (-6.51 + 0.11\,t_z) + (0.84 - 0.026\,t_z)\,\log \frac{M_\star}{M_\odot}\,. \tag{4.4}$$

where t_z is the age of the Universe at redshift z in units of Gyr. We will show in Sect. 4.3.2 the effect of adopting a different main sequence prescription.

4.2.2 BH growth due to dynamical friction

Boco et al. 2020, 2021 have pointed out that the central BH can grow, especially in the early stages, by a continuous rain of stellar mass BHs that are funnelled toward the nuclear region via dynamical friction against the gas-rich background of high-redshift star-forming galaxies. The related growth rate is computed following Boco et al. 2020, to which we refer the interested reader for details. For consistency, in this Chapter we initialise the computation basing on the stellar BH mass function and light seed distribution derived in Chapter 3, along the following lines.

First of all, we extract from the stellar and binary evolutionary code SEVN (see Spera et al. 2019) the so-called stellar term, i.e. the number of BHs originated per unit of stellar mass formed M_{SFR} and BH mass $m_\bullet$:

$$
\frac{\mathrm{d}^2 N_\bullet}{\mathrm{d} M_{\mathrm{SFR}} \mathrm{d} \log m_\bullet}(m_\bullet | Z) = \frac{\mathrm{d}^2 N_{\star \to \bullet}}{\mathrm{d} M_{\mathrm{SFR}} \mathrm{d} \log m_\bullet} \\
+ \frac{\mathrm{d}^2 N_{\star\star \to \bullet}}{\mathrm{d} M_{\mathrm{SFR}} \mathrm{d} \log m_\bullet} + \sum_{i=1,2} \frac{\mathrm{d}^2 N_{\star\star \to \bullet\bullet}}{\mathrm{d} M_{\mathrm{SFR}} \mathrm{d} \log m_{\bullet,i}} \,.
\tag{4.5}
$$

This includes three different contributions from isolated stars evolving into BHs ($\star \to \bullet$), from stars that are originally in binary systems but end up as an isolated BH because one of the companions has been ejected or destroyed or cannibalised ($\star\star \to \bullet$), and from stars in binary systems that evolve into binary BHs ($\star\star \to \bullet\bullet$). All these terms are strongly dependent on metallicity Z, which affects the efficiency of the various processes involved in stellar and binary evolution, like mass loss rates, mass transfers, core-collapse physics, etc. (see Chapter 3 for details).

We then derive the birthrate of stellar BHs with mass $m_\bullet$ at time τ in an individual galaxy with SFR ψ at redshift z from the expression

$$
\frac{\mathrm{d}\dot{N}_{\mathrm{birth}}}{\mathrm{d} \log m_\bullet}(m_\bullet, \tau | \psi, z) = \psi \int \mathrm{d} \log Z \frac{\mathrm{d}^2 N_\bullet}{\mathrm{d} M_{\mathrm{SFR}} \mathrm{d} \log m_\bullet}(m_\bullet | Z) \\
\times \frac{\mathrm{d} p}{\mathrm{d} \log Z}[Z | Z_{\mathrm{FMR}}(\psi, M_\star(\tau))] \,.
\tag{4.6}
$$

The integrand is the product of the stellar term from the previous Eq. (4.5) and of the metallicity distribution $\mathrm{d}p/\mathrm{d}\log Z$. For the latter we adopt a lognormal shape centred around the fundamental metallicity relation $\log Z_{\mathrm{FMR}}(\psi, M_\star)$ by Mannucci et al. 2011 (for a review, see Maiolino & Mannucci 2019), with a dispersion of $\Delta \log Z_{\mathrm{FMR}} \approx 0.15$ dex, and $M_\star(\tau)$ given by Eq. (4.2).

We then compute the migration rate per unit stellar BH mass due to gaseous dynamical friction at time τ inside a galaxy with SFR ψ at redshift z

$$\frac{\mathrm{d}\dot{N}_{\mathrm{DF}}}{\mathrm{d}\log m_\bullet}(m_\bullet, \tau|\psi, z) = \int \mathrm{d}r \frac{\mathrm{d}p}{\mathrm{d}r}(r) \int \mathrm{d}v_\theta \frac{\mathrm{d}p}{\mathrm{d}v_\theta}(v_\theta|r)$$
$$\times \int \mathrm{d}v_r \frac{\mathrm{d}p}{\mathrm{d}v_r}(v_r|r) \frac{\mathrm{d}\dot{N}_{\mathrm{birth}}}{\mathrm{d}\log m_\bullet}(m_\bullet, \tau - \tau_{\mathrm{DF}}|\psi, z)\,; \tag{4.7}$$

here $\mathrm{d}p/\mathrm{d}r$ and $\mathrm{d}p/\mathrm{d}v_{r,\theta}$ are the probability distributions of initial radii and velocities and $\tau_{\mathrm{DF}}(m_\bullet, r, v_r, v_\theta)$ is the dynamical friction timescale against the gaseous background for a compact remnant of mass $m_\bullet$. All these quantities are detailed in Boco et al. 2020; where the reader can find a full account of how the dynamical friction timescale depends on such quantities and on the parameters ruling the gas distribution (this is also covered in brief in Chapter 2, Sect. 2.3.2).

Finally, the growth rate of the central BH due to the dynamical friction mechanism is just

$$\dot{M}_{\bullet,\mathrm{DF}}(\tau|\psi, z) = \Theta_{\mathrm{H}}[\tau \le \tau_{\mathrm{b}}] \int \mathrm{d}\log m_\bullet\, m_\bullet\, \frac{\mathrm{d}\dot{N}_{\mathrm{DF}}}{\mathrm{d}\log m_\bullet}(m_\bullet, \tau|\psi, z)\,, \tag{4.8}$$

where the step function $\Theta_{\mathrm{H}}[\cdot]$ specifies that the mechanism is no longer active after τ_{b} since the gaseous medium is expected to have been at least partly evacuated from the nuclear regions due to feedback processes.

4.2.3   BH growth due to gas accretion

In parallel, the central BH can grow due to standard gas disk accretion. We adopt a BH accretion rate curve with shape (e.g., Yu & Lu 2004, 2008; Shen 2009; Li 2012; Lapi et al. 2014; Aversa et al. 2015)

$$\dot{M}_{\bullet,\mathrm{acc}}(\tau) = \begin{cases} \dfrac{M_\bullet(\tau)}{\tau_{\mathrm{ef}}} & ,\ \tau \le \tau_{\mathrm{b}} \\[2ex] \dot{M}_{\bullet,\mathrm{acc}}(\tau_{\mathrm{b}})\, e^{-(\tau-\tau_{\mathrm{b}})/\tau_{\mathrm{d}}} & ,\ \tau_{\mathrm{b}} < \tau \le \tau_{\mathrm{b}} + \zeta\, \tau_{\mathrm{d}} \\[2ex] 0 & ,\ \tau > \tau_{\mathrm{b}} + \zeta\, \tau_{\mathrm{d}} \end{cases} \tag{4.9}$$

This describes a growth due to disk accretion in two stages, separated at the galaxy age τ_{b} where star formation is quenched. The rationale behind the

above expression is the following: at early epochs (ages $\tau \lesssim \tau_b$) when there is plenty of material to accrete onto the BH in the nuclear galaxy regions, a demand-limited, Eddington-type BH accretion rate over a characteristic e−folding timescale τ_{ef} is assumed. At late times (ages $\tau \gtrsim \tau_b$) the BH mass and radiative/kinetic power may be so large as to quench the star formation and partly evacuate gas from the host; however, if residual gas mass is still present in the central regions, it can be accreted in a supply-driven fashion, thus originating the exponentially declining part of the accretion curve with a characteristic timescale τ_d. The IR-detected fraction of X-ray selected AGNs (see Mullaney et al. 2012; Page et al. 2012; Rosario et al. 2012; Azadi et al. 2015; Stanley et al. 2015; Carraro et al. 2020) suggests $\tau_d \approx 2\,\tau_{ef}$, as shown by Lapi et al. 2014 and adopted by Aversa et al. 2015 and Mancuso et al. 2016b, 2017. Eventually, we consider the accretion to stop for ages $\tau \gtrsim \tau_b + \zeta\,\tau_d$ with $\zeta \approx 3$ (our results are anyway weakly affected by the value of this latter quantity); this is reasonable since at that point the accretion rate becomes so small with $\dot{M}_{\bullet,acc}\,\tau_{ef}/M_\bullet \lesssim 10^{-2}$ as to enter in an ADAF (i.e., advection-dominated accretion flow) regime, where the mass growth can be safely neglected with respect to that accumulated during the slim/thin disk accretion. We will show in Sect. 4.3.2 the effect of adopting a different, scale-free declining portion (e.g., Shen 2009) of the BH growth curve, that also avoids the inclusion of the quantity ζ.

Provided that $L = \epsilon\,\dot{M}_\bullet\,c^2$ is the accretion luminosity and $\lambda \equiv L/L_{Edd}$ the (luminous) Eddington ratio in terms of the Eddington luminosity[2] L_{Edd}, the e−folding time of the early growth reads

$$\tau_{ef} = \frac{\epsilon}{(1-\epsilon)\,\lambda}\,t_{Edd}\ , \tag{4.10}$$

where $t_{Edd} = M_\bullet\,c^2/L_{Edd} \approx 0.45$ Gyr is the Eddington timescale and ϵ is the radiative efficiency. As to the latter, it is worth considering that in the early stages the demand-limited accretion may be prone to the development of a slim accretion disk (e.g., Abramowicz et al. 1988), while at late-times the supply-limited accretion tends to originate a classic thin-disk accretion (e.g., Shakura & Sunyaev 1973). To describe both conditions we express the radiative efficiency via the prescription by Aversa et al. 2015 valid for both thin and slim disks (see also Mineshige et al. 2000; Watarai et al. 2001; Li 2012;

---

[2]The Eddington luminosity $L_{Edd} \equiv 4\pi\,G\,\mu_e\,m_p\,c\,M_\bullet/\sigma_T \approx 1.3 \times 10^{38}\,(M_\bullet/M_\odot)$ erg s^{-1} is the limiting value for which the continuum radiation force emitted by the accretion disk balances gravity in isotropic conditions; in the above definition G is the gravitational constant, μ_e is the mean molecular weight per electron, m_p is the proton mass, c is the speed of light, and σ_T is the Thomson cross section.

Madau et al. 2014):

$$\epsilon \approx \epsilon_{\text{thin}} \frac{\lambda/2}{e^{\lambda/2} - 1} \; ; \tag{4.11}$$

here ϵ_{thin} is the efficiency during the thin-disk phase, which may range from ≈ 0.057 for a nonrotating BH to ≈ 0.32 for a maximally rotating Kerr BH (see Thorne 1974). We will adopt $\epsilon_{\text{thin}} \approx 0.15$ as our fiducial value (see Davis & Laor 2011; Raimundo et al. 2012; Trakhtenbrot et al. 2017; Shankar et al. 2020b), but will show in Sect. 4.3.2 the effect of adopting a larger efficiency $\epsilon_{\text{thin}} \approx 0.3$. Note that in principle ϵ_{thin} may even depend on the galactic age since in the early stages the accretion is likely chaotic and so the spin of the BH should stay rather small, while in the late stages a coherent accretion is expected to set in and the spin can rapidly increase to maximal values (see Lapi et al. 2014); however, we neglect such spin/efficiency evolution in the present framework.

4.2.4   Overall BH growth

The overall growth of the central BH mass due to both dynamical friction and gaseous accretion writes

$$\dot{M}_\bullet(\tau) = \dot{M}_{\bullet,\text{DF}}(\tau) + \dot{M}_{\bullet,\text{acc}}[M_\bullet(\tau)] \; . \tag{4.12}$$

Given Eqs. (4.8) and (4.9), the previous equation can be formally integrated to yield the overall central BH mass growth

$$M_\bullet(\tau|\psi, z) = \begin{cases} \displaystyle\int_0^\tau \mathrm{d}\tau' \, e^{(\tau-\tau')/\tau_{\text{ef}}} \, \dot{M}_{\text{DF}}(\tau') & \tau \le \tau_{\text{b}} \\[4mm] M_\bullet(\tau_{\text{b}}) \left[1 + \dfrac{\tau_{\text{d}}}{\tau_{\text{ef}}} \left(1 - e^{-(\tau-\tau_{\text{b}})/\tau_{\text{d}}} \right) \right] & \tau_{\text{b}} < \tau \le \tau_{\text{b}} + \zeta \, \tau_{\text{d}} \\[4mm] M_\bullet(\tau_{\text{b}}) \left[1 + \dfrac{\tau_{\text{d}}}{\tau_{\text{ef}}} \left(1 - e^{-\zeta} \right) \right] & \tau > \tau_{\text{b}} + \zeta \, \tau_{\text{d}} \end{cases} \tag{4.13}$$

where the value on the last line corresponds to the final, relic BH mass $M_{\bullet,\text{relic}}(\psi, z) = M_\bullet(\tau_{\text{b}}) \left[1 + (\tau_{\text{d}}/\tau_{\text{ef}}) \times (1 - e^{-\zeta}) \right]$.

The dynamical friction process dominates in the initial growth stage for $\tau \ll \tau_{\text{ef}}$; we will show that it provides, by inducing the migration of stellar BHs originated from star formation, heavy seeds of order $10^{3-5} \, M_\odot$ within some 10^7 yr, before standard Eddington-type accretion takes over as the dominant mechanism for BH growth. Remarkably, our modelling above, at

variance with other approaches in the literature, does not require assumptions regarding the seed BH from which to start gas accretion: the light seeds are provided by star formation and stellar evolution, and the heavy seeds by the gaseous dynamical friction mechanism, in a consistent way.

As a consequence, for any galaxy with SFR ψ at redshift z, the evolution of the BH mass is completely specified by assigning the Eddington factor λ of the early growth stage, which determines the radiative efficiency ϵ via Eq. (4.11) and hence the e–folding timescale τ_{ef}. We empirically determine the Eddington ratio (see Shankar et al. 2020b) by requiring that the relic BH and stellar mass just after the quenching at τ_{b} satisfy a Magorrian-like relation $M_{\bullet,\text{Mag}}(M_\star, z)$, with a possible redshift dependence. In other words, from the condition

$$M_{\bullet,\text{relic}}(\psi, z) = M_{\bullet,\text{Mag}}[M_{\star,\text{relic}}(\psi, z), z] \tag{4.14}$$

one can determine $\lambda(\psi, z)$ for any galaxy with SFR ψ and redshift z. We rely on the debiased determination of the Magorrian relationship by Shankar et al. 2016, 2020a

$$
\begin{aligned}
\log \frac{M_{\bullet,\text{Mag}}}{M_\odot}(M_\star, z) &\approx 7.574 + 1.946 \log \frac{M_\star}{10^{11}\, M_\odot} \\
&- 0.306 \log^2 \frac{M_\star}{10^{11}\, M_\odot} - 0.011 \log^3 \frac{M_\star}{10^{11}\, M_\odot} + \eta \, \log(1 + z)
\end{aligned}
\tag{4.15}
$$

holding in the range $M_\star \sim 10^{10-12}\, M_\odot$, with an intrinsic scatter $\sigma_{\log M_{\bullet,\text{Mag}}} \approx 0.32 - 0.1 \log(M_\star/10^{12}\, M_\odot)$ dex. The parameter η in the above equation allows for a possible evolution with redshift $M_{\bullet,\text{Mag}}(M_\star, z) \propto (1 + z)^\eta$; this is considerably debated in the literature (e.g., Merloni et al. 2010; Schulze & Wisotzki 2014; Ding et al. 2020; Suh et al. 2020; Li et al. 2021; Habouzit et al. 2022), but the latest studies suggest a mild evolution with $\eta \approx 0.2$, that we take as our fiducial value (our results are anyway weakly affected by this choice). We will show in Sect. 4.3.2 the effect of adopting a different Magorrian relationship.

We stress that at least two low-redshift processes, that can in principle affect the BH mass function, have not been considered in our framework: (i) relic supermassive BHs can be reactivated by accretion of gas funnelled toward the central regions by galaxy mergers or internal disk instabilities (e.g., Di Matteo et al. 2005; Capelo et al. 2015), that can trigger spectacular radio-mode activity in terms of relativistic jets; (ii) relic supermassive BHs can coalesce following, with some delay, a galaxy merger. In fact, the impact of these processes on the supermassive BH mass function is still somewhat debated: an important role of galaxy mergers in reproducing the massive end of the mass function has been claimed in semi-analytic models (e.g., Marulli

et al. 2008; Bonoli et al. 2009), while other semi-empirical and numerical approaches have instead pointed out a much more limited relevance of mergers on the BH mass function (e.g., Aversa et al. 2015; Steinborn et al. 2018; McAlpine et al. 2020). The detailed treatment of galaxy and BH mergers is beyond the main scope of this thesis, and is deferred to future work.

4.2.5 BH growth rate function

Toward a statistical description, we start from the SFR function $\mathrm{d}^2 N / \mathrm{d} \log \psi \, \mathrm{d} V$, i.e., the number density of galaxies with given SFR ψ per unit comoving cosmological volume V at redshift z. For this we adopt the determination by Boco et al. 2021 (see Fig. 3.2; for an analytic Schechter fit see Eq. 2 and Table 1 in Mancuso et al. 2016a) derived from an educated combination of the dust-corrected UV (e.g., Oesch et al. 2018; Bouwens et al. 2021), IR (e.g., Gruppioni et al. 2020; Zavala et al. 2021), and radio (e.g. Novak 2017; Ocran 2020) luminosity functions, appropriately converted into SFR (see Kennicutt & Evans 2012) using our assumed Kroupa 2001 IMF.

We first compute the central BH growth rate function

$$\frac{\mathrm{d}^2 N}{\mathrm{d} \log \dot{M}_\bullet \, \mathrm{d} V}(\dot{M}_\bullet, z) = \int \mathrm{d} \log \psi \, \frac{\mathrm{d}^2 N}{\mathrm{d} \log \psi \, \mathrm{d} V}(\psi, z) \, \frac{1}{\tau_\mathrm{b}} \sum_i \frac{\mathrm{d} \tau_i}{\mathrm{d} \log \dot{M}_\bullet}(\dot{M}_\bullet | \psi, z) \,,$$

(4.16)

where $\dot{M}_\bullet(\tau | \psi, z)$ is provided by Eq. (4.13) and $\mathrm{d} \tau / \mathrm{d} \log \dot{M}_\bullet$ is the related time spent by the BH in a logarithmic bin of given growth rate; the summation allows for multiple solutions τ_i of the equation $\dot{M}_\bullet(\tau | \psi, z) = \dot{M}_\bullet$, that are typically two for the growth curve assumed in this work. Note that the SFR dependence in $\dot{M}_\bullet(\tau | \psi, z)$ is twofold: on the one hand it is related to the growth rate of heavy seeds by migration of stellar-mass BHs, whose birthrate ultimately depends on star formation; on the other hand, such a dependence is encoded in the Eddington ratio $\lambda(\psi, z)$ derived after Eq. (4.14) and in the radiative efficiency given by Eq. (4.11). To allow for some scatter induced by the Magorrian-like relationship, one can write

$$\sum_i \frac{\mathrm{d} \tau_i}{\mathrm{d} \log \dot{M}_\bullet} = \int_0^{\tau_\mathrm{b} + \zeta \, \tau_\mathrm{d}} \mathrm{d} \tau \, \delta_\mathrm{D} \left[\log \dot{M}_\bullet - \log \dot{M}_\bullet(\tau | \psi, z) \right] \simeq$$

(4.17)

$$\simeq \int_0^{\tau_\mathrm{b} + \zeta \, \tau_\mathrm{d}} \mathrm{d} \tau \, \frac{\mathrm{sech}^2 \left\{ [\log \dot{M}_\bullet - \log \dot{M}_\bullet(\tau | \psi, z)] / 2 \, \tilde{\sigma}_{\log \dot{M}_\bullet} \right\}}{4 \, \tilde{\sigma}_{\log \dot{M}_\bullet}}$$

the first equality follows trivially from the properties of the Dirac $\delta_D[\cdot]$ function, while in the second we have substituted a log-logistic distribution with dispersion $\tilde{\sigma}_{\log \dot{M}_\bullet} \simeq (\sqrt{3}/\pi)\,\sigma_{\log \dot{M}_\bullet}$ in terms of the standard log-normal dispersion $\sigma_{\log \dot{M}_\bullet}$. The reason for using a log-logistic distribution in place of the standard log-normal one is that having heavier tails it tends to maintain intrinsic power-law distributions at the high-mass end, as indicated by the data relating to the AGN luminosity functions and BH mass function (see discussion by Ren & Trenti 2021). Agreement with the latter statistics requires to adopt $\sigma_{\log \dot{M}_\bullet} \approx 0.3$–$0.4$ dex, in line with the scatter of the Magorrian.

4.2.6 AGN luminosity functions, Eddington ratios and mean SFRs

The broadband emission of AGNs is energised by the gas accretion onto the (super)massive BHs; thus a relevant statistics to validate our semi-empirical approach is the redshift-dependent bolometric AGNs luminosity function. This may be computed analogously to Eq. (4.16) as

$$\frac{\mathrm{d}^2 N}{\mathrm{d}\log L_{\mathrm{AGN}}\,\mathrm{d}V}(L_{\mathrm{AGN}}, z) = \int \mathrm{d}\log\psi\,\frac{\mathrm{d}^2 N}{\mathrm{d}\log\psi\,\mathrm{d}V}(\psi, z)\,\frac{1}{\tau_{\mathrm{b}}}\sum_i \frac{\mathrm{d}\tau_i}{\mathrm{d}\log L_{\mathrm{AGN}}}(L_{\mathrm{AGN}}|\psi, z)\,,$$

(4.18)

where the times τ_i are now determined from the condition $L_{\mathrm{AGN}} = \epsilon\,\dot{M}_{\bullet,\mathrm{acc}}\,c^2/(1-\epsilon)$, with the gas accretion curve $\dot{M}_{\bullet,\mathrm{acc}}(\tau|\psi, z)$ specified by Eq. (4.9). Notice that the Eddington ratio λ and the radiative efficiency ϵ here are not free parameters but are self-consistently computed, for any SFR ψ and redshift z, by Eqs. (4.14) and (4.11). We will compare our results with the bolometric luminosity function determination by Shen et al. 2020, reconstructed from a large compilation of rest-frame B-band/UV (e.g., Hopkins et al. 2007; Giallongo et al. 2012; Manti et al. 2017; Kulkarni et al. 2018), soft/hard X-ray (e.g., Fiore et al. 2012; Ueda et al. 2014; Aird et al. 2015a, 2015b; Miyaji et al. 2015), and IR data (e.g., Assef et al. 2011; Lacy et al. 2015) collected in the past decades (see Shen et al. 2020 for details concerning bolometric and obscuration corrections).

Notice that the integrand in Eq. (4.18) constitutes the number density of galaxies $\mathrm{d}^3 N/\mathrm{d}\log\psi\,\mathrm{d}\log L_{\mathrm{AGN}}\,\mathrm{d}V$ per comoving volume in bins of SFR and AGN luminosity. Thus it may be exploited to build up the so-called coevolution plane SFR vs. L_{AGN}, and the mean relationship between these two quantities. Finally, the previous expressions can also be adapted to derive the Eddington-ratio distribution by simply substituting L_{AGN} with $\lambda = L_{\mathrm{AGN}}/L_{\mathrm{Edd}}$.

4.2.7 Relic BH mass function

To derive the relic (super)massive BH mass function $\mathrm{d}^2N/\mathrm{d}\log M_\bullet\,\mathrm{d}V$ we exploit a generalised version of the continuity equation (see Yu & Lu 2004, 2008; Aversa et al. 2015); this is basically a technique to relate the BH growth functions (or AGN luminosity functions) to the BH mass functions. The outcome reads

$$
\frac{\mathrm{d}^2N}{\mathrm{d}\log M_\bullet\,\mathrm{d}V}(M_\bullet,z) = -\int_z^\infty \mathrm{d}z' \left|\frac{\mathrm{d}t_{z'}}{\mathrm{d}z'}\right| \left.\frac{\partial_{\log \dot M_\bullet}\frac{\mathrm{d}^2N}{\mathrm{d}\log \dot M_\bullet\,\mathrm{d}V}(\dot M_\bullet,z')}{\sum_i \frac{\mathrm{d}\tau_i}{\mathrm{d}\log \dot M_\bullet}\times\partial_{\log \dot M_\bullet}\log M_\bullet}\right|_{\dot M_\bullet=\frac{M_\bullet}{\tau_{\mathrm{ef}}+\tau_{\mathrm{d}}\,(1-e^{-\zeta})}} .
$$
$$(4.19)$$

Here the quantity $\mathrm{d}^2N/\mathrm{d}\log \dot M_\bullet\,\mathrm{d}V$ is the growth rate function from Eq. (4.16), all the integrand is computed at the maximum accretion rate for a given relic BH mass $\dot M_\bullet = M_\bullet/[\tau_{\mathrm{ef}} + \tau_{\mathrm{d}}\,(1 - e^{-\zeta})]$, and the various quantities implicitly entering there (e.g., λ, τ_{ef}, τ_{d}) must be referred to a relic BH mass $M_\bullet$ and redshift z. We stress that in our framework, at variance with many previous approaches based on continuity equation, the input AGN luminosity functions are not just taken from observations, but are derived from the galaxy statistics via Eq. (4.18). The related relic (super)massive BH mass density can be computed as

$$
\rho_\bullet(z) = \int \mathrm{d}\log M_\bullet\, M_\bullet\, \frac{\mathrm{d}^2N}{\mathrm{d}\log M_\bullet\,\mathrm{d}V}(M_\bullet,z) , \tag{4.20}
$$

where typically the integral is taken over BH masses $M_\bullet \gtrsim 10^6\,M_\odot$.

Fig. 4.1 summarises in an illustrative way all the steps followed to compute the (super)massive BH mass function and described in this Section.

4.3 Results and Discussion

In this Section we will show results of our empirical model concerning the growth of the central BH mass, AGN luminosity functions and Eddington ratio distribution, relationship of the AGN luminosity with the host SFR, and BH mass function. We will highlight the role played by the gaseous dynamical friction process in providing a physical mechanism to originate heavy seeds, so allowing the growth of the central BH to the supermassive regime at moderate Eddington ratios within the typical star-formation timescale of
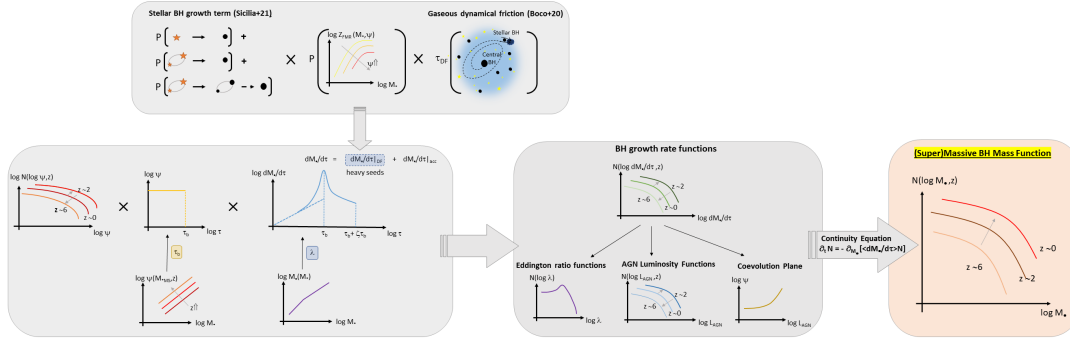
FIGURE 4.1: Schematics showing the main steps to compute the (super)massive relic BH mass function. The starting point is the stellar term from Chapter 3, representing the number of BHs originated per unit of star formed mass, and includes contributions from the evolution of isolated or binary stars into isolated or binary BHs (light seeds; see Eq. 4.5). This is coupled to the metallicity distribution (extracted from the fundamental metallicity relation) and with the timescale for gaseous dynamical friction by Boco et al. 2020 (see Eq. 2.24) to derive the growth rate of the central BH by migration of stellar remnants (see Eqs. 4.7 and 4.8). In parallel, galaxy statistics provided by the SFR functions are coupled with model growth curves of the stellar and BH mass (see Eqs. 4.2 and 4.13); the latter includes the growth by dynamical friction migration and by gaseous Eddington-type accretion. Crucial parameters of these growth curves, like the star formation duration and the Eddington factor, are derived by requiring consistency with the main sequence of star-forming galaxies (see Eqs. 4.3 and 4.4) and with the local Magorrian relationship (see Eqs. 4.14 and 4.15). The main outcome of this procedure are BH growth rate functions (see Eq. 4.16), and byproducts are Eddington ratio functions, AGN luminosity functions (Eq. 4.18) and the coevolution plane SFR vs. L_{AGN}. Finally, a generalized continuity equation approach allows to convert the growth rate functions into the (super)massive BH mass function (Eq. 4.19).

the host. We will also discuss the dependence of our basic results on various assumptions.

4.3.1 Basic results

To start with, in the top row of Fig. 4.2 we illustrate the time evolution of the central BH mass (left panels) and BH growth rate (right panels) in a proto-typical star-forming galaxy with SFR $\psi \sim 300\,M_\odot$ yr^{-1} at reference redshifts $z \approx 2$ (top and middle rows) and $z \approx 6$ (bottom row). In the top row the final BH mass is assumed to satisfy the average Magorrian relationship, while in the middle and bottom rows it is taken as a 3σ upper outlier with respect to the Magorrian; these latter instances are representative of extremely massive BHs, that are possibly sampled because of observational biases (especially at high redshifts). The overall growth is illustrated as black solid lines, and the corresponding Eddington ratio is reported in the first entry of the legend, while the contribution from migration of stellar BHs via gaseous dynamical friction is shown by the blue dot-dashed lines. It is seen that in all these cases the evolution of the total BH mass at small galactic ages is dominated by the growth due to migration of stellar BHs via gaseous dynamical friction; such a process can effectively build up a heavy central BH seed of mass $M_\bullet \sim 10^{3-5}$ within $\lesssim 10^8$ yr. Thereafter Eddington-type gas disk accretion takes over and can grow the central BH to the (super)massive regime $M_\bullet \gtrsim 10^{8-9}\,M_\odot$. Remarkably, the overall effect of the early growth by dynamical friction is twofold. First, it allows the central BH to attain the final mass within a rather short timescale of some 10^8 yr; this can contribute to alleviate, or even to solve, the high-redshift quasar problem, i.e. the buildup of billion-solar-mass BHs in quasar hosts at $z \gtrsim 6$, when the age of the universe $\lesssim 1$ Gyr constitutes a demanding constraint. Second, such a growth can be obtained with reasonable values of the Eddington ratios $\lambda \sim 0.3$, that are in sound agreement with the observational determinations (see below); even in the extreme instance of an upper 3σ outlier of the Magorrian at $z \approx 6$ (bottom panels), the growth can be achieved with sub-Eddington conditions $\lambda \lesssim 1$.

In addition, in Fig. 4.2 we also illustrate what happens in the absence of the dynamical friction process, hence enforcing a BH growth by pure disk accretion. In particular, the orange dashed lines depict the evolution of a central BH with the same final mass as the solid lines but starting from a stellar mass seed $\approx 10^2\,M_\odot$; such a case is seen to imply an appreciably higher Eddington ratio (reported in the last entry of the legend). In other words, growing the BH from light seeds of stellar origin to the supermassive regime would require a time $\gtrsim 0.8/\lambda$ Gyr. Thus especially at high redshifts and/or
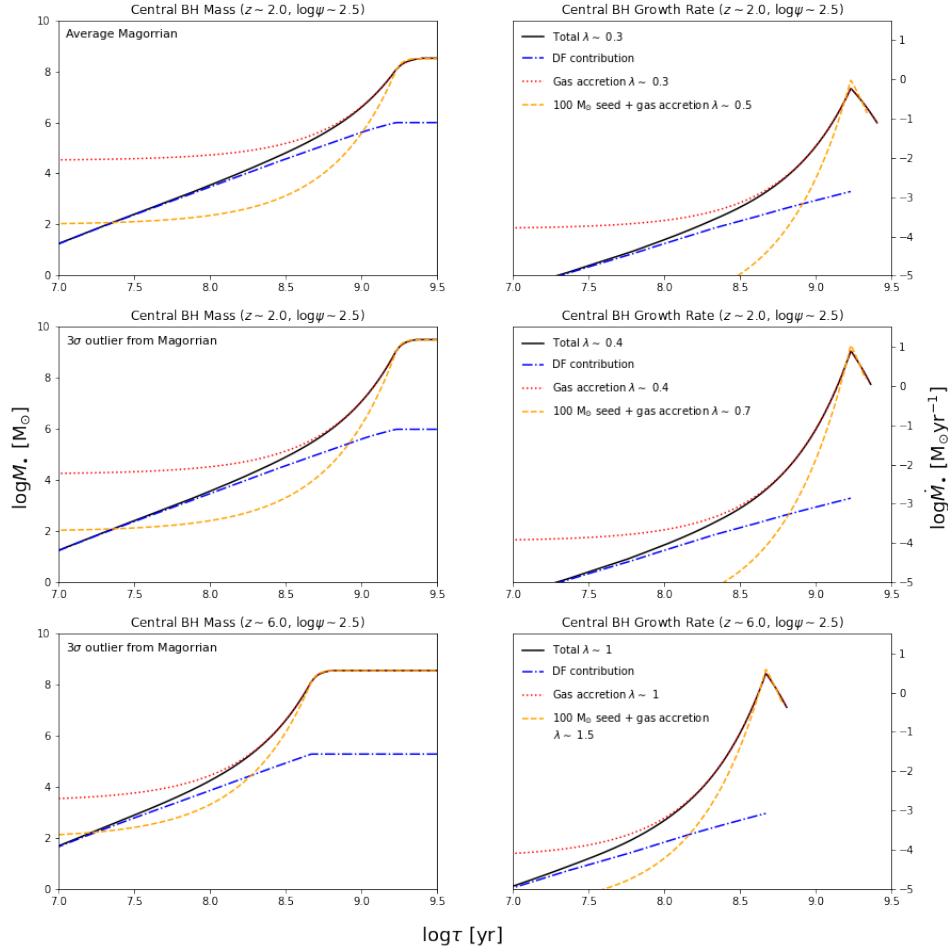
FIGURE 4.2: Time evolution of the central BH mass (left panels) and BH growth rate (right panels) in a star-forming galaxy with SFR $\psi \sim 300\,M_\odot\,\mathrm{yr}^{-1}$ at $z \approx 2$ (top and middle rows) and $z \approx 6$ (bottom row); in the top row the final BH mass is on the average Magorrian relationship, in the middle and bottom rows it is a 3σ upper outlier of the Magorrian relationship. The overall growth of the central (super)massive BH is illustrated by black solid line (and the corresponding Eddington ratio λ is indicated in the first entry of the legend) while the contribution from migration of stellar BHs via gaseous dynamical friction is shown by the blue dot-dashed line. The red dotted line represents the evolution of a central BH growing by pure disk accretion (i.e., without dynamical friction) with the same final mass and with the same λ as the solid line, implying that the initial seed must be $\gtrsim 10^4\,M_\odot$. Finally, the orange dashed line shows the evolution of a central BH growing by pure disk accretion (i.e., without dynamical friction) with the same final mass as the solid line from a stellar mass seed $\approx 100\,M_\odot$, implying an appreciably higher Eddington ratios (indicated in the last entry of the legend).

for upper outliers of the Magorrian relationship (i.e., BHs with billion solar masses), the growth of the central BH should proceed at appreciably high values of λ, and possibly in super-Eddington conditions (as in the bottom panels). Though this instance can be partially justified theoretically (e.g., Li 2012; Madau et al. 2014) and there are hints of a few cases at $z \gtrsim 6$ (e.g., Fujimoto et al. 2022), it struggles somewhat against the bulk of present observational estimates at $z \lesssim 6$ (see references below and Fig. 4.5). On the other hand, the red dotted lines refer to the evolution of a central BH growing to the same final mass and with the same Eddington ratio λ as the solid lines; such a case is seen to imply that the initial seeds must be $\gtrsim 10^4 \, M_\odot$. Therefore a specific mechanism, alternative to dynamical friction, must be in any case envisaged to obtain such massive seeds (e.g., Volonteri et al. 2021; see also Sect. 4.1).

In Fig. 4.3 we illustrate the growth rate function of the central BH at different redshifts $z \sim 1-8$ (colour-coded). As it can be seen from Eq. (4.16), its shape as a function of $\dot{M}_\bullet$ is determined by a combination of galaxy statistics (i.e., the SFR functions) and the time spent by the central BH in a given bin of growth rate. The latter is in turn determined by the shape of the BH growth rate as a function of galactic age plotted in Fig. 4.2: at early times the BH rate grows almost linearly due to dynamical friction, at intermediate times it raises almost exponentially over the timescale τ_{ef} due to disk accretion, and at late times it diminishes exponentially over the timescale τ_{d}. The redshift evolution mirrors that of galaxy statistics, with the knee of the function first increasing toward larger $\dot{M}_\bullet$ out to $z \approx 2$ and then receding at higher redshifts. The turnover of the function at $z \lesssim 1$ at low accretion rates reflects the progressive inefficiency of the dynamical friction process (in turn mirroring the decreased efficiency of star-formation and stellar mass BH generation) toward late cosmic times.

In Fig. 4.4 we show the bolometric AGN luminosity functions at different redshifts $z \approx 1, 2, 4$ and 6, computed from Eq. (4.18). The results from our approach are compared with the observational estimates collected by Shen et al. 2020 (see full list of references therein) from selections in the rest-frame B-band/UV (e.g., Hopkins et al. 2007; Giallongo et al. 2012; Manti et al. 2017; Kulkarni et al. 2018), soft/hard X-ray (e.g., Fiore et al. 2012; Ueda et al. 2014; Aird et al. 2015a, 2015b; Miyaji et al. 2015), and IR (e.g., Assef et al. 2011; Lacy et al. 2015), converted using appropriate bolometric corrections (see Table 1 and Section 3 in Shen et al. 2020). The agreement is pretty good, both in terms of shape and redshift evolution. It is worth mentioning that the number density for AGNs with bright luminosities (especially toward high redshifts) may be overestimated in the data due to the uncertainties in the bolometric corrections. Note that we do not attempt a comparison with the
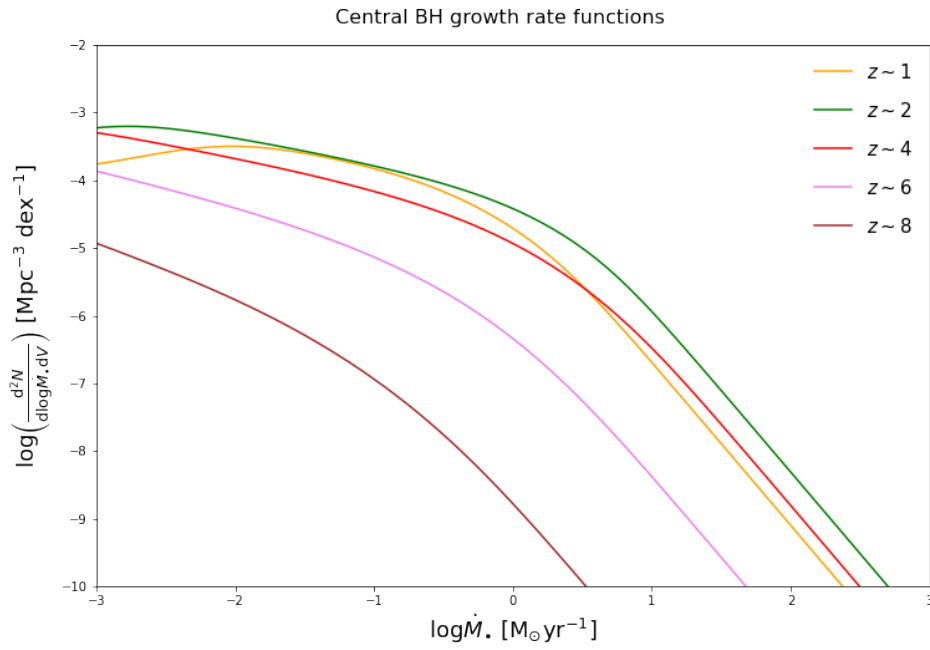
FIGURE 4.3: The BH growth rate function (see Eq. 4.16) at different redshifts $z \approx 1$ (orange), 2 (green), 4 (red), 6 (magenta), and 8 (brown).
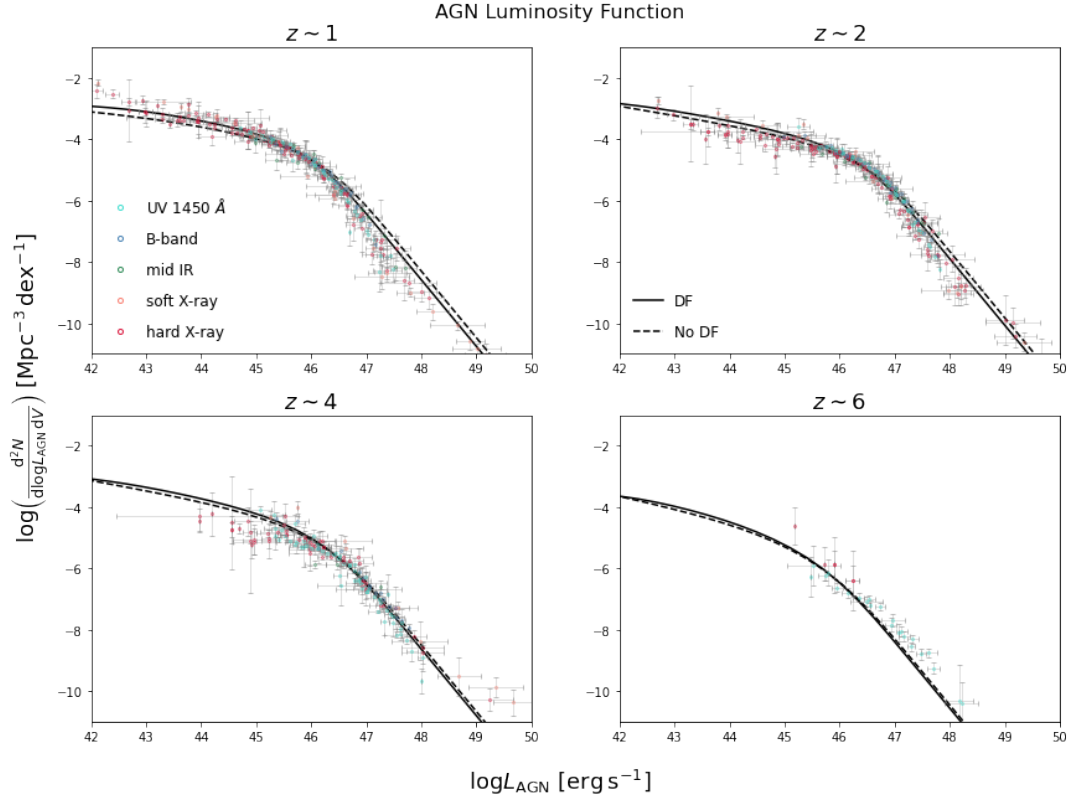
FIGURE 4.4: The bolometric AGN luminosity functions (see Eq. 4.18) at different redshifts $z \approx 1$ (top left panel), 2 (top right), 4 (bottom left) and 6 (bottom right). Solid lines illustrate the result of our approach, which are compared with the data compilation by Shen et al. 2020 (circles) from selections in the UV 1450 Å (cyan), $B-$band (blue), mid-IR (green), soft X-rays (orange), and hard X-rays (red). For comparison, dashed lines show the results when the gaseous dynamical friction mechanism is switched off (see comment in main text).

observed AGN luminosity functions at $z \lesssim 1$ since our framework does not include BH reactivations from late-time mergers and disk-instabilities (see Sect. 4.2); the latter are known to be a fundamental ingredient in determining the low-z AGN luminosity functions, especially at the faint end, though reproducing these observables has demonstrated to be a highly non-trivial task even for detailed models incorporating the aforementioned processes (see Griffin et al. 2019; Izquierdo-Villalba et al. 2020).

In Fig. 4.5 we illustrate the Eddington ratio distribution $d^2N/dV \, d\log\lambda$ and the average Eddington ratio $\langle\log\lambda\rangle$ with its dispersion as a function of redshift. This is compared with observational estimates from different samples (see Duras et al. 2020; Kim & Im 2019; Vignali et al. 2018; Dai et al. 2014;

Nobuta et al. 2012; Vestergaard & Osmer 2009). In our fiducial framework, the average Eddington ratio slowly increases from values $\lambda \approx 0.1$ at $z \approx 1$ to values $\lambda \sim 0.6$ at $z \gtrsim 4$. The Eddington ratio distribution is quite broad, with a 1σ dispersion of 0.4 dex almost independent of the redshift. The outcome from our approach is in good agreement with the observational estimates, although the latter, being mainly based on single-epoch estimators, are still subject to considerable uncertainties, especially toward high redshift. Note that recently in the literature a lot of attention has been paid to observational estimates of the Eddington ratio distribution as a function of host galactic properties, most noticeably stellar mass and specific SFR (e.g., Bongiorno et al. 2016; Georgakakis et al. 2017; Aird et al. 2018, 2022; Yang et al. 2019; Ananna et al. 2022; Carraro et al. 2020, 2022); however, the estimates are still subject to considerable uncertainties, especially at $z \gtrsim 0.5$ and for massive galaxies. The comparison with, and the interpretation of such distributions is beyond the scope of this thesis, and we defer it to a future work.

In the above Figs. 4.4 and 4.5 we also illustrate (dashed lines) the expected luminosity functions and average Eddington ratio when the dynamical friction mechanism is switched off and light BH seeds $\approx 10^2 \, M_\odot$ are assumed (a value taken as representative for the most massive seeds of stellar origin). The results on the luminosity functions are almost indistinguishable from our fiducial case, since by construction our approach imposes that, with or without dynamical friction, the final BH masses must adhere to the same Magorrian relationship and are obtained within the same timescales set by the main sequence; in turn, this implies that the peak AGN luminosities are very close to each other. However, without dynamical friction, this is at the cost of increasing somewhat the average Eddington ratio, because the growth starts from a lighter seed. Albeit in a statistical sense these higher values of λ are still within the large dispersion of the observational data, the problem may be exacerbated for the very massive BHs $M_\bullet \gtrsim 10^9 \, M_\odot$, and especially so at high $z \gtrsim 6$ whose formation would require $\lambda \sim$ a few (see Fig. 4.2 and related discussion above).

In Fig. 4.6 we illustrate the coevolution plane at a reference redshift $z \approx 2$; this represents the number density of objects in the SFR ψ vs. AGN bolometric luminosity L_{AGN} diagram (grey-scale colour-coded); the average relationship and its $1 - 2\sigma$ scatter (solid line and shaded areas) are computed from such a distribution, taking into account the typical SFR detection threshold of present observations, around $\psi \approx 150 \, M_\odot \, \mathrm{yr}^{-1}$. The distribution of objects in the coevolution plane is again determined mainly by the number density of galaxies with a given value of the SFR, implying that galaxies with higher SFRs are rarer, and by the time a galaxy spends in different AGN luminosity
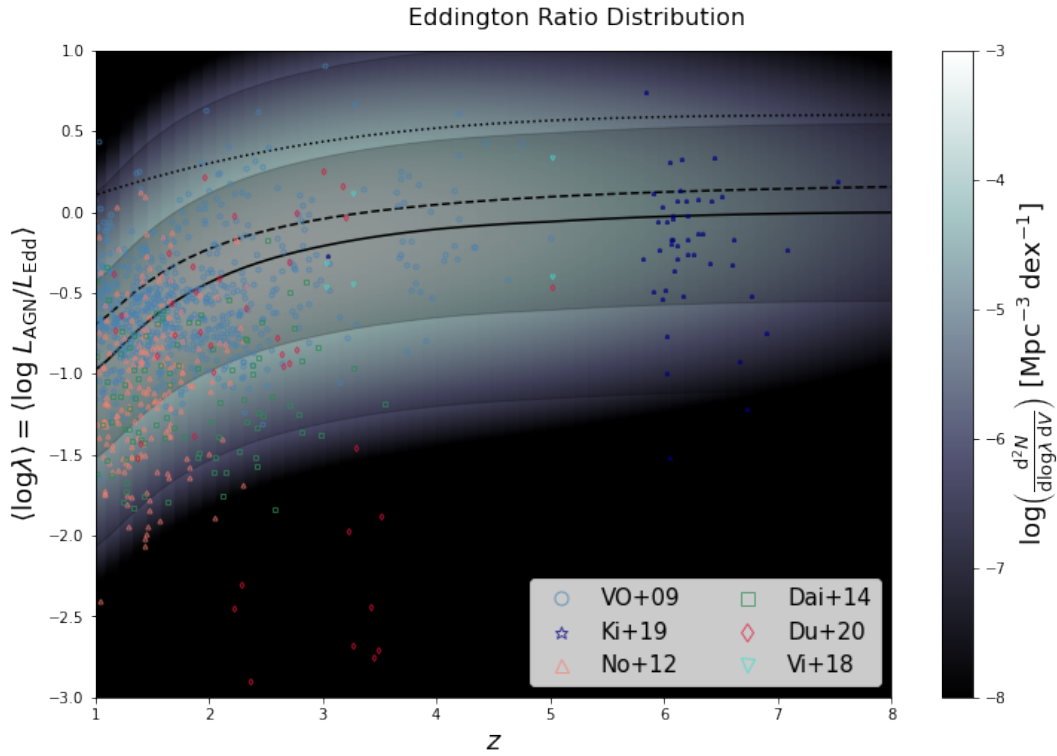
FIGURE 4.5: The Eddington ratio distribution and average Eddington ratio as a function of redshift z. The intensity of the black and white background illustrates the Eddington ratio distribution, while the black solid line is the average relationship expected from our approach (dark and light grey shades represents the 1σ and 2σ dispersion). In addition, the dashed line is the average Eddington ratio when the gaseous dynamical friction mechanism is switched off, and the dotted line is the average Eddington ratio adopted on an empirical basis by Aversa et al. 2015. Data are from Duras et al. 2020 (red diamonds), Kim & Im 2019 (navy stars), Vignali et al. 2018 (cyan inverted triangles), Dai et al. 2014 (green squares), Nobuta et al. 2012 (orange triangles), and Vestergaard & Osmer 2009 (blue circles).

bins. The average SFR and its scatter, computed taking into account the typical SFR detection threshold mentioned above, stays roughly constant with AGN luminosity out to $L_{\mathrm{AGN}} \approx 10^{46}$ erg s^{-1} and then slowly increases. Such a rise occurs just because, statistically, to achieve a higher AGN luminosity, the BH must reside in a more massive galaxy with a higher initial SFR. For comparison, in Fig. 4.6 we report various observational determinations (see Page et al. 2012; Netzer et al. 2015; Stanley et al. 2015, 2017; Fan et al. 2016; Bianchini et al. 2019; Rodighiero et al. 2019) concerning different primary AGN selections in the optical, X-ray, IR or mixed (colour-coded); detections are highlighted with full symbols and stacked data with open symbols. Our findings are remarkably consistent with observations, with the detections being distributed around the average relationship within its scatter, and the stacked measurements settling at the margin of the expected 2σ dispersion.

In Fig. 4.7 we illustrate the (super)massive relic BH mass function as derived from the continuity equation Eq. (4.19) at different redshifts $z \approx 0 - 8$ (colour-coded). The redshift evolution is quite strong down to $z \approx 2$, with the knee (characteristic BH mass) strongly increasing from $M_\bullet \lesssim 10^7 \, M_\odot$ at $z \gtrsim 8$ up to $M_\bullet \gtrsim 10^9 \, M_\odot$ for $z \lesssim 2$; the evolution slows down considerably, especially at the high mass end, for $z \lesssim 2$, such that essentially below $z \approx 1$ the mass function undergoes only a minor evolution.

In Fig. 4.8 we show the related BH mass density computed after Eq. (4.20). It increases quite steeply from $\rho_\bullet \lesssim 10^3 \, M_\odot \, \mathrm{Mpc}^{-3}$ at $z \gtrsim 6$ up to some $\rho_\bullet \gtrsim 10^5 \, M_\odot \, \mathrm{Mpc}^{-3}$ at $z \lesssim 1$. The local BH mass density amounts to $\rho_\bullet \approx 6 \times 10^5 \, M_\odot \, \mathrm{Mpc}^{-3}$, in sound agreement with the available observational determinations (see Shankar et al. 2004, 2009: Hopkins et al. 2007; Marconi et al. 2004; Graham et al. 2007; Yu & Lu 2008). Fig. 4.8 also displays the contribution to the mass density from different BH mass ranges, to highlight that at $z \lesssim 6$ and for $M_\bullet \lesssim 10^9 \, M_\odot$, more massive BHs tend to accumulate their mass faster, displaying a kind of downsizing behaviour.

In Fig. 4.9 we present the local BH mass function, and compare it with theoretical and observational estimates. In particular, the green shaded area refers to the uncertainty region in the current estimates of the BH mass function (see Shankar et al. 2016, 2020a), obtained when combining the local stellar mass/velocity dispersion functions with various literature relationships linking BH mass to stellar mass/velocity dispersion of the host. We also report for comparison the classic estimates by Marconi et al. 2004 (see also Shankar et al. 2009) via a simplified continuity equation approach, and by Vika et al. 2009 via an object-by-object analysis of the BH mass-host luminosity relationship. Our mass function is in agreement with most determinations for BH masses $M_\bullet \lesssim$ some $10^8 \, M_\odot$. At the high-mass end it lies
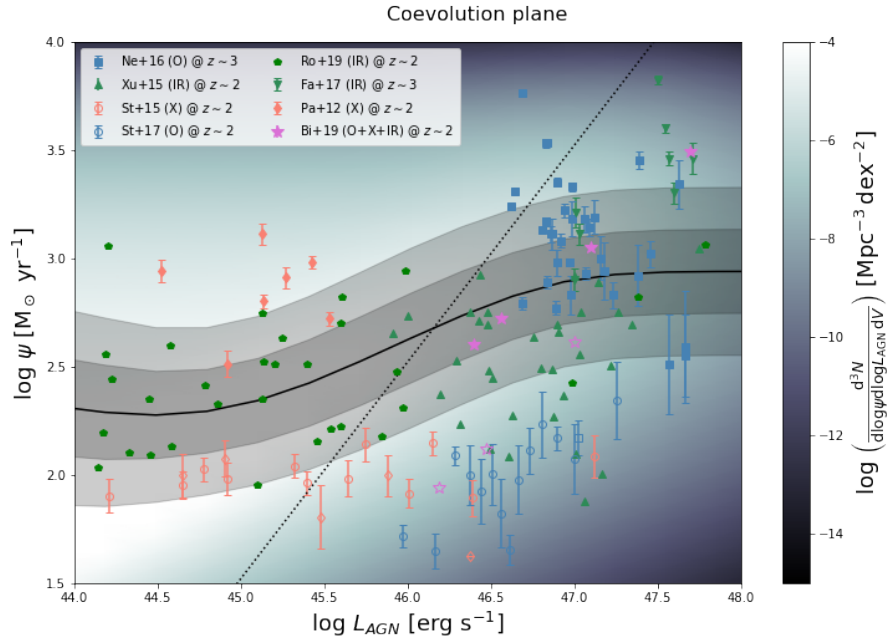
FIGURE 4.6: The coevolution plane, namely the relationship between SFR of the host galaxy and the bolometric AGN luminosity L_{AGN} at a reference redshift $z \approx 2$. The intensity of the black and white background illustrates the number density of galaxies expected in the different portions of the diagram, and the solid line is the average relationship from our approach (dark and light grey shades represents the 1σ and 2σ dispersion). For reference, the dotted line represents the locus where the bolometric luminosity from the AGN and from the star formation in the host are equal. Data are from Netzer et al. 2015 (squares), Xu et al. 2015 (triangles), Stanley et al. 2015, 2017 (circles), Fan et al. 2016 (inverted triangles), Page et al. 2012 (diamonds), Bianchini et al. 2019 (stars), Rodighiero et al. 2019 (pentagons). Symbol colours refer to observational selection in the optical (blue), X-ray (orange), IR (green), or mixed (magenta); moreover, filled symbols refer to detections, while empty symbols refer to stacking estimates.
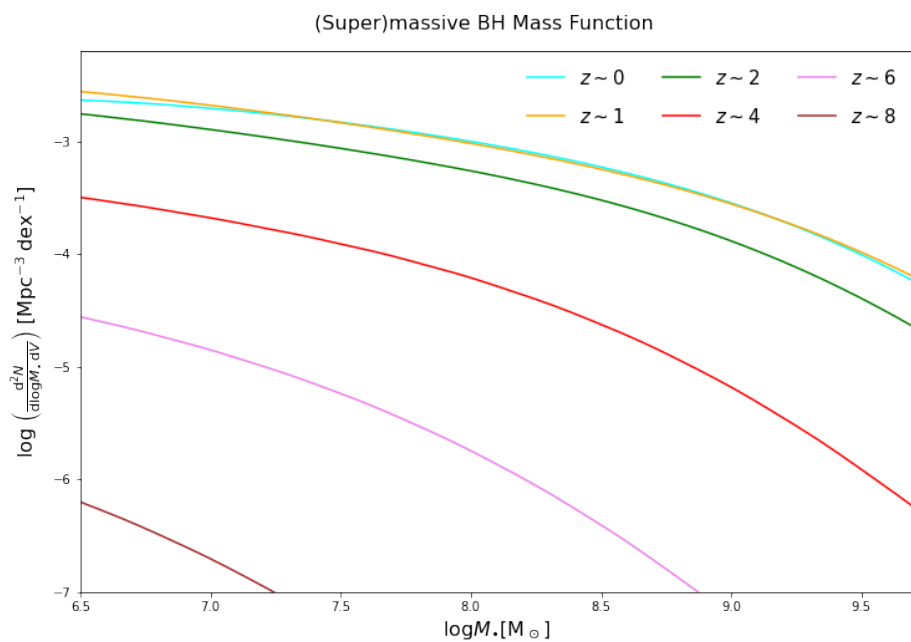
FIGURE 4.7: The relic (super)massive BH mass function (see Eq. 4.19; solid lines) at different redshifts $z \approx 0$ (cyan), 1 (orange), 2 (green), 4 (red), 6 (violet), 8 (brown).
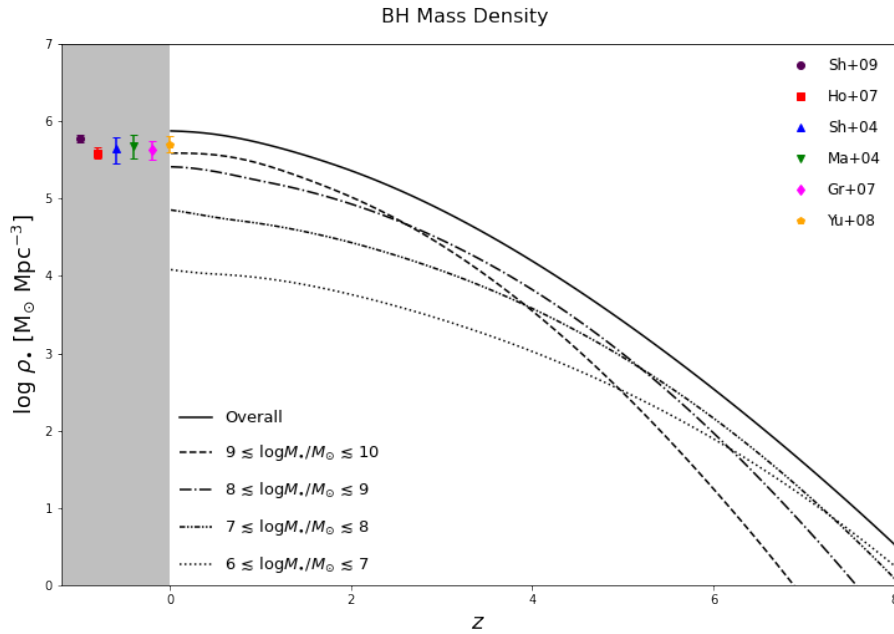
FIGURE 4.8: The (super)massive relic BH mass density (see Eq. 4.20) as a function of redshift z. The overall mass density is illustrated (solid) together with the contributions from the mass ranges $10^6 \, M_\odot \lesssim M_\bullet \lesssim 10^7 \, M_\odot$ (dotted), $10^7 \, M_\odot \lesssim M_\bullet \lesssim 10^8 \, M_\odot$ (triple-dot-dashed) and $10^8 \, M_\odot \lesssim M_\bullet \lesssim 10^9 \, M_\odot$ (dot-dashed) and $10^9 \, M_\odot \lesssim M_\bullet \lesssim 10^{10} \, M_\odot$ (dashed). Observational estimates at $z \approx 0$ are from Shankar et al. 2009 (brown circle), Hopkins et al. 2007 (red square), Shankar et al. 2004 (blue triangle), Marconi et al. 2004 (green inverted triangle), Graham et al. 2007 (magenta diamond), Yu & Lu 2008 (orange pentagon).
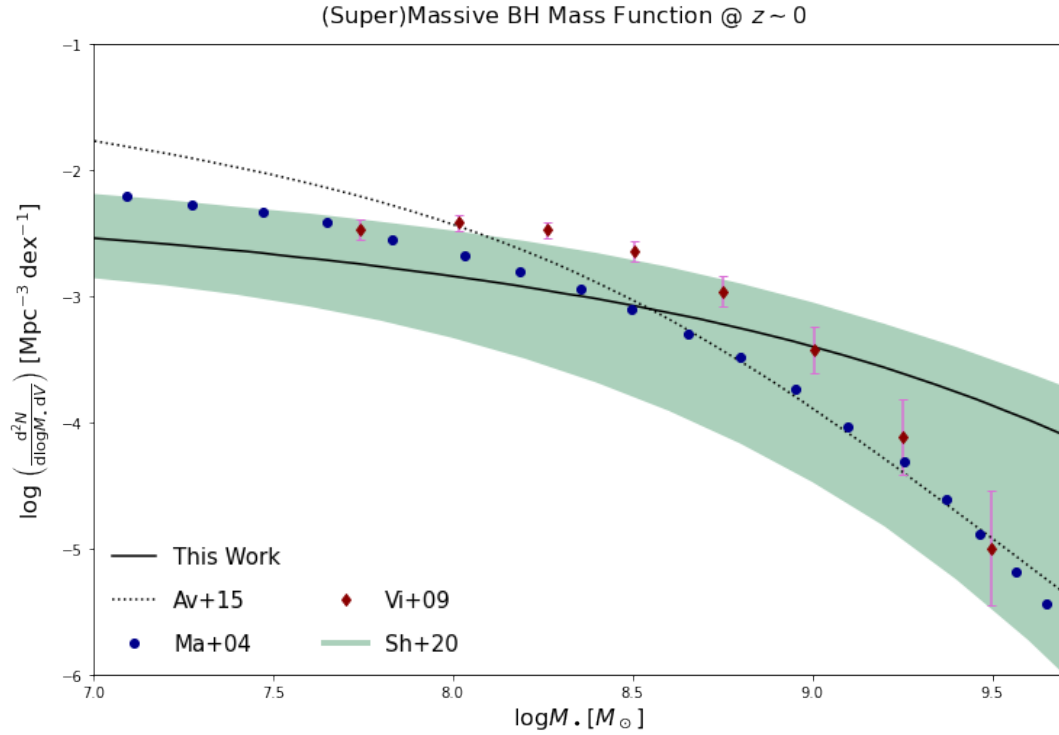
FIGURE 4.9: The (super)massive BH mass function at $z \approx 0$. The solid line illustrates the outcome of our framework, while the dotted line is the mass function originated when coupling the observed AGN luminosity functions with the average Eddington ratio adopted by Aversa et al. 2015. Observational estimates are from Marconi et al. 2004 (blue circles), Vika et al. 2009 (red diamonds), and Shankar et al. 2009, 2016, 2020 (green shaded area); the latter reflects the overall uncertainty region when determining the BH mass function from the local stellar mass/velocity dispersion functions combined with various relationships of these observables with the BH mass.

well within the Shankar et al. 2020a uncertainty region, but it declines substantially slower with respect to the classic estimates by Marconi et al. 2004 and Vika et al. 2009.

We stress that to obtain a BH mass function with a steep behaviour at the high mass end is a non-trivial task. Specifically, in our framework we determine λ from the empirical Magorrian relation and main sequence timescale, obtaining values $\lambda < 1$ that are in good agreement with the observed Eddington ratios; we also predict AGN luminosity functions closely matching the data. However, when inserted into the continuity equation these low λ values originate a rather flat BH mass function at the high mass end since

large BH masses correspond to moderate peak AGN luminosities (approximately $L_{\mathrm{AGN}} \propto \lambda\, M_{\bullet}$ holds) falling in the rather flat portion of the luminosity function. Even the slightly higher λ values we obtain when switching off dynamical friction (see dashed line in Fig. 4.5) are not sufficient to appreciably steepen the BH mass function, which features a high mass end similar to our fiducial case. Contrariwise, in other literature studies (e.g., Aversa et al. 2015; Shen et al. 2020) a steep behaviour of the mass function is enforced by starting from the observed AGN luminosity functions (not self-consistently predicting them, as in this work) and by assuming values $\lambda \gtrsim 1$ designed on purpose. For example, the redshift-dependent parameterisation $\lambda(z) \approx 4\,\{1 - 0.5 \times \mathrm{erfc}[(z-2)/3]\}$ proposed by Aversa et al. 2015 works quite well in producing a steep BH mass function, but at the price of assuming λ values somewhat in tension with the observed average Eddington ratios (see dotted lines in Figs. 4.5 and 4.9). Insisting on such high λ values in a self-consistent approach while maintaining a good prediction of the AGN luminosity functions is still possible, but requires BH growth timescales $\lesssim 100$ Myr, much shorter than derived via the main sequence prescription.

4.3.2   Robustness of results against main assumptions

In Fig. 4.10 we highlight the dependence of our results concerning the AGN luminosity function, redshift evolution of the average Eddington ratio, and local (super)massive BH mass function on various assumptions/relationships used in our reference framework.

First, we vary the main sequence relationship, switching from Speagle et al. 2014 to the recent determination by Popesso et al. 2022. In analogy with Eq. (4.4), this can be rendered as

$$
\log \frac{\psi_{\mathrm{MS}}(M_{\star}, z)}{M_{\odot}\,\mathrm{yr}^{-1}} \approx (-27.58 + 0.26\, t_z)
$$
$$
+ (4.95 - 0.04\, t_z)\, \log \frac{M_{\star}}{M_{\odot}} - 0.2\, \log^2 \frac{M_{\star}}{M_{\odot}}\,. \tag{4.21}
$$

With respect to the almost linear relation by Speagle et al. 2014, the above is characterised by a steepening toward the lower stellar masses and a progressive flattening toward higher stellar masses, that have some relevance in galaxy formation since they may be interpreted as the effects of stellar feedback and mass quenching, respectively (e.g., Lapi et al. 2018; Daddi et al. 2022).
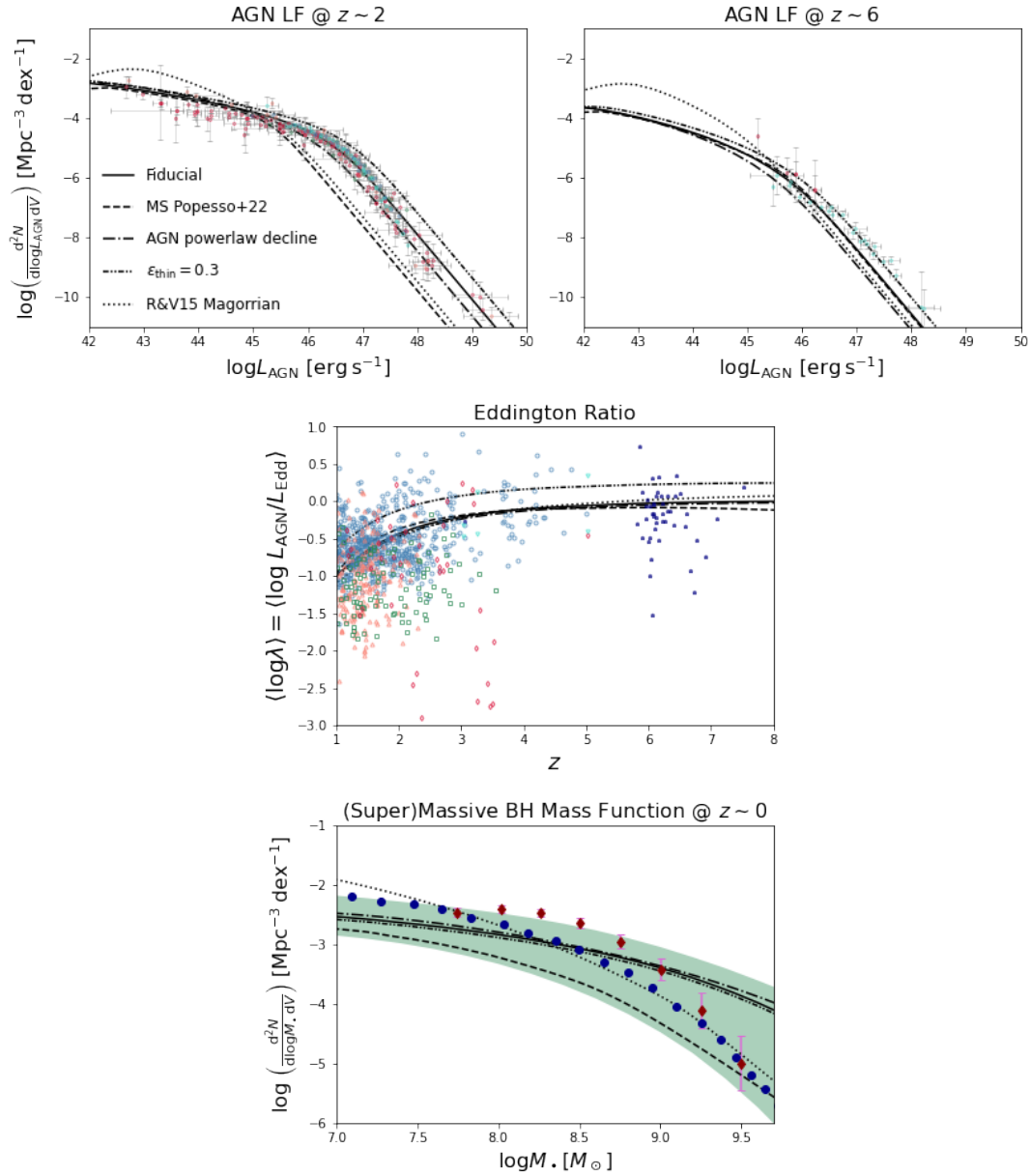
FIGURE 4.10: Dependence of our results concerning AGN luminosity function at $z \sim 2$ (top left) and $z \sim 6$ (top right), average Eddington ratio as a function of redshift (middle), and local supermassive BH mass function (bottom) to various assumptions/relationships employed in this work. In all panels solid lines refer to our fiducial assumptions, dashed lines to our results when the main sequence relation by Popesso et al. 2022 is used in place of Speagle et al. 2014, dot-dashed line to our results when the BH accretion rate curves is characterised by a powerlaw decline instead of an exponential one, dotted lines to our results when the Magorrian relation by Reines & Volonteri 2015 for AGNs is employed in place of the one by Shankar et al. 2016, 2020a, and triple-dot-dashed line to our results when the thin disk efficiency $\epsilon_{thin} \approx 0.3$ is adopted instead of our fiducial value $\epsilon_{thin} \approx 0.15$. See Sect. 4.3.2 for details.

Second, we vary the shape of the declining portion of the accretion rate curve in Eq. (4.9). In particular, we switch from an exponential to a scale-free, powerlaw shape $\dot{M}_{\bullet,\mathrm{acc}}(\tau) = \dot{M}_{\bullet,\mathrm{acc}}(\tau_{\mathrm{b}}) \, (\tau/\tau_{\mathrm{b}})^{-\omega}$ for $\tau > \tau_{\mathrm{b}}$. Here $\omega > 1$ rules the steepness of the decline, and we set $\omega \approx 2.5$ as in Shen 2009. Correspondingly, the overall BH growth at late times (cf. Eq. 4.12) follows

$$M_{\bullet}(\tau|\psi, z) = M_{\bullet}(\tau_{\mathrm{b}}) \left[1 + \frac{\tau_{\mathrm{b}}}{\tau_{\mathrm{ef}}} \frac{1 - (\tau/\tau_{\mathrm{b}})^{1-\omega}}{\omega - 1}\right] \quad , \qquad \tau > \tau_{\mathrm{b}} \qquad (4.22)$$

and the relic mass for $\tau \gg \tau_{\mathrm{b}}$ reads $M_{\bullet,\mathrm{relic}}(\psi, z) = M_{\bullet} \left[1 + \tau_{\mathrm{b}}/(\omega - 1)\,\tau_{\mathrm{ef}}\right]$. Such a powerlaw behaviour is often adopted in empirical BH evolution models and generically ascribed to a residual accretion related to viscosity in a thin accretion disk (e.g., Yu & Lu 2008; Shen 2009); it has also been claimed to be consistent with a few numerical simulations present in the literature (see discussion by Habouzit et al. 2022).

Third, we vary the adopted Magorrian relationship (cf. Eq. 4.15) from the debiased determination by Shankar et al. 2016, 2020a based on dynamical BH masses to that by Reines & Volonteri 2015 based on single-epoch virial estimators for locally active BHs (calibrated on a subsample of reverberation-mapped AGNs):

$$\log \frac{M_{\bullet,\mathrm{Mag}}}{M_{\odot}}(M_{\star}, z) \approx 7.45 + 1.05 \log \frac{M_{\star}}{10^{11}\,M_{\odot}} + \eta \log(1 + z) \, , \qquad (4.23)$$

where for consistency we retain the same redshift dependence adopted in Eq. (4.15).

Finally, we vary the radiative efficiency ϵ_{thin} of the thin disk regime (see Eq. 4.11) from our fiducial value 0.15 to 0.3; the latter is close to the limit applying for maximally spinning BHs. In fact, some theoretical works (e.g., Volonteri et al. 2013; Sesana et al. 2014; Griffin et al. 2019; Izquierdo-Villalba et al. 2020) have pointed out that the population of high-z BHs might be maximally spinning, so it is interesting to check the effect of this assumption especially on the AGN luminosity function at high redshift $z \gtrsim 6$.

Fig. 4.10 shows that the most critical assumptions are, not surprisingly, the adopted main sequence and Magorrian relationships, that clearly affect the timescale of BH growth and the final BH masses, hence the resulting AGN luminosity function and BH mass function. As for the Popesso main sequence, it causes both a reduced number density of galaxies with high SFR, and a smaller stellar mass at a given SFR. This yields smaller BH masses hence a lower and steeper BH mass function. At the same time, with the

Popesso main sequence shorter timescales are available for BH growth, implying minor variations in the Eddington ratio and correspondingly lower luminosities. As for the Magorrian relation by Reines & Volonteri 2015, it is flatter than our reference case and tends to yield lower BH masses for stellar masses $M_\star \gtrsim$ a few $10^{10}\, M_\odot$, and vice versa. Overall, this naturally originates an AGN luminosity function and a local BH mass function pumped at the faint end and depressed at the bright one, while the change in the average Eddington ratio is minor. Adopting a power-law shape of the declining portion in the BH accretion rate curve affects somewhat the AGN luminosity functions, while the impact on the Eddington ratio distribution and on the BH mass function is limited. Finally, we also highlight that adopting a high value $\epsilon_{\rm thin} \approx 0.3$ of the thin disk radiative efficiency implies higher Eddington ratio λ. This is seen by combining Eqs. (4.10) and (4.11) given that $\tau_{\rm ef}$ stays put since it is determined for a final BH mass by the Magorrian relation and the main sequence timescale. In the end this originates higher AGN luminosity functions, which better agree with observational estimates for $z \gtrsim 6$; this is particularly interesting since, as mentioned above, higher efficiencies associated to quickly spinning BHs are mostly expected toward such high redshifts.

4.3.3 The Overall BH mass function

In Fig. 4.11 we illustrate the overall black hole mass function, from the stellar to the (super)massive regime, over more than ten orders of magnitude in BH mass. The stellar regime for $M_\bullet \lesssim 10^2\, M_\odot$ is taken from Chapter 3 and strictly associated to the star formation process in galaxies. In our framework, the intermediate mass regime $M_\bullet \sim 10^{2-5}$ is mainly associated to the formation of heavy BH seeds by migration of stellar BHs via gaseous dynamical friction at the centre of star-forming galaxies; the migrating stellar mass BHs are a very tiny fraction of the total number, so that the number density of these intermediate BHs is substantially lower than the stellar one. Finally, the (super)massive regime $M_\bullet \sim 10^{6-10}\, M_\odot$ is mainly populated by the BHs that have grown to large masses (from heavy seeds) via Eddington-type gas disk accretion. Most of such massive BHs are *active* at high redshifts $z \gtrsim 6$, so that the BH mass function in the intermediate and (super)massive regime is continuously connected. On the other hand, moving toward lower redshifts the mass function in the (super)massive range increases because *relic* BHs grown by disk accretion accumulate, while the number of intermediate mass BHs diminishes since the dynamical friction process becomes less efficient and the overall production of stellar mass BHs also lowers (following the progressive decline in the amount of star-formation within galaxies).
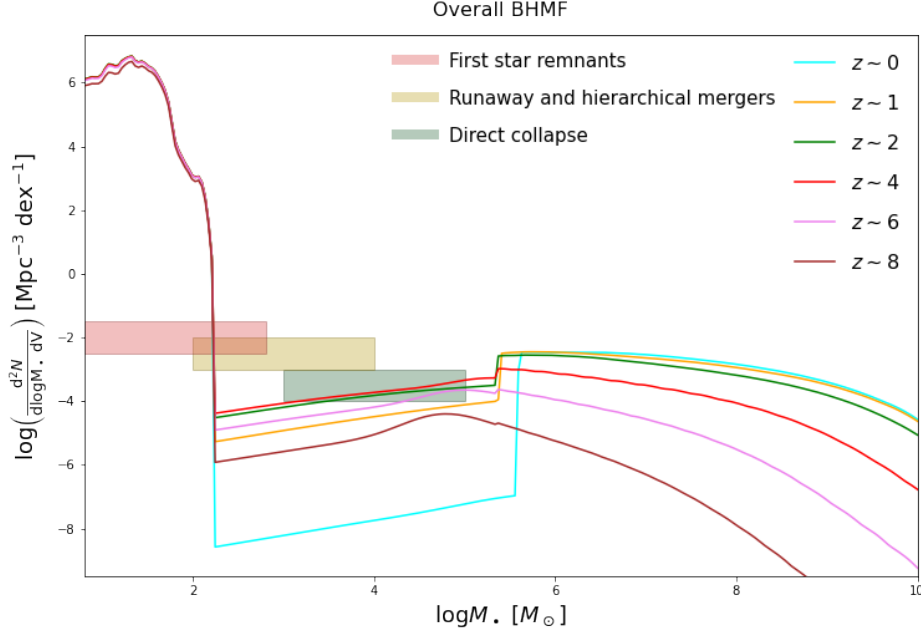
FIGURE 4.11: The overall BH mass function from our semi-empirical framework, from the stellar to the intermediate to the (super)massive regime, at different redshifts $z \approx 0$ (cyan), 1 (orange), 2 (green), 4 (red), 6 (purple), and 8 (brown). The coloured boxes illustrate the mass and density ranges from other seed formation channels (see Volonteri et al. 2021): remnants of the first massive pop-III stars (red box), direct collapse of primordial gas clouds (green box), and runaway stellar or BH mergers in compact primeval star clusters (yellow box).

This is at the origin of the discontinuity (or gap; see Trinca et al. 2022 and Spinoso et al. 2022 for a similar behaviour) between the intermediate and (super)massive mass function around $M_\bullet \lesssim 10^6 \, M_\odot$; it is pleasing that this transition occurs at around the typical value usually considered to separate intermediate from supermassive BHs.

For reference, in Fig. 4.11 we have also illustrated as coloured boxes the mass and density ranges expected from other classic seed formation channels (taken from Volonteri et al. 2021, see Fig. 4.12): remnants of the first massive pop-III stars (red box), direct collapse of primordial gas clouds (green box), and runaway stellar or BH mergers in compact primeval star clusters (yellow box). These distributions mainly originates in (proto)galaxies at $z \gtrsim 10$, and are then progressively eroded (but not substantially refurnished) at lower redshifts, when the seeds merge together or accrete gas and become more massive BHs (e.g., Mayer & Bonoli 2019;
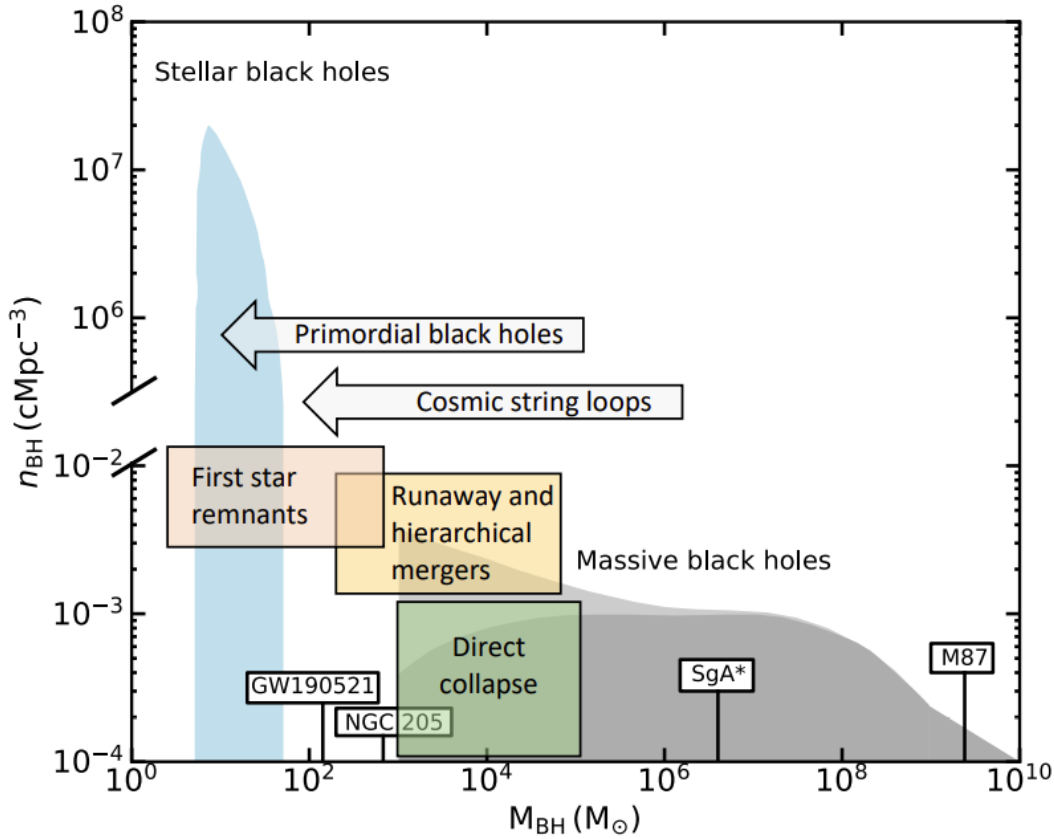
FIGURE 4.12: From Volonteri et al. 2021. Cartoon of the general shape of stellar BHMFs (blue shaded area) and supermassive BHMF (light and dark grey area). Shaded red, yellow, and green boxes show the number density of possible origins of BHs for first star Pop-III remnants, runaway and hierarchical mergers and direct collapse of gas clouds respectively.

Volonteri et al. 2021; Trinca et al. 2022; Spinoso et al. 2022). This is at variance with our framework, where heavy seeds are continuously produced across cosmic times by the migration and merging of stellar-mass BHs associated to star formation in galaxies. In view of the above, if present, such classic seed formation channels are expected to enhance somewhat the BH mass function in the range $M_\bullet \sim 10^{2-5}\,M_\odot$ especially at redshifts $z \gtrsim 8$. At later cosmic times, classic formation channels will feature a substantially eroded distribution in the intermediate mass range, so that their impact on our BH mass function should be minor. However, in a future work it would be interesting to perform a detailed investigation of the cooperative action of all these seed formation mechanisms across cosmic history.

4.4   Summary and Outlook

In this Chapter we have provided an ab-initio computation of the (super)massive BH mass function across cosmic times (see Fig. 4.1). To this purpose, we have started from the redshift-dependent galaxy statistics (constituted by the SFR functions) and have modelled the joint evolution of the central BH mass and the stellar mass of the host (see Fig. 4.2). We have considered two mechanisms to grow the central BH, that are expected to cooperate in the high-redshift star-forming progenitors of local massive galaxies. One is the gaseous dynamical friction envisaged by Boco et al. 2020, that can cause the migration of stellar-mass BHs originated during the intense bursts of star formation toward the gas-rich central regions of the host progenitor galaxies; this leads to the buildup of an heavy BH seeds $\lesssim 10^5 \, M_\odot$ within short timescales $\lesssim$ a few 10^7 yr. The second mechanism is the standard Eddington-type gas disk accretion onto the heavy seed, through which the central BH can become (super)massive within the typical star-formation timescales $\lesssim 1$ Gyr of the host galaxy, as set by the galaxy main sequence. We have self-consistently combined these mechanisms to compute the overall growth rate functions of the central (super)massive BHs (see Fig. 4.3).

We have validated our approach by consistently reproducing the observed redshift-dependent bolometric AGN luminosity functions (Fig. 4.4), the observed Eddington ratio distributions (Fig. 4.5), and the observed relationship between the star-formation of the host galaxy and the bolometric luminosity of the accreting central BH (Fig. 4.6). We have then derived the relic (super)massive BH mass function (Fig. 4.7) and BH mass density (Fig. 4.8) via a generalised continuity equation approach, finding a pleasing agreement with the most recent observational estimates at $z \approx 0$ (Fig. 4.9). All in all, we have found that the present (super)massive BH mass density amounts to $\rho_\bullet \approx 6 \times 10^5 \, M_\odot \, \mathrm{Mpc}^{-3}$, in accord with available estimates.

We have stressed that in the absence of the dynamical friction process, statistical observables like the AGN luminosity functions are not substantially affected, since most of the BH mass is accumulated in the gas disk accretion phase. However, to attain BH masses $\gtrsim 10^9 \, M_\odot$ within the typical star-formation duration $\lesssim 1$ Gyr of the host galaxy without such dynamical friction process is challenging, especially at high redshifts $z \gtrsim 6$ or for overmassive BHs that are upper outliers of the average Magorrian relationship. In such a case, the BH growth must proceed at appreciably high Eddington ratios $\lambda \gtrsim 1$ and/or starting from heavy BH seeds $M_\bullet \sim 10^{3-5} \, M_\odot$. The first instance can be partially justified theoretically but struggles somewhat against present observational estimates, the second would require a specific mechanism, alternative to gaseous dynamical friction, designed to obtain such

massive seeds.

Finally, putting together the results from Chapters 3 and 4, we have reconstructed the overall BH mass function from the stellar to the (super)massive regime over more than ten orders of magnitude in BH mass. At the same time, we have provided a robust theoretical basis for a physically-motivated heavy seed distribution as a function of redshift. At variance with classic seed production channels, in our framework the heavy seed distribution is time-dependent: heavy seeds are continuously produced by the merging of light seeds originated from star formation via the gaseous dynamical friction mechanism; but they also grow via standard Eddington-type accretion, and soon leave the intermediate mass regime to become (super)massive. It would be extremely interesting to implement such a time-dependent seed distribution in analytic and numerical models of BH formation and evolution.

Chapter 5

Conclusions, Secondments, and Future Prospects

Below will be a summary of all which had been discussed throughout this thesis, highlighting the main elements and results from Chapters 3 and 4 and laying out avenues of future development which could be undertaken.

5.1 Summary

The foundational idea of this thesis has been to derive the complete black hole mass function from stellar to supermassive. We have taken a statistical approach, seeking to recreate observational restraints, by taking as an input basic empirical relations and simulation outcomes with added minimal modelling. This approach has worked to the model's strength, allowing it to be modular in it construction and able to test alternative scaling relations and stellar evolution simulations, where in the instances of replacement of said elements of the foundations we have seen the model remains consistent.

Due to the breath of the task, a requirement to understand a full range of astrophysical fields is necessary. Our stellar black hole mass function stands at the end of stellar evolution, whilst the supermassive variant require the knowledge of accretion models necessary to overcome the observational restraints of the high-z quasar problem. Chapters 1 and 2 have, therefore, been expansive, requiring a working understanding of many disciplines tangential to the main body of this work. This vast net does, however, provides our model with multiple observational checks to ensure it remains consistent with current understanding. We, therefore, appreciate the wide reaching nature of deriving a complete black hole mass function, and the challenges self-consistency has presented to ensure the results of this work are robust.

In Chapter 3, we consider the results of the stellar evolution code SEVN to

analysis three pathways - single stellar evolution, failed binaries, and binaries - allowing for the formation of stellar mass black holes. Using galactic statistics we were able to expand this further into the formation of a stellar black hole mass function. The model remained robust when using alternate scaling relations, alternative stellar evolution codes revealed the critical impact of our model's pathways, and the implementation of the mergers of binaries allowed for comparisons to LIGO/Virgo observations and consideration of (young) star clusters, whose addition had limited impact on the overall stellar mass function whilst increasing our merger binary distribution.

We completed our total mass function in Chapter 4 through the derivation of the supermassive black hole mass function via gaseous dynamical friction and standard Eddington accretion through the use of the continuity equation. Our stellar black hole mass function provided the distribution for stellar mass black holes that would inspiral towards a central black hole allowing for it to rapidly grow through its lower mass phase ($M_\bullet < 10^{8-9}$ M$_\odot$), when accretion is much slower. The combination allowed for the overcoming of the high-z quasar problem, and analysis via the creation of a luminosity function through the tracking of Eddington ratios. Additionally, we found our method to show good agreement with other determinations of the supermassive black hole mass function.

5.1.1   Conclusions

The derivation of our stellar black hole mass function concluded with the following:

- Through the use of galaxy distribution statistic, parameterised via star formation rate, stellar mass, and metallicity, along with the compact remnant distribution calculated through the use of stellar evolutionary codes, a stellar black hole mass function can be derived. See Sect. 3.2 and Figs. 4.1.

- Such a function consists of a flat shape up until $m_\bullet < 50$ M$_\odot$, predominantly made up of black holes birthed from single stellar evolution when assuming a binary fraction of $f_{\star\star} = 0.5$; A rapidly declining high mass tail obtained through binary and failed binary star systems, where mass exchange is able to push remnants to higher masses culminating in a peak at $m_\bullet \approx 10^{2.1}M_\odot$. See Fig. 3.7.

- Binaries provide a limited contribution to the mass function, but serve as a invaluable tool for comparison to observational data through their

possible mergers (see Fig. 3.10). Overall the implementations of mergers in the mass function provides a limited transfer of mass from low to high masses (see Sect. 3.2.3 and Fig. 3.9).

- The distribution of primary masses for black hole binaries agree remarkable with LIGO/Virgo gravitational wave data for $m_\bullet \lesssim 40\ M_\odot$. Whilst the mass gap caused by both pulsational and non pulsational pair instability supernovae, as well as the mass loss due to the common envelope of tight black hole binaries, caused a rapid drop at higher masses. The possible solution of high merger environments, such as (young) star clusters, can be implemented with limited cost to the overall stellar mass function. See Sect. 3.4.2 and Fig. 3.14.

- The mass function remains of consistent form when undergoing changes in key fundamental relations, such as the star forming main sequence of galaxies and the fundamental metallicity relation. The most dramatic changes occur when shifting the stellar evolutionary code, though further investigation into additional algorithms would be required to determine the exact cause of these changes. Numerical simulations of stellar evolution are subject to large uncertainties in parameterising factors, such as the common envelope parameter, and further work could be completed regarding the interactions with this model and the underlying numerical simulations. See Sect. 3.4.1 and Fig. 3.12.

- The local stellar black hole relic mass density amounts to $\rho_\bullet \approx 5 \times 10^7\ M_\odot\ \mathrm{Mpc}^{-3}$, exceeding by more than two orders of magnitude that in supermassive black holes; this translates into an energy density parameter $\Omega_\bullet \approx 5 \times 10^{-4}$, implying that the total mass in stellar black holes amounts to $\lesssim 1\%$ of the local baryonic matter. See Fig. 3.8.

- This stellar black mass function will be able to serve as a light seed distribution at high-z. We see good comparison between our model and alternate channels - such as Pop-III stars, direct collapse of gas clouds, and mergers in nuclear star clusters - for the formation of high mass ($m_\bullet \gtrsim 150\ M_\odot$) stellar mass black holes at $z \sim 10$. See. Sect. 3.4.3 and Fig. 3.16. It is note worthy that this light seed distribution could be implemented in the prediction of future gravitational wave observatories, in particular those of the Einstein Telescope and LISA.

Regarding the supermassive black hole mass function our key takeaways:

- Supermassive black holes can grow in a reasonable time through the implementation of a twofold accretion model. Beginning with initial growth via gaseous dynamical friction, through the migration and merging of stellar mass black holes, allows for the rapid overcoming of the low mass accretion hurdle. After which standard Eddington gas accretion becomes the dominant channel of mass growth. The resulting supermassive black holes are concordant with observational restraints set out by the discovery of high mass ($M_\bullet > 10^9 M_\odot$) quasar at $z > 7$. See Sect. 4.2 and Fig. 4.1.

- Our model is able to recreate the observed luminosity function of AGNs, and is in good agreement with other estimation of the supermassive black hole mass function. Though our approach does not include a rapid decline at higher masses, this is due to our choice of standard (not super) Eddington accretion, which does not compromise our AGN luminosity function. See Sect. 4.2.6 and Fig. 4.4.

- Both our Eddington ratio distribution and co-evolution plane ($L_{AGN} - \psi$ relation) are in remarkable agreement with observed data. See Sect. 4.2.6 and Figs. 4.5 and 4.6.

- The model does not rely on gaseous dynamical friction, though the act of turning off the mechanism forces Eddington ratios $\lambda \gtrsim 1$, particular for $z \gtrsim 6$ candidates, so that seeds can arrive at masses in agreement with the extreme end of our Magorrian relation. Such rates of accretion are not theoretically restricted, but constitute a challenge when compared to observational restrictions; the formation of a heavy seed through an alternate channel could alleviate this tension but presents challenges of justification through detection. See, in particular, the comparison between the solid and dashed line in Fig. 4.4 and Fig. 4.2.

- Once more we have tested our model through the exchanging of fundamental relations. We find the most variation in the derived AGN luminosity function, that in most instances is recovered in the Eddington ratio distribution and supermassive black hole mass function showing a robustness to change. We believe our original assumptions are the most applicable under current observational restraints. See Sect. 4.3.2 and Fig. 4.10.

- We find a present supermassive black hole mass density of $\rho_\bullet \approx 6 \times 10^5 \ M_\odot \ \mathrm{Mpc}^{-3}$, in accordance with available estimates. See Fig. 4.8.

Separately, our conclusion for the total black hole mass function:

- The ultimate goal of this thesis has been to produce a self-contained, self-consistent black hole mass function from stellar to supermassive spanning ten orders of magnitude of mass. See Fig. 4.11.

- We have allowed the growth of black holes to supermassive masses, via gaseous dynamical friction and kept track of their movement through redshift using the continuity equation. This approach allows us to track the formation of intermediate mass black holes as they become supermassive, meaning we are able to connect our stellar and supermassive black hole mass functions; as well as serving as a heavy seed distribution.

- Our time dependent complete black hole mass function could find service in numerical simulations and semi-analytical models, and the use of it would be of keen interest; such as TOPSEM (Boco et al. 2023).

- Lastly, the integration of our total black hole mass function returns a staggering prediction for the number of black holes in the observable Universe, 40×10^{18}, with the overwhelming majority coming from stellar mass black holes.

5.2 Additional Work During ITN Secondments

Tangential to this thesis, time was spent undertaking secondments working with observational catalogues of AGNs to produce their Eddington ratio distributions. In particular, we examined IR and X-ray catalogues since this data would capture different phases of a supermassive black hole's growth. Sadly, this work is highly preliminary, thus these results will be presented without explanation and are to show additional avenues taken during the course of this thesis.

The IR work was undertaken, during a secondment in Durham, using the same catalogue as seen in Andonie et al. 2022. Analysing IR data is of crucial importance, because the dusty atmosphere of the host galaxy absorbs optical/UV light and reemits it in the Far-IR band. Since we expect the main growing phase of a central supermassive black hole to occur during the main star forming period of the host galaxy, the IR luminosity L_{IR} of AGNs allows for the probing of this period (this is the rise towards the peak seen in Fig. 4.2). This is reflected in the top panel of Fig. 5.1 where you can see typical Eddington values clustering around $\lambda \sim 0.3$.

The X-ray work was undertaken, during a secondment in Athens, using the catalogue of Georgakakis et al. 2017. X-ray observations of AGNs cover
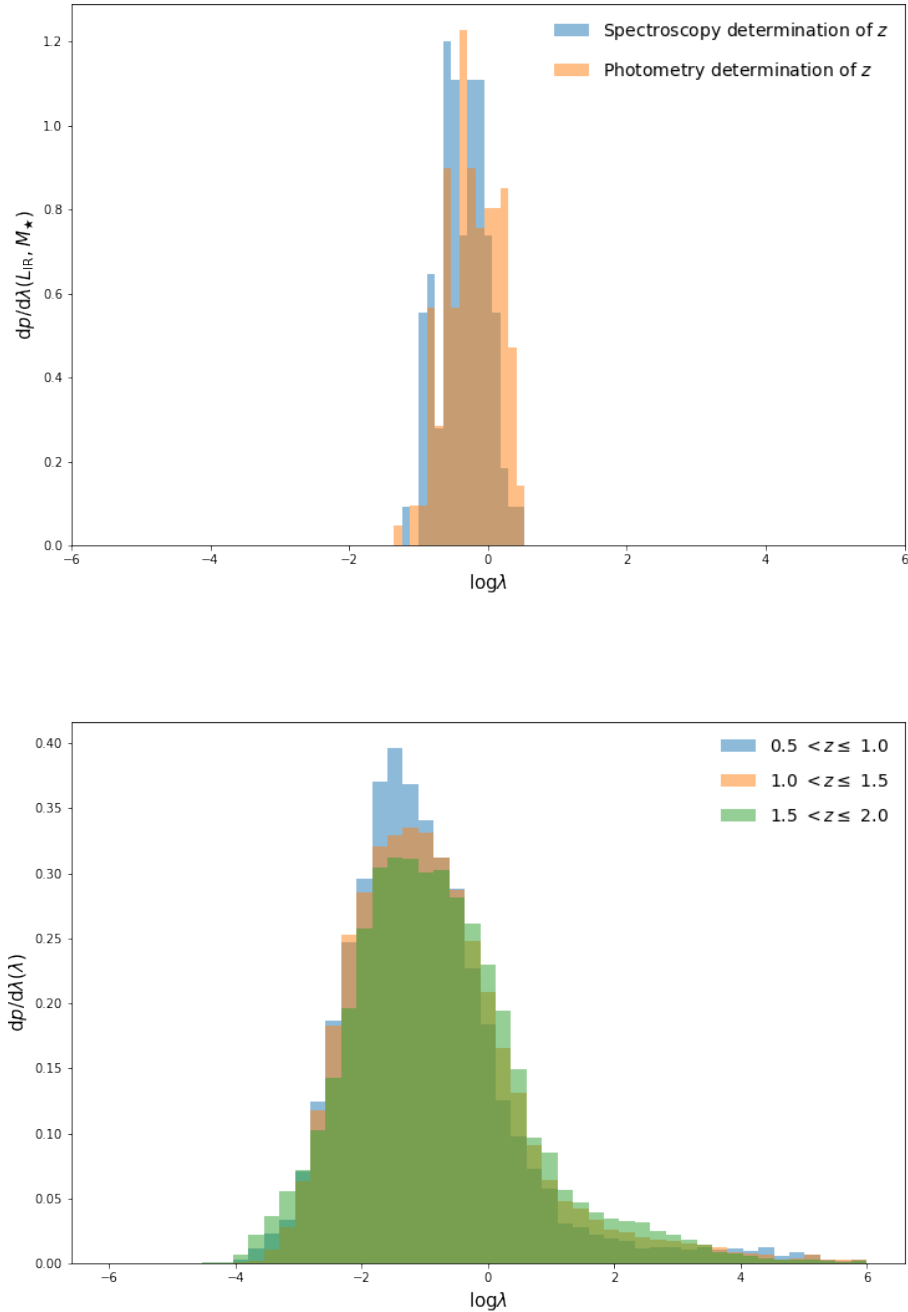
FIGURE 5.1: Top panel: Eddington ratio distribution for IR sources using the catalogue from Andonie et al. 2022. The blue histogram shows sources with z determined using spectroscopy methods, whilst the orange those using photometry. Bottom panel: Eddington ratio distribution for X-ray sources using the catalogue from Georgakakis et al 2017. Sources are divided into z bins spanning ranges $0.5 < z \leq 1.0$ (blue), $1.0 < z \leq 1.5$ (orange), $1.5 < z \leq 2.0$ (green).

the complete spectrum of black hole growth phases, including both the very early phase as well as the later decline. As a consequence the derived Eddington ratio distribution is very broad with a prominent tail towards low λ, centred around $\lambda \sim 1.8$. See the bottom panel of Fig. 5.1

The goal of this supplementary work was to begin a series of comparisons between the outputs of our model and the wider observational community. In particular, we see that IR and X-ray data will provide us an opportunity to scrutinise further the complete model. It should be stressed that the time possible for secondment work allowed for the ignition of ideas that have led to potential projects that could improve the model beyond its current form, and that we enjoy the prospect of spending more time working with the teams developing these catalogues to greater understand the benefits of our mutual aspirations.

5.3 Future Prospects

It would be interesting to exploit the galactic and stellar evolution prescriptions adopted here to populate a $N-$body simulation via subhalo clustering abundance matching technique (e.g., Ronconi et al. 2020) in order to derive a mock catalogue encapsulating the three-dimensional spatial distribution of stellar-mass BHs and of their galactic hosts. Another development could be a more detailed comparison of the properties of (super)massive BHs and host star forming galaxies, for example in terms of Eddington distributions as a function of BH environment and host galaxy properties (SFR, stellar mass, nuclear obscuration, etc.; e.g., Aird et al. 2018; Ananna et al. 2022).

Moreover, we plan to work out predictions for upcoming or future observations via space instruments like the James Webb Space Telescope and *Athena*. Specifically, young BHs lying at the centre or wandering in the nuclear regions of dusty starforming hosts may be detectable, even in the early stages of growth, via their X-ray and/or strongly extincted UV emissions; the latter could constitute a probe for the existence and abundance of intermediate mass BHs and could provide a characterisation of their main growth mechanisms. Finally, we aim to exploit the BH mass function derived here to estimate the rate of (super)massive BH mergers. Although their effect on the overall mass function is expected to be mild and confined at the very massive end and late cosmic times, these events can constitute powerful sources of gravitational waves (e.g., Barausse & Lapi 2021). Thus we will provide detailed forecasts for their detectability by the Laser Interferometer Space Antenna mission and by present and future Pulsar-Timing Array experiments.

Bibliography

[1] Abbott, R., Abbott, T.D., Abraham, S., et al. 2020, ApJ, 896, L44

[2] Abbott, R., Abbott, T.D., Abraham, S., et al. 2021a, ApJL, 913, L7

[3] Abbott, R., Abbott, T.D., Abraham, S., et al. 2021b, PRX, 11, 021053

[4] Abbott, R., Abbott, T.D., Abraham, S., et al. 2021c, ApJL, 915, L5

[5] Abramowicz, M., Czerny, B., Lasotas, J., et al., 1988, ApJ, 332, 646

[6] Ackley, K., Amati, L., Barbieri, C., et al. 2020, A&A, 643, A113

[7] Adamo, A., Zeidler, P., Kruijssen, J.M.D., et al. 2020, Sp. Sc. Rev., 216, 69

[8] Aird J., Coil A. L., Georgakakis A., et al. 2015b, MNRAS, 451, 1892

[9] Aird, J., Alexander, D. M., Ballantyne, D. R., et al. 2015a, ApJ, 815, 66

[10] Aird, J., Coil, A. L., & Georgakakis, A. 2018, MNRAS 474, 1225

[11] Aird, J., Coil, Alison L., & Kocevski, D.D. 2022, MNRAS, 515, 4, 4860

[12] Alexander, D.M., & Hickox, R.C. 2012, NewAR, 56, 93

[13] Alexander, T., & Natarajan, P. 2014, Science, 345, 1330

[14] Allevato, V., Shankar, F., Marsden, C., et al. 2021, ApJ, 916, 34

[15] Ananna, T.T., Weigel, A.K., Trakhtenbrot, B., et al. 2022, ApJS, 261, 1, 9

[16] Antoniadis, J., Arzoumanian, Z., Babak, S., et al. 2022, MNRAS, 510, 4873

[17] Antonini, F., Gieles, M., & Gualandris, A. 2019, MNRAS, 486, 5008

[18] Antonini, F., & Rasio, F. A. 2016, ApJ, 831, 187

[19] Arca Sedda, M., Mapelli, M., Spera, M., Benacquista, M., et al., 2020, ApJ, 894, 133

[20] Artale, M.C., Tissera, P.B., & Pellizza, L.J. 2015, MNRAS, 448, 3071

[21] Assef, R. J, Kochanek, C.S., Ashby, M.L.N., et al. 2011, ApJ, 728, 56

[22] Aversa, R., Lapi, A., De Zotti, G., et al. 2015, ApJ, 810, 74

[23] Azadi, M., Aird, J., Coil, A., et al. 2015, ApJ, 806 ,187

[24] Banados, E., Carilli, C., Walter, F., et al. 2018, ApJL, 861, L14

[25] Banados, E., Mazzucchelli, C., Momjian, E., et al. 2021, ApJ, 909, 80

[26] Banerjee, S. 2021, MNRAS, 500, 3002

[27] Barausse, E., & Lapi, A. 2021, Massive Black Hole Mergers, in Handbook of Gravitational Wave Astronomy, eds. C. Bambi, S. Katsanevas and K. Kokkotas (Singapore: Springer)

[28] Baron, D. & Ménard, B., 2019, MNRAS, 487, 3, 3404

[29] Barro, G., Faber, S. M., Dekel, A., et al. 2016, ApJ, 820, 120

[30] Baxter, E.J., Croon, D., McDermott, S.D., & Sakstein, J. 2021, ApJL, 916, L16

[31] Behroozi, P., Wechsler, R.H., Hearin, A.P., & Conroy, C. 2019, MNRAS, 488, 3143

[32] Belczynski, K., Benacquista, M.,& Bulik, T. 2010, ApJ, 725, 816

[33] Belczynski, K., Heger, A., Gladysz, W., et al. 2016, A&A, 594, A97

[34] Benson, A. J., Džanović, D., Frenk, C., et al., 2007, MNRAS, 379, 841

[35] Bernal, C. G., & Sanchez-Salcedo, F. J. 2013, ApJ, 775, 72

[36] Bialy, S. & Sternberg, A., 2019, APJ, 881, 2, 160

[37] Bianchini, F., Fabbian, G., Lapi, A., et al. 2019, ApJ, 871, 136

[38] Binney, J. & Tremaine, S., 2008, Galactic Dynamics: Second Edition

[39] Bisigello, L., Caputi, K. I., Grogin, N., & Koekemoer, A. 2018, A&A, 609, A82

[40] Blanton, M. R., Hogg, D. W., Bahcall, N. A., et al., 2003, ApJ, 592, 819

[41] Boco, L., Lapi, A., Chruslinska, M., et al. 2021, ApJ, 907, 110

[42] Boco, L., Lapi, A., Goswami, S., et al. 2019, ApJ, 881, 157

[43] Boco, L., Lapi, A., Sicilia, A.M., et al. 2021a, JCAP, 10, 035

[44] Boco, L., Lapi, A., & Danese, L. 2020, ApJ, 891, 94

[45] Bongiorno, A., Schulze, A., Merloni, A., et al. 2016, A&A, 588, A78

[46] Bonnor, W. B., 1956, MNRAS, 116, 351

[47] Bonoli, S., Marulli, F., Springel, V., et al. 2009, MNRAS, 396, 423

[48] Boogaard, L. A., Brinchmann, J., Bouche, N., et al. 2018, A&A, 619, A27

[49] Bouwens, R. J., Oesch, P. A., Stefanon, M., et al. 2021, AJ, 162, 47

[50] Breivik, K., Coughlin, S., Zevin, M., et al. 2020, ApJ, 898, 71

[51] Buitrago, F., Trujillo, I., Curtis-Lake, E., et al. 2017, MNRAS, 466, 4888

[52] Caffau, E., Ludwig, H. G., Steffen, M., Freytag, B., & Bonifacio, P. 2011, SoPh, 268, 255

[53] Cao, X., 2010, ApJ, 725, 388

[54] Capelo, P.R., Volonteri, M., Dotti, M., et al., 2015, MNRAS, 447, 2123

[55] Caputi, K. I., Deshmukh, S., Ashby, M. L. N., et al., 2017, ApJ, 849, 45

[56] Carnall, A.C., McLure, R.J., Dunlop, J.S., et al., 2019, MNRAS, 490, 417

[57] Carraro, R., Rodighiero, G., Cassata, P., et al., 2020, A&A, 642, A65

[58] Carraro, R., Shankar, F., Allevato, V., et al., 2022, MNRAS, 512, 1185

[59] Cassará, L. P., Maccagni, D., Garilli, B., et al., 2016, A&A, 593, A9

[60] Castro, T., Marra, V. & Quartin, M., 2016, MNRAS, 463, 1666

[61] Chabrier, G., 2003, ApJL, 586, L133

[62] Chabrier, G., 2003, PASP, 115, 809, 763

[63] Chan, C., Müller, B., Heger, A., et al., 2018, APJ, 852, 1, L19

[64] Chan, C., Müller, B., Heger, A., 2020, MNRAS, 495, 4, 3751

[65] Chandar, R., Fall, S.M., Whitmore, B.C., & Mulia, A.J. 2017, ApJ, 849, 128

[66] Chiappini, C., Matteucci, F., & Gratton, R. 1997, ApJ, 477, 765

[67] Chruslinska, M., & Nelemans, G. 2019, MNRAS, 488, 5300

[68] Cimatti, A., Fraternali, F., & Nipoti, C. 2020, Introduction to Galaxy Formation and Evolution (Cambridge: Cambridge Univ. Press)

[69] Citro, A., Pozzetti, L., Moresco, M., & Cimatti, A. 2016, A&A, 592, A19

[70] Courteau, S., Cappellari, M., de Jong, R. S., et al. 2014, RvMP, 86, 47

[71] Cueli, M. M., 2021, A&A, 645, A126

[72] Cuesta, J., 2008, Panaramic Views of Galaxy Formation and Evolution, 399, 121

[73] Curti, M., Mannucci, F., Cresci, G., & Maiolino, R. 2020, MNRAS, 491, 944

[74] D'Amato, Q., Gilli, R., Vignali, C., et al., 2010, A&A, 636, 37

[75] Daddi, E., Alexander, D. M., Dickinson, M., et al., 2007, ApJ, 670, 173

[76] Daddi, E., Delvecchio, I., Dimauro, P., et al., 2022, A&A, 661, L7

[77] Dai, Y. S., Wilkes, B.J., Bergeron, J., et al., 2018, MNRAS, 478, 4238

[78] Dai, Y. S., Elvis, M., Bergeron, J., et al., 2014, ApJ, 791, 113

[79] Das, A., Schleicher, D.R.G., Leigh, N.W.C., & Boekholt, T.C.N., 2021, MNRAS, 503, 1051

[80] Davidzon, I., Ilbert, O., Laigle, C., et al., 2017, A&A, 605, A70

[81] Davis, B. L., Graham, A. & Cameron, E., 2018, ApJ, 869, 2, 113

[82] Davis, S. W., & Laor, A. 2011, ApJ, 728, 98

[83] Delvecchio, I., Gruppioni, C., Pozzi, F., et al. 2014, MNRAS, 439, 2736

[84] Devecchi, B., Volonteri, M., Rossi, E. M., Colpi, M., & Portegies Zwart, S., 2012, MNRAS, 421, 1465

[85] Di Carlo, U.N., Giacobbo, N, Mapelli, M., et al., 2019, MNRAS, 487, 2947

[86] Di Carlo, Ugo N., Mapelli, Michela, Giacobbo, N., et al., 2020, MNRAS, 498, 495

[87] Di Matteo, T., Croft, R. A. C., Feng, Y., Waters, D., & Wilkins, S., 2017, MNRAS, 467, 424

[88] Di Matteo, T., Khandai, N., de Graf, C., et al., 2012, ApJL, 745, L29

[89] Di Matteo, T., Springel, V., Hernquist, L. 2005, Nature, 433, 604

[90] Diemand, J., 2005, IAU Colloq. 198: Near-fields cosmology with dwarf elliptical galaxies, 211

[91] Diemer, B., Kravtsov, A. & More, S., 2013, ApJ, 779, 2, 159

[92] Ding, X., Liao, K., Biesiada, M., & Zhu, Z.-H. 2020, ApJ, 891, 7

[93] Ding, X., Silverman, J., Treu, T., et al., 2020, ApJ, 888, 37

[94] Dominik, M., Berti, E., O'Shaughnessy, R., et al., 2015, ApJ, 806,263

[95] Driver, S. P., Robotham, A., Kelvin, L., et al., 2012, MNRAS, 427, 3244

[96] Dullo, B.T., Gil de Paz, A., & Knapen, J.H., 2021, 908, 134

[97] Dunstall, P. R., Dufton, P. L., Sana, H., et al., 2015, A&A, 580, A93

[98] Duras, F., Bongiorno, A., Ricci, F., et al., 2020, A&A, 636, A73

[99] Ebert, R., 1955, ZAP, 37, 217

[100] Einstein, A., 1915, Sitzungsberichte der Königlich Preußischen Akademie der Wissenchaften zu Berlin, 844

[101] El-Badry, K., Quataert, E., Weisz, D.R., Choksi, N., & Boylan-Kolchin, M. 2019, MNRAS, 482, 4528

[102] eLisa Consortium 2013, arXiv e-print, 1305.5720

[103] Elmegreen, B.G. 2018, ApJ, 869, 119

[104] Ertl, T., Janka H.-Th., Woosley, S., et al., 2016, ApJ, 818, 2, 124

[105] Escala, A., Larson, R. B., Coppi, P. S., & Mardones, D. 2004, ApJ, 607, 765

[106] Event Horizon Telescope Collaboration, 2019, ApJ, 875, L1

[107] Event Horizon Telescope Collaboration, 2022, ApJ, 930, L12

[108] Fan, L., Han, Y., Nikutta, R., Drouart, G., & Knudsen, K. K. 2016, ApJ, 823, 107

[109] Farr, W.M., Sravan, N., Cantrell, A., et al. 2011, ApJ, 741, 103

[110] Ferrarese, L., 2002, ApJ, 578, 1, 90

[111] Ferrarese, L., & Merritt, D. 2000, ApJL, 539, L9

[112] Ferre-Mateu, A., Mezcua, M., Trujillo, I., et al. 2015, ApJ, 808, 79

[113] Fiore, F., Feruglio, C., Shankar, F., et al. 2017, A&A, 601, A143

[114] Fiore, F., Puccetti, S., Grazian, A., et al. 2012, A&A, 537, A16

[115] Fowler, W. & Hoyle F., 1964 ApJS, 9, 201

[116] Fragione, G., Leigh, N.W.C., Perna, R. 2019, MNRAS, 488, 2825

[117] Fraley, G., 1968, Ap&SS, 2, 1, 96

[118] Friedmann, A., 1922, Zeitschrift f"ur Physik, 10, 377

[119] Fryer, C. & Kalogera, V., 2001, ApJ, 554, 1, 548

[120] Fryer, C., 1999, ApJ, 522, 1, 413

[121] Fryer, C., Belczynski, K., Wiktorowicz, G., et al., 2012, ApJ, 749, 1, 91

[122] Fujimoto, S., Brammer, G.B., Watson, D., et al. 2022, Nature, 604, 261

[123] Fukugita, M., & Peebles, P.J.E. 2004, ApJ, 616, 643

[124] Gaia Collaboration, 2018, A&AP, 616, A10

[125] Gabriella, A., Anumarlapudi, A., Archibald, A. M., et al., 2023, ApJL, 951, 2, L50

[126] Gallazzi, A., Bell, E. F., Zibetti, S., Brinchmann, J., & Kelson, D. D. 2014, ApJ, 788, 72

[127] Gallazzi, A., Charlot, S., Brinchmann, J., & White, S. D. M. 2006, MN-RAS, 370, 1106

[128] Gebhardt, K., Bender, R., Bower, G., et al., 2000, ApJL, 539, 1, L13

[129] Georgakakis, A., Aird, J., Schulze, A., et al. 2017, MNRAS, 471, 1976

[130] Ghez, A. M., Salim, S., Weinberg, N., 2008, ApJ, 689, 2, 1044

[131] Giacobbo, N., & Mapelli, M. 2018, MNRAS, 480, 2011

[132] Giallongo E., Menci N., Fiore F., et al. 2012, ApJ, 755, 124

[133] Giersz, M., Leigh, N., Hypki, A., Lutzgendorf, N., & Askar, A. 2015, MN-RAS, 454, 3150

[134] Goddard, Q.E., Bastian, N., & Kennicutt, R.C. 2010, MNRAS, 405, 857

[135] Gompertz, B.P., Levan, A.J., Tanvir, N.,R. 2020, ApJ, 895, 58

[136] Gonzalez Delgado, R.M., Perez, E., Cid Fernandes, R., et al. 2017 A&A, 607, A128

[137] Graham, A. W. 2007, MNRAS, 379, 711

[138] Granato, G. L., Silva, L., Monaco, P., et al. 2001, MNRAS, 324, 757

[139] Granato, G.L, De Zotti, G., Silva, L., Bressan, A., Danese, L. 2004, ApJ, 600, 580

[140] Griffin, A.J., Lacey, C.G., Gonzalez-Perez, V., et al. 2019, MNRAS, 487, 198

[141] Grisoni, V., Spitoni, E., Matteucci, F., et al. 2017, MNRAS, 472, 3637

[142] Grudic, M.Y., Kruijssen, J.M.D., Faucher-Giguere, C.-A., et al. 2021, MNRAS, 506, 3239

[143] Gruppioni, C., Bethermin, M., Loiacono, F., et al. 2020, A&A, 643, A8

[144] Gültekin, K., Richstone, D., Gebhardt, K., et al., 2009, ApJ, 698, 1, 198

[145] Häring, N. & Rix, H.-W., ApJL, 2004, 604, 2, L89

[146] Habouzit, M., Onoue, M., Banados, E., et al. 2022, MNRAS, 511, 3751

[147] Haehnelt, M.G., Natarajan, P., Rees, M.J. 1998, MNRAS, 300, 817

[148] Harokane, Y., Ouchi, M., Oguri, M., et al., 2023, ApJS, 265, 1, 5

[149] Hayashi, C., 1961, PASJ, 13, 450

[150] Hill, D. T., Driver, S., Cameron, E., et al., 2010, MNRAS, 404, 1215

[151] Hopkins, P. F., Richards, G. T., & Hernquist, L. 2007, ApJ, 654, 731

[152] Hubble, E., 1929, Proceedings of the National Academy of Science, 15, 168

[153] Hunt, L., Dayal, P., Magrini, L., & Ferrara, A. 2016, MNRAS, 463, 2002

[154] Hurley, J. R., Tout, C. A., & Pols, O. R. 2002, MNRAS, 329, 897

[155] Iben, I. Jr., 1966, APJ, 143, 483

[156] Inayoshi, K., Visbal, E., & Haiman, Z. 2020, ARA&A, 58, 27

[157] Inoue, Y., Tanaka, Y.T., & Isobe, N. 2016, MNRAS, 461, 4329

[158] Ivanova, N., Justham, S., Chen, X., et al. 2013, A&ARv, 21, 59

[159] Izquierdo-Villalba, D., Bonoli, S., Dotti, M., et al. 2020, MNRAS, 495, 4681

[160] Johansson, J., Thomas, D., & Maraston, C. 2012, MNRAS, 421, 1908

[161] Johnson, L. C., Seth, A. C., Dalcanton, J. J., et al., 2012, ApJ, 752, 2, 95

[162] Justham, S., & Schawinski, K. 2012, MNRAS, 423, 1641

[163] Kalirai, J., Anderson, J., Dotter, A., et al., 2013, ApJ, 763, 2, 110

[164] Karashi, S., Ivison, R. J., Caputi, K. I., et al. 2015, ApJ, 810, 133

[165] Kawamura, S., Ando, M., Seto, N., et al. 2021, PTEP, 2021eA105

[166] Kelly, B. C., & Merloni, A. 2012, AdAst, 2012, 7

[167] Kelly, B. C., & Shen, Y. 2013, ApJ, 764, 45

[168] Kelvin, L. S., Driver, S. P., Robotham, A., et al., 2014b, MNRAS, 439, 1245

[169] Kennicutt, R. C. Jr, 1983, ApJ, 272, 54

[170] Kennicutt, R. C. Jr, 1989, ApJ, 344, 685

[171] Kennicutt, R. C. Jr, & Evans, N. J. 2012, ARA&A, 50, 531

[172] Kim, Y., & Im, M. 2019, ApJ, 879, 117

[173] Kimpson, T.O., Spera, M., Mapelli, M., Ziosi, B.M. 2016, MNRAS, 463

[174] King, A. R. 2005, ApJL, 635, L121

[175] King, A., & Pounds, K. 2015, ARA&A, 53, 115

[176] Kormendy, J. & Ho, L. C., 2013, ARA&A, 51, 1, 511

[177] Kovetz, E.D., Cholis, I., Breysse, P.C., & Kamionkowski, M. 2017, PRD, 95, 103010

[178] Kravtsov, A. & Borgani, S., 2012, ARAA, 50, 353

[179] Kroupa, P., 2001, MNRAS, 322, 2, 231

[180] Kroupa, P., Subr, L., Jerabkova, T., Wang, L. 2020, MNRAS, 498, 5652

[181] Kruijssen, J.M.D. 2012, MNRAS, 426, 3008

[182] Krumpe, M., Miyaji, T., Coil, A., et al., 2018, MNRAS, 474, 2, 1773

[183] Krumpe, M., Miyaji, T., Husemann, B., et al., 2015, ApJ, 815, 1, 21

[184] Kulkarni G., Worseck G., & Hennawi J. F. 2018, MNRAS, 488, 1035

[185] Kumamoto, J., Fujii, M. S., & Tanikawa, A. 2019, MNRAS, 486, 3942

[186] Lacey, C. G., Baugh, C. M., Frenk, C. S., et al. 2010, MNRAS, 405, 2

[187] Lacey, C. & Cole, S., 1993, MNRAS, 262, 627

[188] Lacy M., Ridgway S. E., Sajina A., et al. 2015, ApJ, 802, 102

[189] Lang, P., Schinnerer, E., Smail, I., et al. 2019, ApJ, 879, 54

[190] Lapi, A., Gonzalez-Nuevo, J., Fan, L., et al. 2011, ApJ, 742, 24

[191] Lapi, A., Pantoni, L, Boco, L,, & Danese, L., 2020, ApJ, 897, 81

[192] Lapi, A., Pantoni, L., Zanisi, L., et al. 2018, ApJ, 857, 22

[193] Lapi, A., Raimundo, S., Aversa, R., et al. 2014, ApJ, 782, 69

[194] Lapi, A., Shankar, F., Mao, J., et al. 2006, ApJ, 650, 42

[195] Larson, R.B. 1998, MNRAS, 301, 569

[196] Latif, M. A., & Ferrara, A. 2016, PASA, 33, 51

[197] Lee, J., Yi, S., Elahi, P., et al., 2014, MNRAS, 445, 4, 4197

[198] Lehmer, B.D., Eufrasio, R.T., Basu-Zych, A., et al. 2021, ApJ, 907, 17

[199] Leja, J., Speagle, J.S., Ting, Y.-S., et al. 2022, ApJ, 936, 2, 165

[200] Lemaître, G., 1927, Annales de la Soci'et'e Scientifique de Bruxelles, A47, 49

[201] Li, C., de Grijs, R., & Deng, L. 2013, MNRAS, 436, 1497

[202] Li, J., Silverman, J.D., Ding, X., et al. 2021, ApJ, 922, 142

[203] Li, L.-X. 2012, MNRAS, 424, 1461

[204] Li, P., Lelli, F., McGaugh, S., et al., 2019, ApJL, 886, L11

[205] Li, Y.-R., Ho, L. C., & Wang, J.-M. 2011, ApJ, 742, 33

[206] Lin, X., Fang, G., Xue, Y., Fan, L., & Kong, X. 2021, ApJ, 911, 59

[207] Lin, X., Xue, Y., Fang, G., Fan, L., Le, H.A.N, Ayubinia, A. 2022, RAA, 22, 015010

[208] Lodato, G., & Natarajan, P. 2006, MNRAS, 371, 1813

[209] Lodato, G., & Natarajan, P. 2007, MNRAS, 377, L64

[210] Loveday, J., Norberg, P., Baldry, I., et al., 2012, MNRAS, 420, 1239

[211] Luo, F., Zhao, Y.-H., Li, J., Guo, Y.-J., & Liu, C., 2021, 21, 11, 272

[212] Lupi, A., Haardt, F., Dotti, M., et al., 2016, MNRAS, 456, 299

[213] Lynden-Bell, D. 1969, Nature, 223, 690

[214] Madau P., & Rees, M.J. 2001, ApJL, 551, L27

[215] Madau, P., Haardt, F., & Dotti, M. 2014, ApJ, 784, L38

[216] Madau, P., & Dickinson, M. 2014, ARA&A, 52, 415

[217] Madau, P., & Fragos, T. 2017, ApJ, 840, 39

[218] Magorrian, J., Tremaine, S., Richstone, D., et al. 1998, AJ, 115, 2285

[219] Maiolino, R., & Mannucci, F. 2019, A&ARv, 27, 3

[220] Mancuso, C., Lapi, A., Prandoni, I., et al. 2017, ApJ, 842, 95

[221] Mancuso, C., Lapi, A., Shi, J., et al. 2016a, ApJ, 823, 128

[222] Mancuso, C., Lapi, A., Shi, J., et al. 2016b, ApJ, 833, 152

[223] Mannucci, F., Cresci, G., Maiolino, R., Marconi, A., & Gnerucci, A. 2010, MNRAS, 408, 2115

[224] Mannucci, F., Salvaterra, R., & Campisi, M. A. 2011, MNRAS, 414, 1263

[225] Manti S., Gallerani S., Ferrara A., Greig B., Feruglio C., 2017, MNRAS, 466, 1160

[226] Mao, S. 2012, RAA, 12, 947

[227] Mapelli, M. 2016, MNRAS, 459, 3432

[228] Mapelli, M. 2020, Fr. Astron. Sp. Sci., 7, 38

[229] Mapelli, M., Colpi, M. & Zampieri, L., 2009, MNRAS, 395, 1, L71

[230] Mapelli, M., Ripamonti, E., Zampieri, L., Colpi, M., & Bressan, A. 2010, MNRAS, 408, 234

[231] Mapelli, M., Santoliquido, F., Bouffanais, Y., et al. 2021, MNRAS, 505, 339

[232] Marconi, A., Risaliti, G., Gilli, R., et al. 2004, MNRAS, 351, 169

[233] Martin-Navarro, I., Shankar, F., & Mezcua, M. 2022, MNRAS, 513, L10

[234] Marulli, F., Bonoli, S., Branchini, E., Moscardini, L., Springel, V. 2008, MNRAS, 385, 1846

[235] Massardi, M., Enia, A.F.M., Negrello, M., et al. 2018, A&A, 610, A53

[236] Mayer, L., Fiacconi, D., Bonoli, S., et al. 2015, ApJ, 810, 51

[237] Mayer, L., Kazantzidis, S., Escala, A., & Callegari, S. 2010, Nature, 466, 1082

[238] Mayer, L., & Bonoli, S. 2019, RPPh, 82, 6901

[239] McAlpine, S., Harrison, C.M., Rosario, D.J., et al. 2020, MNRAS, 494, 5713

[240] McConnell, M.J., Ma, C.-P., Gebhardt, K., et al. 2011, Nature, 480, 215

[241] McConnell, N. J., & Ma, C.-P. 2013, ApJ, 764, 184

[242] McKernan, B., Ford, K.E.S., Lyra, W., & Perets, H.B. 2012, MNRAS, 425, 460

[243] McLeod D. J., Donnan, C., McLure, R., et al., 2023, arXiv e-print, 2304.14469

[244] McLure, R. & Dunlop, J., 2003, The Mass of Galaxies at Low and High Redshift, 26

[245] Mehrgan, K., Thomas, J., Saglia, R., et al. 2019, ApJ, 887, 195

[246] Merloni, A., Bongiorno, A., Bolzonella, M., et al. 2010, ApJ, 708, 137

[247] Merloni, A., & Heinz, S. 2008, MNRAS, 388, 1011

[248] Mészáros, P., 1974, A&AP, 37, 2, 225

[249] Miller, M.C., & Hamilton, D.P. 2002, ApJ, 576, 894

[250] Mineshige, S., Kawaguchi, T., Takeuchi, M., & Hayashida, K. 2000, PASJ, 52, 499

[251] Mirabel, I.F., Dijkstra, M., Laurent, P., Loeb, A., & Pritchard, J. R. 2011, A&A, 528, A149

[252] Miyaji T. et al., 2015, ApJ, 804, 104

[253] Mo, H., van den Bosch, F., & White, S. D. M. 2010, Galaxy Formation and Evolution (Cambridge: Cambridge Univ. Press)

[254] Moffett, A. J., Ingarfield, S. A., Driver, S., et al., 2016, MNRAS, 457, 1308

[255] Montero-Dorta, A. D. & Prada, F., 2009, MNRAS, 399, 1106

[256] Mor, R., Netzer, H., Trakhtenbrot, B., Shemmer, O., & Lira, P. 2012, ApJL, 749, L25

[257] Morishita, T., Abramson, L. E., Treu, T., et al. 2019, ApJ, 877, 141

[258] Mortlock, D. J., Warren, S. J., Venemans, B. P., et al. 2011, Nature, 474, 616

[259] Moster, B.P., Naab, T., & White, S.D.M. 2013, MNRAS, 428, 3121

[260] Moster, B.P., Naab, T., & White, S.D.M. 2018, MNRAS, 477, 1822

[261] Moustakas, J., Coil, A. L., Aird, J., et al. 2013, ApJ, 767, 50

[262] Mullaney, J. R., Pannella, M., Daddi, E., et al. 2012, MNRAS, 419, 95

[263] Mullaney, J., Daddi, E., Béthermin, M., et al., 2012, ApJL, 753, 2, L30

[264] Mutlu-Pakdil, B., Seigar, M.S., & Davis, B.L. 2016, ApJ, 830, 117

[265] Natarajan, P. 2014, Gen. Rel. Grav., 46, id. 1702

[266] Natarajan, P. 2021, MNRAS, 501, 1413

[267] Nguyen, N.H., Lira, P., Trakhtenbrot, B., et al. 2020, ApJ, 895, 74

[268] Nobuta, K., Akiyama, M., Ueda, Y., et al. 2012, ApJ, 761, 143

[269] Novak, M., Smolcic, V., Delhaize, J., et al. 2017, A&A, 602, 5

[270] Ocran, E. F., Taylor, A. R., Vaccari, M., et al., 2020, MNRAS, 491, 5911

[271] Ocran, E. F., Taylor, A. R., Vaccari, M., et al., 2021, MNRAS, 500, 4685

[272] Oesch, P. A., Bouwens, R. J., Illingworth, G. D., et al. 2018, ApJ, 855, 105

[273] Oppenheimer, J. R. & Volkoff, G. M., 1939, Physical Review, 55, 4, 374

[274] Ostriker, E. C. 1999, ApJ, 513, 252

[275] O'Connor, E. & Ott, C., 2011, APJ, 730, 2, 70

[276] Pacucci, F., Natarajan, P., Volonteri, M., Cappelluti, N., & Urry, C.M. 2017, ApJ, 850, L42

[277] Paczynski, B. 1986, ApJ, 304, 1

[278] Page, M. J., Brindle, C., Talavera, A., et al. 2012, MNRAS, 426, 903

[279] Pantoni, L., Lapi, A., Massardi, M., Goswami, S., & Danese, L. 2019, ApJ, 880, 129

[280] Pantoni, L., Lapi, A., Massardi, M., et al. 2021, MNRAS, 504, 928

[281] Papovich, C., Finkelstein, S. L., Ferguson, H. C., Lotz, J. M., & Giavalisco, M. 2011, MNRAS, 412, 123

[282] Paynter, J., Webster, R., & Thrane, E. 2021, Nature Astron., 5, 560

[283] Perna, R., Wang, Y.-H., Farr, W.M., Leigh, N., & Cantiello, M. 2019, ApJL, 878, L1

[284] Pezzulli, G., & Fraternali, F. 2016, MNRAS, 455, 2308

[285] Pfeffer, J., Kruijssen, J.M.D., Crain, R.A., & Bastian, N. 2018, MNRAS, 475, 43092

[286] Piro, A. L. & Thompson, T. A., 2014, ApJ, 794, 1, 28

[287] Planck Collaboration 2020, A&A, 641, A6

[288] Planck Collaboration, Aghanim, N., Akrami, Y., et al. 2020, A&A, 641, A6

[289] Popesso, P., Concas, A., Cresci, G., et al. 2022, MNRAS, 519, 1, 1526

[290] Portegies Zwart, S. F., & Yungelson, L. R. 1998, A&A, 332, 173

[291] Portegies Zwart, S.F., Baumgardt, H., Hut, P., Makino, J., McMillan, S.L.W. 2004, Nature, 428, 724

[292] Posti, L. & Helmi, A., 2019, A&AP, 621, A56

[293] Postnov, K.A., & Yungelson, L.R. 2006, Liv. Rev. Rel., 9, 6

[294] Powell, M. C., Cappelluti, N., Urry, C. M., et al., 2018, ApJ, 858, 2, 110

[295] Prada, F., Klypin, A., Simonneau, E., et al., 2006, ApJ, 645, 2, 1001

[296] Raghavan, D., McAlister, H. A., Henry, T. J., et al. 2010, ApJS, 190, 1

[297] Raimundo, S. I., Fabian, A. C., Vasudevan, R. V., Gandhi, P., & Wu, J. 2012, MNRAS, 419, 2529

[298] Reed, S. L., Banerji, M., Becker, G. D. 2019, MNRAS, 487, 1874

[299] Reines A. E. & Volonteri M., 2015, APJ, 812, 82

[300] Ren, K., & Trenti, M. 2021, ApJ, 923, 110

[301] Ricarte, A., & Natarajan, P. 2018, MNRAS, 481, 3278

[302] Riess, A. G., Casertano, S., Yuan, W., et al., 2021, ApJL, 908, 1, L6

[303] Rinaldi, P., Caputi, K.I., van Mierlo, S., et al. 2022, ApJ, 930, 128

[304] Rodighiero, G., Brusa, M, Daddi, E., et al. 2015, ApJL, 800, L10

[305] Rodighiero, G., Daddi, E., Baronchelli, I., et al. 2011, ApJL, 739, L40

[306] Rodighiero, G., Enia, A., Delvecchio, I., et al. 2019, ApJ, 877, L38

[307] Rodriguez, C.L., Kremer, K., Chatterjee, S., et al. 2021, RNAAS, 5, 19

[308] Rodriguez, C.L., Morscher, M., Pattabiraman, B., et al. 2015, PhRvL, 115e1101

[309] Rodriguez-Gomez, V., Pillepich, A., Sales, L. V., et al. 2016, MNRAS, 458, 2371

[310] Roper, W. J., Thomas, P., A. & Srisawat, C., 2020, MNRAS, 494, 3, 4509

[311] Rosario, D. J., Santini, P., Lutz, D., et al. 2012, A&A, 545, 45

[312] Ruderman, M. A. & Spiegel, E. A., 1971, ApJ, 165, 1

[313] Ruiter, A., Ferrario, L., Belczynski, K., et al., 2019, MNRAS, 484, 1, 698

[314] Sahu N., Graham A. W., Davis B. L., 2019, ApJ, 876, 155

[315] Salpeter, E. E. 1955, ApJ, 121, 161

[316] Salucci, P., Szuszkiewicz, E., Monaco, P., & Danese, L. 1999, MNRAS, 307, 637

[317] Sana, H., de Mink, S. E., de Koter, A., et al. 2012, Science, 337, 444

[318] Sanchez-Salcedo, F., & Brandenburg, A. 2001, MNRAS, 322, 67

[319] Sanders, R. L., Shapley, A. E., Jones, T., et al. 2021, ApJ, 914, 19

[320] Saracco, P., Marchesini, D., La Barbera, F., et al. 2020, ApJ, 905, 40

[321] Sargent, M. T., Bthermin, M., Daddi, E., & Elbaz, D. 2012, ApJL, 747, L31

[322] Savorgnan, G. A. D., 2016, APJ, 821, 2, 134

[323] Scalo J. M., 1986, Fundamentals Cosmic Phys., 11, 1

[324] Schmedt, M., 1959, ApJ, 129, 243

[325] Schreiber, C., Pannella, M., Elbaz, D., et al. 2015, A&A, 575, 74

[326] Schulze, A., & Wisotzki, L. 2014, MNRAS, 438, 3422

[327] Scoville, N., Aussel, H., Sheth, K., et al. 2014, ApJ, 783, 84

[328] Scoville, N., Sheth, K., Aussel, H., et al. 2016, ApJ, 820, 83

[329] Sesana, A., Barausse, E., Dotti, M., Rossi, E. M. 2014, ApJ, 794, 104

[330] Sesana, A., Shankar, F., Bernardi, M., & Sheth, R.K. 2016, MNRAS, 463, L6

[331] Seth, A., Agüeros, M., Lee, D., et al., 2008, ApJ, 678, 1, 116

[332] Shakura, N. I., & Sunyaev, R. A. 1973, A&A, 24, 337

[333] Shankar, F., Allevato, V., Bernardi, M., et al. 2020a, Nature Astron., 4, 282

[334] Shankar, F., Bernardi, M., Sheth, R.K., et al. 2016, MNRAS, 460, 3119

[335] Shankar, F., Marulli, F., Mathur, S., et al., 2012, AAP, 540, A23

[336] Shankar, F., Salucci, P., Granato, G. L., de Zotti, G., & Danese, L. 2004, MNRAS, 354, 1020

[337] Shankar, F., Weinberg, D. H., & Miralda-Escude, J. 2009, ApJ, 690, 20

[338] Shankar, F., Weinberg, D.H., Marsden, C., et al. 2020b, MNRAS, 493, 1500

[339] Shankar, F., Weinberg, D.H., & Miralda-Escude, J. 2013, MNRAS, 428, 421

[340] Shanker F., 2020, Nature Astronomy, 4, 282

[341] Shen, Y., 2009, ApJ, 704, 89

[342] Shen, X., Hopkins, P.F., Faucher-Giguere, A.-A., et al. 2020, MNRAS, 495, 3252

[343] Shi, J., Lapi, A., Mancuso, C. 2017, 843, 105

[344] Sicilia, A., Lapi, A., Boco, L., et al. 2022, ApJ, 924, 56

[345] Sicilia, A., Lapi, A., Boco, L., et al., 2022, ApJ, 934, 1, 66

[346] Silk, J. 1968, ApJ, 151, 459

[347] Silk, J., & Rees, M. J. 1998, A&A, 331, L1

[348] Simpson, J. M., Smail, I., Swinbank, A. M., et al. 2015, ApJ, 807, 128

[349] Slipher, V. M., 1913, Lowell Observatory Bulletin, 2, 56

[350] Smail, I., Dudzeviciute, U., Stach, S. M., et al. 2021, MNRAS, 502, 3426

[351] Small, T. A., & Blandford, R. D. 1992, MNRAS, 259, 725

[352] Smartt, S., 2015, PASA, 32, e016

[353] Smit, R., Bouwens, R. J., Franx, M., et al. 2012, ApJ, 756, 14

[354] Soltan, A. 1982, MNRAS, 200, 115

[355] Sota, A., Maız Apellaniz, J., Morrell, N. I., et al. 2014, ApJS, 211, 10

[356] Speagle, J. S., 2014, ApJS, 214, 15

[357] Speagle, J. S., Steinhardt, C. L., Capak, P. L., & Silverman, J. 2014, ApJS, 214, 15

[358] Spera, M. & Mapelli, M., 2017, MNRAS, 470, 4, 4739

[359] Spera, M., Mapelli, M., Giacobbo, N., et al. 2019, MNRAS, 485, 889

[360] Spera, M., Mapelli, M., & Bressan, A. 2015, MNRAS, 451, 4086

[361] Spera, M., & Mapelli, M. 2017, MNRAS, 470, 4739

[362] Spilker, J. S., Marrone, D. P., Aravena, M., et al. 2016, ApJ, 826, 112

[363] Spinoso, D., Bonoli, S., Valiante, R., Schneider, R., Izquierdo-Villalba, D. 2022, MNRAS, 518, 3, 4672

[364] Srisawat, C., Knebe, A., Pearce F. R., et al., 2013, 436, 1, 150

[365] Stanley, F., Alexander, D. M., Harrison, C. M., et al. 2017, MNRAS, 472, 2221

[366] Stanley, F., Harrison, C. M., Alexander, D. M., et al. 2015, MNRAS, 453, 591

[367] Steinborn, L.K., Hirschmann, M., Dolag, K., et al. 2018, MNRAS, 481, 341

[368] Steinhardt, C. L., Speagle, J. S., & Capak, P. 2014, ApJL, 791, L25

[369] Sternberg, A., et al., 2014, APJ, 790, 1, 10

[370] Stone, M., Pope, A., McKinney, J., et al., 2022, ApJ, 934, 1, 27

[371] Strömgren, B., 1939, ApJ, 89, 526

[372] Suh, H., Civano, F., Trakhtenbrot, B., et al. 2020, ApJ, 889, 32

[373] Sutherland, R. & Dopita, M. A., 1993, APJS, 88, 253

[374] Tadaki, K., Iono, D., Yun, M. S., et al. 2018, Nature, 560, 613

[375] Tadaki, K.-I., Genzel, R., Kodama, T., et al. 2017a, ApJ, 834, 135

[376] Tadaki, K.-I., Kodama, T., Nelson, E. J., et al. 2017b, ApJL, 841, L25

[377] Talia, M., Cimatti, A., Giulietti, M., et al. 2021, ApJ, 909, 23

[378] Talia, M., Pozzi, F., Vallini, L., et al. 2018, MNRAS, 476, 3956

[379] Tanaka, T., & Haiman, Z. , 2009, A&A, 696, 1798

[380] Tang, S.-P., Wang, H., Wang, Y.-Z., et al. 2020, ApJ, 892, 56

[381] Tauris, T., Sanyal, D., Yoon, S.-C., et al., 2013, A&A, 558, A39

[382] Thomas, D., Maraston, C., Bender, R., & Mendes de Oliveira, C. 2005, ApJ, 621, 673

[383] Thomas, D., Maraston, C., Schawinski, K., Sarzi, M., & Silk, J. 2010, MNRAS, 404, 1775

[384] Thomas, D., Maraston, C., Schawinski, K., et al., 2010, MNRAS, 404, 4, 1775

[385] Thomas, J., McConnell, N.J., Greene, J., et al. 2016, Nature, 532, 340

[386] Thomas, P. A., Onions, J., Tweed, D., et al., 2015, arXiv e-print, 1508.05388

[387] Thorne, K. S. 1974, ApJ, 191, 507

[388] Timmes, F., Woosley S., Weaver, T., 1996, ApJ, 657, 834

[389] Tinker, J., Kravtsov, A., Klypin, A., et al., 2008, ApJ, 688, 709

[390] Tinsley, B. M. 1980, Fund. Cosm. Phys., 5, 287

[391] Trakhtenbrot, B., Volonteri, M., & Natarajan, P. 2017, ApJ, 836, L1

[392] Tremaine, S., Gebhardt, K., Bender, R., et al. 2002, ApJ, 574, 740

[393] Tremonti, C., Heckman, T. M., Kauffmann, G., et al., 2004, ApJ, 613, 2, 898

[394] Trinca, A., Schneider, R., Valiante, R., et al. 2022, MNRAS, 511, 616

[395] Ueda Y., Akiyama M., Hasinger G., Miyaji T., & Watson M. G. 2014, ApJ, 786, 104

[396] van Dishoeck E. & Black, J., 1988, ApJ, 334, 771

[397] van Dokkum, P., & Conroy, C., 2010, Nature, 468, 940

[398] Venemans, B. P., Walter, F., Decarli, R., et al. 2017a, ApJL, 851, L8

[399] Venemans, B. P., Walter, F., Decarli, R., et al. 2017b, ApJ, 845, 154

[400] Venemans, B.P., Decarli, R., Walter, F. 2018, ApJ, 866, 159

[401] Vestergaard, M., & Osmer, P.S. 2009, ApJ, 699, 800

[402] Vignali, C., Piconcelli, E., Perna, M., et al. 2018, MNRAS, 477, 780

[403] Vika, M., Driver, S. P., Graham, A. W., & Liske, J. 2009, MNRAS, 400, 1451

[404] Volonteri, M. 2010, A&ARv, 18, 279

[405] Volonteri, M. 2010, A&ARv, 18, 279,

[406] Volonteri, M., Capelo, P., Netzer, H., et al., 2015, MNRAS, 449, 2, 1470

[407] Volonteri, M., Habouzit, M., & Colpi, M. 2021, Nature Rev. Physics, 3, 732

[408] Volonteri, M., Sikora, M., Lasota, J.-P., Merloni, A. 2013, ApJ, 775, 94

[409] Volonteri, M., Silk, J., & Dubus, G. 2015, ApJ, 804, 148

[410] Wang, B. & Liu, D., RA&A, 2020, 20, 9, 135

[411] Wang, F., Yang, J., Fan, X., et al. 2019, ApJ, 884, 30

[412] Wang, F., Yang, J., Fan, X., et al. 2021, ApJ, 907, L1

[413] Wang, R., Wagg, J., & Carilli, C. L. 2013, ApJ, 773, 44

[414] Wang, T., Elbaz, D., Alexander, D. M., et al. 2017, A&A, 601, A63

[415] Warren, M. S., Abazajian, K., Holz, D. E., et al., 2006, ApJ, 646, 881

[416] Watarai, K.-Y., Fukue, J., Takeuchi, M., & Mineshige, S. 2000, PASJ, 52, 133

[417] Watson, W. A., Iliev, I. T., D'Aloisio, A., et al., 2013, MNRAS, 433, 1230

[418] Whitaker, K. E., Franx, M., Leja, J., et al. 2014, ApJ, 795, 104

[419] Wiersma, R., Schaye, J. & Smith, B. D., et al., 2009, MNRAS, 393, 1, 99

[420] Williams, C.C., Spilker, J.S., Whitaker, K.E., et al. 2021, ApJ, 908, 54

[421] Willott, C. J., Bergeron, J., & Omont, A. 2015, ApJ, 801, 123

[422] Willott, C., Delorme, P., Reylé, C., et al., 2010, AJ, 139, 3, 906

[423] Woosley, S. E., 2017, ApJ, 836, 2, 244

[424] Woosley, S. E., Heger, A., & Weaver, T. A. 2002, RvMP, 74, 1015

[425] Woosley, S., Sukhbold, T., Janka, H.-T., et al., 2020, ApJ, 896, 1, 56

[426] Xu, L., Rieke, G. H., Egami, E., et al. 2015, ApJS, 219, 18

[427] Yang, G., Brandt, W. N., Alexander, D. M., et al. 2019, 485, 3721

[428] Yang, Y., Bartos, I., Gayathri, V., et al. 2019, Phys. Rev. Lett., 123, 181101

[429] Yu, Q., & Lu, Y. 2004, ApJ, 602, 603

[430] Yu, Q., & Lu, Y. 2008, ApJ, 689, 732

[431] Yu, Q., & Tremaine, S. 2002, MNRAS, 335, 965

[432] Zahid, H. J., Kewley, L., Bresolin, F., 2011, ApJ, 730, 2, 137

[433] Zavala, J. A., Casey, C. M., Manning, S. M., et al. 2021, ApJ, 909, 165

[434] Zhu, P., Ho, L.C., & Gao, H. 2021, ApJ, 907, 6